Apport à la compréhension du comportement sous irradiation des aciers austénitiques

Kan Ma

PSL UNIVERSITÉ PARIS

THÈSE DE DOCTORAT
DE L'UNIVERSITÉ PSL

Préparée à Chimie ParisTech

Irradiation behavior of Ni-based model materials: towards a better understanding of solute effects on fcc structure under ion irradiation

Soutenue par
Kan MA
Le 25 11 2020

École doctorale n°388
Chimie Physique et Chimie Analytique de Paris-Centre

Spécialité
Chimie Physique

Composition du jury :

Brigitte DÉCAMPS Directrice de recherche, IJCLab	Présidente, examinatrice
Jean-Philippe COUZINIÉ Maître de conférence, ICMPE	Rapporteur
Philippe CASTANY Maître de conférence, INSA-Rennes	Rapporteur
Robin SCHÄUBLIN Directeur de recherche, ETH Zurich	Examinateur
Marie LOYER-PROST Ingénieur de recherche, CEA	Encadrante
Frédéric PRIMA Professeur, ENSCP	Directeur de thèse
Philippe VERMAUT Maître de conférences, ENSCP	Invité

Chimie Paris ParisTech | PSL

Declaration

I hereby declare that except where specific reference is made to the work of others, the contents of this dissertation are original and have not been submitted in whole or in part for consideration for any other degree or qualification in this, or any other university. This dissertation is my own work and contains nothing which is the outcome of work done in collaboration with others, except as specified in the text and Acknowledgments. This dissertation contains fewer than 65,000 words including appendices, bibliography, footnotes, tables and equations and has fewer than 150 figures.

Kan MA
December 2020

Acknowledgements

I would like to write this part in French because I believe it is the best language to express my gratitude to the people that I have met and with whom I have worked in this thesis.

Cette thèse est le fruit de trois années de travail au Service de Recherches de Métallurgie Physique (SRMP) au CEA-Saclay, avec une belle collaboration avec le laboratoire de Métallurgie Structurale à Chimie ParisTech et le Laboratoire de Physique des 2 infinis Irène Joliot-Curie (IJCLab) dans l'Université Paris-Saclay. Je tiens donc d'abord à remercier sincèrement à mes encadrants Dr. Marie Loyer-Prost et professeur Frédéric Prima. Merci à Marie pour les savoirs, les compétences et les bonnes pratiques transmises dans la thèse, et aussi pour tes guides, tes aides, tes présences et tes compréhensions à tout moment dans ces trois années. Tu es toujours motivée et m'encourage souvent. Merci à Frédéric pour tous les réunions régulières d'avancement, tes soutiens et tes encadrements derrière ce travail malgré la quantité de travail que tu avais. J'ai énormément de chance d'être encadré par vous deux.

Je remercie Jean-Philippe Couzinié et Philippe Castany pour avoir accepté d'être rapporteurs et également à Brigitte Décamps et Robin Schäublin, qui font partie du jury en tant qu'examinateurs. Merci aussi à Philippe Vermaut de participer en tant qu'invité.

Je n'oublie évidemment pas mes collègues du laboratoire d'accueil : l'équipe JANNuS du SRMP au CEA-Saclay. Je remercie d'abord Jean-Luc Bécharde et Céline Cabet en tant que chef du service et chef du labo qui ont fourni tous les soutiens pour la réalisation de cette thèse ; Gaëlle Gutierrez, Frédéric Leprêtre, Ana-Paula Barabé, Hervé Martin, Guillaume Adroit, Stéphanie Pellegrino, Laurent Roux en tant qu'une équipe soudée, compétente et accueillante. Merci pour leur soutien sur les manipes d'irradiation et de m'avoir fait goûter plein de chose pendant les pique-niques JANNuS. J'ai énormément apprécié les deux courses de relais et les repas de découvert que nous avons fait ensemble. J'aimerais aussi remercier Brigitte Décamps et l'équipe JANNuS-Orsay du IJCLab pour leur accueil et les irradiations in-situ avec le soutien du réseau national d'accélérateurs pour les études des Matériaux sous Irradiation (EMIR). Je tiens à remercier particulièrement Brigitte pour les manipes in-situ, les cours et les séances au microscope, les investissements du temps et les riches discussions sur les résultats de cette thèse.

J'aimerais remercier mes collègues au SRMP qui ont participé à cette thèse. Merci à Adrien Morrellec, Anne-Hélène, Camille Flament, Patrick Bonnaillie qui m'ont beaucoup aidé sur les utilisations des équipements, les préparations des échantillons et les caractérisations. Merci particulièrement à Patrick pour les déjeuners ensemble quand nous étions seuls au 2ième étage et pour ton esprit critique sur le travail « chinois ». Même si vous êtes tous parti du SRMP, je n'oublie Merci aussi à Estelle Meslin en tant que responsable du MET qui maintient le MET toujours en bon état. Je remercie aussi Thomas Jourdan, Mihai-Cosmin Marinica, Maylise Nastar pour leur temps consacré à faire d'excellentes modélisations dans le cadre de ce travail. Ils ont toujours plein d'idée et sont très ouvert pour les discussions. Leur travail a permis de faire de belles couplage expérience-simulation qui ont beaucoup approfondi mes compréhensions sur les résultats de la thèse. Je remercie également Olivier Tissot et Thierry Vandenberghe pour les manipes du microscope à haute tension (THT) malgré toutes les difficultés qu'ils ont eu à redémarrer ce microscope pendant deux ans. Merci à Benoît Arnal pour ses maintiens solides et régulières au FIB qui fonctionnent toujours bien.

Je n'oublie pas de remercier les personnes qui m'ont fourni des soutiens hors de la France. Robin Schaeublin qui nous a accueilli à ETH Zurich dans son labo pour les manipes TEM-EDS. Ses connaissances et riches d'expériences au MET et les équipements très performants dans le laboratoire ScopeM m'ont beaucoup impressionné. Un grand merci aussi à Lu Chenyang et Xiu Pengyuan pour leur aide sur le flash-polishing. Vous m'avez encouragé d'aller jusqu'au fond sur cette technique. Sans la réussite du flash-polishing, nous ne pourrions pas répondre à certaines questions importantes.

Je n'oublie pas tous mes amis qui m'ont accompagné pendant la thèse. Les jeunes du JANNuS : Marion Bricout, Gauthier Muller, Marie José Saleh Afif. Il est très agréable d'être dans le même bureau que vous. Mes amis doctorants au SRMP : Marie Landeiro Dos Reis, Thomas Soyez, Quentin Tencé, Liangzhao Huang, Kangmin Li et Yimi Wang. Mes amis doctorants au SRMA anciens camarades à l'IFCEN : Yang Li et Yanjun Wang. Mes amis à Chimie ParisTech : Fan Sun, Richard Portier et Bingnan qui m'ont bien accueilli chaque fois quand je suis allé à l'école. Merci tous les voyages et toutes les séances que nous avons fait pendant la thèse. Je garde de beaux souvenirs de vous tous et je vous souhaite une bonne continuation après la thèse.

Enfin, je remercie sincèrement mes parents qui m'ont soutenu toujours derrière dans la vie. C'était toujours difficile à cause de la distance (>10 milles km) mais je pense toujours à vous. Je remercie infiniment ma copine Ziling Peng. Depuis sept ans, nous nous entendons et nous soutenons l'un à l'autre y compris ces trois ans de thèse. Je ne me doute jamais que tu vas enfin réussir ta thèse malgré toutes les difficultés..

C'est avec une grande joie que j'ai pu faire cette thèse et vous rencontrer. En vous remerciant tous, je vous souhaite la bonne santé et les meilleurs.

Contents

Chapter 1

Introduction

Austenitic Stainless Steels (ASSs) are foreseen as cladding material for next generation reactors even though their swelling under irradiation will limit the fuel burn-up (Yvon, 2016). The void swelling is a macroscopic volume extension induced by irradiation which affects the physical dimension and mechanical properties of materials. The improvements of swelling resistance of austenitic steels remains a key issue for the development of next generation reactors. The swelling of austenitic steels is a complicated phenomenon composed of two stages, an incubation period and a steady swelling state (Garner, 2012; Was, 2016; Yvon, 2016). During the steady swelling state, all the austenitic steels exhibit a constant swelling rate independent of their chemical compositions and initial microstructure. On the contrary, the incubation period is sensitive to compositional and microstructural factors. Massive studies are devoted to improve the irradiation tolerance of advanced austenitic steels. An efficient way is the fine tuning of major elements (ratio of Ni/Cr) and the addition of minor solutes like Ti (Garner and Wolfer, 1984; J.L. Seran, 2015). However, a descriptive mechanism of the effects of these solutes has not yet been unambiguously demonstrated.

The objective of this thesis is to better understand the behavior of austenitic structure under irradiation and the mechanism of Cr and Ti (alone in solid solution or combined with carbon) on the microstructure evolution in the early stages of irradiation. However, austenitic steels have very complex composition composed of a dozen alloying elements and impurities. It is difficult to study the fine influence of a specific solute and makes the study beyond the capability of simulation. To simplify the system, pure nickel (Ni) and its alloys (Ni-Cr, Ni-Ti and Ni-Ti-C) are used as fcc model materials for austenitic steels.

The manuscript is presented as the following plan. The next chapter (**Chapter 2**) is a detailed bibliography which summarizes the industrial context of the subject, a brief review of radiation damage, and current studies on the Ni-based model materials and solute effects. In **Chapter 3**, the studied materials, sample preparations, irradiation experiments

and characterization techniques are described. Then, it is followed by three chapters on experiment results.

Firstly, we study the irradiation behavior of Ni in **Chapter 4** as it is important to fully characterize the reference system in order to identify the real solute effects in future comparative experiments. The characterization focuses on 3 characteristic features of the microstructure: Frank loop nature, irradiation microstructure (loop density, size and Burgers vectors) and microstructural evolution under irradiation (growth rate of dislocation loops).

1. The nature of Frank loops is an important feature indicating the dominant point defect (interstitials or vacancies). In the literature, Frank loops were identified as interstitial-type in most cases (Chen and Ardell, 1976; Ishino et al., 1984; Mazey and Hudson, 1970; Urban, 1971; Yoo and Stiegler, 1977) while small meta-stable vacancy loops were also claimed (Ishino et al., 1984; Robinson and Jenkins, 1981; Urban, 1971; Wakai et al., 2002). To conclude unambiguously on this point, high purity Ni is irradiated using self-ions in order to avoid effects of impurities and the influence of sample form, dose and temperature is investigated;
2. The influence of thickness on irradiated microstructure is characterized at different temperatures as the presence of surfaces affects significantly radiation-induced defects in Ni (Ishino, 1997; Ishino et al., 1984). The thickness-dependency of loop density and size shows directly surface effects which should be identified. Meanwhile, the influence of surfaces on loop type is also studied;
3. Influence of thickness on microstructure evolution is revealed at different temperature also to identify surface effects to provide guideline for comparative studies in the alloys.

In **Chapter 5**, we study the influence of an addition of Cr and Ti on the three parameters presented above. The influence of an addition of 0.4 weight percent (0.4%) of solute (Cr or Ti) on Frank loop nature is shown in function of sample form and temperature. Then the influence of Ti variation on Frank loop nature is studied at 510°C to investigate the existence of a critical solute concentration for a change of loop nature. Then, influence of an addition of solute on the irradiated microstructure (loop density, size and type) is shown. Finally, solute effects on microstructural evolution (loop growth rate) is studied.

The addition of Ti and C is well know to affect strongly the swelling of austenitic structure (Mazey et al., 1980; Sekimura and Ishino, 1991). Thus, the influence of a carbon addition in Ni-Ti is studied in **Chapter 6** to reveal the combining effects of Ti and C on the three characteristic features of microstructure. Then, the existence of TiC precipitates is revealed by diffraction and chemistry analysis.

Chapter 7 is devoted to the discussion of results. Finally, the general conclusions and some perspectives are presented in the last chapter.

Chapter 2

Bibliography

Austenitic stainless steels are foreseen as the first candidates for the fuel cladding material in next-generation Sodium-cooled Fast Reactors (SFRs). As the cladding in SFRs will undergo a very harsh service environment (high neutron displacement damage at high temperature), a great amount of research on the irradiation behavior of austenitic steels has been conducted to improve the reliability and the performance of austenitic steels in future nuclear systems (Garner, 2012; Was, 2016; Yvon, 2016). Empirically, the fine-tuning of major elements (Ni, Cr) and the addition of some minor solutes (such as Ti) improve the radiation resistance of austenitic steels (Yvon, 2016). However, descriptive mechanisms of these solute effects are still not unambiguously demonstrated.

To better understand fundamental mechanisms of these solute effects, it is essential to well control the studied system avoiding effects of other factors (impurities, secondary phases etc.). One way to do so is to use model materials. For this purpose, Ni and Ni-based model alloys have been commonly used as model materials for austenitic steels because Ni is the major constituent of austenitic steels that hold the face-centered cubic (fcc) structure.

In this chapter, we present the state of the art on the subject. The first section describes the industrial context of the application of austenitic steels in SFRs. It details the key issue of these materials, the voids swelling induced by irradiation, and current research on the swelling impact of effects of alloying elements. In the second section, we briefly present some fundamental aspects of radiation damage and major modifications of microstructure induced by irradiation in the fcc structure, including the creation of structural defects and segregation. The third section presents the current research status of radiation damage in fcc model materials: Ni and Ni-based alloys (Ni-Ti and Ni-Cr). Then, the fourth part gives a brief introduction to the current study on possible mechanisms of solute effects in Ni systems. Finally, a summary of bibliographic research and key points in this study is presented.

2.1 Industrial context: austenitic stainless steels in Gen-IV reactors

2.1.1 Development of Sodium-cooled Fast Reactors

The population growth and the industrial expansion require a fast increase in energy supply. Considering the limited quantity of fossil reserves and the environmental dependence of renewable energy, it is of primary importance to develop sustainable, stable and low-carbon energies. The nuclear industry seems to offer a good solution even after two severe accidents. The Generation IV (Gen IV) nuclear reactors with inherent safety is designed in order to improve the nuclear safety and to make a better use of uranium and transmute long-life radioactive waste. They are required to provide a permanent energy solution and produce electricity at a reasonable cost with better sustainability and greater security.

Based on these requirements, six families of reactors were selected as Gen IV reactors in the beginning of 21st century in Gen IV forum (Pioro, 2016). Among these concepts, the Sodium-cooled Fast Reactors (SFRs) have relatively rich exploitation experiences and engineering feedback thanks to researches and operations for several decades in different countries (France, the UK, Germany, Japan, the United States, and the Russian Federation) (Aoto et al., 2014). Long before the Gen IV forum, France, as a pioneer developer of nuclear reactors, has successfully exploited three SFRs, Rapsodie (20MWt, 1967-1983), Phénix (560MWe, 1973-2010) and Superphénix (1240MWe, 1984-1998). Despite several incidents, the success of Phénix and Superphénix provides a sound basis for the development of future SFR systems.

In France, the development of the next-generation SFRs for industrial demonstration is expected. Its development is directly related to material improvements. The requirement for an increased service life of 60 years compared to 40 years for former sodium-cooled systems is a key challenge for in-core materials (Yvon, 2016). It requires to revisit and refine the behavior of the established materials in terms of their high-temperature strength under irradiation over very long periods. Improvements in the manufacture process, the heat treatment, and the chemical composition for their reliability and performance will be demanded and a deep insight into these improvements should be obtained.

2.1.2 Service environment and candidates of cladding materials

In-core materials in SFRs are subjected to a severe service environment with aggressive operation conditions (Figure 2.1). Due to a high operating temperature together with a high fast neutron flux, the SFR concept is a huge challenge for in-core materials. They must have an excellent mechanical performance at high and low temperature (including high thermal

creep properties), good compatibility with coolant (avoiding liquid metal embrittlement and corrosion). The fuel cladding should also have good resistance to radiation (swelling and irradiation-induced creep).

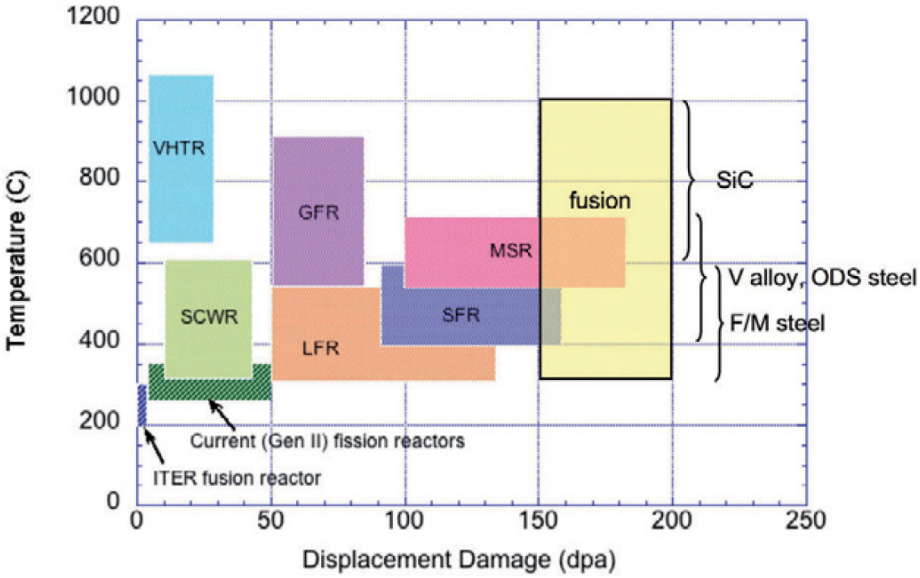

Figure 2.1 Service environment of fuel cladding materials in different types of reactors (Zinkle and Busby, 2009)

Fuel cladding is the first barrier for the nuclear safety, preventing any leakage of radioactive matters into the primary circuit coolant then into the environment. Thus, several factors have to be taken into consideration when selecting cladding materials: i) compatibility with reactor design considering neutron adsorption, moderating factor; ii) mature industrial production; iii) adapted mechanical properties along the fuel cycle; iv) resistance to corrosion; v) resistance to irradiation; vi) resistance against a combined effect of the above damages.

Austenitic Stainless Steels (ASSs) present remarkable inherent advantages for a nuclear application. Firstly, iron-based materials absorb few fast neutrons, which allows optimizing neutron utilization. Secondly, their mechanical properties are satisfying (good ductility and fatigue-creep resistance) over a large temperature range. Then, austenitic steels resist well against corrosion in various environments. Finally, their production is controlled, industrialized and mature. Thus, austenitic steels were widely used in SFRs for in-core components (fuel cladding and structural components) (Garner, 2012; Was, 2016). As presented above, the cladding of SFRs undergoes harsh environmental conditions in terms of irradiation and temperature. Particular attention is drawn by their behavior under irradiation.

2.1.3 Void swelling of austenitic stainless steels under irradiation

Unlike the vessel and structural components, the cladding is subjected closely and directly to neutron radiation. Despite all the other advantages, ASSs present a main limitation which is a macroscopic volume extension induced by irradiation, so-called void swelling (Bates and Powell, 1981; Cawthorne and Fulton, 1967; Lauritzen et al., 1969). It was firstly observed in austenitic steels in 1967 (Cawthorne and Fulton, 1967). Figure 2.2 presents the swelling that occurred in a 20% cold work (CW) 316 austenitic steel irradiated up to approximately 75 dpa (displacement per atom) in a liquid metal fast reactor (Straalsund et al., 1982). This phenomenon draws attention of communities since decades and ample evidences indicate a severe swelling issue of ASS cladding in SFRs. It remains an important safety issue and a crucial factor limiting the lifetime of the fuel assemblies. Although some innovative iron-based materials (such as Oxides Dispersed-Strengthened Steels (ODS)) are developed and exhibit excellent resistance against swelling (Yvon et al., 2015) , the stability and fabrication procedure still need further research. Therefore, austenitic steels are nowadays considered as the most reliable and promising cladding materials for the future SFRs and their swelling remains an unavoidable subject.

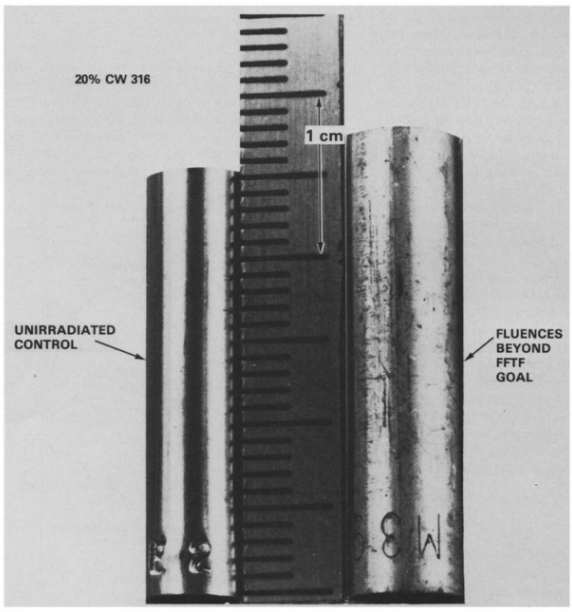

Figure 2.2 Swelling in 20% CW 316 ASS irradiated by fast neutron to 1.5×10^{23} $neutrons/cm^2$ (Straalsund et al., 1982).

ASS swelling is a complex phenomenon sensitive to material parameters (crystallographic structure, microstructure, etc.), chemical composition and environmental variables (temperature, damage rate, etc.) (Bates and Powell, 1981; Garner and Wolfer, 1984). Figure 2.3(a) shows the dose-dependency of swelling at 600°C. There are two regimes in the swelling process

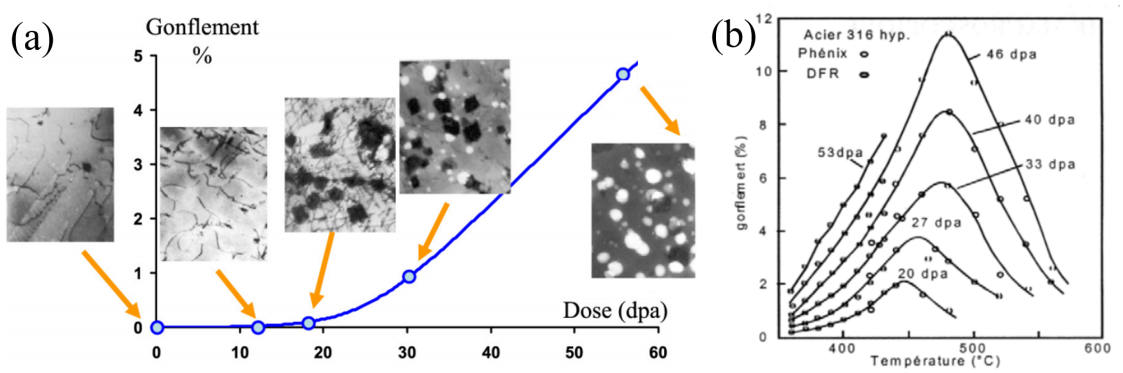

Figure 2.3 Swelling of SA 316 steels in function of (a) dose irradiated at 600°C in Phénixa; (b) temperature irradiated in Phénix and DFR (modified from (Dubuisson, 2011)).

of austenitic steels. The first regime is a transient regime, so-called incubation period that corresponds to the early stages of irradiation where no macroscopic change takes place but microstructure evolves as illustrated by TEM images in Figure 2.3(a)). S.J. Zinkle et al. and Etienne et al. reported that dislocation loops are formed, grow and then develop a network during this phase (Etienne et al., 2010; Zinkle et al., 1993). Once the irradiation dose exceeds a threshold, austenitic steels start to swell and rapidly achieve a steady state with a constant swelling rate (Garner, 2012; Garner and Brager, 1985) as shown in (Figure 2.3(a)) for doses $>$ 30 dpa.

Figure 2.3(b) shows the temperature dependency of swelling depends. With given irradiation conditions (neutron flux, temperature) in SFRs, the swelling is found to be the most severe between 450°C and 500°C (Dubuisson, 2011). The temperature-dependency of the swelling rate in the steady state is reported by many authors and it is related to the formation of voids under irradiation (Garner and Brager, 1985; Garner et al., 1985; Johnston et al., 1974; Yvon et al., 2015).

Factors affecting the swelling of ASSs has been a popular topic for decades in order to reduce the swelling. In the following subsection, the role of two major factors, the chemical composition and initial microstructure, is presented to find the key point of reducing the swelling.

2.1.4 Impact factors on swelling

2.1.4.1 Chemical composition

To improve the performance of materials, it is a natural idea to optimize the chemical composition In France, massive experiments on ASSs were performed since decades to accumulate swelling data in function of composition. Figure 2.4 summarizes these results. It

shows that the threshold of the swelling has been significantly increased over one hundred dpa (J.L. Seran, 2015). The improvements are mainly attributed to the fine-tuning of major solute content (Ni/Cr) and minor solute (Ti), as indicated in Figure 2.4. However, the swelling rate at steady-state seems insensitive to the composition. This phenomenon was observed by other authors (Garner and Wolfer, 1984). These experiments contribute to the development of an advanced austenitic materials, so-called austenitic improved materials (AIM) or 15/15Ti, from the 316 series in France. A first austenitic steel AIM1 is foreseen as the first candidate for the cladding material for the next SFR. Table 2.1 presents the chemical composition of AIM1.

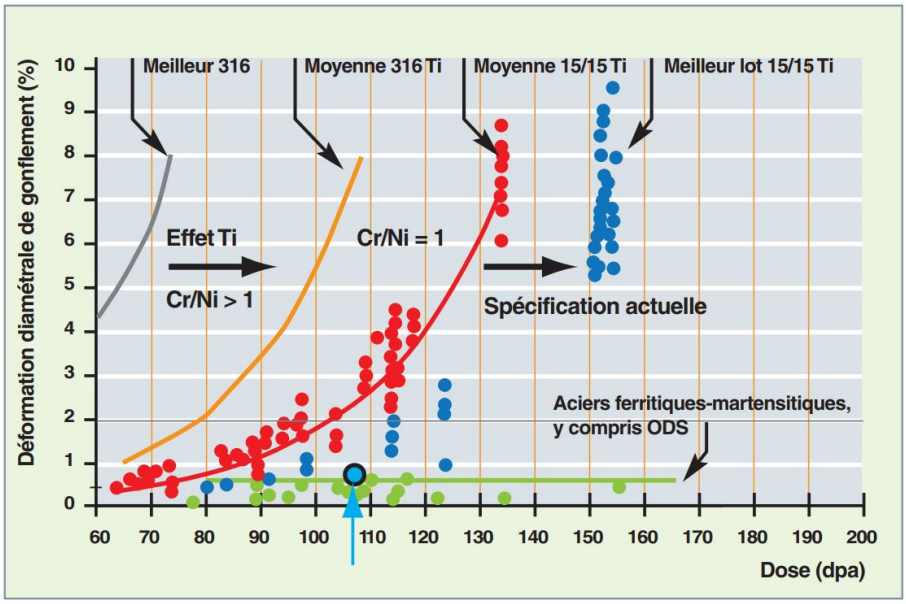

Figure 2.4 Swelling behavior of different austenitic stainless steels and ferritic-martensitic (F/M) steels used as core structure in Phénix (J.L. Seran, 2015).

Table 2.1 Chemical composition of AIM1 (wt%) (Yvon, 2016)

Elements	C	Cr	Ni	Mo	Mn	Si	Ti	Nb	N	P	B	Fe
Max.	0.1	15	15.5	1.5	1.6	0.9	0.44	-	-	0.045	0.006	bal.
Min.	0.05	14.5	15	1.5	1.5	0.8	0.4	-	-	0.04	-	bal.

2.1.4.2 Initial microstructure

The initial microstructure of the steel impacts also greatly its irradiation behavior of materials. One of the most important factors is the initial dislocation network, usually developed by cold work or aging. Neutron irradiations proved that cold work can in most cases strongly reduce the swelling of austenitic steels in terms of threshold dose of incubation

period but has no effect on the swelling rate (Brager, 1975; Wakai et al., 2002). 20% of cold work is optimal for the use of ASS in SFRs. However, some articles (Garner et al., 1997; Wakai et al., 2002) show that the efficiency of cold work against swelling depends clearly on the composition and the irradiation temperature. In certain cases, a cold work can even favor the swelling and reduce the incubation period to 0 dpa (Garner et al., 1997).

2.1.5 Effect of chromium and titanium on swelling

As shown in Figure 2.4, Ti and Cr are two important solutes affecting the swelling of ASSs. In this subsection, we present some studies on their effects.

2.1.5.1 Ti-stabilization

According to numerous studies, titanium (Ti) is a remarkable minor solute found to greatly affect the swelling of ASS under neutron (Boothby and Williams, 1988; Garner et al., 1985; Lee et al., 1979; Muroga and Yoshida, 1992; Sekimura and Ishino, 1991; Yvon, 2016), ion (David et al., 2008) and electron (Gilbon et al., 1981; Watanabe et al., 1991) irradiation. Figure 2.5(a) shows the swelling of austenitic steels in function of its initial state and composition and Figure 2.5(b-d) are observed microstructures. In general, Ti suppresses the swelling but the suppression depends on the temperature and initial state of steels. Ti shows a significant beneficial effect on cold work materials at high temperatures. Two explanations for the complex role of Ti are suggested:

1) On one hand, Ti is a carbon-stabilizing solute. A simultaneous addition of titanium and carbon may result in the precipitation of secondary phases metal-carbon such as TiC (Mazey et al., 1980; Sekimura and Ishino, 1991), as shown in Figure 2.5(d). These homogeneous and nano-scale precipitates are thought to pin down the dislocations in movement and therefore block restoration of the initial cold working (Yvon et al., 2015). This may explain the lower swelling in CW316-Ti than SA316-Ti, since these precipitates block the initial dislocation network that is beneficial to suppress swelling.
2) On the other hand, Ti alone can play also a role in solid solution. A recent work on austenitic steels at atomic scale suggests a strong binding between Ti and vacancy which enhances the recombination of point defects and increases the effective diffusion coefficient of vacancy (David et al., 2008; Neklyudov and Voyevodin, 2008). It is suggested that Ti diffuses towards dislocations to form Corttrell-type atmospheres (Yvon, 2016). These clusters of oversize substitutional impurity atoms or interstitials impurity turn dislocations into neutral sinks (Weertman and Green, 1976). Weertman and Green believed that this would cause unbiased elimination of point defects thus a further increase in the swelling resistance.

However, descriptive mechanisms of Ti effects are still not demonstrated.

2.1.5.2 Role of chromium

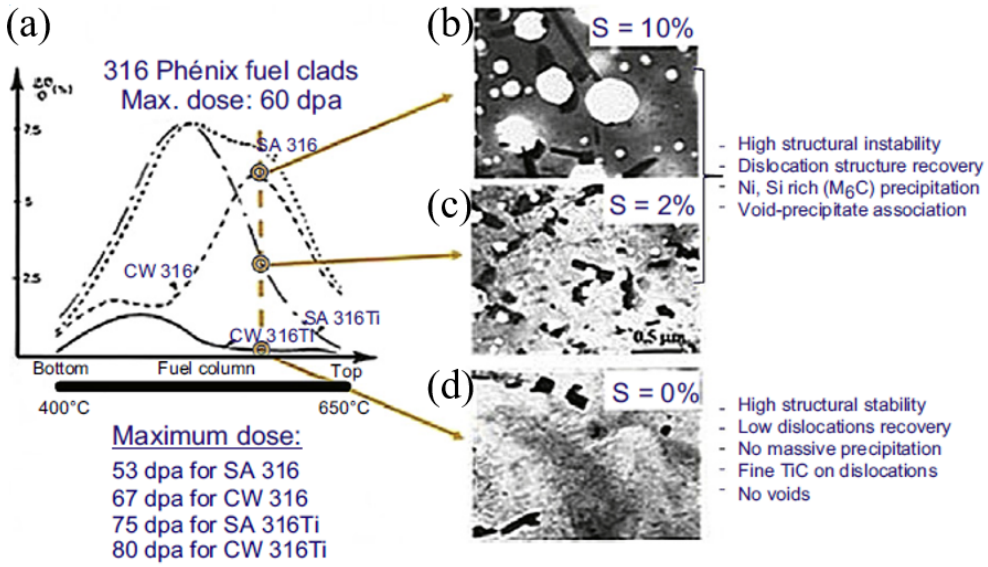

Figure 2.5 Effects of Ti on swelling of ASSs: (a) typical deformations of Phénix cladding observed on different nuances of 316 (C 0.05%) and 316Ti (C=0.064%) (Dubuisson and Gilbon, 1991); (b)-(d) microstructure observed at high irradiation temperature (600°C) on CW 316, SA 316Ti, and CW 316Ti (Yvon, 2016).

Chromium (Cr) is an essential and indispensable element in ASSs that improves the corrosion resistance. The role of Cr on swelling was widely studied in commercial alloys and Fe-based model alloys. Massive data of commercial alloys and Fe-Ni-Cr alloys are summarized in the articles of Johntson et al. (Johnston et al., 1974) (Figure 2.6), Bates (Bates and Powell, 1981) and Garner (Garner et al., 1985). They show that the incubation period is very sensitive to Cr content in combination of Ni as well as other minor solutes such as Si. The dependency is not monotonic and varies in a complex manner with other contents. Therefore, the trend of swelling as a function of Cr content is still not clearly confirmed.

To sum up, the improvement of ASS irradiation resistance lies on increasing the incubation period and the modulation of composition is an efficient way to realize it. To further increase the threshold dose of AIM or other radiation-resistant ASSs, the crucial point is to revisit the effects of alloying elements and further optimize their composition based on a better understanding of the mechanisms controlling their radiation damage.

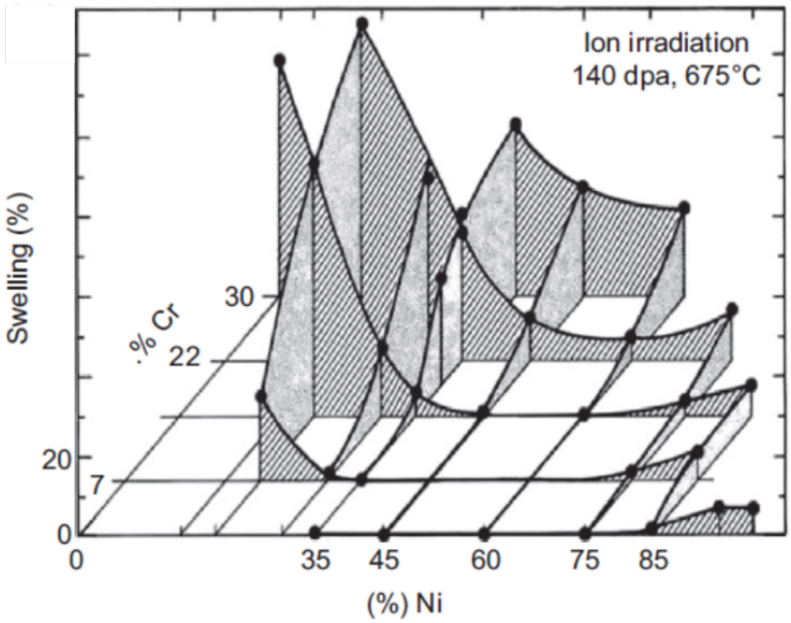

Figure 2.6 Effect of Ni and Cr on swelling in Fe-Ni-Cr alloys under 5 MeV ions (Johnston et al., 1974).

2.2 Radiation damage and physical effects

The first part pf this section is a brief summary of the basis of radiation damage from the handbooks of G.S. Was (Was, 2016) and C. Lemaignan (Lemaignan, 2012). It will be helpful to understand the radiation-induced phenomena. The second part focuses on two important phenomena (the formation of structural defects and modification of composition) in face-centered cubic structure resulting directly from radiation damage.

2.2.1 Basic damage process

2.2.1.1 Collision and cascade

During irradiation, an incident particle with a kinetic energy E interacts with a target atom of the irradiated material. Three types of interaction can occur.

1) Nuclear reaction: two nuclei or a nucleus and a subatomic particle (neutron, proton, etc.) can collide and produce nuclides different from the previous ones.
2) Elastic collision: it takes place between low-energy incident particles and nuclei of target atoms. When the energy transferred to the target nuclei is high enough, the target atom can be knocked out of its original site. If the total kinetic energy remains the same before and after collision, it is an elastic collision. This collision predominates the creation of defects under irradiation.

3) Inelastic collision: in contrast to an elastic collision, the kinetic energy is not conserved before and after collision. A part of energy is lost through, for example, the ionization and excitation of electrons. Inelastic collisions usually take place between the high-energy particle and target atoms.

In metallic alloys, the main interaction that leads to radiation damage is the elastic collision. In that case, a part of the kinetic energy T of the incident particle is transferred to the target atom. If T exceeds the displacement energy threshold E_d, a material dependent parameter, the target atom will be knocked out from its original lattice leaving a vacancy behind. The knocked-out atom becomes an interstitial. The couple composed of a vacancy and an interstitial is a Frenkel pair.

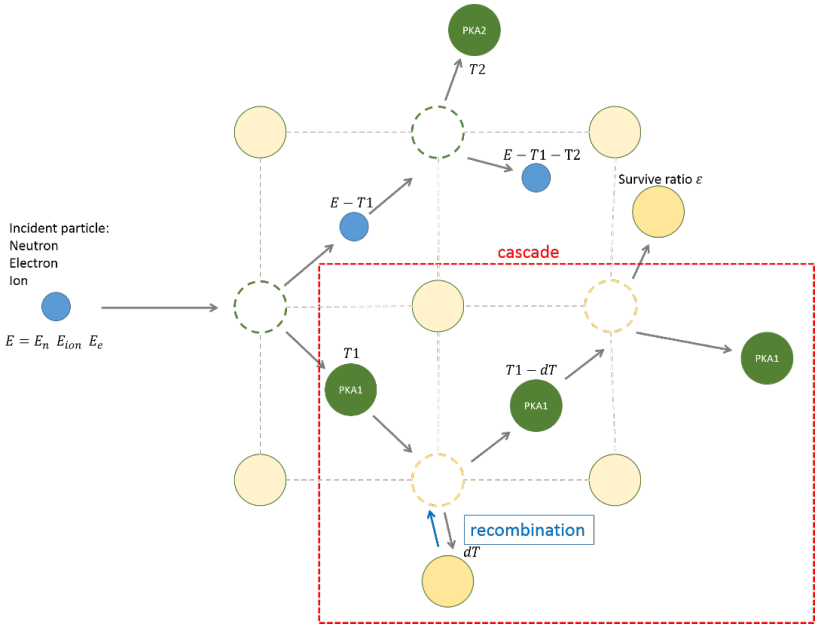

Figure 2.7 Schema of collision and cascade produced by an incident particle during irradiation.

The first knocked-out atom is called the Primary Knocked-out atom (PKA). If the PKA have enough energy, it becomes a new projectile and triggers series of collisions. This process is the collision cascade, as shown in Figure 2.7. Many atoms are knock-out off their lattice inducing lots of Frenkel pairs. Shortly after the collision, interstitials can recombine with vacancies (either by returning to the original lattice or to another empty lattice). The vacancies and interstitials that survive become point defects (PDs). The displacement efficiency is defined as the fraction of the produced Frenkel pairs that survive from the cascade recombination. This parameter describes the efficiency of creating freely migrating PDs.

2.2.1.2 Damage by different types of irradiation

G.S. Was and T. Allen suggests that the energy of PKA ($\bar{T}$) and the displacement efficiency ($\bar{\varepsilon}$) depend strongly on the type of incident particle (Was and Allen, 1993). Figure 2.8 presents $\bar{T}$ and $\bar{\varepsilon}$ for difference incident particles as reported by them. Although the energy transferred by the neutron and heavy ion is much higher than the proton and electron, the latter two particles create indeed more efficiently PDs. Table 2.2 presents a further comparison of different types of irradiation concerning several features of irradiation experiments. In fact, neutron experiments present several inconvenients: extremely time-consuming, few range of irradiation conditions (flux, temperature), material activation etc. Therefore, ions and electrons are used to simulate neutron damage in materials. It is worth to note that ion irradiation is more comparable to neutron irradiation than electron in terms of PD creation. Ion irradiations are therefore very commonly used to study radiation damage.

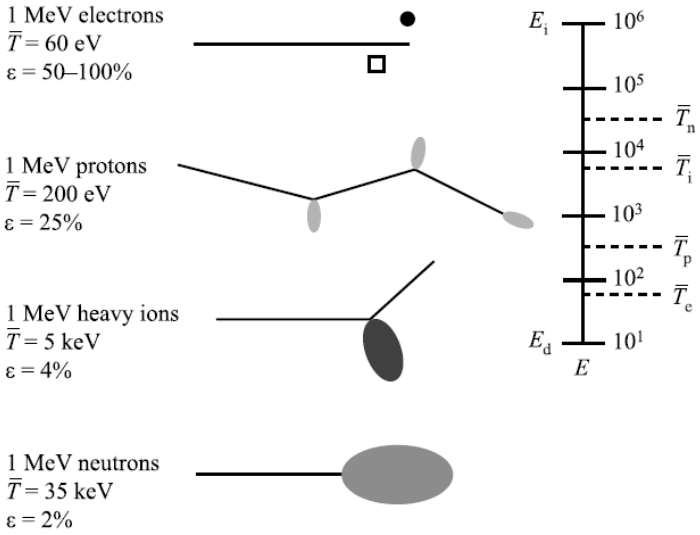

Fig. 3.7. Difference in damage morphology, displacement efficiency and average recoil energy for 1 MeV particles of different type incident on nickel (after [6])

Figure 2.8 Schema of collision and cascade produced by an incident particle in nickel during irradiation (Was and Allen, 1993).

2.2.2 Point defects formation and diffusion

During irradiation, mobile PDs are continuously created and produces a super-saturation of interstitials and vacancies is produced. The evolution of these PDs induces different radiation effect. Several cases are possible:

1) Recombination of a vacancy and an interstitial;

Table 2.2 Difference between neutron, ion and electron irradiation (Klueh and Harries, 2001; Was, 2016)

Features	Neutron	Ion	Electron
Primary defects	cascades Frenkel pairs clusters	cascades Frenkel pairs clusters	Frenkel pairs
Typical damage rate	$10^{-6} - 10^{-10}$ dpa/s	10^{-3} dpa/s (heavy ions); 10^{-6} dpa/s (light ions)	10^{-3} dpa/s
Sample form	Bulk	Bulk or thin foils	Thin foils
Damage distribution	Homogeneous in sample volume	Few nm to 100 µm under irradiated surface	Few 100 nm under irradiated surface

2) Absorption of PDs by sinks present in the material such as dislocations and grain boundaries;

3) Agglomeration of PDs of same nature to form clusters that can then develop into defects like dislocation loops or cavities.

The concentration of PDs is not homogeneous in the irradiated material. There are fewer PDs around the sinks due to the absorption by the sinks. This absorption induces two consequences. The first one is the development of structural defects (dislocation loops and cavities). The second is the modification of chemical composition around sinks. As chemical elements have different affinities with the PDs, gradients of solute concentration can be found towards sinks inducing local enrichment or depletion near sinks (Was, 2016). The gradient in vacancies and interstitials near a sink can induce a net flux of alloying elements. This effect is called inverse Kirkendall effect, as illustrated in Figure 2.9. A binary alloy 50%A-50%B is taken as an example.

Diffusion via interstitials The interstitial flux $\vec{J}_i$ generates a flux of interstitials (self-interstitials or solute atoms) toward the sink as shown in Figure 2.9(a) and Figure 2.9(d). Any difference in diffusion coefficient via interstitials will result in the different magnitude of flux. The faster diffusing component induces a larger net flux toward the sink and causes a local enrichment around the sink.

Diffusion via vacancies The vacancy flux $\vec{J}_v$ toward the sink generates an atom flux $(\vec{J}_A^v + \vec{J}_B^v)$ of equal magnitude at the inverse direction, called inverse Kirkendall effect. The respective magnitudes of $\vec{J}_A^v$ and $\vec{J}_B^v$ depend on the local concentration and the diffusion coefficient of alloying elements. It is obvious that the composition near the sink will not change if $D_A^v = D_B^v$. If an element diffuses faster than the other via vacancy diffusion, this

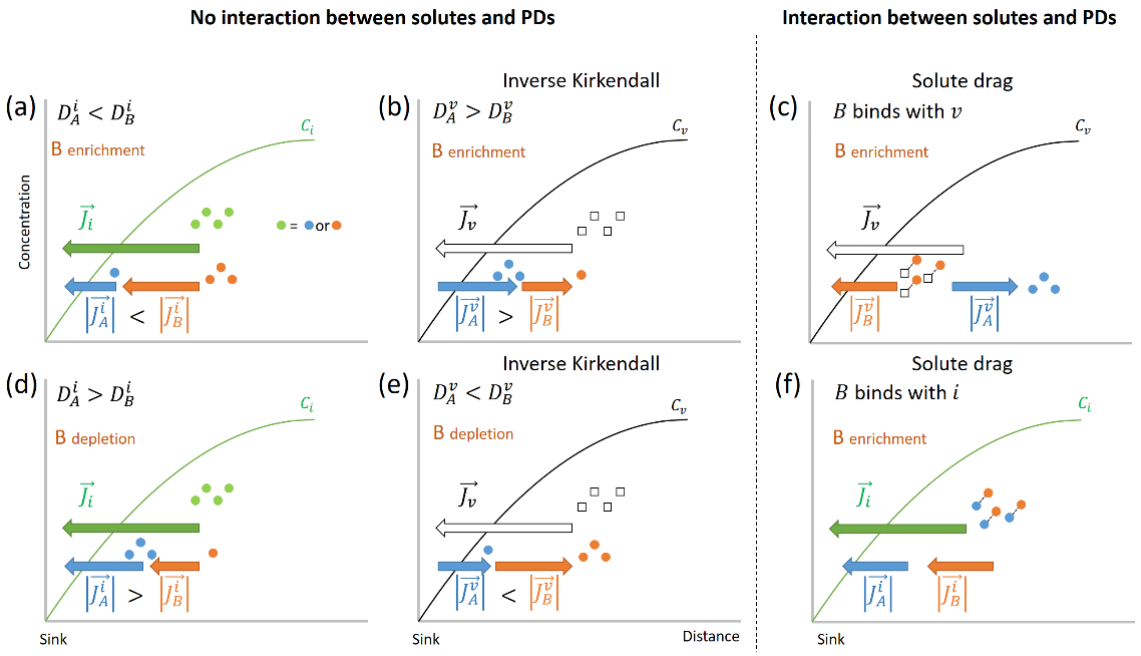

Figure 2.9 Schematic illustration of different diffusion processes inducing solute segregation at sink: enrichment of solute B due to respectively (a) fast diffusivity of B, (b) inverse Kirkendall effect, (c) solute drag by B-v binding or (f) by B-i binding; depletion of solute B respectively due to (d) low diffusivity of B, (e) inverse Kirkendall effect; C_i and C_v denotes the concentration of interstitials and vacancies, D_X^Y and $\vec{J_X^Y}$ the diffusion coefficient and the flux of species X (X=A or B) via interstitial (Y=i) or vacancy (Y=v).

faster diffuser will induce a larger net flux, as shown in Figure 2.9(b) and Figure 2.9(e), thus causes depletion at the sink of the faster diffusing element.

Solute drag If solute atoms bind with PDs and form PD-solute complexes, the flux of PDs generates also a flux of alloying elements toward the sink, as illustrated in Figure 2.9(c) and Figure 2.9(f). The solute drag depends significantly on the binding energy $E_{PD-solute}^{bind}$ and the migration energy of PD-solute complexes $E_{PD-solute}^{m}$.

2.2.3 Radiation-induced structural defects in austenitic steels

Structural defects are created by the agglomeration of PDs that are in super-saturation. These structural defects play an important role on the continuous evolution of the microstructure under irradiation and will finally affect the macroscopic behavior of the material.

2.2.3.1 Brief introduction to face-cubic centered structure

Fcc structure is a close packed crystalline structure with a sequence $ABCABCABC$ along $< 111 >$ direction. The unit cell of f.c.c. structure is shown in Figure 2.10(left). A tetrahedron is drawn and developed to visualize all the faces and edges, as illustrated in Figure 2.10(right). This tetrahedron is defined as Thompson Tetrahedron (Weertman and Green, 1976). The four faces of Thompson Tetrahedron are the close-packed planes of fcc structure, the 111 planes. The Thompson Tetrahedron is helpful to visualize the characteristics of structural defects like stacking fault tetrahedra or dislocations. It indicates the four surfaces of stacking fault tetrahedra (SFT) and all the possible Burgers vectors ($\mathbf{b}$) of dislocations in the fcc structure which will be detailed in following sections.

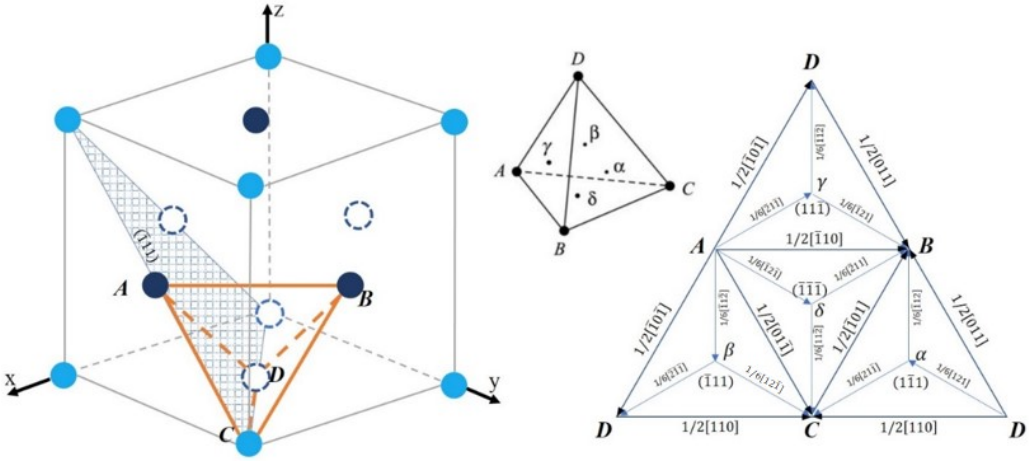

Figure 2.10 Unit cell of f.c.c. (left) and Thompson Tetrahedron (right) (Hull and Bacon, 2011).

2.2.3.2 Some defects in fcc crystals

2.2.3.2.1 Dislocations and dislocation loops

Types of dislocation

Three types of dislocations are observed in the fcc structure:

1) Frank partial dislocation. Its BV is normal to $\{111\}$ plane i.e. $\mathbf{b} = \frac{1}{3}\langle 111\rangle$.
2) Perfect dislocation. Its Burgers vector is $\mathbf{b} = \frac{1}{2}\langle 110\rangle$.
3) Shockley partial: its BV is $\mathbf{b} = \frac{1}{6}\langle 112\rangle$. It lays in the $\{111\}$ plane and it is envisaged that this partial dislocation spreads across a stacking fault in the $\{111\}$ planes.

Frank partial dislocations can only exist as Frank loops with a stacking fault inside. In terms of nature, Frank loops are either vacancy-type with an intrinsic stacking fault inside

or interstitial-type with an extrinsic stacking fault. Shockley partial only exist inside Frank loop when unfaulting occurs. Shockley partial sweeps the area inside a Frank loop removing the stacking fault and turn the Frank loop into a perfect loop. Perfect dislocation can be both dislocation lines (network) or dislocation loops (in short perfect loops).

Movement of dislocations

There are two basic types of dislocation movement: slip and climb.

Slip occurs when the dislocation moves in the surface which contains both its line and Burgers vector: a dislocation able to move in this way is glissile, otherwise it is sessile (Hull and Bacon, 2011). Frank loops are sessile while perfect dislocations (loops) are glissile. Perfect dislocations can slip in 111 planes in <110> directions. A slip plane and a slip direction in the plane constitute a slip system. fcc crystals have four 111 planes with three <110> directions, in total 12 slip systems. Slip is a conservative motion i.e. the total number of point defects contained in the dislocation remains the same.

Climb occurs when the dislocation moves out of the glide surface, and thus normal to the Burgers vector (Hull and Bacon, 2011). Climb is a non-conservative motion i.e. the total number of point defects contained in the dislocation changes during the climb, usually leading to the growth or shrinkage of the dislocation loop.

2.2.3.2.2 Stacking fault and stacking fault tetrahedron

A stacking fault is a planar defect that describes the disordering of crystallographic planes that exists in close-packed structure (f.c.c. or hexagonal close-packed). In the fcc structure, when the perfect stacking sequence $ABCABCABC$ is interrupted, a stacking fault is produced. It can either be intrinsic stacking fault $ABCA\not{B}CABC$ (Figure 2.11(a)) or an extrinsic stacking fault $ABCA\underline{C}BCABC$ (Figure 2.11(b)). The stacking fault is only located in the 111 planes in the form of a stacking fault tetrahedron or a Frank partial dislocation.

The stacking fault an extra entropy per unit area. This energy is defined as the Stacking Fault Energy (SFE) usually denoted as $gamma_{SFE}$. The stacking fault energy (SFE) is an intrinsic parameter of a material. The value of SFE influences the dissociation of perfect dislocations into partial dislocations and their movement. Therefore, the characteristics and the evolution of stacking faults is partially determined by SFE. Detailed studies of SFE have been conducted since 1950s regarding the SFE measurement technique and the determination of SFE in fcc materials including austenitic steels. Table 1.3 shows some measurement techniques using Transmission Electron Microscope (TEM) and relative results (Cockayne et al., 1971; Dobson et al., 1967; Edington and Smallman, 1965; Howie and Swann, 1961; Murr, 1969). It should be noticed that ASS has a low SFE among the commonly studied fcc materials.

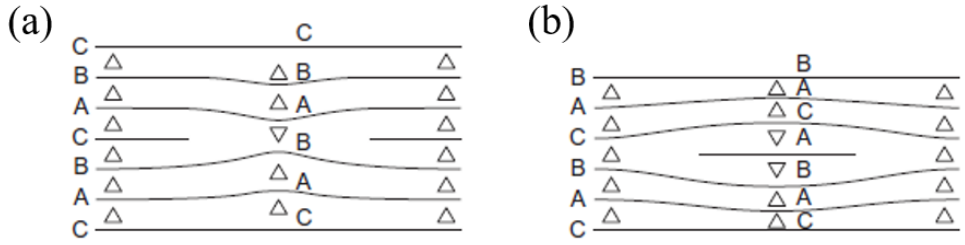

Figure 2.11 Stacking faults in the face-centered cubic structure. The normal stacking sequence of (111) planes is denoted by $ABCABC...$ Planes in normal relation to one another are separated by Δ, those with a stacking error by ∇: (a) intrinsic stacking fault; (b) extrinsic stacking fault (Hull and Bacon, 2011).

Table 2.3 Some studies on SFE measurement in fcc materials (SFE in $mJ.m^{-2}$)

Methods	Techniques	Materials			
		ASS	Ni	Al	Cu
Dislocation nodes (Howie and Swann, 1961)	TEM	13	150	/	40
Separation of partials (Cockayne et al., 1971)	TEM weak-beam	/	/	/	41±9
Annealing of faulted loops (Edington and Smallman, 1965)	TEM in-situ annealing	/	/	280±50	/
Annealing of faulted loops (Dobson et al., 1967)	TEM in-situ annealing	/	240	135	80
Dislocation nodes (Murr, 1969)	TEM	21	/	/	/
Dissociated edge dislocation faulted dipoles (Carter and Holmes, 1977)	TEM weak-beam	/	120-130	/	/

Stacking fault tetrahedra (SFT) are 3D stacking fault configuration in the shape of tetrahedron. Silcox and Hirsch reported firstly the observation of SFT in pure gold (fcc) and proposed a formation mechanism (Silcox and Hirsch, 1959). R. Schibli and R. Schäublin presented a detailed review of the formation of SFTs in austenitic steels (Schibli and Schäublin, 2013). They identified a difference between high purity model austenitic steels (high purity Fe-Cr-Ni alloys) and commercial steels regarding the formation of SFT. In model austenitic steels Fe-Ni-Cr, the SFTs were certainly formed but in commercials steels, they were either absent or present in high density.

2.2.3.3 Dislocations and dislocation loops

Frank loops in austenitic steels

The agglomeration of PDs forms clusters that can develop into dislocation loops as shown in Figure 2.12. Frank loops were commonly detected in ASSs under neutron irradiations (Brager et al., 1970; Cawthorne and Fulton, 1967; Maziasz and McHargue, 1987) and ion irradiations (Etienne et al., 2010; Pokor et al., 2004). Figure 2.12 presents the microstructures of dislocations and dislocation loops in austenitic steels irradiated by neurons at different temperatures and fluences (Brager et al., 1970). In terms of Frank loop nature, some authors identified,Frank loops as interstitial-type (Brager et al. (Brager et al., 1970), Horiki and Kiritani (Horiki and Kiritani, 1994)) but a study of D.J. Edwards et al. (Edwards et al., 2003) suggested that both type of Frank loops (size of 1-30 nm) existed. Recently, B. Michaut (Michaut, 2017) studied the evolution of Frank loops at different temperatures and doses experimentally (TEM, APT) and numerically (cluster dynamics). Interstitial Frank loops were found.

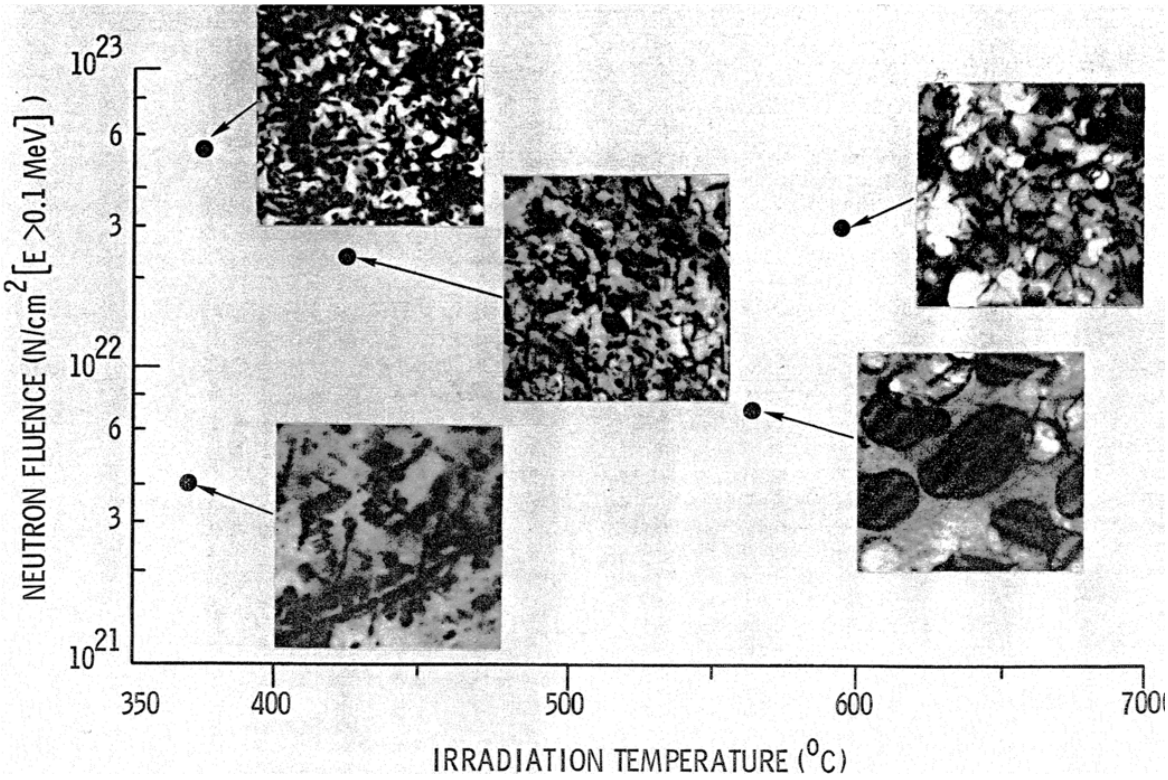

Figure 2.12 Interstitial clusters and loops in stainless steel in function of irradiation temperature and fast neutron fluence (Brager et al., 1970).

Perfect dislocations and loops

Dislocation networks consist of an agglomeration of perfect dislocation lines. They are commonly observed in irradiated austenitic steels regardless the initial metallurgical state (cold work or solute annealing). Perfect loops were also observed by Brager et al. (Brager

et al., 1970) and Holmes et al. (Holmes et al., 1968) in austenitic steels but they were much less frequently observed than Frank loops.

2.2.3.4 Evolution of dislocation microstructure under irradiation

Many studies pointed out a similar evolution of dislocation microstructure in austenitic steels in early stages of irradiation (Brager et al., 1970; Garner, 2012; Maziasz, 1993; Zinkle et al., 1993):

1) Nucleation of dislocation loops
2) Formation of Frank loops
3) Growth of loops
4) Unfaulting of Frank loops that turn into perfect loops
5) Development of steady dislocation network

As dislocations act as defect sinks for PDs, their evolution is crucial for the growth of voids in austenitic steels. The microstructural evolution can be characterized by two transient regimes (Garner, 2012; Zinkle et al., 1993). In the first regime, dislocation loops are formed. This regime is a relatively rapid and last for a damage level of about 1 dpa. In the second one, dislocation network is present and evolves very slowly. The overall microstructure in this regime typically remains up to very high damage levels (>50 dpa). Thus this regime is considered approximately as a steady-state. With the dislocation bias (preferential absorption for interstitials), a super-saturation of vacancies is produced by the dislocation network, leading to an intense nucleation of voids and their growth.

Growth of dislocation loops

Fisher et al. irradiated an ASS in a High Voltage Electron Microscope (HVEM) and observed directly the growth of interstitial Frank loops in austenitic steels (Fisher et al., 1980). To explain the growth of interstitial dislocation loop, Greenwood et al. firstly suggested that dislocations were not a neutral sink for interstitials and vacancies (Greenwood et al., 1959). Indeed, there is a preferential absorption of interstitials by interstitial dislocations and interstitial loops. It is indicated by the fact that interstitial loops grow (Makin, 1968; Urban, 1971) or by the formation of vacancy-type defects near dislocations (Chen and Ardell, 1976; Ishino et al., 1992; Urban, 1971). This preference is called bias of dislocation and is defined by a bias factor B:

$$B = \frac{k_i^2 - k_v^2}{k_i^2} \tag{2.1}$$

where k_i^2 and k_i^2 represent respectively the sink strength to absorb interstitials and vacancies.

Unfaulting process of Frank loops

A stacking fault can be removed by a dislocation reaction (Cockayne et al., 1971). This process is called unfaulting. A commonly observed unfaulting mechanism in the fcc structure is the nucleation of a Shockley partial (**b**=1/6<112>). Take a Frank loop in the plane 111 as an example. An intrinsic stacking fault can be removed if the crystal above is sheared so that C-> B, B-> A, A -> C. The unit vector for this displacement is 1/6<112>, corresponding to the glide of a Shockley partial dislocation across the fault. For one given stacking fault, there are three variants of Shockley partials. One of three possible reactions is shown by Equation 2.2 (by Kuhlmann-Wilsdorf (Kuhlmann-wilsdorf, 1958)). An extrinsic Frank loop requires two Shockley partials to remove the stacking fault. One partial glides below the fault and another above. A possible reaction is shown by Equation 2.3. With the Thompson Tetrahedron shown in Figure 2.10, this reaction can be easily understood by adding the vectors in the tetrahedron.

$$\frac{1}{3}[111]+\frac{1}{6}[11\bar{2}]=\frac{1}{2}[110] \tag{2.2}$$

$$\frac{1}{3}[111]+\frac{1}{6}[2\bar{1}\bar{1}]+\frac{1}{6}[\bar{1}2\bar{1}]=\frac{1}{2}[110] \tag{2.3}$$

The number density of Frank loops in ASSs decreased with the increase of the dose. From ex-situ irradiation experiments (Brager et al., 1970; Garner, 2012; Maziasz, 1993; Zinkle et al., 1993). To explain this reduction of Frank loops, many authors proposed that Frank loops were unfaulted during the irradiations. Suzuki et al. observed directly the unfaulting process in a model ASS during HVEM experiments (Suzuki et al., 1992). From their experiments, the unfaulting process of interstitial Frank loops may be caused by shear loops generated inside the Frank loop or by glide dislocations from outside. Figure 2.13 shows an experimental observation of a partially unfaulted loops (Suzuki et al., 1992). The Burgers vector of the faulted part is $\frac{1}{3}[1\bar{1}\bar{1}]$ (Frank loop) and the Burgers vector of the inner dislocations is $\frac{1}{6}[11\bar{2}]$ (Shockley partial dislocation).

Smallman and Westmacott point out that the SFE is one of the important factors that affected the type of loops (Smallman and Westmacott, 1972). Then, Zinkle et al. found that Frank loops with a diameter beyond 50-100 nm tended to unfault to form perfect loops (Zinkle et al., 1993). They also claimed that the loop growth caused the unfaulting.

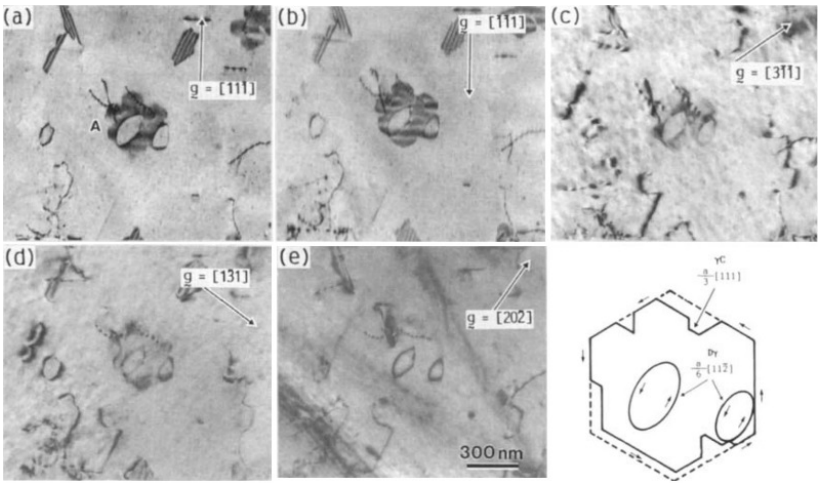

Figure 2.13 Unfaulting in a proton-irradiated ASS in HVEM. (a)-(e) taken with different two-beams conditions **g** with $s > 0$. Fault boundary dislocations found to be Shockley partial (Suzuki et al., 1992).

2.2.3.5 Cavities in austenitic steels

The maximum of average void size occurred around 600°C and the highest density was around 400°C for both 304 and 316 austenitic steels. Voids are formed by the clustering of vacancies and grow by the absorption of mobile vacancies or other clusters. Brager et al. observed the formation of voids in austenitic steels under neutron irradiation in a very large temperature range (300-700°C) (Brager et al., 1970). The density and size of voids were found to depend strongly on irradiation temperature.

2.2.4 Radiation-induced composition redistribution in austenitic steels

As presented in the first part of this chapter, the super-saturation of PDs and their diffusion can increase the transport of atoms and finally induce a local spatial redistribution of solutes. Here, we will briefly present two important phenomena due to the redistribution of alloying elements under irradiation.

2.2.4.1 Radiation-induced segregation

Under irradiation, the redistribution of solutes leads to an enrichment or depletion of solutes near PD sinks (such as free surfaces, dislocations, grain boundaries, phase interfaces etc). This phenomenon is called radiation-induced segregation (RIS). A schematic process of RIS has been presented in Figure 2.9 in a binary A-B alloys with different cases of diffusivity. Figure 2.14 shows a real plot of solute concentration across a grain boundary in stainless steel irradiated in a reactor around 300°C (Bruemmer et al., 1999). It is worth noting that the

depletion of (Cr, Mo, Fe) and the enrichment of (Ni, Si) are significant. The drastic change in the composition around grain boundaries or other structural defects will induce a variation of local properties of the defects. For instance, the depletion of Cr near grain boundaries shown in Figure 2.14 is assumed responsible for the inter-granular corrosion under irradiation. Meanwhile, such drastic changes at sinks will also cause a change of solutes concentration in matrix. The variation of local properties and solute concentration in matrix may change the designed properties (mechanical properties, corrosion resistance, swelling resistance) of the material. For this reason, understanding radiation-induced segregation (RIS) in the fcc structure is of great importance for the application of austenitic steels in reactors.

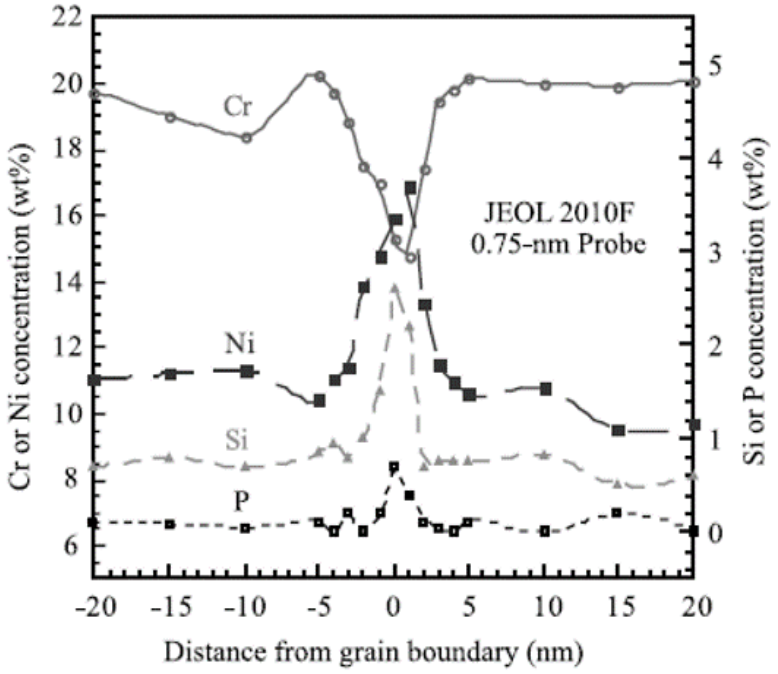

Figure 2.14 Radiation-induced segregation of Cr, Ni, Si and P at the grain boundary of a 300 series stainless steel irradiated in a light water reactor core to several dpa at about 300°C (Bruemmer et al., 1999).

2.2.4.2 Radiation-induced precipitation

When the concentration of solute(s) increases above the solubility limit, RIS can lead to the formation of precipitates at a sink, called radiation-induced precipitation. The radiation-induced precipitation was detected in austenitic steels under neutron irradiation. The formed phases observed were commonly carbides ($M_{23}C-6, M_6C, MC$) (Bragers et al.(Brager et al., 1970), Lee et al.(Lee et al., 1981), Maziasz (Maziasz, 1993)) and silicides (Maziasz (Maziasz,

1989)). As shown in Figure 2.5(d), Ni, Si rich precipitates (M_6C) and fine TiC appear in the materials after irradiation.

On one hand, these precipitates play an important role on the mechanical properties (hardening, ductile-brittle transition etc.). On the other hand, the presence of precipitates indicates changes of solute content in the matrix, which again may cause a fundamental change of the irradiation behavior. Thus, it is also essential to obtain insight of the formation of important precipitates under irradiation like TiC.

2.3 Ni-based model materials: a simple analogue of austenitic steels

As presented in the first section, the swelling is a complex phenomenon depending on many factors (composition, microstructure and environmental conditions). To better understand the effect of a specific solute, the composition and the phases must be strictly controlled. However, Austenitic steels have a very complex composition with a dozen of constituents, as shown in 2.1. Moreover, the microstructure of austenitic steels can be composed of several phases. Consequently, model alloys are developed to simplify the system so that effects of each factor on swelling can be individually treated .

The model alloys denote usually binary or trinary alloys with high purity of studied elements and low concentration of irrelevant solute impurities. The simplification from stainless steel to model alloy allows us not only to focus on solutes of interest but also to have a well-controlled initial microstructure. At the same time, a diluted binary alloy is codable for most numerical approaches, allowing the coupling of experiments and modeling, which contributes certainly to a deeper understanding of mechanisms of radiation damage. Several metals holding face-centered cubic (fcc) structure are chosen as model materials for austenitic steels, including Ni, Al, Cu and Au. Nickel (Ni) is a major constituent of austenitic steels and play a crucial role on stabilizing the fcc structure. The crystallographic structure of pure nickel is well known. Thus, nickel and nickel-based alloys are very commonly used to study the radiation damage in the fcc structure. Mass of charged-particle irradiations have been performed in the literature to understand the irradiation behavior of pure nickel. Here, we will summarize some studies in pure nickel.

2.3.1 Radiation damage in pure nickel

2.3.1.1 Brief summary of some irradiation experiments in Ni-based systems

A batch of neutron irradiation experiments in pure nickel were conducted firstly in 1960's to study the formation and stability of voids by the group of Mastel and Brimhall (Brimhall and Mastel, 1969a,b; Mastel and Brimhall, 1968). Voids and dislocations were both found in Ni irradiated up to 5x10^{19} n/cm^{-2} at 380°C. Later, other experiments in Ni and its alloys studied the effects of alloying elements on defect evolution under neutron irradiation (Kiritani et al., 1990; Kojima et al., 1988; Porollo et al., 2013; Yoshiie et al., 2000; Zinkle and Snead, 1995).

However, since neuron irradiation experiments are extremely time-consuming and irradiation conditions are quite limited, charged particle irradiations have been extensively used (Was, 2016; Zinkle and Snead, 2018). A great advantage of charged particle irradiation is that it can be performed over a large range of conditions in terms of temperature, flux, doses with various elements. It is helpful for the investigation of fundamental mechanisms of radiation damage. Another significant advantage of charged particle experiments is that it allows performing in-situ irradiations in a Transmission Electron Microscope (TEM), which provides possibilities to study the real-time microstructural evolution under irradiation. In-situ experiments provide reliable details for atomic-scale modeling to investigate dynamic mechanisms of cascade damage and defect evolution (Abe et al., 2003; Birtcher et al., 2005; Chen et al., 2019; Ishino et al., 1992; Urban, 1971).

The investigation of in-situ behavior in thin-foil pure nickel was conducted mainly in the last century and focused on two areas: (i) defect evolution under electron irradiation in High Voltage Electronic Microscope (HVEM, voltage generally of 1 MV) (Harbottle and Norris, 1973; Norris, 1970; Urban, 1971; Yoo and Stiegler, 1977) and (ii) cascade damage under ion irradiation (Chen et al., 2016; Chen and Ardell, 1976; Ishino et al., 1984; Kitagawa et al., 1985; Lu et al., 2016a,b; Mazey and Hudson, 1970; Pinizzotto et al., 1978; Robertson et al., 1991; Robinson and Jenkins, 1981; Yao et al., 2003).

Here, we summarize briefly some irradiation experiments in Ni with used materials, their irradiation conditions for general observations respectively for neutron (Table 2.4), electron (Table 2.5) and ion irradiations (Table 2.6). Then, the characteristic features of structural defects in irradiated Ni are presented in the following parts.

Table 2.4 Conditions of some neutron irradiation experiments in the literature

Authors	**Matel** (Mastel and Brimhall, 1968) **Brimhall** (Brimhall and Mastel, 1969a)	**Kojima** (Kojima et al., 1988)	**Yoshiie** (Yoshiie et al., 2000)	**Zinkle** (Zinkle and Snead, 1995)
Materials and treatment				
Composition	99.997% Ni	99.99% Ni Ni-2Cu Ni-2Si Ni-2Sn Ni-2Ge	99.99% Ni Ni-2Si Ni-2Sn Ni-2Ge	Ni with impurities<37 ppm
Annealing	Vaccum 1h 700°C	Vaccum 1h 1173 K	Vaccum 1h 1173 K	Vaccum 2h 750°C
Sample form	Bulk	Bulk and thin foils	Bulk	Thin foils
Irradiation				
Temperature	40-450°C	room temperature - 720 K	573 K	230°C
Neutron	E>1 MeV	E>1 MeV	E>1 MeV	E>0.1 MeV
Fluence	<1.2x10^{20} n/m^2 (dpa not given)	10^{22-23} n/m^2 (dpa not given)	10^{22-23} n/m^2 (dpa not given)	10^{22-23} n/m^2 (0.098, 0.25 dpa)
Detected defects	Voids, dislocations	Thin foils: only SFT Bulk: I-loops and SFT (300K); I-loops, SFT and voids(473K); Only voids (673K);	<0.0049 dpa: I-loops and SFT >0.0049 dpa: voids	High density of small SFT and dislocation loops

Table 2.5 Conditions of some electron irradiation experiments in the literature

Authors	**Norris** (Norris, 1970)	**Urban** (Urban, 1971)	**Yoo** (Yoo and Stiegler, 1977)	**Harbottle** (Harbottle and Norris, 1973)
Preparation				
Nickel purity	99.995%	99.995% 99.999%	20Cu,15Al,10Cr,10Fe,7K	Ni (99.995%)
Annealing	Not specified	Vaccum 1350°C	Vaccum 1h 800°C	Vaccum 2h 700°C
Sample preparation	Not specified	100µm electropolished	500µm electropolished	Not specified
Irradiation				
Pre-irradiation	no	no	no	Neutron irradiation in water at 50°C
Electron beam	$> 450keV$ flux not specified but current noted $0.5\,\mu A$	$650keV$ 1-2x$10^{18} e/cm^2/s$	$650keV$ 3.8x$10^{19} e/cm^2/s$ (equal to $6.4x10^{-5} dpa/s$)	$1MeV$ 1.6x$10^{23} e/cm^2/s$ (equal to $10^{-3} dpa/s$)
Temperature	450°C	20-540°C	450°C	500°C
Thickness	400 nm	3 µm	4 µm spot	Not specified
Irradiated surface	450°C	3µm spot	450°C	500°C
Observations	Growth of interstitial Frank loops	Growth of interstitial Frank loops v.s. temperature; metastable vacancy loops near dislocations	Growth of interstitial Frank loops; depth distribution of loops	Growth of interstitial Frank loops v.s. temperature

Table 2.6 Conditions of some ion irradiation experiments in the literature

	Materials	**Sample form**	**T°C**	**Ion beam**	**Flux**	**Final dose**	**Detected defects**
Mazey (Mazey and Hudson, 1970)	99.95% Ni	Bulk	450°C	4MeV H^+	/	$\approx 1dpa$	Large interstitial Frank loops, double-faulted loops
Chen (Chen and Ardell, 1976)	99.999% Ni	Bulk	350-550°C	400keV N^+	$1\mu A/cm^2$	peak$\approx 6dpa$	Frank loops, Multi-layer loops
Pinizotto (Pinizzotto et al., 1978)	Ni, Ni-Al, Ni-Ti, Ni-Cr	Bulk	400-650°C	3.5MeV Ni^+	$10^{-3}dpa/s$	peak$<20dpa$	Loops, voids
				400keV N^+	$10^{-3}dpa/s$	peak<20	Loops, voids
Robinson (Robinson and Jenkins, 1981)	Ni, Ni-Cr	Bulk	350-550°C	80 keV W^{2+}	/	2x10^{15} $ions/m^2$	Frank loops, some perfect loops
Kitagawa (Kitagawa et al., 1985)	Ni	Thin foils	/	65keV Ni^+	/	10^{11-14} $ions/cm^2$	Small SFT
Robertson (Robertson et al., 1991)	99.999% Ni	Thin foils	-243°C, 27°C	50keV Kr^+ 50/100keV Ni^+	2x10^{14} $ions/m^2/s$	10^{15-17} $ions/m^2$	Frank loops, perfect loops
Yao (Yao et al., 2003)	Ni	Bulk	60°C	590MeV H^+	5x10^{-7} dpa/s^{-1}	0.001-0.01 dpa	Loops, SFT, small dots
Lu (Lu et al., 2016a)	Ni	Bulk	RT	3MeV Au^+	/	2x10^{13} $ions/cm^2$	SFT, Frank loops
Lu (Lu et al., 2016b)	Ni	Bulk	500°C	1.5MeV Ni^+	/	3x10^{15} $ions/cm^2$	Voids near surface, loops in deep zones
Chen (Chen et al., 2016)	Ni	Thin foils	300-500°C	30keV H^+	/	2x10^{16} $ions/cm^2$	perfect loops
Ishino (Ishino et al., 1984)	99.995% Ni	Thin foils	27-500°C	300/400keV Ar^+	8x10^{-4} dpa/s	0.1 dpa	metastable V-loops in thin zones I-loops in thick zones)

2.3.1.2 Dislocation loops induced by irradiation in Ni

From the summary presented above, in the early stages of irradiation, there is a transition from a SFT-dominated microstructure to a loop-dominated one (Zinkle and Snead, 1995). Then, dislocation loops grow and lead to the formation of a dislocation network, which is involved in the nucleation and growth of voids after an incubation period (Garner, 2012; Stubbins and Garner, 1992). Meanwhile, the microstructure (density and size of dislocation loops and voids) is affected by the addition of solutes and impurities (like oxygen) over a wide range of metal materials (fcc, body-centered cubic (bcc)) and even novel concentrated solid solutions (Bhattacharya et al., 2016; Lu et al., 2016b; Porollo et al., 1998, 2013; Seitzman et al., 1986; Singh et al., 1981; Watanabe et al., 1991). Thus, it can be seen that dislocation loops play an important role in the microstructural evolution in the early stages of irradiation.

In Ni, Frank partial dislocation loops (Burgers vector of 1/3<111>) and perfect loops (Burgers vector of 1/2<110>) were observed under neutron (Brimhall and Mastel, 1969a; Yoshiie et al., 2000), electron (Norris, 1970; Urban, 1971; Yoo and Stiegler, 1977) and ion (Chen and Ardell, 1976; Mazey and Hudson, 1970; Pinizzotto et al., 1978; Robinson and Jenkins, 1981) irradiation in a large range of temperatures (from 25 to 650°C). The type of dislocation loops observed under different irradiation is in consistence in the literature. However, uncertainties remain on the nature of irradiation-induced Frank loops. They were identified as interstitial-type in most cases for all kinds of irradiation. However, small metastable vacancy loops were claimed in irradiated nickel with electrons (Urban, 1971) and ions (Ishino et al., 1984; Robinson and Jenkins, 1981). It has to be stressed that the existence of grown stable vacancy loops in nickel is unavailable in the literature.

2.3.1.3 Growth of dislocation loops under electron irradiation

An important subject of irradiation behavior of Ni is the defect evolution under electron irradiation in High Voltage Electronic Microscope (HVEM, voltage generally of 1 MV). The growth of Frank loops are found to be a characteristic feature in nickel during electron irradiation. Norris (Norris, 1970), Urban (Urban, 1971), Yoo and Stiegler (Yoo and Stiegler, 1977) observed a linear growth of faulted loops over a large range of temperatures. Figure 2.15(a) shows the loop growth by Norris and Figure 2.15(b) the enormous Frank loops result from the loop growth at high temperature by Urban.The linear growth rate of Frank loops was found to be temperature-dependent and increase dramatically when the temperature exceeds 400°C (Urban, 1971). The growth of interstitial loops under electron irradiation is explained by the preferential absorption of interstitials by dislocations. The development of a chemical rate theory model with the dislocation bias factor was applied to electron irradiated Ni and allowed a good prediction of defect evolution by several authors (Harbottle and Norris, 1973; Kiritani et al., 1975; Miller, 1983; Norris, 1970; Yoo and Stiegler, 1977). Based on the

model of Norris (Norris, 1970), as the "diameter" (largest apparent distance between opposite edges) of each interstitial loop d is experimentally proportional to time t, free surfaces are the dominating sink for interstitials controlling the microstructure evolution. Yoo and Stiegler (Yoo and Stiegler, 1977) and Miller et al. (Miller, 1983) improved the model and also obtained a good agreement between experiment and simulation for the loop growth rate.

However, electron irradiations have their own limitations in representing the radiation damage induced by neutrons. Electron bombardments create no cascades which are a characteristic phenomenon of neutron and ion bombardments (Nordlund et al., 2015; Was, 2016). The defect evolution during electron irradiation takes no account of the influence of cascades that may drastically modify the nature of defects. The data of loop growth rate under ion with the influence of cascades is unavailable in the literature.

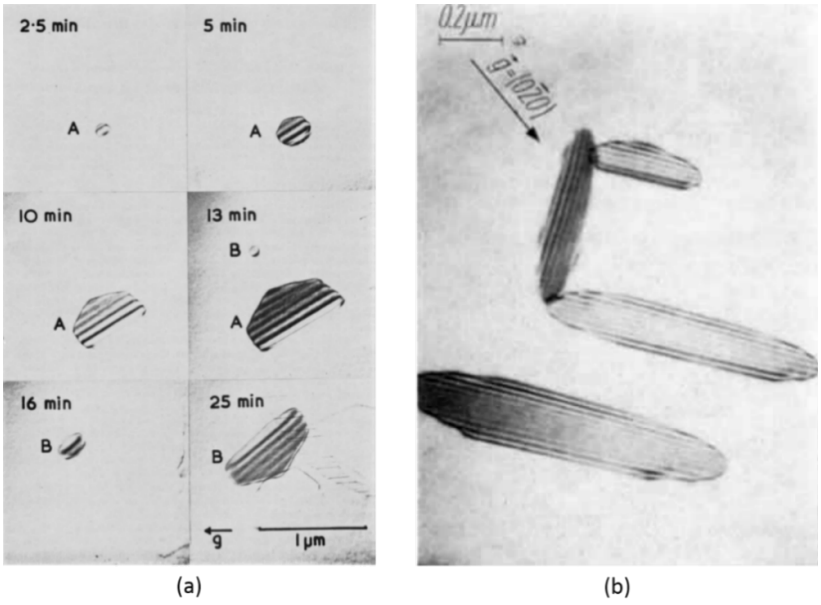

Figure 2.15 Dislocation loop formation and evolution in nickel in HVEM: (a) at 450°C with 1MeV electrons (Norris, 1970); (b) at 540°C at a dose of 3e21 e/cm2 (Urban, 1971).

2.3.1.4 Voids induced by irradiation in Ni systems

The formation of voids in bulk nickel has been extensively studied at high doses under neutron irradiations (Brimhall and Mastel, 1969a; Kojima et al., 1988; Mastel and Brimhall, 1968; Porollo et al., 2013; Yoshiie et al., 2000; Zinkle and Snead, 1995) and under ion irradiations (Lu et al., 2016b; Pinizzotto et al., 1978). Generally, voids are formed in the shape of octahedron after the formation of dislocations in the microstructure (Yoshiie et al., 2000). In this thesis, we will focus on the early stages of irradiation, voids are not the main feature of interest. However, the formation of voids is indeed an important phenomenon to

investigate and crucially depend on materials parameters like surface energy of voids and stacking fault energy.

2.3.1.5 Important factors affecting the irradiated microstructure of Ni

As presented in previous sections, the diffusion of radiation-induced point defects is studied via the growth of Frank loops under electron irradiation. This phenomenon contributes to a better understanding of fundamental mechanisms of defect evolution under irradiation combined with the rate theory simulation. However, two limitations are found in these HVEM experiments. The first one has been mentioned above and is that the electron irradiation creates few cascades. The influence of cascades can not be taken into account in the microstructure evolution during irradiation. The second one is that HVEM experiments were performed in thin foils samples in which the influence of surfaces play an important role. This is indicated also by the modeling of linear growth rate (Norris, 1970; Urban, 1971). Although parameters are adjusted to obtain a good fitting with experiment results, the influence of surface is still not quantitatively determined.

Surface effects on loop formation and stability

The group of Ishino performed in-situ ion irradiations in pure nickel using heavy gaseous ions (argon, xenon, and krypton) and aimed to investigate the cascade damage in thin foils under ion irradiation and the influence of free surfaces (Ishino et al., 1992; Ishino, 1997; Ishino et al., 1984).Their in-situ experiments using 300/400 keV argon ions at 27-500°C showed that clustering of point defects (PDs) was strongly influenced by the presence of point defect sinks: surfaces, pre-existing dislocations, loops and cavities (Ishino et al., 1984). Wedge-shaped specimens are used to study the sink effect of surfaces. Two phenomena are of great importance. Firstly defect-free zones were detected and the thickness of these zones increases with temperature. The second one is the observation of small metastable vacancy defects in thin zones with a very short lifetime during irradiation at 500°C. In thick zones, interstitial loops are formed and grow. These two phenomena show that microstructural evolution depends strongly on the thickness of the specimen, especially at high temperatures indicating a significant influence of surfaces. A summary of results are presented in Figure 2.16.

The in-situ gaseous ion irradiation of Ishino et al. indeed provides a better understanding of the cascade damage in fcc metals. It points out that the sink effect of surfaces for mobile PDs is strong and that the damage strongly depends on the depth (Ishino, 1997). However, some important effects are not considered. Since accelerating voltages were mostly on the order of 10-100 kV (Hinks, 2009). Low energy ions were used. These ions induce several issues: strong heterogeneous damage through the thickness, the injection of interstitial atoms

and gaseous impurities (Brailsford and Mansur, 1977; Garner, 1983; Seitzman et al., 1986). These parameters can radically change the defect nature and final microstructure.

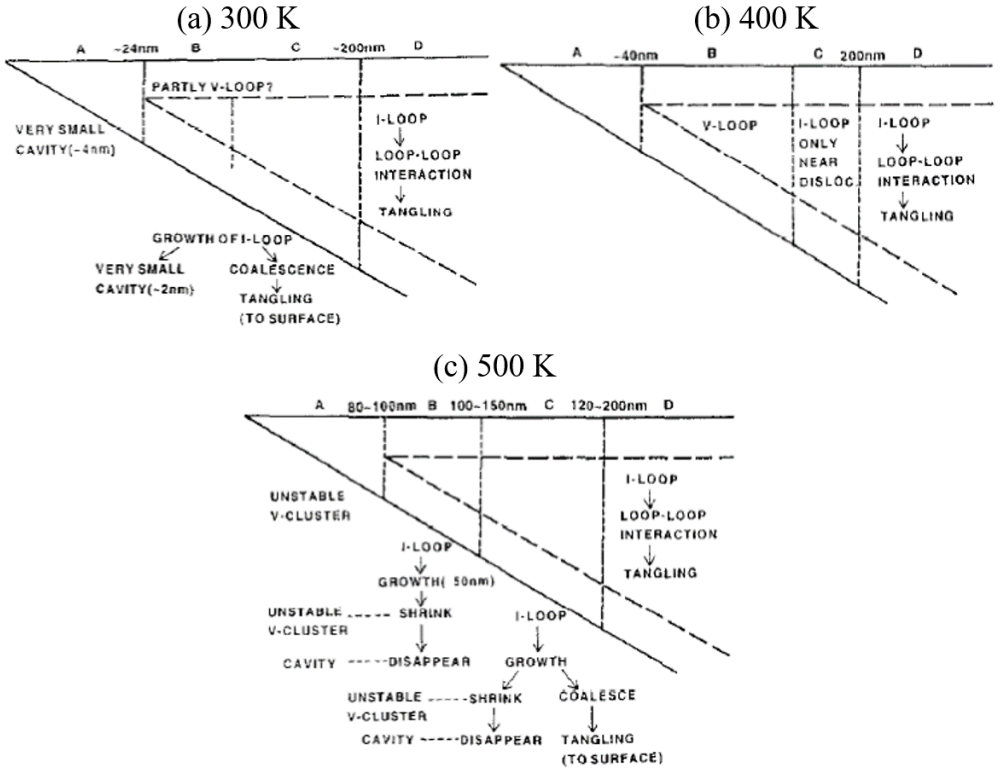

Figure 2.16 Specimen thickness dependence of microstructural evolution in wedge-shaped nickel specimen during irradiation with 300 keV Ar+ ions at (a) 300°C, (b) 400°C and (c) 500°C. There are at least four characteristic regions, A, B, C, D, where evolution in region D is similar to the one in the bulk specimens (Ishino et al., 1992) (figure modified from (Ishino, 1997)).

Impurities effects on the form of vacancy-type defects

Theoretical studies show that gaseous impurities can stabilize voids in Ni (Seitzman et al., 1986; Wang et al., 1986), as indicated in Figure 2.17. It is suggested that gaseous impurities can decrease the surface energy of voids which will affect the relative stability of vacancy defects. The modeling was tested by irradiating oxygen-pre-injected Ni with 14 MeV nickel ions at 500°C. A concentration of 75 ppm pre-injected oxygen was found to dramatically increase the void nucleation rate.

The effect of impurities on voids clearly point outs the limitations of the experiments of Ishino due to the injected gaseous atoms into observed area. To better study the radiation

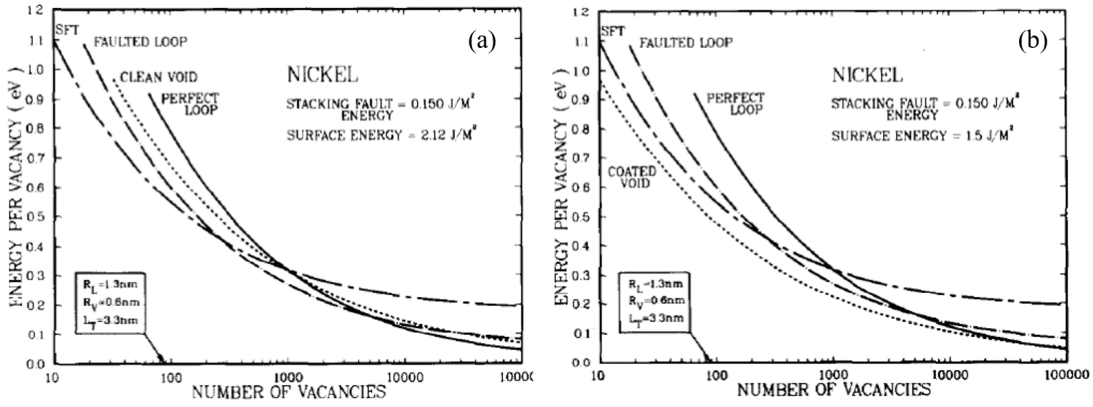

Figure 2.17 Effect of surface energy on vacancy defect stability in function of number of vacancies contained (modified from (Seitzman et al., 1986)).

damage by displacements, the influence of injected atoms and gaseous impurities must be considered and minimized. Relevant experiment data are not available in the literature.

2.3.2 Radiation damage in Ni-Ti and Ni-Cr alloys

Ni-based alloys are studied to investigate the effect of alloying elements on the irradiation behavior, mainly in two aspects: influence of solutes on the irradiated microstructure and the radiation-induced segregation. Experiment data on Ni model allyos coupled with appropriated modeling could contribute to a better understanding of fundamental mechanisms of solute effects. However, data of irradiated Ni-Ti and Ni-Cr alloys are too sparse to clarify the mechanisms and to couple with simulations. In following sub-sections, we present a brief review of studies on irradiation behavior of Ni-Ti and Ni-Cr alloys.

2.3.2.1 Radiation-induced structural defects in Ni-Ti and Ni-Cr

Data on the irradiation behavior of Ni-Ti alloys are limited in the literature. Chen and Ardell (Chen and Ardell, 1976) irradiated pure nickel and Ni-based alloys (Ni-Ti and Ni-Al containing up to 6 at.% solute and Ni-Cr up to 14 at.%) at elevated temperature (350°C-550°C) under H^+ and N^+ beam. Multiple-layer faulted loops in Ni-6%Ti and Ni-4%Cr were observed in the three alloys under N^+ irradiation but no other details of Ni-Ti were presented.

Pinizzotto, Chen and Ardell reported in a later article (Pinizzotto et al., 1978) more results on their experiments in Ni alloys irradiated by Ni^+ and N^+ in the temperature range of 400°C to 650°C up to 20 dpa. Detailed conditions are listed in Table 2.7. The Ti content was respectively 0%, 2%, 4%, 6% and 8% by atomic weight. Figure 2.18(a) and

Figure 2.18(b) show respectively Ni^+-ion irradiated microstructure in Ni-6 wt.%Ti and Ni-4 wt.%Cr. Multi-layer loops, voids and a dislocation network was observed in Ni-Ti alloys while only voids were detected in Ni-Cr. Pinizzotto et al. found that the Ti addition reduced the cavity size and the void density thus swelling. Moreover, void size decreased and dislocation density increased with Cr content (Pinizzotto et al., 1978). The void density increased firstly to a maximum at 2% of Cr and then decreased. To explain solute effects observed on the microstructure, the authors suggests two competing effects. The first one is the stabilization of embryos of cavities by solutes, which increases the void density. The second one is the modification of PD diffusion by solutes, which suppresses the vacancies and reduces the voids.

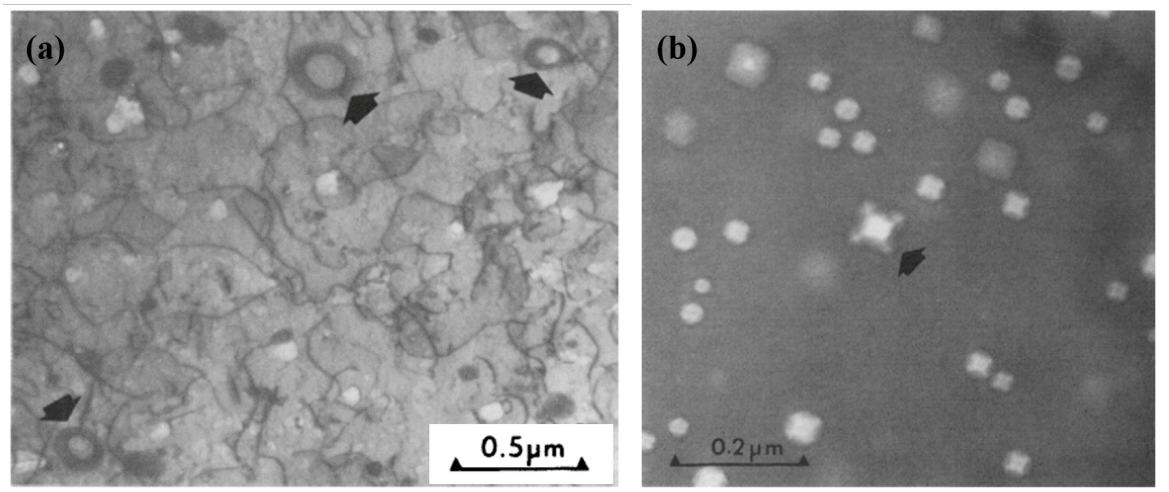

Figure 2.18 Microstructure irradiated by 3.5 MeV Ni^+ ions at 550°C in Ni-based alloys: (a) Ni-6 wt.%Ti irradiated up to 9 dpa with multiple layer loops (indicated by arrows); (b) Ni-4 wt.%Cr irradiated up to 20 dpa with dendritic voids (indicated by the arrow) (Pinizzotto et al., 1978).

Recently neutron irradiation experiments on Ni, Ni-0.6Ti, Ni-1.0Si and Ni-0.5Al were conducted by Porollo et al. in a fast breed reactor up to 18 dpa (Porollo et al., 2013). Microstructures are shown in Figure 2.19. An addition of Ti led to a reduction of swelling

Table 2.7 Irradiation conditions using 3.5 MeV Ni^+ ions in pure nickel and Ni-based alloys in the article of Pinizzotto (Pinizzotto et al., 1978).

Temperature (°C)	Dose (dpa)	Irradiated samples			
		Ni	Ni-Al	Ni-Ti	Ni-Cr
550	9	X	X	X	X
550	18		X		X
600	20	X	X	X	
650	12	X	X	X	

producing a microstructure filled with dislocation networks, faulted loops and cavities. And the addition of Si or Al also significantly reduced the swelling while Ni-Si presents a perfect loop microstructure and Ni-Al showed no dislocation loop. The different microstructures in function of the solute addition may imply different mechanisms of solute on defect formation and evolution. If we compare more carefully Figure 2.19(b) and Figure 2.19(c), the microstructure of Ni-Ti and cold worked pure nickel are quite similar, which may indicate an effect of Ti on the formation of dislocation networks.

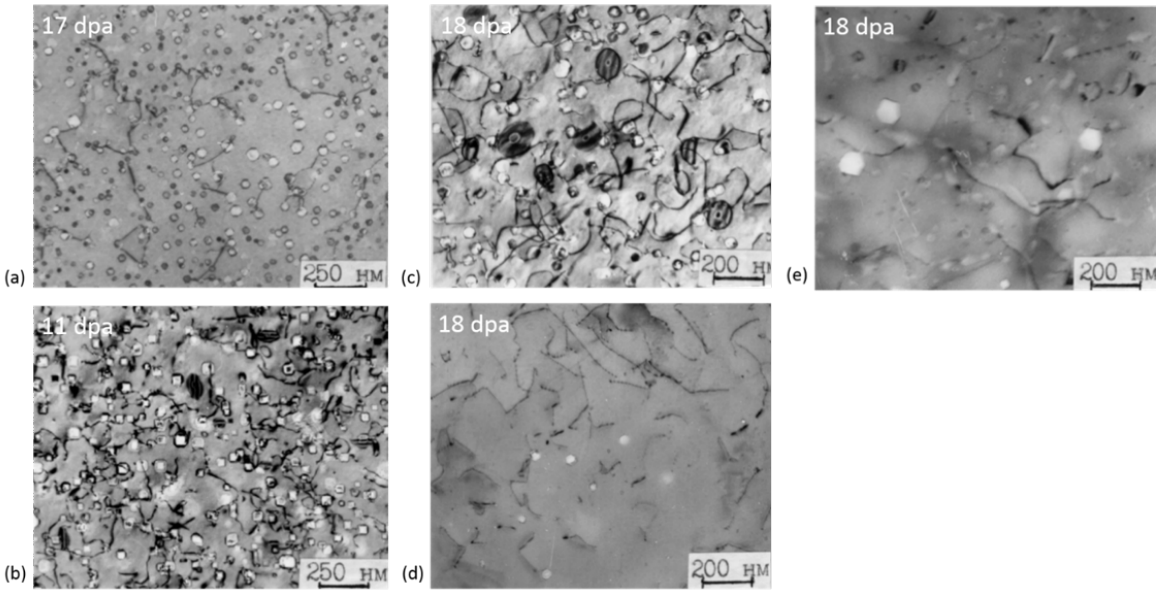

Figure 2.19 Microstructure of neutron irradiated materials at 550°C: (a) 2-3% CW pure nickel; (b) 15-20% CW pure nickel; (c) Ni-0.6 at.% Ti; (d) Ni-1.0 at.% Si; (e) Ni-0.5 at.% Al (Porollo et al., 2013).

Another work (Briggs et al., 2016) focuses on the structural defects in Ni-5%Cr and Ni-18%Cr irradiated using 2 MeV protons at 400 and 500°C and 20 MeV Ni^{4+} ions at 500°C up to 1.6-3.4 dpa. Frank loops and voids were both found in all samples. With the increase of Cr content, the density of loops and voids increases while their size decreases. They also found that heavy ion irradiations result in a larger density of smaller voids compared to proton irradiations.

2.3.2.2 Radiation-induced segregation of Ti and Cr in nickel

There is few experimental data of RIS in Ni systems, especially in Ni-Ti. Marwick and Piller studied the depth profile of several solute (Ti, Cr, Al and Mn) near the surface in Ni (atomic concentration: 0.025%Ti, 0.044%Cr, 0.06%Al and 0.15%Mn) (Marwick and Filler, 1977; Marwick et al., 1979). This alloy was irradiated by 75 KeV Ni^{+} ions at 23-500°C. The ion range was about 30 nm. The depth profile was measured by simultaneous suptter-profiling

and secondary ion mass spectrometry (SIMS) before and after irradiation. Mn was chosen as example to show the redistribution of solute before and after irradiation at 500°C, as illustrated in Figure 2.20(a). The depth distribution of all solutes are plotted in Figure 2.20(b). A segregation of Ti, Cr, Al and Mn is shown at a depth of 20 nm. Combined with their modeling, they pointed out that PD gradients can be the dominant factor affecting the solute migration near surfaces under irradiation (Marwick and Filler, 1977). The solute redistribution at 500°C was found to be associated with the concentration of vacancies and possibly divacancies. In a further work (Marwick et al., 1979), they suggested that, when the temperature is above 100°C, Al, Cr and Mn exhibit a negligible binding to vacancies thus segregate by relatively rapid exchange with vacancies (the inverse Kirkendall effect). So does Ti above 400°C. But below 400°C, another mechanism is dominant in the case of Ti.

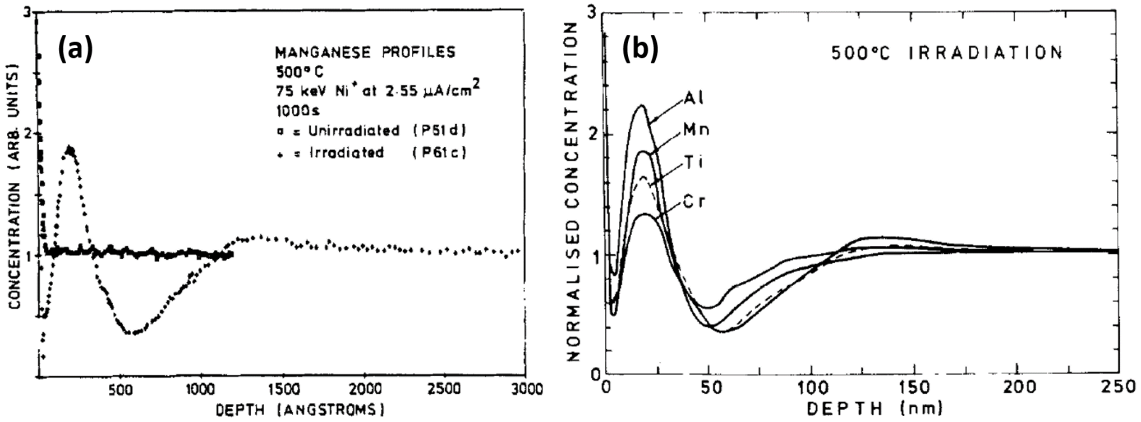

Figure 2.20 Depth profiles normalized to unit bulk concentration of some solutes in a mixed dilute nickel alloy irradiated with 75 keV Ni+ ions for 1000 s. The peak at 20 nm reflects the existence of an underlying peak in PD concentration (Marwick et al., 1979).

Another experimental work focused on the grain boundary (GB) character dependence of radiation-induced segregation in proton-irradiated Ni-5%Cr at 500°C presented above (Barr et al., 2015). A depletion of Cr at grain boundary was detected and and examined by a kinetic rate theory model. Figure 2.21 shows a RIS profile at one type of GB.

The presented studies describe the RIS near the surface or existing defects like GBs. However, experimental data of the RIS on radiation-induced defects such as dislocation loops or precipitates are not available in the literature. These data are required to better describe the evolution of composition during irradiation and to better understand the dynamic mechanisms of solute effects on irradiation behavior of fcc materials.

To summarize this subsection, Ni and its alloys have been studied as model materials for austenitic steels to better understand fundamental mechanisms of radiation damage in the fcc structure. In Ni, dislocation loops are characteristic defects in the early stages of irradiation and their evolution plays a crucial role on microstructural evolution during the irradiation.

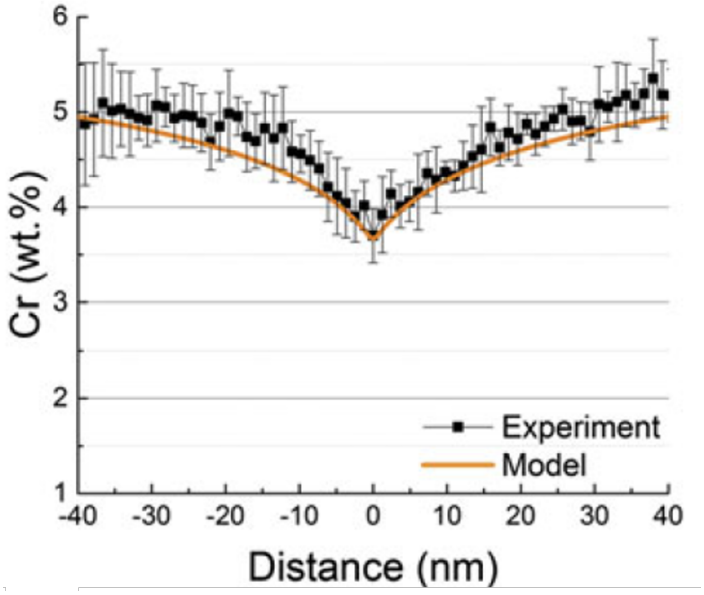

Figure 2.21 Experimental (black) and overlaid model (solid orange line) RIS profiles of Σ3 coherent GB in Ni-5%Cr irradiated at 500°C (Barr et al., 2015).

However, current data in the literature still have limitations: the nature of Frank loops induced by irradiation is unclear, the impurity effects on the irradiated microstructure is not studied and some side effects are not taken into account. In the alloys, Ti and Cr are reported to have an influence on structural defects formed under irradiation. Radiation-induced segregation of Ti and Cr near surface is detected. However, the RIS on radiation induced defects is not available in the literature. Mechanisms of solute effects on radiation damage have not yet been unambiguously understood.

2.4 Current studies of mechanisms of solute effects in Ni systems under irradiation

This section presents some possible mechanisms of solute effects based on dislocation formation and evolution in Ni-based systems. The formation and the evolution of dislocation loops are characteristic features of microstructural evolution under irradiation and sensitive to the addition of alloying elements. The study on dislocation loops in Ni and its alloys would give key mechanisms to understand the fundamental mechanisms of solute effects.

2.4.1 Dislocation bias in Ni and possible modification by solute addition

The dislocation bias denotes the preferential absorption of interstitials by dislocations and its definition has been given by Equation 2.1. Here we present first a brief introduction to the rate theory based on dislocation bias model which has successfully reproduced the growth of interstitial Frank loops under electron irradiation. Brailsford and Bullough developed a rate theory of void swelling (Brailsford and Bullough, 1972). This theory was then extended by Michio et al. to treat the time and the depth dependence simultaneously (Michio et al., 1975). Yoo and Stiegler (Yoo and Stiegler, 1977) formulated a system of rate equations and solved it with more efficient numerical methods in order to calculate the kinetic evolution of clusters controlled by the PD diffusion. The model of Yoo and Stiegler considered the mobility of vacancies and the preference factor was discussed in different cases. They found that the growth rate was very sensitive to the migration energy of vacancy E_v^m, the preference factor of dislocation loops for interstitials δ_i and for vacancies δ_v. The parameters E_v^m=1.2eV, δ_i=0.06 and δ_v=0 provided the best self-consistent results with experiments of loop linear growth in nickel. Miller et al. developed a finite element scheme applied to a rate theory continuum model that was capable to include loop overlap and loop intersection with the surface (Miller, 1983; Miller et al., 1982). A good agreement between experiments and simulations was obtained for pure nickel with two distinct sink strength models with different bias. The best fit with experimental data of Yoo and Stiegler (Yoo and Stiegler, 1977) was obtained by Miller (Miller, 1983; Miller et al., 1982) for E_v^m=1.4eV.

The bias factor affects significantly the absorption of PDs by dislocation loops. Any modification of the dislocation bias could cause a different microstructural evolution. Recently, RIS was reported near radiation-induced dislocation loops in a 50Ni-50Ni alloy (Lu et al., 2017). Based on the observations of Lu et al.Lu et al. (2017), Barashev et al. studied the influence of the RIS on loops and on the global microstructure Barashev et al. (2019). According to the authors Barashev et al. (2019), the resulting segregation profile causes the “direct” Kirkendall effect, when the gradient of alloy composition supports or suppresses the mobile defect flux. They named this phenomenon "segregation bias". By their simulations, the segregation profiles make all sinks (loops and voids) repulsive to vacancies and attractive to interstitials. It explains the absence of voids within the damage production zones and that the microstructure is dominated by interstitial loops. They suggests also that Ni enrichment on voids and interstitial loops. It leads to a depletion of Ni in the matrix, thus creating Fe-enriched “channels” where vacancies migrate preferentially via Fe atoms and escape from recombination with Ni-segregated sinks. Vacancies thus leave the damaged region and form voids beyond the damaged area, inaccessible to interstitials. However, as they used such a concentrated alloy, the diffusion process was not unambiguously described to demonstrate their theory and the segregation bias at lower content was not studied.

Overall, the growth of dislocation loops in nickel is clearly sensitive to the dislocation bias and the migration energy of vacancy. The addition of solutes may modify the composition of nucleated defects and then probably the bias of dislocation, which will exert an influence on the microstructure evolution under irradiation. However, the analysis of bias modification by solute is too scarce in the literature and more experimental data are desired. Besides, the growth rate of loops in Ni under ion irradiation is not available to validate the bias model with the presence of cascades.

2.4.2 Solute-PD interaction: trapping effect and modification of PD diffusion

In alloys, a solute atom can interact with a PD or with another solute. On the one hand, the interaction of PDs with solutes can produce interstitial-solute (i-s) and vacancy-solute (v-s) complexes that act as trapping sites for PDs. On one hand, the binding between PDs and solutes affect the formation of PDs clusters due to the trapping of PDs by solutes. On the other hand, it modifies the diffusion of PDs and solutes. In concentrated alloys, lattice distortion and the interaction solute-solute can as well form trap sites for PDs. In the following part, we will present possible interactions introduced by an addition of Cr or Ti in Ni-based alloys. The convention used is that negative binding energy indicates an attractive interaction.

2.4.2.1 In dilute alloys

A dilute alloy denotes a system in which the concentration of solutes is low enough to neglect the interaction between solute atoms. The content of solute depends on the basal and alloying element and it is usually lower than 1% atomic. Based on the rate theory, Mansur and Yoo (Mansur and Yoo, 1978) suggested that the binding of both solute-interstitial and solute-vacancy enhanced the recombination at high temperature (>400°C) for typically assumed nickel parameters. Considering a preferential absorption of interstitials by dislocations in the model, the reinforcement of recombination is only significant when binding energy is under -0.2eV for solute-vacancy and -1.4 eV for solute-interstitial. Moreover, the strong binding between PD-solute could lead to a preferential diffusion mechanism of solute (either via vacancy or interstitial) and thus modify the net flux direction of the alloying element according to inverse Kirkendall effect presented above (2.1.3).

For Cr, a recent ab-initio study of Tucker et al. (Tucker et al., 2010) of Ni-Cr system showed a weak interaction of Cr-vacancy but a strong binding with Ni interstitials (binding energy $H_{bind}(Cr)$=-0.18 eV). This Cr-I binding reduced the Cr activation energy for interstitial diffusion. Tucker et al. also suggested that Cr diffused faster via both vacancies or interstitials

than Ni in Ni-Cr system. Authors concluded with the calculated diffusion coefficients that two competing tendencies of Cr might exist but lead to a depletion of Cr by vacancies (well-known for RIS, depletion of Cr near grain boundaries) and the enrichment by interstitials (scarcely mentioned).

For Ti, the data of binding energy are quite scarce but can be found for stainless steels. Akimichi et al. conducted irradiation experiments in Ti-modified 316 austenitic steels with 1 MeV HVEM at 550°C. By comparing the calculated void nucleation rate and the experimental void number densities, they estimated that the binding energy of Ti-vacancy is about -0.5 eV in 316SS (Hishinuma and Fukai, 1983). Neklyudov et al. (Neklyudov and Voyevodin, 2008) and Rouxel et al. (Rouxel et al., 2016) adapted the value to -0.3 eV in 15-15Ti but did not specified the determination method. By the model of Mansur and Yoo (Mansur and Yoo, 1978), the magnitude of the binding energy of Ti-V in austenitic steels should significantly increase the trapping effect that enhances the recombination. The fact that the void nucleation decreases with Ti content could be evidence of the enhanced recombination (Neklyudov and Voyevodin, 2008; Rouxel et al., 2016). Moreover, Ti is thought to trap vacancies not only in solid solution but also through precipitates. Indeed, bubbles were found on dislocations and around a carbides in austenitic steels (Sekimura and Ishino, 1991). Pinizzotto et al. showed that the density of voids Nv passed through a minimum at 4 at.%Ti (Pinizzotto et al., 1978). They suggested that the nucleation rate of voids is likely affected by a Ti-vacancy binding and vacancy trapping.

2.4.2.2 In concentrated alloys

A concentrated alloy denotes a system in which the interaction between solute atoms can not be neglected. In concentrated alloys, the interaction between solutes and PDs but also the lattice distortion caused by the size difference of atoms can affect the formation and the mobility of defects. Tucker et al. did some ab-initio calculations in the Ni-Cr system. They found a formation energy of 0.92 eV for Cr-Cr dumbbells and of 0.5 eV for Ni-Ni dumbbells [107]. Thus, the Cr-Cr is considered to be more stable and could trap Cr. According to the authors, this trapping effect could slow down the diffusion of Cr and increases the recombination of interstitials and vacancies. However, this Cr-Cr interaction is not present in dilute alloys (<1 at.%).

The Molecular Dynamic (MD) study and in-situ observations of Lu et al. (Lu et al., 2016b) revealed that interstitial clusters exhibit a 1D motion in pure nickel whereas they have a 3D glide trajectory in Single Phase Concentrated Solid-Solution Alloys (SP-CSAs) such as NiCo, NiCoCrMo, etc. The difference of motions was attributed to a high-level lattice distortion caused by the size difference of atoms. A large volume deviation of 10.34% and 29.43% from Ni were found respectively in Ni-Cr and in Ni-Ti by calculations (King, 1966).

Thus, the distortion caused by Cr and Ti modified the mobility of PDs and clusters and enhance the recombination by trapping mobile defects.

To sum up, the interactions between solutes and PDs can dramatically change the behavior of alloys under irradiation. The binding of Ti-vacancy and Cr-interstitial may play an important role in the formation and mobility of defects. It is of great interest to study the distribution of different defects and the Ti/Cr segregation in order to identify the influence of these binding effects.

2.4.3 Modification of stacking fault energy and surface energy of voids by solute addition

Large amounts of stacking fault energy γ_{Ni} (SFE) in pure nickel were obtained from different experimental techniques but the data are different from one to another. Carter and Holmes (Carter and Holmes, 1977) summarized some values of γ_{Ni} experimentally measured as shown in Figure 2.22(a). By their own measurement, the magnitude of γ_{Ni} were found to be 120-130 mJ/m^2. The SFE of nickel is very high compared to the other fcc metals such as Cu and Au (<100 mJ/m^2).

Regarding the effect of solutes on SFE, Deléhouzée and Deruyttere measured the faulting probability of different Ni-based binary alloys by X-ray technique with results shown in Figure 2.22(b) (Deléhouzée and Deruyttere, 1967). The faulting probability is a parameter that is inversely related to the SFE. The addition of Ti and Cr were found to decrease efficiently the SFE. A very recent DFT study of Kumar showed directly that the SFE of the addition of 1 at.% solute (Ti, Cr, etc.) in nickel reduced the SFE (Figure 2.22(c)). Although the data are still limited, these two studies indicate that the addition of Ti and Cr is likely to reduce the SFE of alloys and that Ti is more efficient in lowering the SFE than Cr.

In Pinizzotto's work, the swelling behavior of Ni and Ni-based alloys was correlated with their SFE (Pinizzotto et al., 1978). The high dose self-irradiation experiments revealed that the swelling decreased with the content of Cr and Ti in dilute Ni-based alloys. Pinizzotto proposed two completing effects to explain the swelling behavior as a function of solute concentration:

1) The first one concerned the increasing stability of void embryo. Data in the article showed that the SFE and the free surface energy were positively correlated. So the addition of Ti and Cr led not only to a lower SFE but also a lower surface energy that could enhance void nucleation. These processes were considered dominant at low solute content and independent of temperature.
2) The second effect was the suppression of vacancy concentration by solute. This mechanism was assumed due to diffusion processes because it strongly depended on the

(a)

γ (mJ m^{-2})	Method	Reference
90	τ_3	Haasen (1954)
95	Creep data	Thornton and Hirsch (1958)
410	τ_3	Seeger, Berner and Wolf (1959)
150	Extrapolated (Ni–Co) node data	Howie and Swann (1961)
300	Extrapolated (Ni–Co) node data	Mader (1963)
300	τ_3	Mader, Seeger and Leitz (1963)
345	Reinterpretation of Howie and Swann result	Brown (1964)
450	Rolling texture	Dillamore and Smallman (1965)
$\leqslant 180 \pm 55$	Faulted dipole	Häussermann and Wilkens (1966)
$\geqslant 375$	Absence of tetrahedra	Jøssang and Hirth (1966)
$\leqslant 160 \pm 16$	Extrapolated (Ni–Co) tetrrahedra data	Humble, Loretto and Clarebrough (1967)
$\leqslant 160$	Extrapolated (Ni–Co) tetrahedra data	Clarebrough, Humble and Loretto (1967)
240	Rolling texture	Beeston, Dillamore and Smallman (1968)
79	Dissociated edge dipole	Forwood and Humble (1970)
250	Comparison of previous data	Gallagher (1970)
415	τ_3	Akhtar and Teghtsoonian (1971)
140	τ_3	Clement and Clement (1974)
234	Flow stress analysis	Sastry and Tangri (1975)

(b)

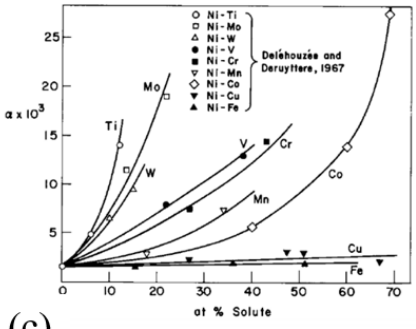

(c)

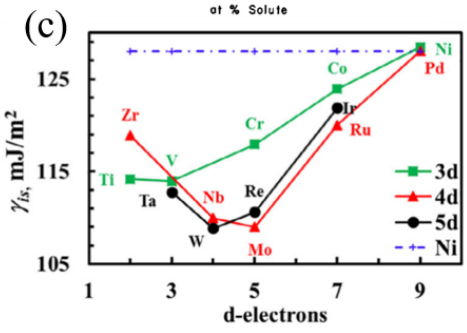

Figure 2.22 Investigation of the stacking fault energy in Ni and Ni-based alloys: (a) review of the determination of SFE of pure nickel from (Carter and Holmes, 1977); (b) variation of the faulting probability with solutes and their contents experimentally determined at room temperature by (Deléhouzée and Deruyttere, 1967); (c) DFT calculations of the SFE of Ni-based alloys at 1 at.% with respect to their number of d-valence electrons in magnetic states by (Kumar et al., 2018).

temperature and was dominant at a high content (Pinizzotto et al., 1978). Pinizzotto suggested that this effect might be through an impact on the bias factor or through defect trapping at solute atoms, either of which will lead to an enhanced vacancy-interstitial recombination rate.

However, the lack of data on SFE, surface free energy, diffusion coefficients and bias factors makes it still ambiguous to determine which mechanisms are responsible for observed phenomena. In the end, while the SFE is widely studied regarding the plastic deformation, its influence on the irradiation behavior is scarcely mentioned, especially at low doses and low solute contents. As the SFE is an intrinsic parameter of materials, its modification could greatly affect the nucleation and the evolution of defects under irradiation and more work is required.

2.5 Summary

Here we present a brief summary of bibliography.

Advanced austenitic steels are candidate materials for current and future nuclear systems. Their main limitation is their macroscopic volume extension under irradiation, so-called void swelling (Bates and Powell, 1981; Lauritzen et al., 1969). Empirically, the fine-tuning of major elements (Ni, Cr) and the addition of some minor solutes (Ti, etc.) improve efficiently the threshold of swelling (Yvon et al., 2015). To further improve the swelling resistance and predict the irradiation behavior of austenitic steels, it is essential to study the fundamental mechanisms of radiation damage and solute effects in the early stages of irradiation.

To do so, Ni and Ni-based model alloys have been commonly used as model materials for austenitic steels. In the early stages of irradiation, dislocation loops play an important role in the microstructural evolution. In Ni-based materials, **Frank loops** (Burgers vector = 1/3<111>) and **perfect loops** (Burgers vector = 1/2<110>) were observed under neutron (Kojima et al., 1988),electron (Norris, 1970; Urban, 1971; Yoo and Stiegler, 1977) and ion (Chen and Ardell, 1976; Lu et al., 2016b; Mazey and Hudson, 1970) irradiation over a large range of conditions. The nature of irradiation-induced Frank loops was identified as **interstitial-type** in most cases for all kinds of irradiation. However, small meta-stable vacancy loops were claimed in irradiated nickel with electron (Urban, 1971) and ion (Ishino et al., 1984; Robinson and Jenkins, 1981; Wakai et al., 2002). From current experiments in Ni, questions are still raised about the nature of Frank loops. Moreover, the evolution of dislocation loops with the presence of cascades has not been unambiguously described due to some side effects (type of irradiation, effects of surfaces and impurities). In Ni-based alloys, Ti and Cr are reported to have an influence on dislocations and voids (Pinizzotto et al., 1978; Porollo et al., 2013). Radiation-induced segregation of Ti and Cr near the surface was detected (Marwick et al., 1979). However, the RIS on radiation-induced structural defects is not available in the literature.

Base on current experiments, some models are suggested to describe the mechanisms of radiation damage in the fcc structure and solute effects. Via the dislocation bias model, the growth of interstitial dislocation loops under electron irradiation has been successfully reproduced by simulation (Urban, 1971; Yoo and Stiegler, 1977). Via the PD-solute interaction model, the difference in irradiated microstructure between Ni and its alloys are intuitively explained (Lu et al., 2016b; Pinizzotto et al., 1978). From energy aspects, the modification of SFE and surface energy of voids by solutes is also helpful to understand the formation of voids. However, current database in Ni-based systems is still insufficient to unambiguously describe elementary mechanisms of radiation effects in Ni and Ni-based alloys. Firstly, systematical studies of defect evolution in Ni have not been reported for ion irradiation which is more representative of neutron irradiation for primary damage (displacement cascades). Secondly,

comparative experiments of Ni, Ni-Ti and Ni-Cr systems are very limited to well elucidate the effect of Ti and Cr on radiation-induced defects. Segregation of these solutes on dislocation loops or voids have not been experimentally reported in Ni systems. Comparative studies of these materials are highly desired.

To sum up this bibliographic part, irradiated Ni and its alloys have been studied since the last century. The evolution of dislocation loops is an essential subject of the irradiated microstructure in these materials. The irradiated pure Ni allows to combine experimental data and simulation to explain the microstructure evolution at the atomic scale. Researches of irradiated alloys show a qualitative effect of solutes on the irradiated microstructure. However, there is still a lack of data that allows describing precisely and quantitatively the solute effect at the atomic scale. Thus, the first and the most important challenge of this thesis is to establish a sufficient and consistent database on the irradiation behavior of Ni and its alloys by different characterization tools. In this thesis, we aim to conduct a detailed and systematical study on Ni-based model materials in the early stages of irradiation. Irradiation conditions and side effects (influence of surface(s) and impurities) will be particularly taken into account. The experiment data will be crucial to well elucidate solute effects and will further be coupled with simulation at different scales, which will lead to a better understanding of mechanisms of solute effects in the fcc structure.

Chapter 3

Methodology

To investigate the effects of alloying elements on the microstructure of Ni under irradiation, pure Ni and its alloys are irradiated with self-ions. The structural defects (in most cases dislocation loops) and composition modification (segregation) induced by irradiation are then characterized and simulated. This chapter describes the materials, the characterization techniques and simulation tools involved in this study. Firstly, the studied materials are briefly presented, followed by the sample preparation for different utilization. Then, the conditions of irradiation experiments are specified. In the third part, the experimental techniques for the characterization of structural defects are presented. The fourth part describes the methods for the composition analysis. In this work, the principal characterization is conducted by convention Transmission Electron Microscopy (TEM) for the analysis of radiation-induced structural defects. The investigation of the segregation is performed by the Energy Dispersive X-ray spectroscopy (EDX) in scanning TEM (STEM) mode and Atom Probe Tomography (APT). Finally, an analytical diffusion model (Huang et al.) is described and used for the simulation of RIS in our study.

3.1 Studied materials and sample preparation

3.1.1 Elaboration of studied materials

In this work, high purity nickel (Ni), nickel-titanium (Ni-0.4/0.8/1.2%Ti by weight, in short, %wt.), nickel-chromium (Ni-0.4%wt.Cr) and nickel-titanium-carbon (Ni-0.4Ti-0.1C, in short Ni-Ti-C) alloys are studied.As the content of Ti in AIM1 is about 0.4%wt., this study focuses firstly on the addition of 0.4%wt. of titanium in Ni. Ni-0.4Cr is also studied in order to investigate the role of Cr. The comparison between Ni-0.4Ti and Ni-0.4Cr allows also to reveal whether the solute effects depends on the type of solute. The 0.4%wt. corresponds

to about 0.48% by atom (%at.) of Ti and 0.44%at. of Cr. These dilute alloys (<1%at.) can be more easily modelized by the numerical simulation. Furthermore, a series of Ni-Ti alloys with higher content of Ti (0.8% and 1.2%) are also used to study the influence of Ti content. According to the binary phase diagrams (Figure 3.1), solutes are completely in solid solution in nickel within the solid-phase temperature range. Thus, the studied alloys are pure fcc structure at initial state (thermodynamic equilibrium). Finally, 0.1%wt. carbon (corresponding to 0.4%at.) is alloyed into the Ni-0.4%wtTi alloy in order to study the combining effects of Ti and C.

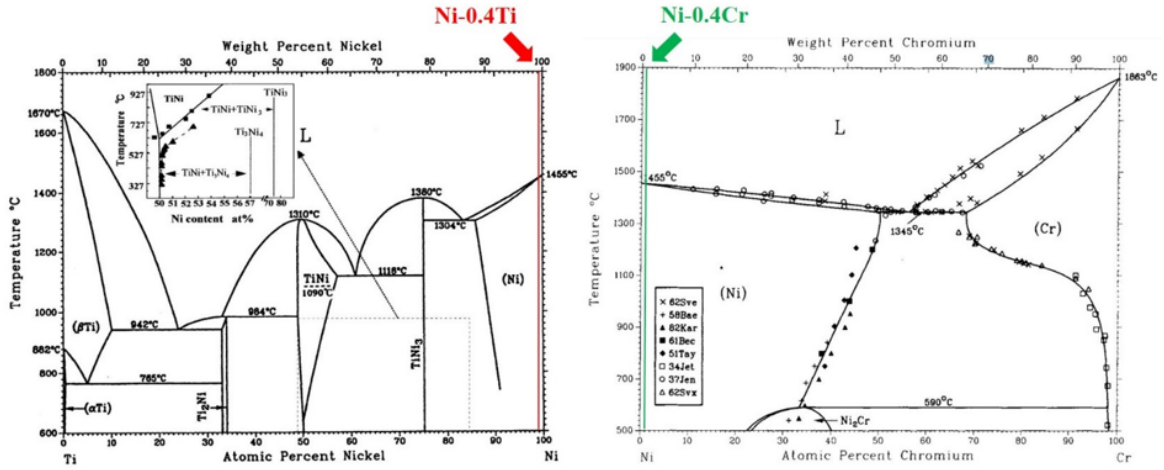

Figure 3.1 Phase diagrams of Ni-Ti (left) (Okamoto Hiroaki et al., 1990) and Ni-Cr (right) (Gupta, 2010).

The ultra-high purity Ni, Ni-0.4wt.%Ti (Ni-0.4Ti for short), Ni-0.4wt.%Cr (Ni-0.4Cr) and Ni-0.4%wt.Ti-0.1%wt.C (Ni-Ti-C) are manufactured by induction melting at the Ecole des Mines de Saint Etienne(EMSE), France. Measured content of solutes and impurities in mass ppm is shown in Table 3.1. The high purity Ni-0.8wt.%Ti (Ni-0.8Ti) and Ni-1.2%wt.Ti (Ni-1.2Ti) were also prepared by induction melting in Service de Recherches Métallurgiques Physiques (SRMP) using 99.99%wt. pure titanium (impurity analysis in ppm: Al <3, Ca <2, Cr <6, Cu <10, Fe <10, Mg <1, Mn <1, Nb <5, Ni <3, S <1, Si <5, V <3, Zn <1, Zr <3) and 99.99%wt. pure nickel (impurity analysis in ppm: Ag 1, Al 1, Ca 1, Cr <1, Cu 3, Fe 15, Mg <1, Mn <1, Si 2, Sn <1.) purchased from Goodfellow company.

3.1.2 Sample preparation before irradiation

High quality samples should be prepared in suitable forms for irradiations and different characterization tools, especially for TEM observations. Attention must be paid to avoid initial defects and impurities induced by the preparation because these two factors can affect strongly the microstructure under irradiation.

Table 3.1 Composition of Ni, Ni-0.4Ti, Ni-0.4Cr, and Ni-Ti-C manufactured by EMSE

Elements (%wt ppm)	**C**	**S**	**O**	**N**	**Ti**	**Cr**	**Ni**
Ni	8	2	3	2	/	/	Bal.
Ni-0.4Ti	2	4	14	1	0.39%wt	/	Bal.
Ni-0.4Cr	6	4	8	1	/	0.39%wt	Bal.
Ni-Ti-C	0.0879wt.%	5	9	1	0.39%wt	/	Bal.

3.1.2.1 Mechanical and thermal treatment

The raw materials are cut into slides of 400 µm thickness by a Struers Accutom-100 cutting machine and then mechanically polished to 50-80 µm thick using a SAPHIR-520 grinding/polishing machine with silicon carbide (SiC) and diamond abrasive discs. 3 mm diameter disks are punched out (suitable form for TEM sample). Although we gradually decrease the grain size of the abrasive discs to minimize the deformation due to the polishing, these mechanical milling and punch-out process may still introduce many dislocations inside the samples.

To further reduce the initial defect density, after 3 times argon atmosphere scanning, 3 mm diameter discs are annealed at 1000°C for 2 hours in a vacuum of 10^{-7} mbar followed by air-cooling to room temperature. Zirconium bands were annealed together near samples in order to absorb residual oxygen and to minimize the oxidation of samples.

3.1.2.2 TEM thin foils by twin-jet electro-polishing

3 mm diameter discs are electro-polished in a solution of 70/30 in the electrolyte of 70% Methanol / 30% HNO_3 at -30°C at about 10 V (current from 70 to 120 mA). After electro-polishing, both sides of the sample disc are mirror-like polished with a hole in the center. Thin zones around the hole are usually clean, large, flat and in good surface condition for the TEM observations. These thin foil samples were characterized before irradiation in TEM. In all the samples, few initial defects were observed. The dislocation density was less than 10^{10} m^{-2}.

3.1.3 Sample preparation after irradiation

Two sorts of samples are used for characterization: as-irradiated thin foils and FIB samples extracted from irradiated foils. FIB samples include transverse thin foil specimens for TEM observations and point-shape specimens for APT analysis.

3.1.3.1 Transverse TEM foils by FIB followed by flash polishing

Transverse TEM foils provide a transversal view of radiation damage in bulk materials that can be compared with thin foils in order to reveal the influence of free surface on the irradiated microstructure. Transverse specimens were lifted out from as-irradiated TEM thin foils in zones far from the thin zones using Focused Ion Beam (FIB) equipped on an FEI Helio 650 NanoLab dual beam Scanning Electron Microscopy (SEM) at SRMA/CEA-Saclay. A scheme is shown in Figure 3.2. In the classic way, extracted specimens are milled by FIB to a thickness less than 200 nm (observable in TEM). However, by testing on unirradiated samples, a great density of defects was induced by FIB in our samples, even with a low energy (5 kV) of gallium ion and a low current. These FIB-induced defects will strongly hinder the observations of radiation-induced ones. Thus, the FIB-induced defects have to be removed. Since these defects from a low energy ion implantation should be localized in near surface layers, a short-time electro-polishing technique, so-called flash polishing (Horváth et al., 2019), is applied.

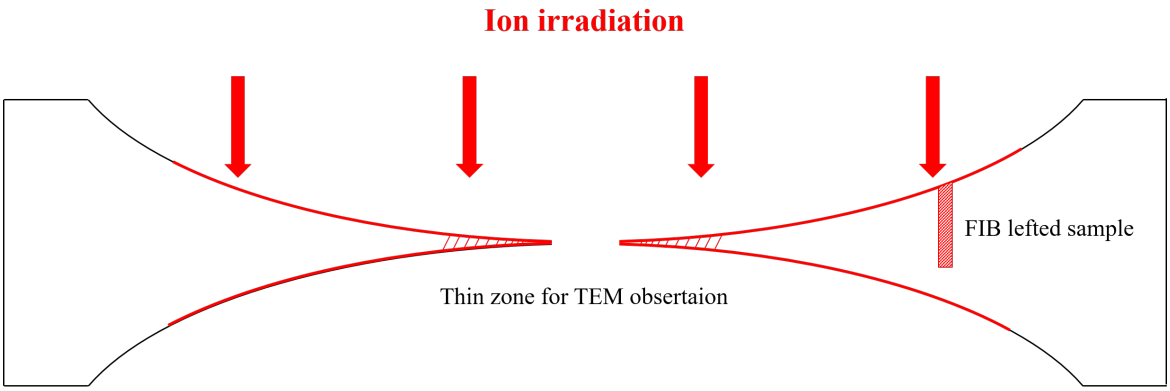

Figure 3.2 Scheme of irradiated sample geometry and FIB sample left-out position.

The setup of the flash polishing experiment is illustrated in Figure 3.3. The extracted specimens are firstly welded to gold (Au) or molybdenum (Mo) grids and pre-thinned by FIB milling at the angles of 52°±2° to 300-400 nm. Then, the grid is connected into an electro-polishing circuit equipped with a DC generator and a timer with a precision of 0.01s. The polishing was conducted in the electrolyte of 96% Ethanol / 4% $HClO_4$ (perchloric acid) at -45°C at 7.5 V for a duration of 0.1s-0.2s. The duration depends on the thickness of pre-thinned samples. After the polishing, samples must be quickly cleaned in an ethanol bath at -50°C followed by two other ethanol baths at room temperature.

In polished FIB samples prepared from irradiated materials, zones distant from the irradiated surface are completely free of defects except a few pre-existing dislocation lines. The distant zones are far way out of range of damage profile and they are not irradiated. Thus,

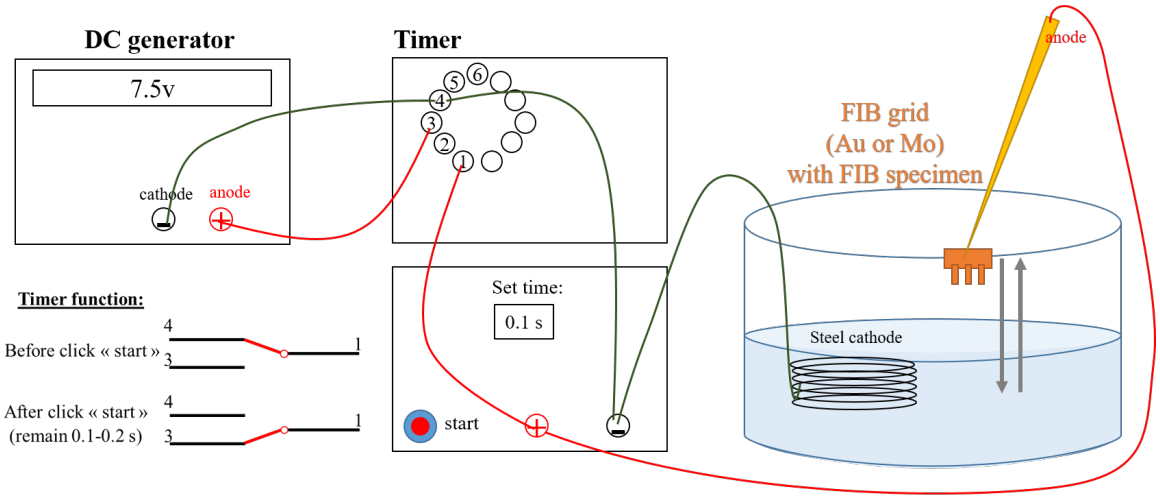

Figure 3.3 Setup of the flash polishing circuit with a DC generator, a timer and a cathode (austenitic steel) and a anode (FIB specimen) in a electrolytic solution; time function allows the connection of the circuit after clicking the button "start" for the set time.

it shows that flash polishing remove all FIB-induced defects in the sample. The irradiated zones with radiation-induced defects are clearly distinguished from unirradiated zones.

3.1.3.2 APT needle preparation by FIB

For the Atomic Probe Tomography (APT) analysis, needle-form specimens are prepared. Thick transverse wall-shape specimens are firstly lifted using the same FIB equipment presented above at SRMA/CEA-Saclay. Then the extreme of the wall shape specimen is welded on a tip of the silicon (Si) micro-coupon. The wall-shape specimen is then cut by FIB so a columnar sample is left on the micro-coupon as shown in Figure 3.4(a). Then, the columnar samples are thinned by annually milling. The needle is formed by successive annular milling with Ga ions as shown in Figure 3.4. In the final step, the milling proceeds until the aimed depth, either at the surface or deep into the sample. The typical final dimension of the tip is 50x50x100 nm^3 as shown in Figure 3.4(f).

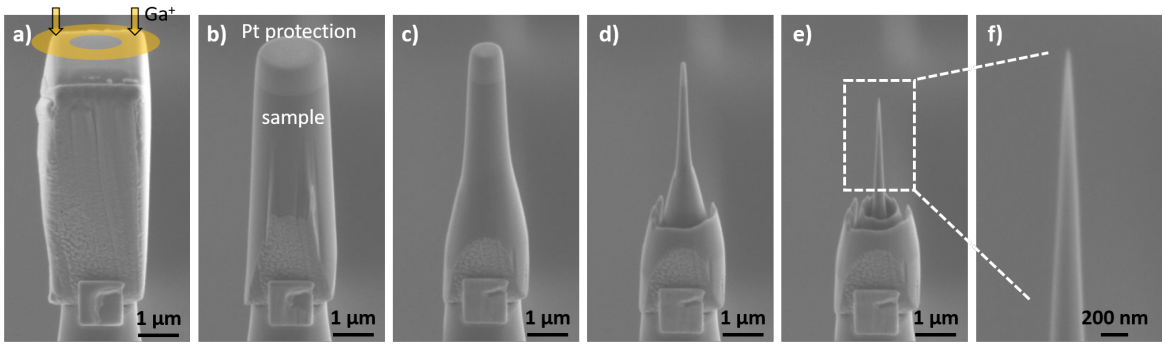

Figure 3.4 Successive milling of FIB lefted-out sample to prepare APT needle.

3.1.4 Irradiation experiments

All irradiations of this study are performed on electro-polished 3 mm diameter foils. In this study, self-ion (Ni^{2+}) irradiations are used to avoid the effect of injected impurities on the microstructure. Different temperatures are explored between 400°C and 700°C, which is the temperature range of the primary coolant in SFRs (Yvon et al., 2015). The swelling of ASSs is also known to be favored at these temperatures.

3.1.5 In-situ ion irradiation experiments

In-situ ion irradiation experiments are performed at the JANNuS-Orsay platform in the Laboratoire de Physique des 2 infinis Irène Joliot-Curie (IJCLab) at Université Paris-Saclay within the framework of the French National Network of accelerators for irradiation and analysis of molecules and materials (EMIR&A). Thin foils are irradiated in a 200 kV FEI Tecnai G2 TEM with 2 MeV Ni^{2+} ions produced by a 2 Megavolts tandem Van de Graaff accelerator (ARAMIS). The TEM and scheme of in-situ irradiation are shown in Figure 3.5(a) and Figure 3.5(b). The vacuum of specimen chamber is about 10^{-5} Pa. The temperature of the sample is controlled by a double tilt heating holder of GATAN with an estimated uncertainty of 25°C. The ion flux was of $4 \pm 0.8\ 10^{11}$ ions.cm^{-2}.s^{-1}. Before irradiation, the thickness of the observed zone is measured by the Converge Electron Beam Diffraction (CBED) technique along the <220> reflection, which will be presented latter in this chapter. A series of irradiation experiments at different temperatures (400, 450, 510, 560°C) and fluences (9 ± 1.8 x10^{13}, 2.7 ± 0.4 x10^{14}, 8.1 ± 1 x10^{14} ions.cm^{-2}) are conducted.

The damage profile shown in Figure 3.5(c) is calculated by the Stopping Range of Ions in Matter (SRIM) 2013 code (Ziegler, 2004) using Kinchin-Pease option with a displacement threshold energy of 40 eV (Stoller et al., 2013) and by the IRADINA code (Crocombette and Van Wambeke, 2019) using the same parameters. The two codes show a good agreement between them. In the thin zone (0-300 nm), the damage rate can be considered as approxi-

mately homogeneous as a constant of 2.7x10^{-4} dpa/s. For a fluence of 9x10^{13} ions.cm^{-2}, the dose is estimated as 0.06 dpa as shown in Figure 3.5(c). The other two fluences (2.7±0.4 x10^{14}, 8.1±1 x10^{14} ions.cm^{-2}) correspond respectively to 0.18 dpa and 0.54 dpa.

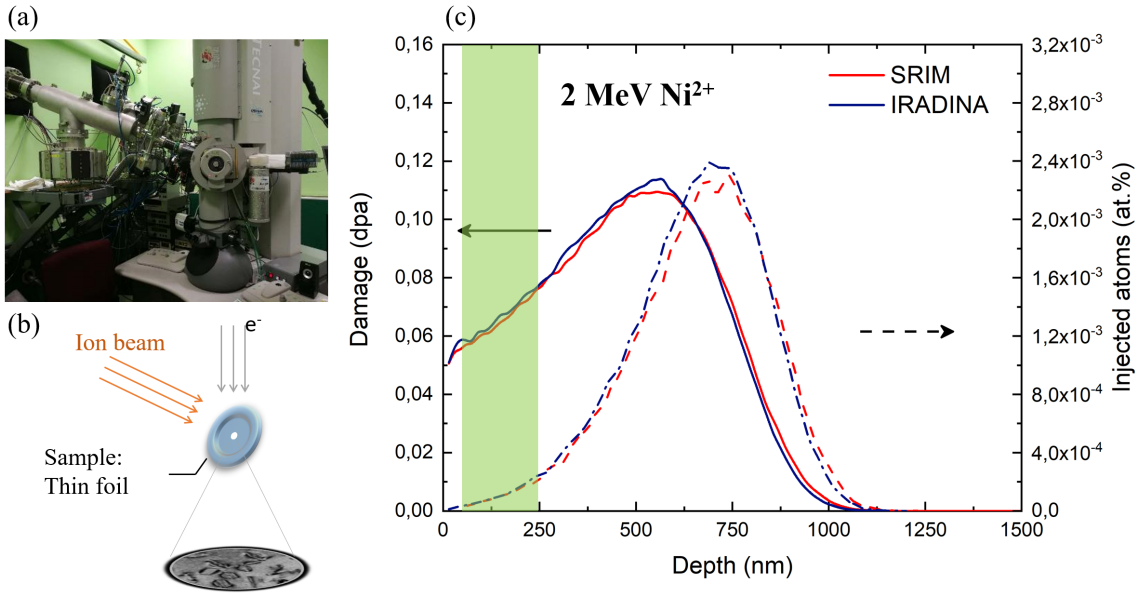

Figure 3.5 In-situ irradiation facility and damage profile by 2 MeV Ni^{2+}*ions*. (a) TEM coupled with accelerators at JANNuS-Orsay; (b) Scheme of in-situ irradiation in TEM; (c) Damage profile of 2 MeV Ni^{2+} ions calculated by SRIM 2013 (Ziegler, 2004) and IRADINA (Crocombette and Van Wambeke, 2019) for a fluence of 9x10^{13} ions.cm^{-2} with a displacement threshold energy of 40 eV using K-P mode.

3.1.6 Ex-situ ion irradiation experiments

Ex-situ ion irradiation experiments are performed at the JANNuS-Saclay platform in CEA Saclay. Thin foils are irradiated by a 5 MeV Ni^{2+} ion beam produced by a 2 MV Tandem Pelletron (JAPET) equipped with an external SNICS II ion source (cesium sputter source). JANNuS-Saclay irradiation facility is presented in Figure 3.6(a). Thin foils are fixed in a sample holder shown in Figure 3.6(b). The sample holder is in contact with a heating plate controlling the temperature during irradiation. The vacuum of specimen chamber is about 10^{-}5 Pa. The temperature is monitored by 4 thermocouples respectively in contact with samples. The uncertainty is about 25°C. The ion flux is of 2.1 ± 0.2 10^{11} ions.cm^{-2}.s^{-1} and the fluence was 2.3 ± 0.3 10^{15} ions.cm^{-2}.s^{-1}.

The damage profile shown in Figure 3.6(c) is also calculated by SRIM 2013 code (Ziegler, 2004) using Kinchin-Pease option with a displacement threshold energy of 40 eV (Stoller et al., 2013) and by the IRADINA code (Crocombette and Van Wambeke, 2019) using the same

parameters. In the thin zone (0-300 nm), the damage rate can be considered as approximately homogeneous as a constant of 6.8x10^{-5} dpa/s. For a fluence of 2.3x10^{13} ions.cm^{-2}, the dose is estimated as 0.75 dpa as shown in Figure 3.6(c).

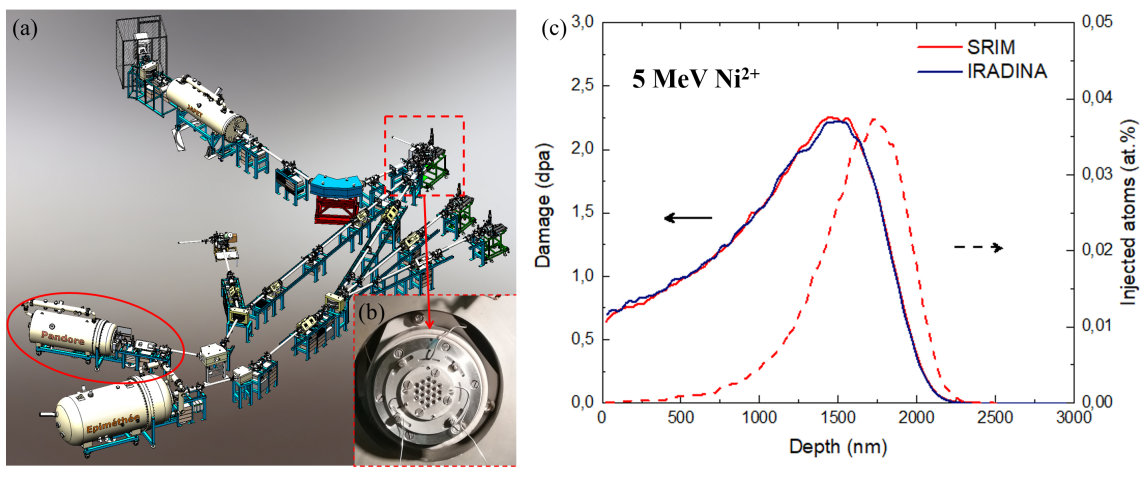

Figure 3.6 Ex-situ irradiation facility and damage profile by 5 MeV Ni^{2+}*ions*. (a) Irradiation platform at JANNuS-Saclay; (b) Sample holder for ex-situ irradiation with thermal-couple in contact with samples; (c) Damage profile of 5 MeV Ni^{2+} ions calculated by SRIM 2013 (Ziegler, 2004) and IRADINA (Crocombette and Van Wambeke, 2019) for a fluence of 2.3x10^{15} ions.cm^{-2} with a displacement threshold energy of 40 eV.

3.2 Characterization techniques

3.2.1 Defect characterization by conventional Transmission electron microscopy (TEM)

During the in-situ irradiation, the microstructural evolution is followed in TEM in real time and recorded on video. After irradiations (both in-situ and ex-situ), microstructure of irradiated samples is characterized by TEM. The characterization after irradiation is also called post-characterization. The post-characterization focused mainly on the analysis of radiation-induced defects in the microstructure, especially dislocation loops and in some cases voids. A brief introduction to the principle of characterization methods and their applications in our samples is presented in this section.

TEM is a microscopy technique using an electron beam that transmits through a specimen to form an image. The main advantage of TEM over other techniques is the direct visualization of the microstructure at a significantly high resolution (nanometer- and atomic-scale). Electrons and the specimen interact in many fundamentally different ways so that the image contrast arises due to different mechanisms. Within conventional imaging, the analysis

of contrasts under different diffraction conditions can indicate the characteristic features of defects in the specimen.

In this study, most characterization works were performed using conventional TEM imaging for the analysis of dislocation loops. The post-characterization was carried out by a FEI TECNAI G2 TEM operated at 200 kV located in Service de Recherches Métallurgiques Physiques (SRMP) at CEA-Saclay in France. This TEM is equipped with a LaB_6 filament and with Tridiem Gatan Imaging Filter (GIF) for Electron Energy Loss Spectroscopy (EELS). A Gatan double tilt sample holder allows us to orientate the sample differently in TEM so that various diffraction conditions could be achieved. Two-beam Kinematic Bright-Field (KBF) mode and Weak-Beam Dark-Field (WBDF) mode are employed to image defects (Loretto and Smallman, 1975). The analysis of voids is performed using a through-focal imaging technique (Hull and Bacon, 2011).

The TEM for in-situ irradiation is a 200 kV FEI TECNAI G2 TEM located in Laboratoire de Physique des 2 infinis Irène Joliot-Curie (IJCLab) at Université Paris-Saclay. A Gatan double tilt heating sample holder is used. Before irradiation, samples are put under KBF conditions using <111> or <002> reflections to optimize the contrast of radiation-induced defects when the irradiation began. The imaging conditions, such as the tilts and the focus, are frequently adjusted during the irradiation to keep the same diffraction conditions and to provide an optimum contrast of visible loops.

In this study, dislocation loops are the main feature of interest. Voids in some samples are also studied. Therefore, in the following sections, characterization methods are outlined in detail for dislocation loops and are briefly presented for voids.

3.2.2 Dislocation contrast

Here, we remind firstly some basic ideas of the diffraction. The diffraction of electrons follows the Bragg's law. The relation between the crystal, incident beam and resultant diffraction is $n\lambda = 2d_{hkl}sin(\theta_{B,hkl})$, where λ is the wavelength of the incident beam, d_{hkl} is the spacing of crystal plane (hkl), $\theta_{B,hkl}$ is the angle between the incident beam and crystal plane, n is a whole number indicating the n^{th} order of diffraction. An equivalent way to present the diffraction obeying the Bragg's law is the Ewald sphere. The construction of Ewald sphere is illustrated in Figure 3.7(a). The diffraction vector in this case is defined as $\mathbf{g}$ with $|\mathbf{g}| = (1/d)$. By its definition in reciprocal lattice, the Braggs' law is geometrically satisfied by the geometry for instance for the 1st order $(n = 1)$.

When Bragg's law is strictly satisfied, the incident beam will be strongly diffracted so the intensity of diffracted beam will be significant. If the incident angle deviates from Bragg's angle, the diffraction will be reduced. The deviation vector $\mathbf{s}_g$ is defined as $\mathbf{k} = \mathbf{g} + \mathbf{s}_g$ where

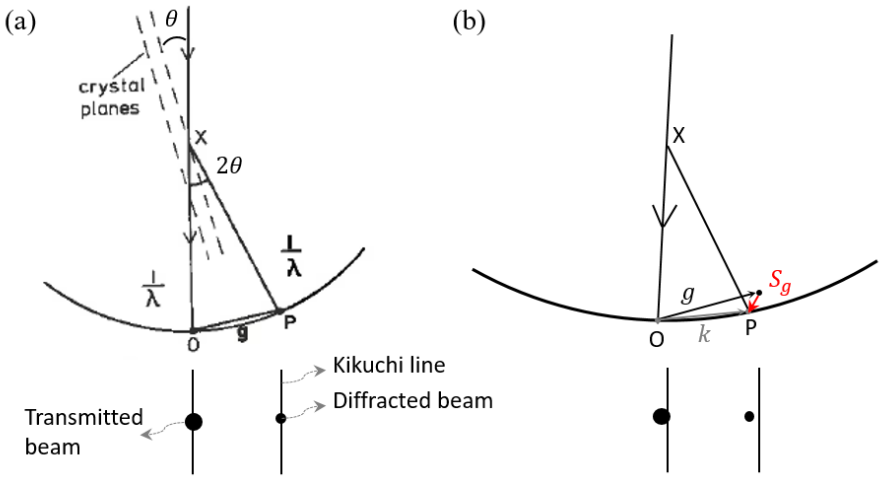

Figure 3.7 Diagram illustrating the Ewald sphere construction. The radius of the sphere is $1/\lambda$ and a diffracted beam is formed parallel to XP where P is a point in the reciprocal lattice. The origin of the reciprocal lattice is marked at O and OX is the direction of the incident electron beam. Two situations are shown: (a) the incident angle is exactly the Bragg's angle (extracted from (Loretto and Smallman, 1975)) and (b) the incident angle is deviated from Bragg's angle for $s_g > 0$. The corresponding position of spots in diffraction and Kikuchi lines are shown for each case.

g is the current diffraction vector and k is the diffraction vector in exact Bragg's conditions (Figure 3.7(b)).

Figure 3.7 also presents the position of diffraction spots and Kikuchi lines. Kikuchi lines will appear when the specimen is thick due to incoherently scattered electrons in all directions (CARTER et al., 1996). Kikuchi lines are frequently used to select the diffraction condition $s_g > 0$ (Figure 3.7(b)). Moreover, the Kikuchi maps are very helpful to index the crystal orientations and diffraction vectors, which is indispensable for the characterization of the Burgers vector and the nature of dislocation loops in this thesis. The Kikuchi maps of fcc structure extracted from (Loretto and Smallman, 1975) are used and will be presented with the results.

Since structural defects especially dislocations (lines and loops) introduce elastic strain, a local change of diffraction conditions is produced, leading to variations of intensity of the transmitted beam and diffracted beams. A dislocation contrast is thus formed in the image. The dislocation contrast depends strongly on the feature of dislocations and diffraction conditions. By analyzing the contrast under given diffraction conditions, the characteristic of dislocations can be revealed. To conduct an accurate analysis of dislocations from their contrast, a mixture of contrast from different planes has to be avoid. Therefore, the imaging conditions is usually chosen by ensuring that only one set of planes is under or close to the Bragg's conditions, so-called two-beam conditions in TEM. As indicated above, two imaging

modes under two-beam conditions (kinematic bright field and weak-beam dark field) are used in our study and described here.

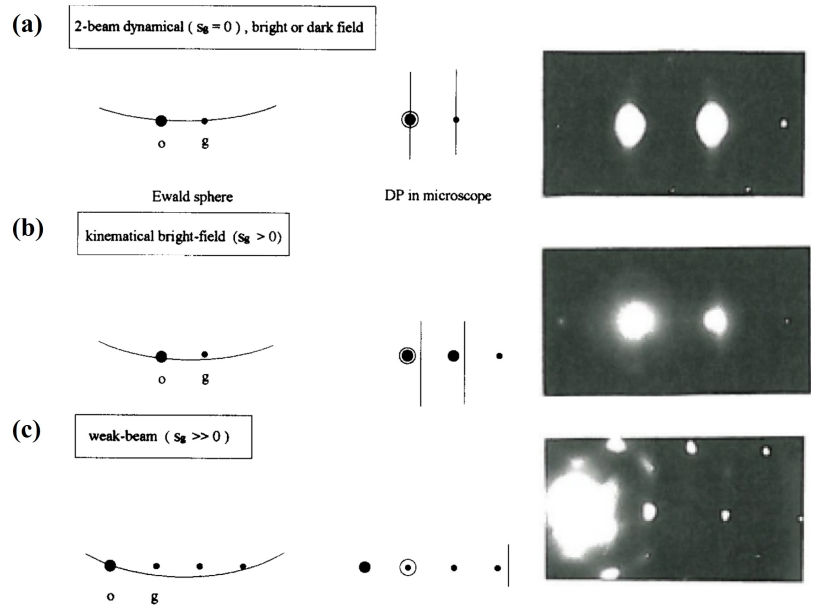

Figure 3.8 Representation of the different diffraction techniques: (a) two-beam dynamic ($s_g = 0$), (b) two-beam kinematic ($s_g > 0$), (c) weak-beam ($s_g \gg 0$) mode. In each case the Ewald sphere is sketched on the left-hand side, and a schematic diffraction pattern (DP) showing the position of the relevant Kikuchi lines in the middle and the experimentally observed diffraction pattern on the right side. The curvature of the Ewald sphere is exaggerated for clarity. The open circle represents the objective aperture (Bhattacharya, 2014; Jenkins, 1994)).

3.2.2.1 Kinematic bright field (KBF)

Bright field (BF) is the most utilized image mode for the analysis of structural defects. BF is performed using the transmitted beam to image objects. As the local distortion due to dislocations cause a further diffraction compared to the matrix, dislocations appear dark in BF images.

When the diffraction is under exact Bragg's conditions, so-called dynamic conditions ($s_g = 0$), the transmitted beam is strongly diffracted and the intensity of the projected image becomes low, which makes the observation difficult (even impossible). If the diffraction conditions are slightly deviated from the exact Bragg's law (the deviation parameter $s_g > 0$), the intensity of transmitted spot will increase significantly while the local diffraction due to dislocations remain strong (see Figure 3.8(b)). Under these conditions ($s_g > 0$), a clear contrast of dislocations can be achieved and employed for the analysis of dislocations.

3.2.2.2 Weak-beam dark field (WBDF)

WBDF is achieved by tilting the sample far from the exact Bragg conditions while letting only one set of planes diffracting. In this condition, the deviation parameter is very large $s_g \gg 0$. However, the local strain field in regions close to the dislocation cores may bend the diffracting planes back towards the Bragg condition. Therefore, weak beam images have a substantial enhancement of the contrast relative to the surrounding background (Jenkins, 1994) (see Figure 3.8(c)). Since $s_g \gg 0$, crystal will not diffract unless regions adjacent to dislocations, leading to the main advantage of WBDF that is a fine-scale contrast of dislocation. So, WBDF is useful to resolve small defects (like small dislocation loops and stacking fault tetrahedra) and the fine dislocation structure.

3.2.3 Analysis of Burgers vector of dislocation

3.2.3.1 Burgers vector of a dislocation under FS/RH convention

The general definition of the Burgers vector **b** of a dislocation in a crystal is the Burgers circuit construction using finish-start/right-hand (FS/RH) convention (Hirsch, 1967). FS/RH convention is given for an edge dislocation as shown in Figure 3.9.

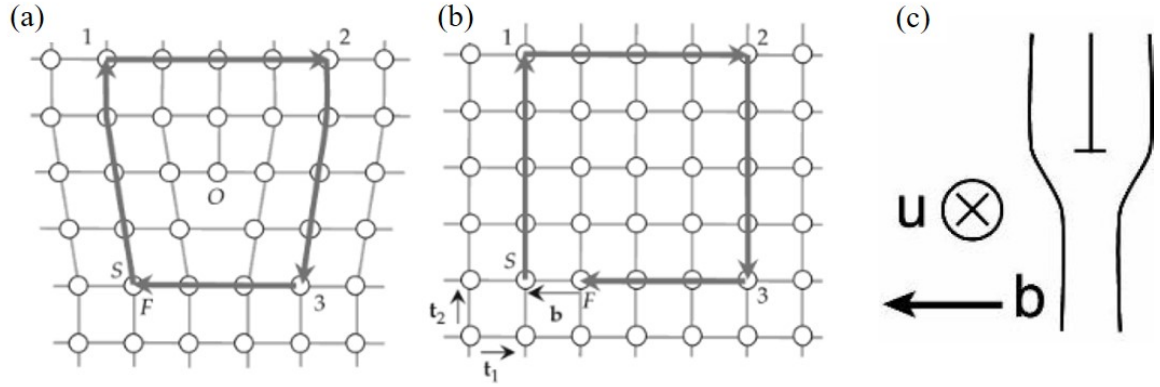

Figure 3.9 Schematic diagram showing the Burgers vector under FS/RH convention: FS/RH Brugers circuits in (a) a distorted crystal and (b) a perfect crystal with the dislocation direction **u** pointing into the paper so that the right-handed (RH) convention produces a clockwise Burgers circuit S-1-2-3-F ((a) and (b) extracted from (Anderson et al., 2017)); (c) a simplified scheme showing the FS/RH convention.

The Burgers vector of a dislocation can be defined only when the dislocation direction **u** is clearly defined. In this work, if we view along the electron beam, from the top to the bottom, the dislocation line sense **u** of a dislocation loop is defined as clockwise. With the FS/RH convention, the Burgers vector of a vacancy edge loop and an interstitial edge loop is given respectively in Figure 3.10(a) and Figure 3.10(b). If we view along the electron

beam, from the top to the bottom, the dislocation line sense is defined as clockwise. A closed Burgers circuit is drawn around the dislocation in a sense related by a right-hand rule to the positive sense of the dislocation. The circuit taken in perfect crystal fails to close and the gap from F to S defines the Burgers vector of the loop. Beside, within the convention, the normal of the loop habit plane is always upward by definition.

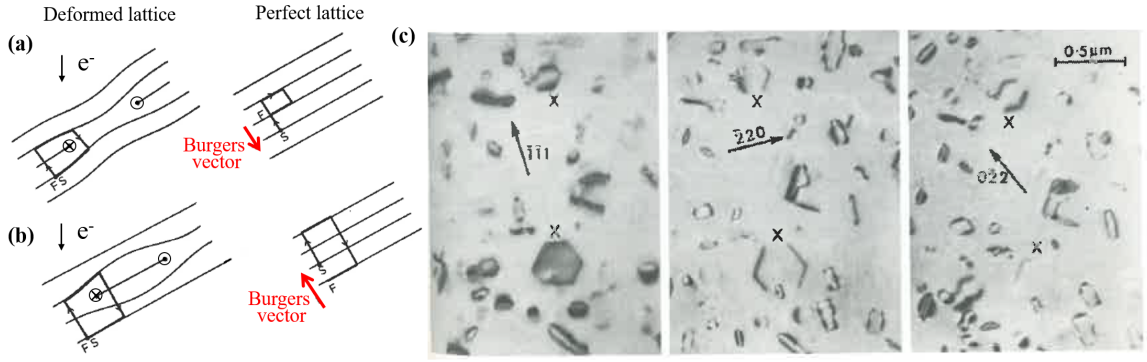

Figure 3.10 Schematic diagram showing the Burgers vector under FS/RH convention and experimental observation of the visibility in function of diffraction conditions: definition of dislocation line direction and Burgers vector of (a) a vacancy loop and (b) an interstitial loop; (c) experimental observations of visibility of loops marked X under different diffraction conditions in silicon (extracted from (Loretto and Smallman, 1975)).

3.2.3.2 Invisibility criterion

The amplitude of the diffracted beam ϕ_g including crystal imperfections (such as dislocations and stacking faults) is given by the equations of Howie and Whelan (Howie and Whelan, 1961):

$$\phi_g = (\pi i \xi/_g) \int_0^t exp\{-2\pi i(s_g z + \mathbf{g}.\mathbf{R})\}\, dz$$

where t is the specimen thickness, $\xi/_g$ the extinction distance for the reflection $\mathbf{g}$, s_g the deviation parameter, $\mathbf{R}$ the displacement field of an unit cell from its lattice position in the perfect crystal. $\mathbf{R}$ in an isotropic solid for the general case can be written as:

$$\mathbf{R} = \frac{1}{2\pi}\left\{\mathbf{b}\phi + \mathbf{b}_e \frac{sin2\phi}{4(1-\nu)} + \mathbf{b}\wedge\mathbf{u}\left[\frac{1-2\nu}{2(1-\nu)} lnr + \frac{cos2\phi}{4(1-\nu)}\right]\right\}$$

$\mathbf{R}$ is given here in polar coordinates (r and ϕ) of the studied point in the foil; $\mathbf{b}$ is the Burgers vector, $\mathbf{b}_e$ is the edge component of the Burgers vector, $\mathbf{u}$ is the unit vector along the dislocation line (the line direction), and ν is Poisson's ratio.

The first term in exponential $s_g z$ results from the perfect lattice, the second term $\mathbf{g}.\mathbf{R}$ are produced from the distortion. Therefore the contrast of dislocation depends on $\mathbf{g}.\mathbf{R}$. A

dislocation line or loop is completely invisible only when $\mathbf{g}.\mathbf{b} = 0$ and $\mathbf{g}.\mathbf{b} \wedge \mathbf{u} = 0$. However, the latter one cause a very faint contrast when it is not zero, negligible to the contrast from the former one. For a mixed dislocation, which produces a combination of edge and screw displacements, there is no condition for which $\mathbf{g}.\mathbf{b} \wedge \mathbf{u} = 0$ is exactly zero (Hull and Bacon, 2011). Thus, in practice, we usually consider that when a dislocation loop is invisible or shows a residual contrast, its Burgers vector satisfies $\mathbf{g}.\mathbf{b} = 0$. Figure 3.10(c) shows the visibility of a dislocation loop (X) in function of the diffraction vector.

In fcc structure, three types of dislocations exist: perfect dislocations ($\mathbf{b}$=1/2 < 110 >), Frank partial dislocations ($\mathbf{b}$=1/3 < 111 >) and Shockley partial dislocations ($\mathbf{b}$=1/6 < 112 >) (Hull and Bacon, 2011). Dislocation loops can only be Frank loops (four sub-families) or perfect loops (six sub-families) (Hull and Bacon, 2011). Frank loops can turn into perfect loops due to the unfaulting process by Shockley partials presented in the previous chapter (Equation 2.2 and 2.3). To determine the Burgers vector of a dislocation loops,

1) the loop should be imaged under different diffraction conditions $\mathbf{g}$;
2) the visibility of this loop should be identified for each $\mathbf{g}$;
3) a visibility table containing 4 families of Frank loops and 6 families of perfect loops is established to identify the Burgers vector of the loop $\mathbf{b}$;

The analysis of Burgers vectors is important to understand the origin of this loop, its mobility and its nature. By analyzing many loops in the same zone, we can obtain the proportion of Frank loops and perfect loops, which is a parameter of interest to study the unfaulting process.

3.2.3.3 Statistic method

The method presented above allows us to determine individually the Burgers vector of a specific loop. However, when the sample is tilted with a large angle from one diffraction condition to another, it becomes difficult to track the same loop in some cases, especially when loops are small and there is no reference point in studied zones. Sometimes, we are only interested in the proportion of Frank loops and perfect loops but not a specific loop. To overcome the inconvenient of individual analysis and quickly obtain the proportion, a statistic method was developed (Prokhodtseva et al., 2013). The method is fully described in (Prokhodtseva et al., 2013). Briefly, assuming that each family of Burgers vectors (four families of Frank loops and six of perfect loops) are equal probable, the theoretical proportion of visible loops are known for each diffusion vector $\mathbf{g}$. By counting the number of defects visible in the same zone under different $\mathbf{g}$, an equation system of two unknown can be established and solved by the square-least method. The solution is the number of loops for each type.

Furthermore, the hypothesis of the method can be modified to conduct a more accurate analysis of the proportion. By separating one specific family, an equation system of three unknown can be established. The solution gives the proportion of this specific family and the other families.

Detailed application of the method will be presented in Chapter 4 with results.

3.2.4 Determination of loop nature by inside-outside method

A basic feature of a dislocation loop is its nature (interstitial-type or vacancy-type). Whether a dislocation loop is an agglomeration of interstitials or vacancies is an important question to understand not only the origin of this defect (formation) but also its evolution (growth, unfaulting, interaction with other defects, etc.). It is thus essential to characterize the nature of dislocation loops. The theory for the determination of the nature of dislocation loops is presented in details by Hirsch (Hirsch, 1967), based on the analysis of dislocation contrast. Different practical methods have been presented in (Jenkins, 1994). For a relatively large loop (>10 nm), the most employed method is the inside-outside method (Jenkins, 1994). To demonstrate unambiguously the nature of a dislocation loop, (1) the Burgers vector, (2) the loop habit plane and (3) the inside-outside behavior for $\pm\mathbf{g}$ must be fully analyzed. We present here the principle of inside-outside method.

3.2.4.1 Inside-outside method for pure edge loops

For pure edge loops ($\mathbf{b}.\mathbf{u} = 0$), such as Frank loops, (1) and (3) will be sufficient to fully determine its nature because its Burgers vector is perpendicular to the loop plane. Firstly, the orientation between the Burgers vector and dislocation line must be defined. Under FS/RH convention, interstitial loops have a Burgers vector $\mathbf{b}$ pointing upward (same direction as the loop normal $\mathbf{n}$) giving $\mathbf{n}.\mathbf{b} > 0$ and vacancy loops have a Burgers vector $\mathbf{b}$ pointing downward (opposite direction to $\mathbf{n}$) giving $\mathbf{n}.\mathbf{b} < 0$.

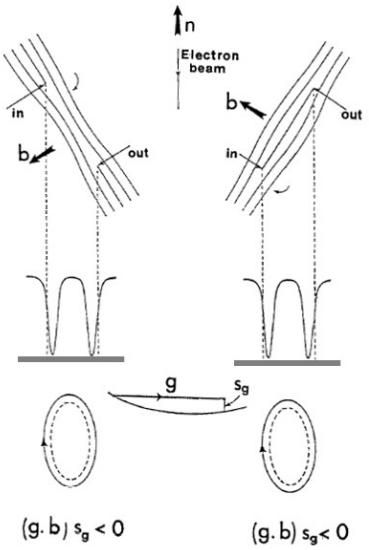

Figure 3.11 Schematic diagram showing inside-outside behavior of a pure edge loop showing how the contrast is influenced by both the loop nature and the sense of inclination with s_g assumed positive (Hirsch, 1967).

Figure 3.11 illustrates the principle for the determination of the nature of an edge loop. It shows schematically how the edge loop contrast changes with the loop nature and inclination. In Figure 3.11, each loop exhibits an inside contrast: the image of the loop in KBF and WBDF (dotted line) lies inside the real projected position (solid line). If the sign of s_g (rarely) or the direction of **g** is reversed, the 2 loops would exhibit an outside contrast: the image of the loop (dotted line) lies outside the real projected position (solid line). The relation between the Burgers vector, the diffraction conditions and the inside-outside contrast is (for $s_g > 0$):

- Inside contrast arises when $(\mathbf{g}.\mathbf{b}).s_g < 0$;
- Outside contrast arises when $(\mathbf{g}.\mathbf{b}).s_g > 0$.

To distinguish the two cases illustrated in Figure 3.11, the inclination of loop plane must be determined. For a pure edge loop, as the loop plane is perpendicular to the Burger vector, the inclination of the loop plane is obtained if the Burgers vector is known. In practical, the determination of the nature of an edge loop (a Frank loop) consist of three steps:

1) determination of the Burgers vector $\pm\mathbf{b}$;
2) determination of the inside-outside behavior for $\pm\mathbf{g}$. It gives the sense of **b**;
3) With the FS/RH convention and the **u** in the clockwise direction: if **b** points upward, the loop is interstitial-type; if **b** points downward, the loop is vacancy-type.

We stress on that the dislocation line direction **u** must be defined in the clockwise direction to used this method. If **u** is reversed, the direction of **b** will also be reversed.

3.2.4.2 Inside-outside method for non-pure edge loops

For non-edge loops, such as some perfect loops, the Burgers vector is not perpendicular to the loop habit plane ($\mathbf{b}.\mathbf{u} \neq 0$). The determination of **b** direction (up or down) can not indicate the loop nature (Figure 3.12). The loop inclination has to be obtained to determine the loop nature. In this study, perfect loops need to be studied. Since perfect loops are not always pure edge, the determination of their nature requires complementary techniques. We present here two techniques based on the inside-outside method.

Determination of unsafe conditions

The method for edge loops still apply in some cases for non-edge loops. The conditions in which the method can be applied are called safe conditions. The other conditions are called unsafe conditions. If the analysis is carried out under safe conditions, the determination of the nature of non-edge loops can be simply conducted as for edge loops. The safe/unsafe method was presented by Maher and Eyre (Maher and Eyre, 1971) in a body-centered cubic material (Molybdenum). Jenkins summarized the method in another bcc material (iron) (Jenkins, 1994). Here we extend the method in the fcc structure (Ni).

In order to determine the safe conditions, the origin of the unsafe conditions has to be understood. Figure 3.12 illustrates the origin of the unsafe conditions with 3 interstitial loops as example. The first loop is assumed pure edge (Figure 3.12(a)). The loop plan normal is indicated by orange arrow and always point upward. Using FS/RH convention with the indicated g (black arrow), the Burgers vector **b** (blue arrow) points upward and an inside contrast is shown. If the loop rotates inside the cylinder keeping the same **b**, the pure edge loop becomes non-edge loop. 2 cases appear:

Case 1 (Figure 3.12(b)): the loop plane rotates but does not exceed the edge-on position ($\mathbf{n}.\mathbf{n}_z = 0$);in this case, the contrast is always inside along the rotation because ($\mathbf{g}.\mathbf{b}$) remains < 0;

Case 2 (Figure 3.12(c)): when the loop habit plane passes the edge-on position, the plane normal changes from the dotted one to the line one by the definition (always pointing to upward); Meanwhile, by FS/RH convention, the sense of **b** changes as well, from dotted one to the line one; in this case, as ($\mathbf{g}.\mathbf{b}$) becomes > 0, the contrast is reversed to outside.

Without the inclination of the loop plane in case 2 (Figure 3.12(c)), the determination of loop nature only with the outside contrast will give the b pointing downward thus result in vacancy nature, which is not true.

Figure 3.12 shows that if the loop plane can rotate at any angle, it is never safe to use directly the inside-outside method for the determination of the loop nature. The safe and

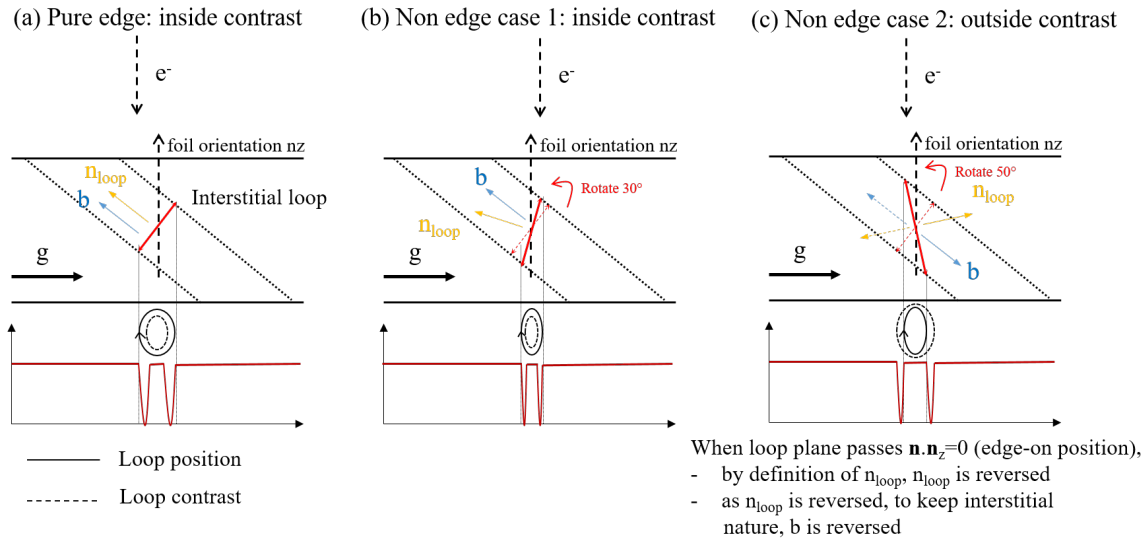

Figure 3.12 Scheme illustrating how the inside-outside behavior of an interstitial loop with a Burgers vector **b** is affected by its inclination. (a) an edge loop showing inside contrast; (b) a non-edge loop from the rotation of edge loop by 30° showing still inside contrast; (c) a non-edge loop from the rotation of edge loop by 30° showing outside contrast (modified from (Föll and Wilkens, 1975)).

unsafe conditions can be defined with the assumption that it is possible to specify an upper limit ϕ_m to the acute angle ϕ between **b** and the loop normal **n** (Jenkins, 1994). Loops for which the angle α between the Burgers vector **b** and the zone axis **z** is $>$ (90° - ϕ_m) are unsafe. In this work, the non-edge loops are perfect loops which is formed usually from the unfaulting process of edge Frank loops. When the unfaulting happens, the Burgers vector of the Frank loop ($\mathbf{b}_F = 1/3 < 111 >$) will change to a Burgers vector of one of the associated perfect loop families ($\mathbf{b}_p = 1/2 < 110 >$). The angle between $\mathbf{b}_F$ and $\mathbf{b}_p$ is the upper limit angle ϕ_m=35°. Any variant of perfect loops satisfies α<(90°-35°)=55° is safe.

This method will be better illustrated with a specific example. Consider now a zone axis **z**=[112]. For the 1/2[011] perfect loops, the angle ϕ between the **b** and **z** is 30° so this type of perfect loops are safe. On the contrary, for the 1/2[110] perfect loops, ϕ=55° so this type is unsafe. The method is illustrated by the stereogram in Figure 3.13. The green area defines orientations of the loop normal **n** where a non-edge loop would show the opposite contrast to a pure edge loop of the same Burgers vector **b**=1/2[110] for **b**=1/2[011]. The 1/2[011] perfect loops are formed from the unfaulting of either 1/3[111] or 1/3[$\bar{1}$11] Frank loops (green △). As none of these Frank loops lies within the green area, the 1/2[011] family is safe. Another example is the 1/2[110] perfect loops. The red area indicates **b**.**z**<0. As one possibility of the original Frank loop (1/3[11$\bar{1}$], red square □) lies within the red area is in the red area so the 1/2[110] perfect loops are under unsafe condition.

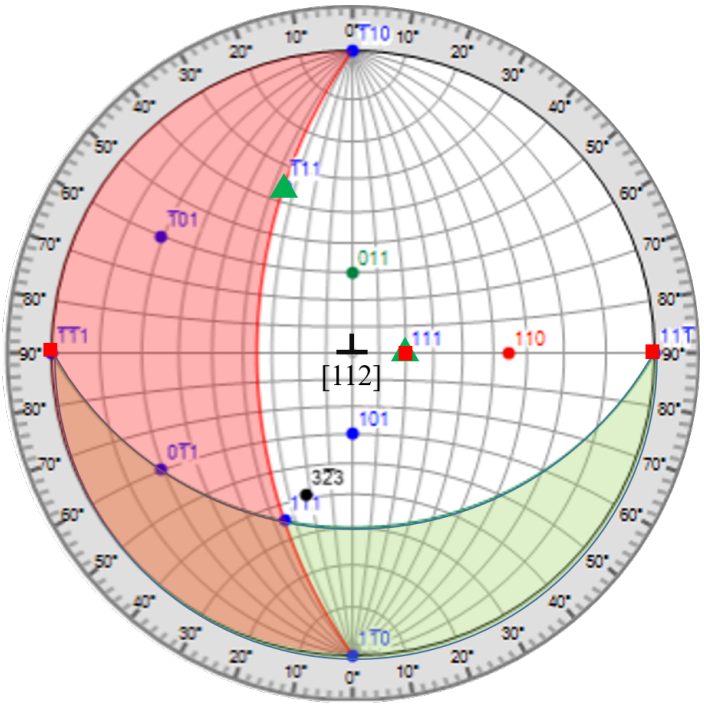

Figure 3.13 Stereogram showing the safe conditions for a non-edge loop to show the same contrast as a pure edge loop of the same Burgers vector. The red area defines orientations of the loop normal **n** where a non-edge loop would show the opposite contrast to a pure edge loop of the same Burgers vector **b**=1/2[110]; the green area defines the similar orientation for **b**=1/2[011]. The green triangles △ show the possible original Frank loops for 1/2[011] perfect loops; red squares □ are Frank loops for 1/2[110] loops.

As a consequence, the determination of the nature of an non-edge loop (a perfect loop) can be conducted in practical by:

1) determination of the Burgers vector of the perfect loop $\pm\mathbf{b}_{perfect}$;
2) drawing the stereogram along the zone axis **z**;
3) calculate the α and compared with (90-ϕ_m)=55°;
4) if $\alpha < 55°$, the perfect loop in under safe conditions and can be treated as edge loop;
5) if $\alpha \geq 55°$, the perfect loop is under unsafe conditions and further information of the inclination of the loop plane should be obtained to determine it nature.

Determination of the inclination of the loop plane

For non-edge loops under unsafe conditions, the inclination of their loop planes should be determined. The inclination can be either determined by stereo-microscopy or a complete determination of the loop habit plane.

Stereo-microscopy is an imaging technique using different viewing angles to produce a 3D visualization of objects. In a TEM, stereo-microscope imaging can be conducted by taking two TEM micrographs with a well known rotation in order to obtain the inclination of objects, for instance, the inclination of loop habit plane. The principle of the technique is illustrated in Figure 3.14. In Figure 3.14(a), a dislocation loop with an inside contrast is imaged. Then the crystal is rotated anti-clockwise 15° and a second image is obtained where the insides contrast is narrower than the first one. From this variation of projected size (from D_0 to D_1), the inclination of loop habit plane is as shown in Figure 3.14(a) and Figure 3.14(b). Then according to Figure 3.14(c) (Edington, 1975), we are in the third case so the loop is interstitial-type. This method allow us to quickly determine the loop nature even without knowing the Burger vector. However, it raises uncertainty in two cases, either the loop is in/near edge-on position (poor inside-outside contrast) or the loop is a near-shear loop (b parallel to the loop habit plane, rare in practice).

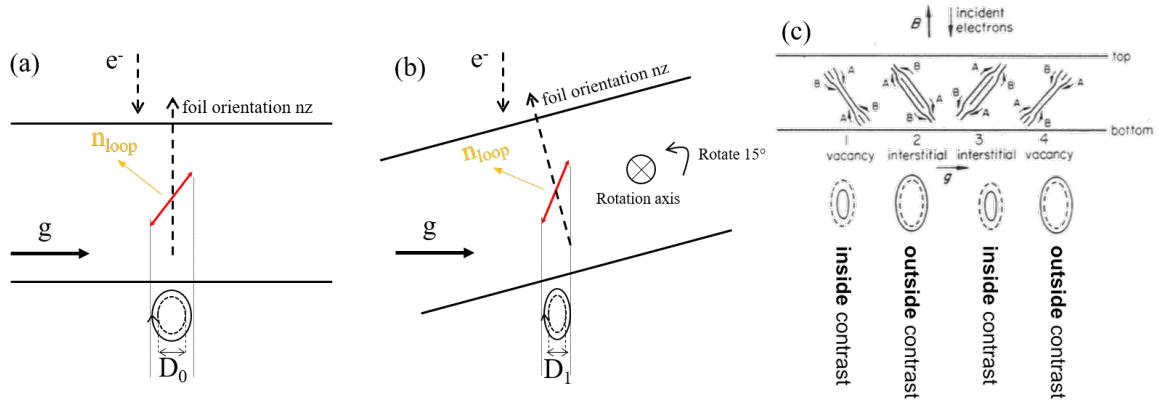

Figure 3.14 Determination of the inclination of loop plane and loop nature by stereo-microscopy. (a) initial inclination of a dislocation loop with associated loop contrast; (b) inclination after titling 15° with associated loop contrast; (c) summary of loop nature determination by stereo-microscopy (Edington, 1975).

3.2.5 Determination of sample thickness by Convergent Beam Electron Diffraction

TEM samples need to be sufficiently thin, from tens of nm to hundreds, so that electrons can transmit through the material. Such a low thickness volume, the thickness can play an important role in some cases. First, the free surfaces of thin foils can act as strong sinks for irradiation defects. Second, as TEM imaging is a 2D projection for 3D microstructure, the density of objects contained in the specimen depends directly on the thickness estimation. Thus, it is essential to measure the thickness of zones of interest in our study. The thickness

of zones of interest in this work is usually in the range of 100 nm to 300 nm. Different techniques can be applied to determine the thickness:

- Fringes of equal thickness;
- Electron Energy Loss Spectroscopy (EELS);
- Convergent Beam Electron Diffusion (CBED);
- stereo-imaging;

In this work, the CBED is the most frequently used method for its measurable range (50 - 280 nm) and it simplicity. For short, the thickness is extracted from the fringe spacing as shown in Figure 3.15(b) The application of CBED technique of this work is presented in Appendix C. The stereo-imaging using a dislocation line or a grain boundary is used to verify the thickness measurement by CBED. In very thin zones (40-100 nm), EELS is applied to determine the thickness. The thickness fringe is not used in this study since the zones near the edge of the hole is often twisted and bent, which makes the measurement by thickness fringes usually difficult and inaccurate.

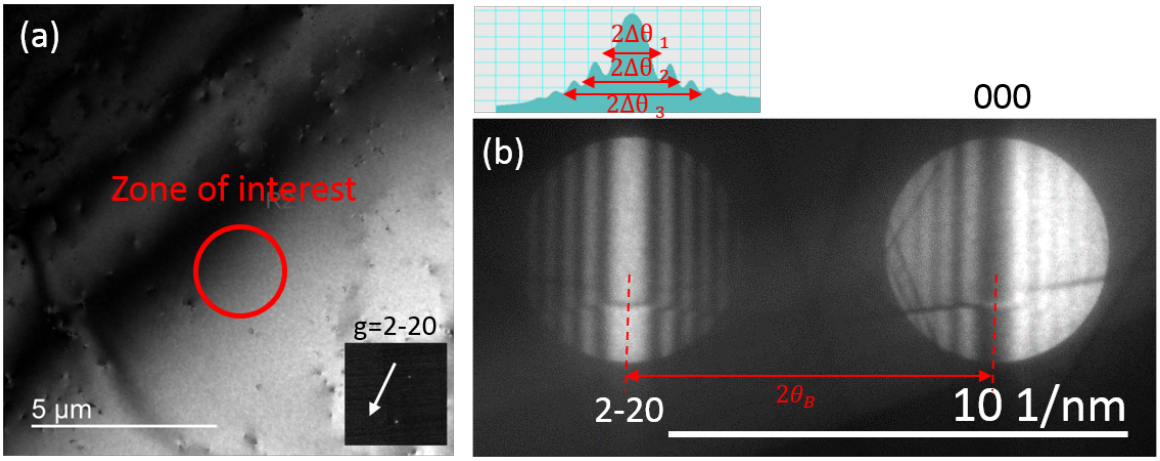

Figure 3.15 Principle of thickness measurement by CBED technique.(a) Zone of interest selected for thickness measurement in Ni; (b) CBED patterns and measurements necessary to extract thickness from K-M fringes.

It is worth to mention that the upper and lower thickness limits of CBED method depend mainly on the orientation and the resolution of patterns. In terms of resolution, especially when the sample is too thick, the fringe spacing becomes ambiguous. In terms of orientation, when the inter-planar spacing is too small, the fringe spacing becomes large and only the first order fringes are visible in the pattern so the fitting can not be conducted. In the case of nickel, the planes of 220 appear to be suitable for the thickness measurement from 50 nm to 280 nm.

The CBED technique gives an estimation of the thickness and the extinction distance along the used reflection. Our measurements led always to an extinction distance of 55 ± 3

nm which is in good agreement with theoretical value between 57 and 58 nm using jems software (Stadelmann, 2004) (lattice parameter a_0=0.352 nm). The error of measurements was always within 5%.

CBED technique estimate the effective thickness of specimen. However, to obtain a two-beam condition, specimen tilting is usually inevitable. Hence, the thickness t obtained is not the real thickness t_{real} but an observed thickness. It is necessary to convert the observed thickness into the real thickness. Practically, we can obtain the closest two-beam condition to zero tilt (usually less than 10° for each tilt angle). The error can be estimated less than 5%.

In terms of the systematic error of the method, the thickness measurement from CBED in pure metals is claimed to be highly accurate: <2% by Kelly (Kelly et al., 1975) and 3% by Allen (Allen and Hall, 1982). In terms of the error of measurements, in our case, thickness measurements were also performed always with small tilt angles (<10°) and repeated on the same zone. The error of measurements were always within 10%. Thus, we take a conservative approach by assuming the final error to be 10%.

3.2.6 Determination of loop size and number density

The size of dislocation loops is determined from images under two-beam conditions in KBF mode. The longest distance within the loops is measured using ImageJ software and is taken as the size (diameter). A statistic analysis is carried out with an important number of loops to calculate the average size of loops. The error bars in graphics of the average loop size are the standard deviation.

The number density of loops is determined with counted loop number in the image under two-beam conditions in KBF mode and the estimated volume of studied zone. The volume is estimated by multiplying the estimated sample thickness and the projected area of the zone. Then, the loop number density is given as

$$Number\,density\,of\,loops = \frac{number\,of\,loops\,in\,the\,zone}{area\,of\,the\,zone \times sample\,thickness} \tag{3.1}$$

Invisible loops in the zone under each two-beam conditions are not contained in the calculated number density. The uncertainty of the density results from the error of loop number and of the sample thickness. The error of the counted loop number is mainly due to small-size indistinguishable defects and large size agglomerated loops. The error is conservatively assumed to be 10%. In the following, the loop number density will be noted as loop density for short.

3.2.7 Determination of spatial distribution of loops by stereoscope technique

The stereo-microscope technique was briefly presented in Section 3.2.4.2 for the determination of the inclination of loop habit plane. Here we present another application of this technique for the determination of the depth of loops inside thin foils. The principle is shown in Figure 3.16(a). The distance between two objects at different depths varies with the tilt angle. The relative distance between the two objects along the depth direction H can be deduced from the tilt angle θ, the distance perpendicular to the rotation axis before tilt d_1 and after tilt d_2.Figure 3.16(b) shows the geometry of the technique. Figure 3.16(c) shows how the distances of interest can be measured from TEM micrographs. From the geometrical relation in Figure 3.16(b), the relative distance along the depth direction H is written as:

$$H = |\frac{d_2 cos\theta_1 - d_1 cos\theta_2}{sin(\theta_1 - \theta_2)}| \tag{3.2}$$

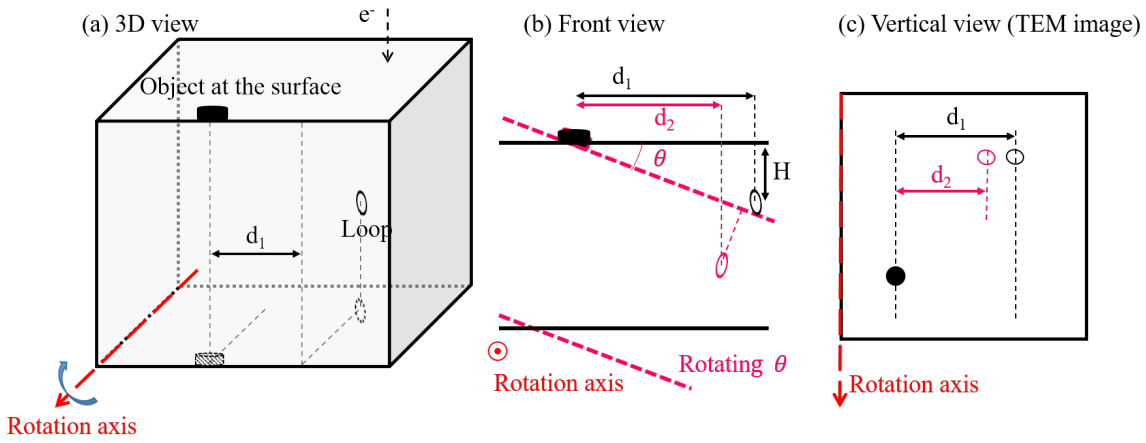

Figure 3.16 Schematic diagram of determination of the depth of object by stereo-imaging. (a) 3D view, (b) front view and (c) vertical view (TEM image view) of stereo-imaging technique.

In practice, we identify an object at the surface (a small area of pollution or an extremity of a dislocation line). H between this surface object and a dislocation will indicate the depth of the loop. By measuring all loops in the zone, we can determine the spatial distribution of dislocation loops inside the sample. Then, the thickness of the studied zone is equally divided into 5 nm intervals and an analysis of loop frequency distribution along depth is performed. The depth, at which the accumulated frequency reaches 5%, defines the loop-denuded thickness.

3.2.8 Voids contrast and measurement of size and density

Voids are three-dimensional defects formed by the agglomeration of vacancies. Voids are best imaged with Fresnel contrast near the edge of voids when they are out-of-focus (Jenkins, 1994). In practice, a series of bright field through-focal TEM images is recorded under two-beam kinematic condition ($s_g > 0$). Voids will appears :

1) as white hole surrounded by a dark Fresnel fringe in underfocus images;

2) as dark dots surrounded by a bright fringe in overfocus images;

3) almost invisible in the in-focus image.

Voids observed in ours samples are usually larger than 5 nm. Considering voids approximately as sphere objects, their diameter of the inner bright area in underfocus images (or dark area in overfocus images) is taken as their size. The error bar is the statistical error arising from the different size of voids. The density of voids is given by Eqs. 3.3 and the error bar is from the thickness measurement.

$$Number\,density\,of\,voids = \frac{number\,of\,voids\,in\,the\,zone}{area\,of\,the\,zone \times sample\,thickness} \tag{3.3}$$

3.3 Composition analysis

This thesis also aims to study the radiation-induced composition modification. The analysis of composition was conducted by the dispersive X-ray spectroscopy (EDS) in scanning TEM mode (STEM/EDS) and atom probe tomography (APT). A brief introduction and the application of STEM/EDS and APT is presented in this section.

3.3.1 TEM-Energy Dispersive X-ray Spectroscopy (EDS)

Energy Dispersive X-ray Spectroscopy (EDS) is used to measure the variation of composition in our samples. The analysis is performed using a Super-X EDS system (4-detector configuration) in a 200 kV FEI Talos F200X TEM equipped with four EDS detectors located in laboratory ScopeM at ETH Zurich in collaboration with Dr. Robin Schäublin. EDS analyses presented in this manuscript are carried out by him. Details about the techniques are given in (CARTER et al., 1996). A general TEM-EDS system is illustrated in Figure 3.17. When a specimen is bombarded by energetic electrons, it emits characteristic X-rays. The EDS detector collects the X-rays and gives their energy which is related to the emission element.

The analysis is performed in scanning TEM (STEM) mode. The spot size is set as 5 (à vérifier). The count rate is adjusted to about 10000 counts/s (à vérifier) for an image

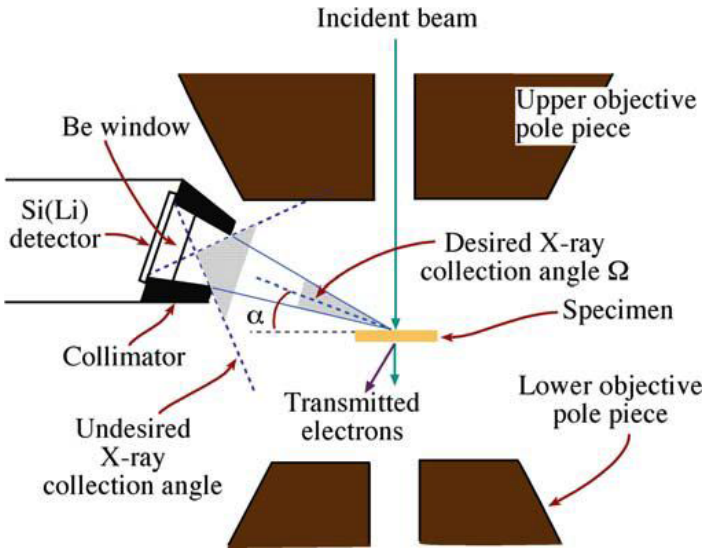

Figure 3.17 Schematic representation of the coupling of EDS system with TEM. Detector placed to collect characteristic X-rays from regions other than undesired collection angle. The (relatively small) desired collection angle Ω and take-off angle α are also shown.

typically 450 pixels * 450 pixels. The counted time is more than 30 minutes in order to have sufficient count number for each pixel.

3.3.2 3D Atom Probe Tomography (APT)

Atom Probe Tomography (APT) is a quantitative destructive analysis technique of the chemical composition and spatial distribution of atoms within a small volume. In this study, APT experiments are performed using CAMECA LEAP 4000 HR located in CEA-Saclay to quantitatively investigate the composition of specimens before and after irradiation.

3.3.2.1 Principal of technique

The principal of atom probe microscope is based on the evaporation of atoms in electric field as illustrated in Figure 3.18. By putting a needle-shape sample with a small curvature (50 nm) subjected to a high voltage (HV) in front of an electrode, the ionization of atoms will be triggered and the ionized atoms will fly under effect of electric field to the electrode and collected by a position sensitive detector. As the evaporation conditions depend on elements, electric pulses or femto-second laser pluses in addition to a standing DC voltage are used to select appropriate analysis conditions from one material to another.

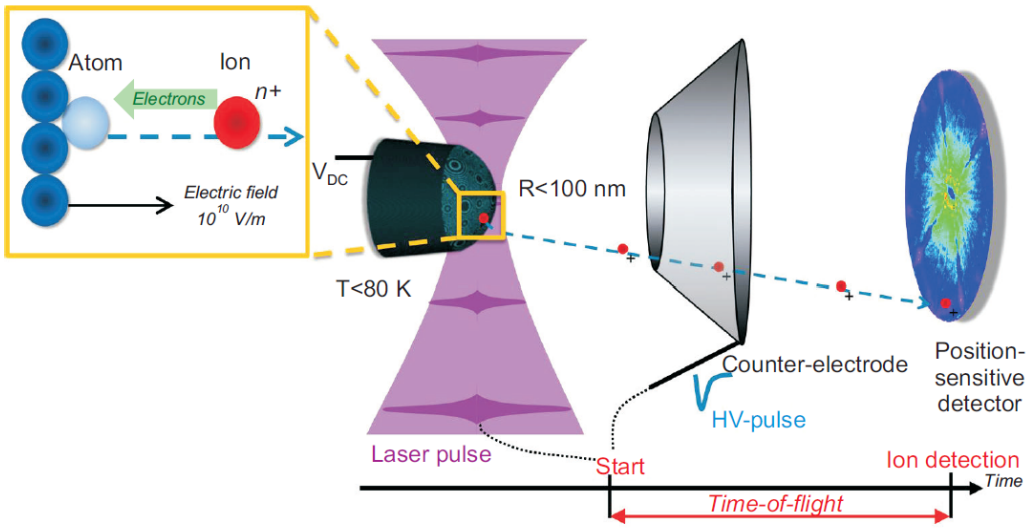

Figure 3.18 Schematic view of an atom probe microscope, with the specimen subjected to a high voltage (HV) and illuminated by laser pulses of HV pulses, triggering the field evaporation of ions that fly through a counter-electrode and are collected by the position-sensitive detector, which also records their time-of-flight allowing for their elemental identification (Gault, 2016).

3.3.2.2 Experimental conditions

In this study, APT analysis was performed on Ni-0.4Ti irradiated by 5 MeV Ni^{2+} ions at 450°C. The sample preparation has been presented in Section 3.1.3.2. During the APT analysis, a high vacuum was maintained up to 10^{-10} Pa. The specimen was cooled down to 50 K. A laser beam (pulse energy 0.4 nJ) is used with a pulse rate of 100 kHz and a power set up of laser representing 25% of the total potential. The detection efficiency of this APT is 42%.

3.4 Analytical modeling of RIS and the application to Ni-based systems

In the Ph.D. thesis of Huang (Huang et al.) at SRMP/CEA-Saclay, an analytical model based on a simple mean-field rate theory is developed to study the radiation-induced segregation (RIS). Using a discretization method, the variation of the steady-state bulk concentration of PDs due to sinks (dislocations, surface, etc.) can be deduced with an analytical expression. Then, an analytical expression of the solute steady-state RIS can be deduced from the RIS profile of PDs and RIS factors. The key parameters in this modeling is the radiation flux, temperature and the overall effective sink strength.

The diffusion of PDs toward sinks can be described with PD flux $\vec{J}_V$ and $\vec{J}_I$

$$\frac{\partial C_V}{\partial t} = \phi - K_R C_V C_I - \nabla \cdot \vec{J}_V, \tag{3.4}$$

$$\frac{\partial C_I}{\partial t} = \phi - K_R C_V C_I - \nabla \cdot \vec{J}_I, \tag{3.5}$$

.

To compute $\vec{J}_V$ and $\vec{J}_I$, we assume $\nabla\mu_V$ and $\nabla\mu_I$ to be the dominant driving force compared to $\nabla\mu_A$ and $\nabla\mu_B$. Thus, we have

$$\vec{J}_V = -L_{VV}\nabla\mu_V = -D_V \nabla C_V, \tag{3.6}$$

$$\vec{J}_I = -L_{II}\nabla\mu_I = -D_I \nabla C_I. \tag{3.7}$$

Considering the PD concentration profile along the direction (coordinate z) normal to the surface of planar PD sinks, Eqs. 3.4 and Eqs. 3.5 can be simplified under stationary-state conditions and given by:

$$0 = \phi - K_R C_V C_I + D_V \frac{\partial^2 C_V}{\partial z^2}, \tag{3.8}$$

$$0 = \phi - K_R C_V C_I + D_I \frac{\partial^2 C_I}{\partial z^2}, \tag{3.9}$$

where $C_V(z)$ and $C_I(z)$ are respectively the concentrations of vacancies and SIAs at different positions z. The schematic representation of this 1D diffusion is illustrated in Figure 3.19.

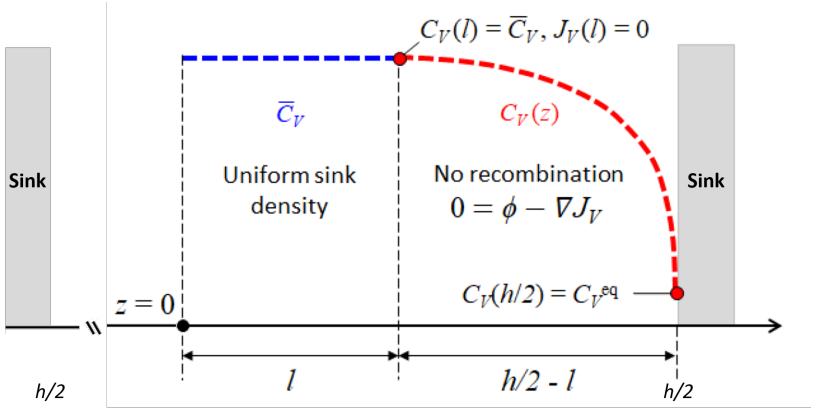

Figure 3.19 Schematic representation of vacancy concentration profile divided into two parts(Huang et al.).

The symmetry gives that the PD flux at the mid-point between two successive sinks ($z = 0$) is zero. Moreover, the PD concentrations at sink ($z = h/2$) are assumed to be the

equilibrium concentrations. Thus, we have:

$$\frac{\partial C_V}{\partial z}(z=0)=0,\ \frac{\partial C_I}{\partial z}(z=0)=0. \tag{3.10}$$

$$C_V(z=h/2)=C_V^{\mathrm{eq}},\ C_I(z=h/2)=C_I^{\mathrm{eq}}. \tag{3.11}$$

By assuming $D_I C_I^{\mathrm{eq}} \ll D_V C_V^{\mathrm{eq}}$ and $D_I \gg D_V$, we have $D_V[C_V(z)-C_V^{\mathrm{eq}}]=D_I C_I(z)$, then Eqs. 3.8 can be written as:

$$\frac{\partial^2 C_V(z)}{\partial z^2}=-\frac{\phi}{D_V}+\frac{4\pi r_c}{\Omega}C_V(z)[C_V(z)-C_V^{\mathrm{eq}}]. \tag{3.12}$$

The recombination terms (i.e. $r_c=0$) is assumed to be negligible since PD concentrations are low close to a PD sink. Then, an analytical solution can be given as:

$$C_V(z)=-a(z^2-\frac{h^2}{4})+C_V^{\mathrm{eq}}, \tag{3.13}$$

where $a=\phi/(2D_V)$, and h is the average spacing between planar sinks. The position of the origin of axis $(0z)$ is chosen to be at the mid-point between two planar sinks (see Figure 3.19). Finally, the boundary conditions lead to the expressions of vacancy concentration:

$$C_V(z)=\begin{cases} a(\frac{h}{2}-l)^2+C_V^{\mathrm{eq}}, & 0\le z<l; \\ -a\left[(z-l)^2-(\frac{h}{2}-l)^2\right]+C_V^{\mathrm{eq}}, & l\le z\le h/2, \end{cases} \tag{3.14}$$

where the characteristic distance l reads

$$l=\frac{h}{2}-\sqrt{\frac{C_V^{\mathrm{exc}}}{a}}, \tag{3.15}$$

where $C_V^{\mathrm{exc}}=\overline{C}_V-C_V^{\mathrm{eq}}$ corresponds to the vacancy excess concentration with respect to the equilibrium one.

Then, based on the analytical expression of PD concentration, the concentration profiles of solute atoms can be deduced with the RIS factor by Wiedersich's approach. The entire model is described in the thesis of Huang (Huang et al.).

It is worth noting that, from Eqs. 3.13, the concentration profile of PDs depends explicitly on the irradiation flux ϕ, the temperature T (diffusion coefficients) and the number density of sinks (to determine h). It also depends implicitly on the sink strength because the C_V^{eq} is deduced by resolving rate theory equations where an overall sink strength k^2 is involved. In this study, results of irradiation experiments on Ni-Ti alloys will be used as input parameters

for this modeling. The experimental segregation profile will be compared with the simulation to better understand mechanisms involved.

3.5 Summary

In this chapter, the studied materials, the experiments conditions of sample preparations/irradiations and characterization techniques involved are presented. In this work, the characterization focuses mainly on radiation-induced dislocation loops, especially the determination of loop nature. Therefore, we stress here again some notions of dislocation loops based on the context of this thesis.

In irradiated Ni (fcc metals), there are mainly 5 types of defects:

- Frank loops which have Burgers vector **b**=1/3<111> (4 sub-families) and were only reported interstitial-type in the literature;
- perfect loops which have **b**=1/2<110> (6 subfamilies);
- dislocation lines/network;
- stacking fault tetrahedron (SFT);
- voids.

In this study, the Burgers vector of dislocation loops are defined using the FS/RH convention (Hirsch, 1967) (Figure 3.9) with the clockwise direction as the positive direction of the dislocation line **u** viewing from top to bottom. In the case of edge loops (Frank loops), this definition results in a Burgers vector pointing upward for interstitial loops and pointing downward for vacancy loops. In the case of perfect loops, either the safe/unsafe conditions have to be determined or the stereo-imaging has to be used to determine the loop nature.

Chapter 4

Irradiation behavior of pure nickel as a reference system

The Frank loop nature, growth rate of dislocation loops and irradiated microstructure (defect density and size) are characteristic features describing the irradiation behavior. The characterization of these parameters in Ni and its alloys will be helpful to better understand the influence of solutes. As a first step, these parameters must be fully characterized in pure nickel in order to identify the real solute effects in future comparative experiments. In this chapter, we firstly focus on the nature of Frank loops in Ni. The Frank loop nature is determined in thin foils and bulk samples. Then, we characterize the irradiated microstructure of Ni. Finally, the microstructural evolution is studied. These results provide guideline for future comparative experiments in the alloys.

4.1 Nature of dislocation loops in irradiated Ni

This section focuses mainly on the determination of the nature of Frank loops and, in some cases, the nature of perfect loops. The Frank loop nature is firstly studied in both thin foil and bulk Ni irradiated at 450°C to 2.3x10^{15} ions.cm^{-2} (0.7 dpa near the surface) in order to investigate the influence of the sample form. Then the characterization is performed in Ni irradiated at 450°C to a lower dose (0.18 dpa) to study the influence of the dose. Finally the nature of Frank loops are studied at 510°C to evaluate the impact of temperature.

4.1.1 Influence of sample form on Frank loop nature in Ni irradiated at 450°C

4.1.1.1 Irradiated microstructure and Frank loops in thin foil Ni

The general microstructure of a studied zone in each material is shown in Figure 4.1(a). TEM micrographs were taken along zone axis <001> with **g**=<200>. In all materials, the microstructure is dominated by dislocation loops. Both Frank loops and perfect loops are detected. Few voids ($<10^{17}$ m^{-3}) are detected occasionally and it is difficult to define its density. Figure 4.1(b) and (c) show two typical Frank loops observed in irradiated Ni. It is worth noting that these loops and all the observed Frank loops in Ni are segmented. In the literature, segmented Frank loops were mostly found in quenched metals and were identified as vacancy-type as a result of super-saturation of vacancies from quenching (Edington and Smallman, 1965; Eikum and Maher, 1975; Humble et al., 1967). However, radiation-induced Frank loops detected in the literature are usually circular (Chen and Ardell, 1976; Mazey and Hudson, 1970; Urban, 1971) and thus the different morphology of Frank loops raises questions about their nature.

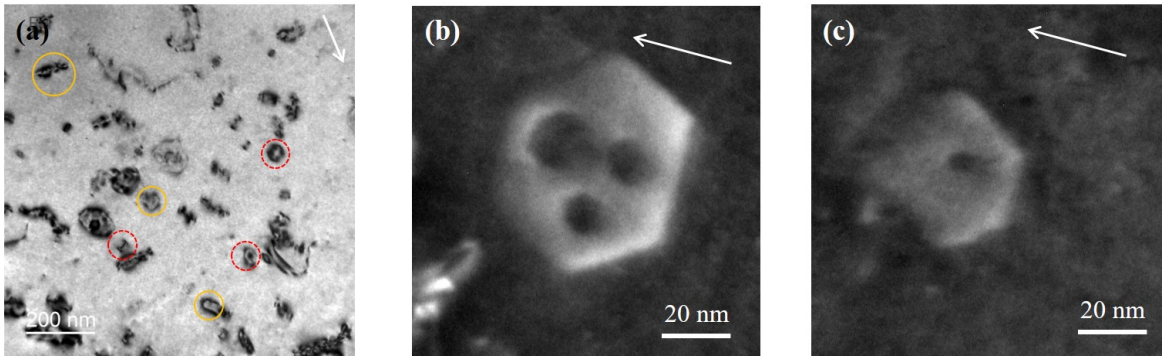

Figure 4.1 TEM micrographs and typical Frank loops showing general microstructure in thin foil Ni irradiated up to 0.7 dpa at 450°C: (a) BF image taken along zone axis <001> with **g**=<200> indicated by red circles; several Frank loops and perfect loops pointed out by respectively red circles and yellow dotted circles; (b) and (c) WBDF images of two typical Frank loops with **g**=<200>. The thickness of the zone is 200 nm.

The nature of Frank loops in Ni is determined in this part. It is important to stress on that the same nature of all defects is identified, independently on their Burgers vectors. In the following, detailed characterizations are given for a representative loop.

The method for the determination of loop nature was presented in Chapter 3. Here we remind that, to demonstrate unambiguously the nature of a dislocation loop, (1) the Burgers vector, (2) the loop plane and (3) the inside-outside behavior in ±g must be fully analyzed. For a pure edge loop, such as a Frank loop, (1) and (3) will be sufficient because the Burgers vector is perpendicular to the loop plane.

A representative Frank loop in Ni is presented in Figure 4.2. The analysis of the Burgers vector is carried out with the invisibility criterion (Howie and Whelan, 1962). It means that for a given two-beam condition with the diffraction vector g, the dislocation loop with the Burgers vector **b** will be invisible or show a residual contrast if $|\mathbf{g}.\mathbf{b}| = 0$. Figure 4.2 presents the TEM micrographs of a dislocation loop in Ni for four different **g** along different zone axes. The zone axis and diffraction vectors were cautiously indexed by comparing the Kikuchi lines and diffraction patterns with the reference schematic maps (Loretto and Smallman, 1975). Since the loop is invisible for $\mathbf{g} = [2\bar{2}0]$ (Figure 4.2(b)) and $\mathbf{g} = [02\bar{2}]$ (Figure 4.2(d)), the Burgers vector of the loop is $\mathbf{b} = \pm 1/3[111]$. The visibility of the loop for the other **g** (Figure 4.2(a) and Figure 4.2(c)) is in agreement with this Burgers vector. The visibility of the loops inside the outer loops (inner loops) is the same as the outer Frank loop for all the **g** analyzed. Thus, their Burgers vectors are also $\pm 1/3[111]$.

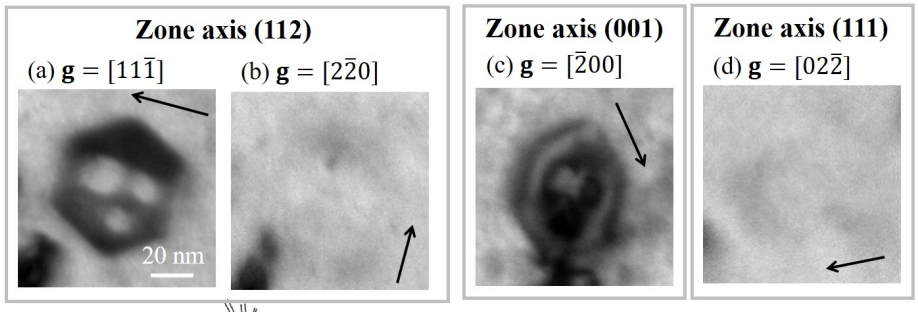

(d)

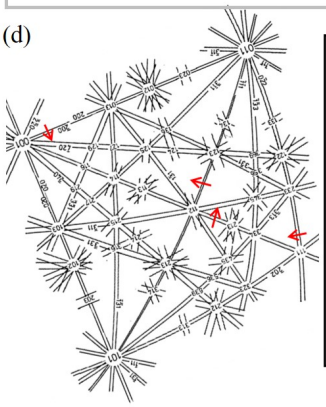

(e)

Table of visibility (V= visible, I= invisible)	Zone axes	[112]		[001]	[111]
	g / Possible b	11$\bar{1}$	2$\bar{2}$0	$\bar{2}$00	02$\bar{2}$
	$\pm\frac{1}{3}$[111]	V	I	V	I
	$\pm\frac{1}{3}$[$\bar{1}$11]	V	V	V	I
	$\pm\frac{1}{3}$[1$\bar{1}$1]	V	V	V	V
	$\pm\frac{1}{3}$[11$\bar{1}$]	V	I	V	V

Figure 4.2 Determination of the Burgers vectors of the Frank loops in thin foil Ni irradiated at 450°C: (a-b) Bright-field TEM images of the Frank loop under different two-beam conditions with diffraction vector **g** indicated by arrows with the same scale bar in (a); (e) table of visibility for both outer and inner loops.

The nature of a loop depends on the sign of its Burgers vector. Figure 4.3 shows the BF and WBDF images of the previous Frank loops in Figure 4.2 for two opposite two-beam conditions $+\mathbf{g} = 200$ and $-\mathbf{g} = \bar{2}00$. The inside-outside behavior of this loops is resumed in Figure 4.3(e). Using the FS/RH convention (Hirsch, 1967), considering the sense of the dislocation line as clockwise, the outside contrast of the outer loop for **g**=[020] gives

$(\mathbf{g}.\mathbf{b}).s_g > 0$. Thus, the Burgers vector of the outer Frank loop is 1/3[111]. The Burgers vector and the loop plane normal [111] point in opposite directions. The outer Frank loop is therefore intrinsic (vacancy-type). On the contrary, the inner loops show a reverse contrast to the outer loop. The Burgers vector of inner loops is therefore $\pm 1/3[\bar{1}\bar{1}\bar{1}]$, corresponding to an extrinsic Frank loop (interstitial-type). No fault contrast is observed inside those inner loops in accordance with a perfect lattice.

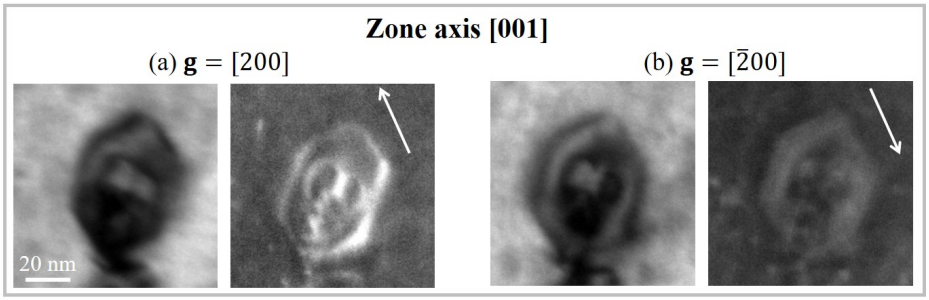

(c)

Loop	Contrast of loops			$\mathbf{g}\cdot\mathbf{b}$ for $\mathbf{g}$	$\mathbf{b}$	Nature
	$\mathbf{b}$ direction	$\mathbf{g}=[200]$	$-\mathbf{g}=[\bar{2}00]$			
Outer	[111]	inside	outside	<0	$a_0/3\,[\bar{1}\bar{1}\bar{1}]$	vacancy
Inner	[111]	outside	inside	>0	$a_0/3\,[111]$	interstitial

Figure 4.3 Determination of Frank loop nature in Ni thin foils irradiated 450°C: BF and WBDF TEM images of the Frank loop under different two-beam conditions with (a) $\mathbf{g}$=200 and (b) $\mathbf{g}$=$\bar{2}$00 indicated by arrows with the same scale bar in (a); (c) table of determination of loop nature for both outer and inner loops.

4.1.1.2 Irradiated microstructure and Frank loops in bulk Ni

In thin foils, the absorption of point defects by free surfaces is known to have a strong impact on microstructure under irradiation (Ishino et al., 1984). To avoid surface effects, bulk samples are studied and this part presents the results.

The depth distribution of radiation damage in Ni is shown in Figure 4.4(a). The microstructure is dominated by dislocations and dislocation loops. The microstructure can be divided into several zones:

- Zones very close to the surface (0-0.3 µm) with a low density of dislocation lines/loops;
- A first damaged zone (0.3-1.3µm) dominated by dislocation loops; Figure 4.4(b) shows several typical segmented Frank loops in the this zones;
- A defect-free zone (1.3-1.8 µm) almost free of defects except only one Frank large loop shown in Figure 4.4(c).

- A second damaged zone (1.8-2.8 µm) dominated by dislocation lines and loops; only perfect loops are detected in this zone as shown in Figure 4.4(d). The density of dislocation lines is relatively high compared with the first damage zone.

The measured average loop size, loop density and dislocation line density are plotted in Figure 4.4(e).

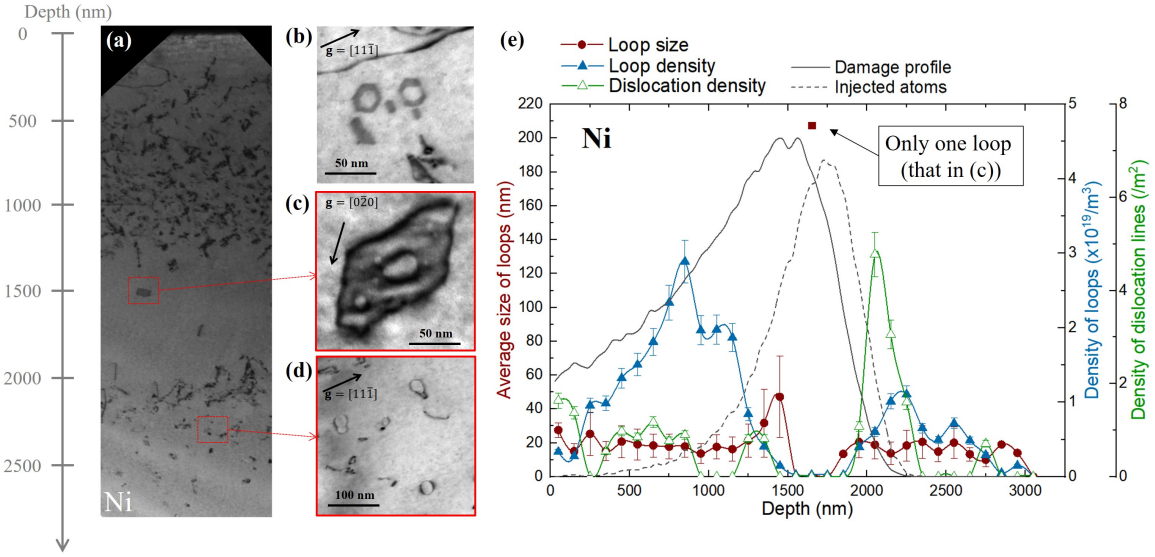

Figure 4.4 General microstructure in the bulk sample of Ni irradiated up to 2.3x10^{15} ions.cm^{-2} at 450°C. (a) Low magnification TEM micrograph showing the global microstructure; (b) and (c) Frank loops in the first damage zone with diffraction vectors **g** indicated by black arrows; (d) perfect loops in the second damaged zone; (e) depth-dependency of the average size and density of loops as well as the density of dislocation lines.

All Frank loops found in the first loop-dominated zone (0.3-1.3 µm) are segmented. The determination of the nature of Frank loops was carried out for tens of characterized loops and they are all vacancy-type. Figure 4.5 presents the determination for one loop. Based on its visibility, the outer loop is a Frank loop with a Burgers vector of $\mathbf{b}=\pm 1/3[11\bar{1}]$ by the analysis in Figure 4.5(l). The inner small loops are also Frank loops with with a $\mathbf{b}=\pm 1/3[11\bar{1}]$.

The nature of Frank loop nature is determined by the inside-outside method (Jenkins, 1994) and shown in Figure 4.5(m). It results that the outer Frank loop is intrinsic (vacancy-type) and the inner Frank loops ae extrinsic (interstitial-type). No fault contrast is observed inside those inner loops. These observations of Frank loops in bulk Ni are similar to the ones in thin foil Ni.

Thereafter, we determine the nature of loops in the second damage zone far from the damage production zone. Figures 4.6(a-g) present a representative zone for a depth about 2.2 µm under different diffraction conditions. The diffraction vector for each micrograph is indicated by the black arrow. Figure 4.6(h) is the Kikuchi map showing the crystal orientation.

At this depth, only perfect loops and dislocation lines are detected. No large Frank loop is identified. Five loops (A, B, C, D and E) are chosen to show the determination of loop nature as indicated in Figure 4.6(a) and Figure 4.6(g). For each g, red circles point out the position of these loops. When a loop is invisible, the circle is dashed. A visibility table is made for used **g** and the Burgers vector for each loop is analyzed in Figure 4.6(j).

To determine the nature, an inside-outside pair ($\pm\mathbf{g}$) is chosen along the zone axis [001] with $\mathbf{g}=\pm[220]$. Four families of perfect loops (1/2[011], 1/2[101], 1/2[0$\bar{1}$1] and 1/2[$\bar{1}$01]) along this zone aixs are under safe conditions by stereo-projection as the angle α for the four families are $45°<\phi_m=55°$. The method is also illustrated by the stereogram in Figure 4.6(i). We take the family $\mathbf{b}$=1/2[011] as example. Perfect loops with $\mathbf{b}$=1/2[011] can be unfaulted from two Frank loop families 1/3[111] and 1/3[$\bar{1}$11]. These two families of Frank loops are not in the red area. So it is under safe condition and the perfect loop shows the same contrast as an edge loop.

Figure 4.6(l) presents the inside-outside analysis for loops under safe conditions (A, C and D). From their inside-outside behavior, they are all interstitial-type. Other perfect loops were analyzed in other zones and the same nature was found. Thus, we assume that loops in the second damage zone are all interstitial-type.

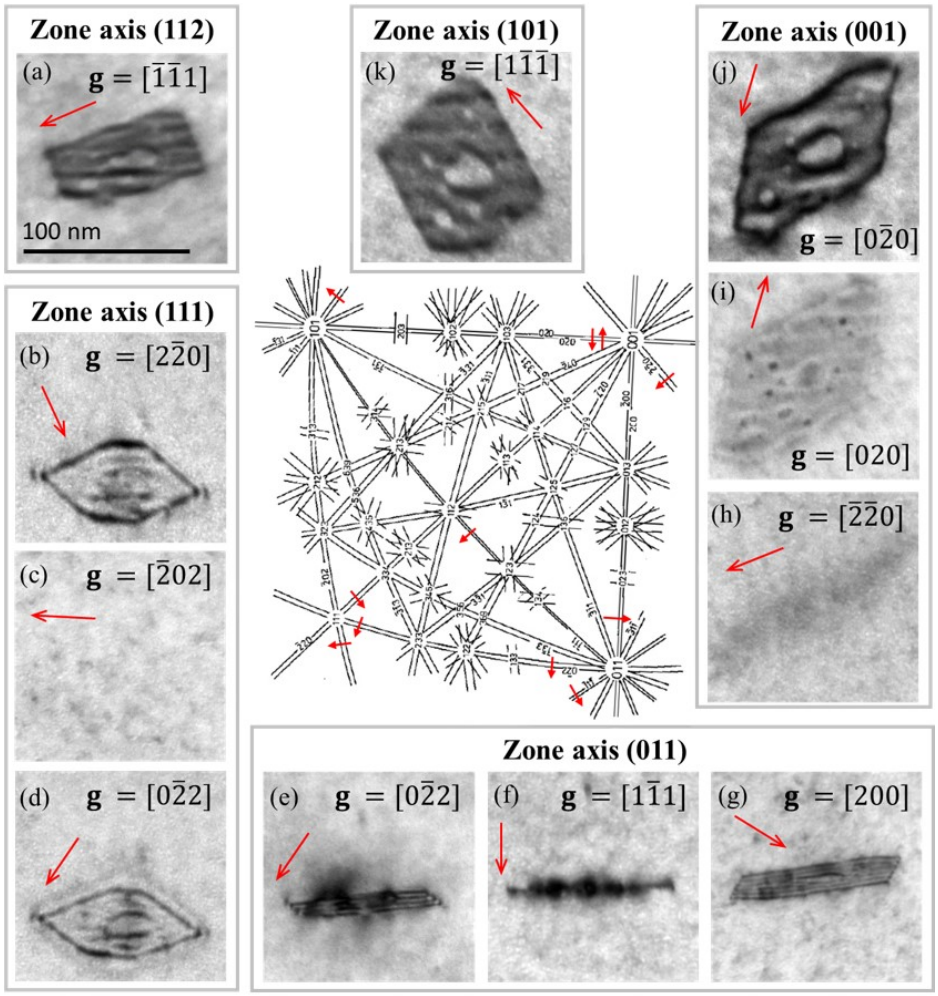

(l)

Table of visibility	Zone axes	[001]		[101]	[111]			[011]		[112]	BV
	g	0$\bar{2}$0	$\bar{2}\bar{2}$0	1$\bar{1}\bar{1}$	2$\bar{2}$0	$\bar{2}$02	0$\bar{2}\bar{2}$	1$\bar{1}$1	200	$\bar{1}\bar{1}$1	
	Visible (V) or invisible (I)	V	I	V	V	I	V	V	V	V	±[1$\bar{1}$1]
	g.b	≠0	0	≠0	≠0	0	≠0	≠0	≠0	≠0	

(m)

Loop	Contrast of loops			g · b for g	b	Nature
	b direction	g = [020]	−g = [0$\bar{2}$0]			
Outer	[1$\bar{1}$1]	outside	inside	>0	$a_0/3$ [$\bar{1}\bar{1}$1]	vacancy
Inner	[1$\bar{1}$1]	inside	outside	<0	$a_0/3$ [1$\bar{1}$1]	interstitial

Figure 4.5 Determination of Burgers vectors of a typical Frank loop in Ni bulk samples irradiated 450°C to 2.3x10^{15} ions.cm^{-2}: (a-k) Bright-field TEM images of irradiated Ni under ten two-beam conditions along different zone axis; central Kikuchi map is extracted from (Loretto and Smallman, 1975) and red arrows indicate the diffraction vector **g** in each micrograph with scale bar for all images indicated in (a); (l) table of visibility for both outer and inner loops based on **g.b** value; (m) analysis of the nature of Frank loops based on inside-outside contrast in (i) and (j).

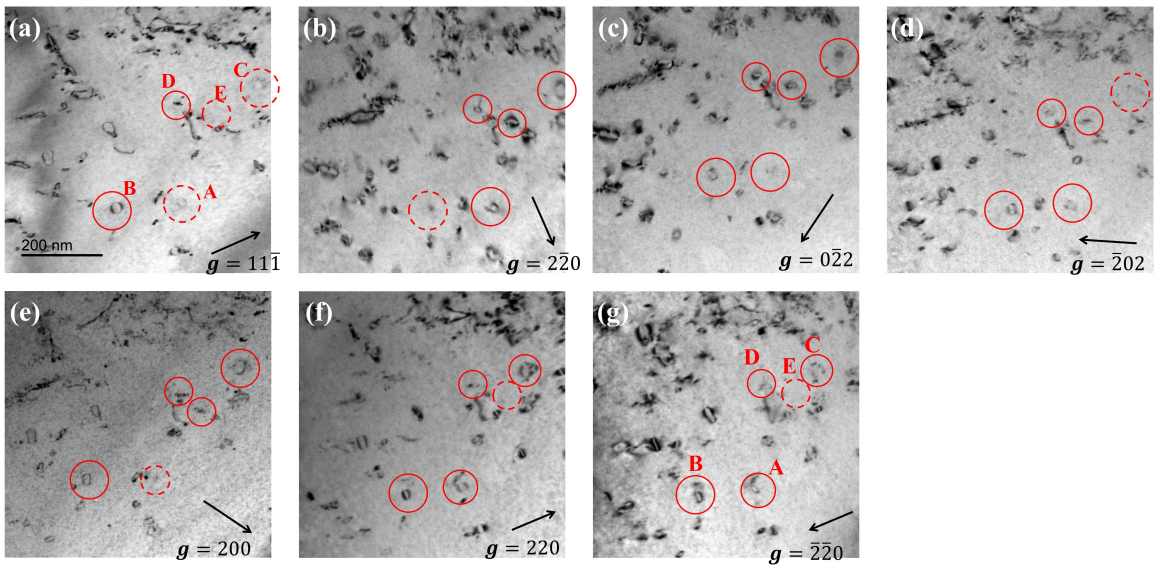

(h)

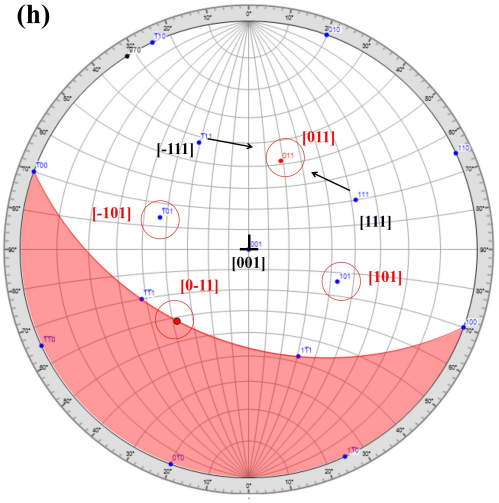

(i)

Table of visibility (V= visible, I= invisible)	Zone axes	[112]	[111]			[011]	[001]		Loop
	g / Possible b	11$\bar{1}$	2$\bar{2}$0	0$\bar{2}$2	$\bar{2}$02	200	220	$\bar{2}\bar{2}$0	
	$\pm\frac{1}{2}$[110]	V	I	V	V	V	V	V	B
	$\pm\frac{1}{2}$[$\bar{1}$10]	I	V	V	V	V	I	I	E
	$\pm\frac{1}{2}$[101]	I	V	V	I	V	V	V	C
	$\pm\frac{1}{2}$[10$\bar{1}$]	V	V	V	V	V	V	V	D
	$\pm\frac{1}{3}$[011]	I	V	I	V	I	V	V	A
	$\pm\frac{1}{3}$[01$\bar{1}$]	V	V	V	V	I	V	V	

(j)

Loops	Contrast of loops along zone axis [001]				**g · b** for **g**	**b**	Nature
	Safe?	**b** direction	**g** = [220]	**−g** = [$\bar{2}\bar{2}$0]			
A	safe	[011]	outside	inside	>0	1/2 [011]	interstitial
B	unsafe	[110]	/	/	/	/	/
C	safe	[101]	outside	inside	>0	1/2 [101]	interstitial
D	safe	[10$\bar{1}$]	inside	outside	<0	1/2 [$\bar{1}$01]	interstitial
E	unsafe	[$\bar{1}$10]	/	/	/	/	/

Figure 4.6 Determination of the perfect loop nature out of the damage production zones in Ni bulk samples irradiated 450°C to 2.3x10^{15} ions.cm^{-2}: (a-g) Bright-field TEM images of irradiated Ni under ten two-beam conditions along different zone axis; diffraction vector **g** indicated by black arrow in each micrograph with the same scale bar for all images in (a); (h) stereogram showing the analysis of safe/unsafe condition; (i) table of visibility based on **g**.**b** value; (j) determination of loop nature based on inside-outside contrast in (f) and (g).

4.1.2 Influence of dose on Frank loop nature in Ni irradiated at 450°C

The observations of vacancy loops in Ni irradiated at 450°C is not expected and it is not related to the sample form (surface effects) from the previous sections. Another possible reason to explain the the growth of vacancy loops is that the dose is too high. At such a dose, dislocation lines are formed by the agglomeration of loops and might absorb a large amount of interstitials, creating a super-saturation of vacancies and leading to the growth of vacancy loops. The characterization is performed on a thin foil Ni irradiated at 450°C to a lower dose (0.18 dpa) to study the influence of the dose on Frank loop nature. Figure 4.7(a) shows the general microstructure and Figure 4.7(b-c) show two typical Frank loops. The observed Frank loops are segmented, suggesting the same nature as the higher dose sample.

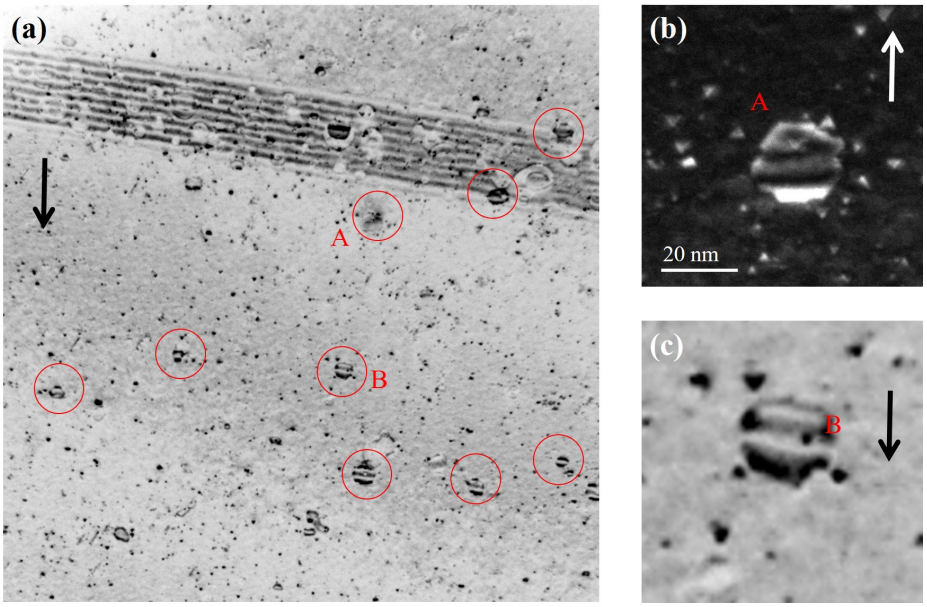

Figure 4.7 General microstructure in Ni irradiated at 450°C to 0.18 dpa: TEM micrographs taken along zone axis [101] with **g**=<020> indicated by white arrows: (a) the general microstructure in a 80 nm thick zone with several Frank loops pointed out by red circles; (b) and (c) two typical Frank loops A and B.

Figure 4.8 shows the determination of the nature of two typical Frank loops A and B. Along the zone axis [101], only 1/3[111] and 1/3[1$\bar{1}$1] Frank loops are "open" while the two other families are in edge-on position. So there are only two possibilities for A and B. By tilting 30° along the rotation axis indicated in Figure 4.8, the direction of loop inclination along the zone axis [001] shows that the Burgers vector of A and B are respectively ±1/3[1$\bar{1}$1] and ±1/3[111]. In Figure 4.8(b), loop A shows an inside contrast so **g**.**b**<0 which gives **b**=[$\bar{1}$1$\bar{1}$]. Loop B shows an outside contrast so **g**.**b**>0 which gives **b**=[$\bar{1}\bar{1}\bar{1}$]. Both Burgers vectors point both downward so these loops are vacancy-type.

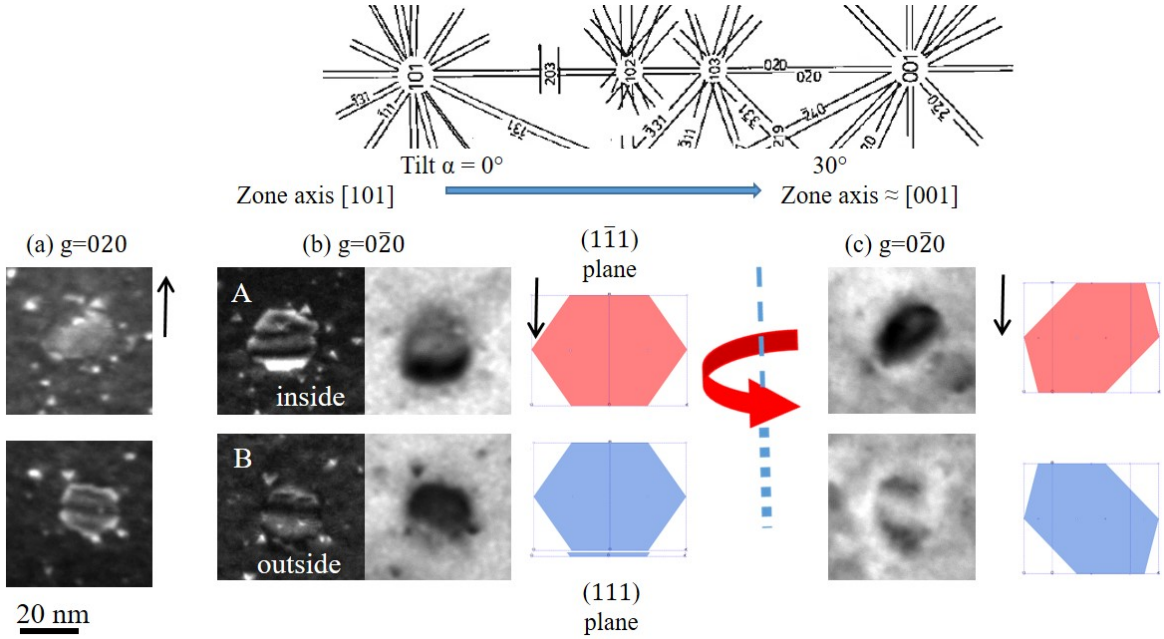

Figure 4.8 Determination of Frank loop nature in Ni bulk samples irradiated 450°C to 0.18 dpa: images taken along the zone axis [101] with (a) **g**=020 and (b) **g**=0$\bar{2}$0; (c) images taken along the zone axis [001] with **g**=0$\bar{2}$0; **g** is indicated by the white arrow for each image; the projection of plane (1$\bar{1}$1) and plane (111) before and after tilt is shown respectively by the red hexagon and the blue one.

4.1.3 Influence of temperature on Frank loop nature in Ni irradiated

In this part, the influence of the temperature on the loop nature is investigated. The irradiation was performed at 500°C to 0.18 dpa. Figure 4.9 shows the general microstructure. Segmented Frank loops are detected. Figure 4.10 shows the visibility and inside-outside behavior of three typical segmented Frank loops (A, B and C). By their visibility in function of **g**, their Burgers vectors are respectively $\pm 1/3[1\bar{1}1]$ for A and $\pm 1/3[111]$ for B and C. Loop A shows an inside contrast (**g**.**b**<0) with **g**=0$\bar{2}$0 along the zone axis [101] while B and C show an outside contrast (**g**.**b**>0). Using the inside-outside method, the Burgers vectors of A and B/C are respectively $1/3[\bar{1}1\bar{1}]$ and $1/3[\bar{1}\bar{1}\bar{1}]$. Therefore they are all vacancy-type.

A particular phenomenon draws attention in thin zones (50-120 nm) in only two specimens. In these zones, only perfect loops are detected (Figure 4.11). Some of them are abnormally large. Figure 4.11 presents the analysis of Burgers vector of a typical perfect loop and the Burgers vector of this loop is $\pm 1/2[\bar{1}10]$. This Burgers vector is unsafe for the direct determination using inside-outside behavior for all zone axes accessible in this foil. To determine its nature, the inclination of loop plane has to be characterized.

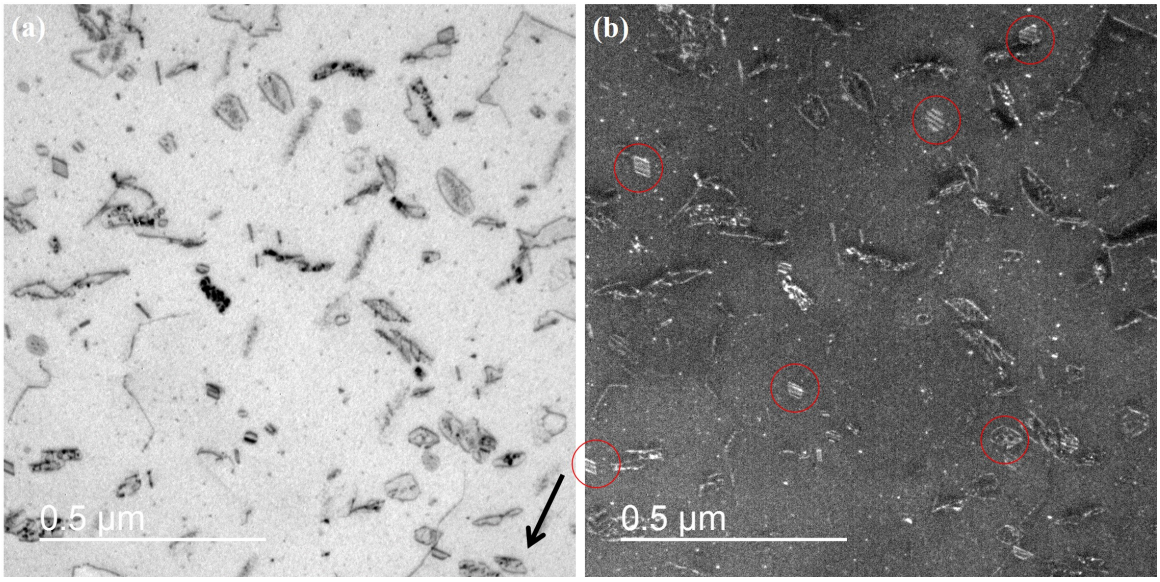

Figure 4.9 General microstructure in Ni irradiated at 500°C to 0.18 dpa: (a) BF and (b) WBDF images taken along the zone axis [101] with **g**=[0$\bar{2}$0] indicated by the black arrow for the general microstructure in a 200 nm thick zone with several Frank loops pointed out by red circles.

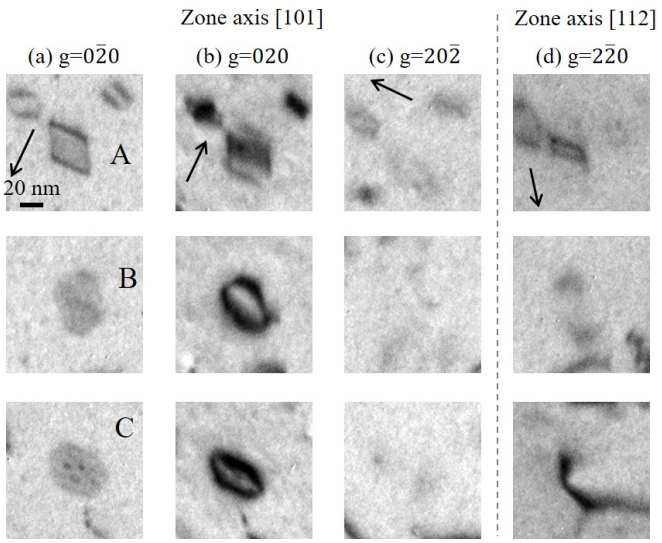

(e)

Table of visibility (V= visible, I= invisible)	Zone axes	[101]		[112]	Loops
	g / Possible b	020	20$\bar{2}$	2$\bar{2}$0	
	$\pm\frac{1}{3}$[111]	V	I	I	B, C
	$\pm\frac{1}{3}$[$\bar{1}$11]	V	V	V	
	$\pm\frac{1}{3}$[1$\bar{1}$1]	V	I	V	A
	$\pm\frac{1}{3}$[11$\bar{1}$]	V	V	I	

(f)

Loop	Loop contrast along [101]		$+\mathbf{g}\cdot\mathbf{b}$	**b**	Nature
	g = [020]	$-\mathbf{g}$ = [0$\bar{2}$0]			
A	outside	inside	>0	$\frac{1}{3}$[$\bar{1}$1$\bar{1}$]	vacancy
B C	inside	outside	<0	$\frac{1}{3}$[$\bar{1}\bar{1}\bar{1}$]	vacancy

Figure 4.10 Determination of Frank loop nature in Ni irradiated 500°C to 0.18 dpa: images taken along the zone axis [101] with (a) **g**=0$\bar{2}$0, (b) **g**=020 and (c) **g**=[20$\bar{2}$]; (d) along the zone axis [001] with **g**=2$\bar{2}$0; **g** is indicated by the black arrow for each image. (e) Table of visibility shows the analysis of the Burgers vector of loop A, B and C. (f) Determination of loop nature.

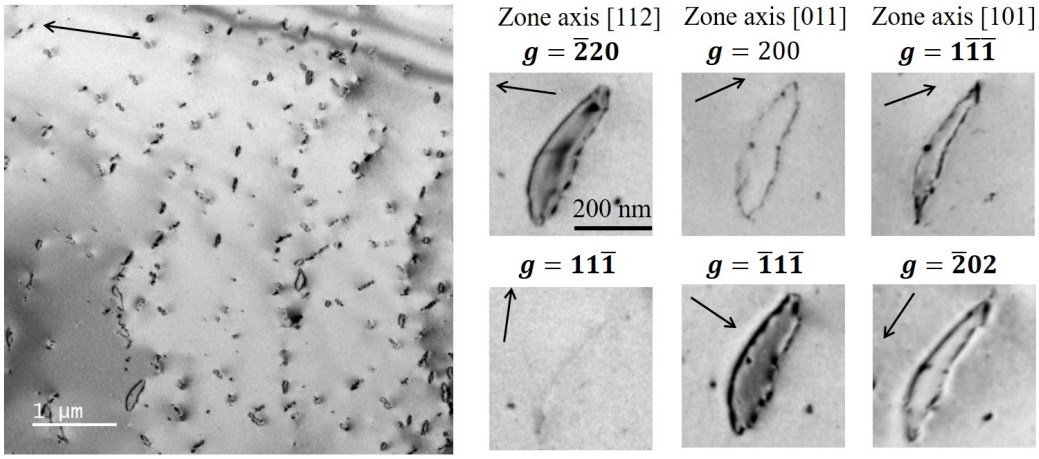

Table of visibility (V= visible, I= invisible)	Zone axes	[112]		[011]		[101]	
	g / Possible b	11$\bar{1}$	$\bar{2}$20	200	$\bar{1}$1$\bar{1}$	1$\bar{1}\bar{1}$	$\bar{2}$02
	$\pm\frac{1}{2}$[110]	V	I	V	I	I	V
	$\pm\frac{1}{2}$[1$\bar{1}$0]	I	V	V	V	V	V
	$\pm\frac{1}{2}$[101]	I	V	V	V	V	I
	$\pm\frac{1}{2}$[10$\bar{1}$]	V	V	V	I	I	V
	$\pm\frac{1}{2}$[011]	I	V	I	I	V	V
	$\pm\frac{1}{2}$[01$\bar{1}$]	V	V	I	V	I	V

Figure 4.11 Perfect loops in thin zones of Ni irradiated at 510°C to 0.18 dpa: image on the left showing the global view of the zone; images in the middle showing the visibility of a large perfect loop in function of diffraction vector **g**; visibility table on the right showing the analysis of the Burgers vector.

A stereo-analysis is performed on this loop. The inside-outside behavior is studied along the zone axes [101] (Figure 4.12(a)), [112] (Figure 4.12(b)) and [011] (Figure 4.12(c)). Firstly the sign of Burgers vector is determine to be 1/2[$\bar{1}$10] as **g**.**b**<0 for **g**=$\bar{2}$02, 2$\bar{2}$0 and 1$\bar{1}$1. Then the loop inclination should be determined. By rotating from the zone axis [101] to [011], the loop becomes larger. It suggests the inclination of loop habit plane as shown in Figure 4.12(d). The Burgers vector **b** and loop plane normal **n** are on the same side (**n**.**b**>0), according to the inside-outside method (Jenkins, 1994), the perfect loop is interstitial-type. This determination can be performed using simply a reference table (Edington, 1975) based on the same principle in Figure 4.12(e). With **g**=2$\bar{2}$0 pointing to the right, the inclination of the loop suggests that this loop in eith the 3rd or the 4th case. As the loop shows an inside contrast with this **g**, it is the 3rd case so the loop is interstitial-type.

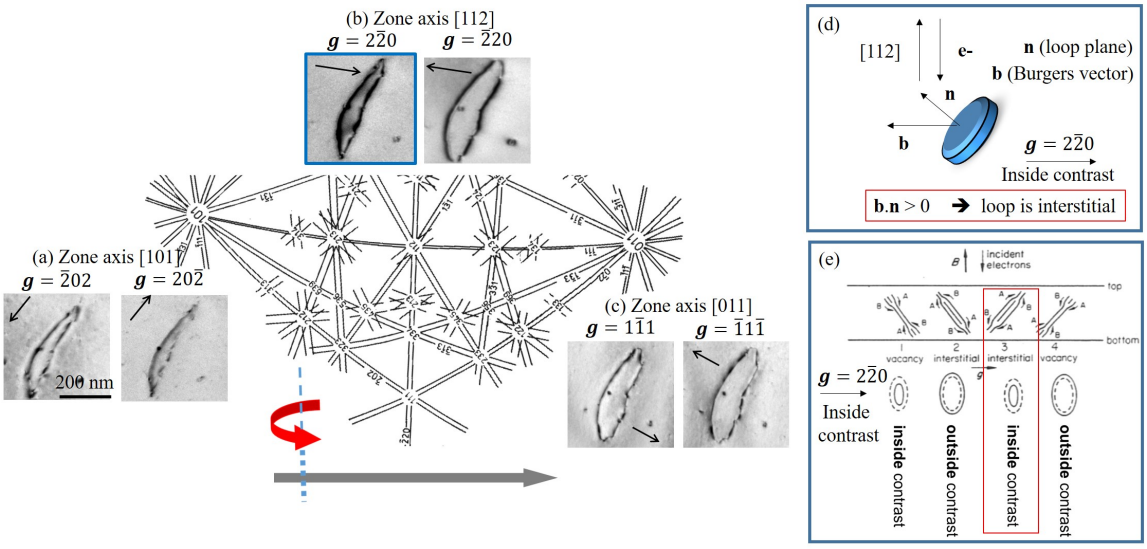

Figure 4.12 Determination of perfect loop nature by stereo-imaging in Ni irradiated 510°C to 0.18 dpa: BF images showing the inside-outside behavior of the 1/2[$\bar{1}$10] perfect loop along zone axes (a) [101] with **g**=±[$\bar{2}$02], (b) [112] with **g**=±[2$\bar{2}$0] and (c) [011] with **g**=±[1$\bar{1}$1]; Kikuchi map (Loretto and Smallman, 1975) showing the orientations; the axis of rotation from the zone axis [101] to [001] indicated by the read arrow; (d) schematic illustration showing the determination of loop nature with the loop inclination + inside contrast along [112] with with **g**=[2$\bar{2}$0]; (e) determination of loop nature with the reference table in the literature (Edington, 1975).

4.2 Irradiated microstructure in thin foil Ni

In this section, the characterization of irradiated microstructure in Ni is performed for different temperatures.

4.2.1 Influence of thickness on irradiated microstructure in Ni at 510°C (loop average size, density, spatial distribution)

Firstly, we focus on the post-characterization of the final microstructure irradiated up to 0.06 dpa at 510°C because the dislocation network is moderately developed at this dose so that more loops of interest can be studied to obtain better statistics.

Loop average size and dislocation line density in function of thickness are presented in Figure 4.13(a). The density of loops measured directly from images is plotted by the red curve in Figure 4.13(b). In Figure 4.13(a), loop average size increases firstly up to a maximum around 190 nm, then decreases and stabilizes to a saturation value. This decrease is attributed to the formation of dislocation lines. During irradiation, the tangle of large

loops contributes to the development of dislocation networks. The formation of such networks reduces the maximum size of loops and therefore their average loop size.

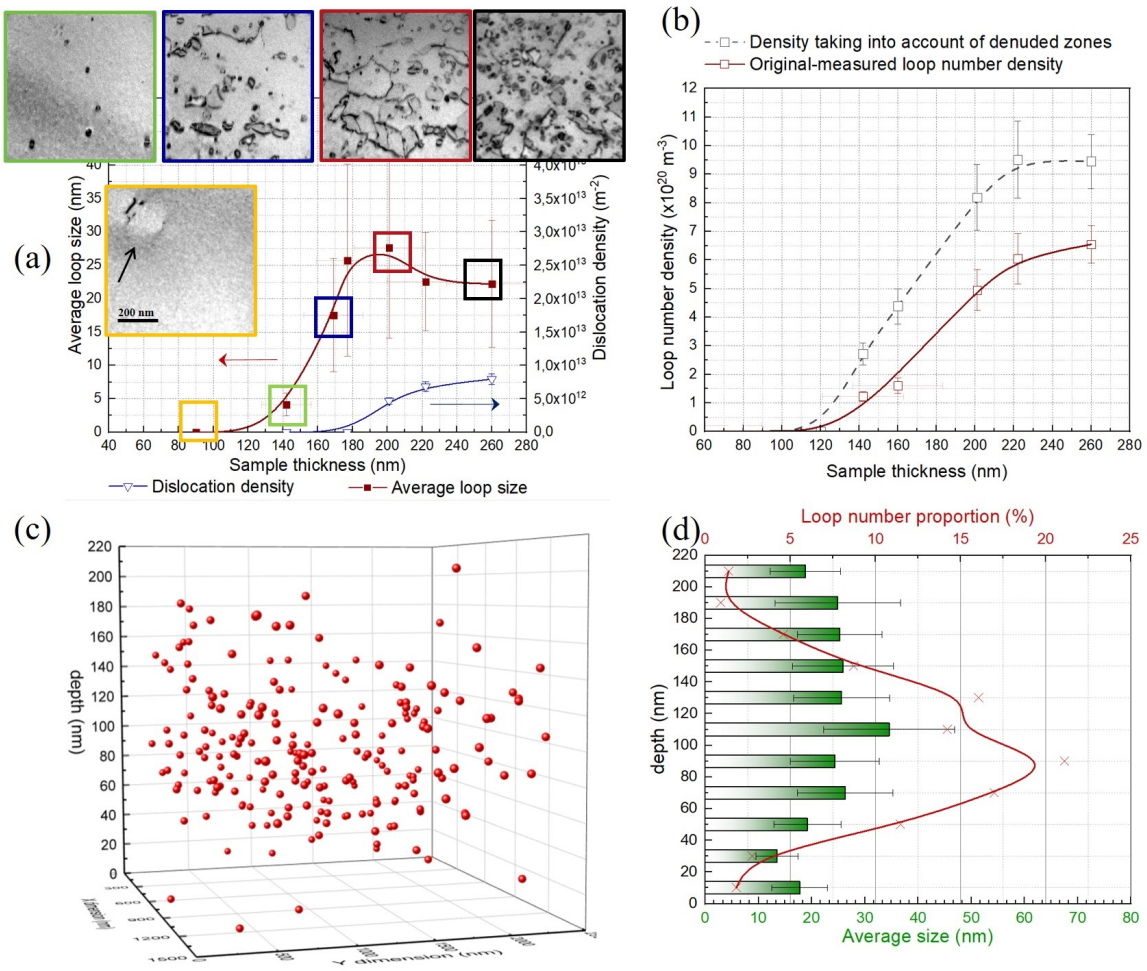

Figure 4.13 Final microstructure in function of foil thickness of Ni irradiated up to 0.06 dpa at 510°C: (a) Loop density and (b) average size; spatial distribution of loops by stereo-imaging technique with (c) 3D visualization of loop position in studied zone of 220 nm thickness and with (d) analysis of loop average size and number proportion v.s. depth.

However, in Figure 4.13(b), the density of loops (red curve) does not show a saturation even up to 260 nm thickness. Since the calculation of loop number density implicates the total thickness of the specimen, questions about the homogeneity of loop spatial distribution raise. The localization of loops is studied using the stereo-imaging technique. Figure 4.13(c) shows the 3D distribution at 220 nm thickness. Figure 4.13(d) is the average loop size and loop number proportion along the thickness. The number proportion is calculated by dividing the counted number of loops in each layer along depth direction by the total loop number in the studied zone. Loop-depleted zones near surfaces are observed. The strong absorption of

near-surface loops by surfaces is accounted for this depletion. The width of loop-depleted zone thickness is approximately 40 nm at each side at 220 nm thickness. Furthermore, at 220 nm thickness, loops in the middle of the foil are slightly larger in terms of average size than those close to surfaces.

Taking into account of these loop-depleted zones near surfaces, a corrected loop density using the thickness of loop-located zones is calculated and plotted in the blue pointed curve. This time, the saturation of loop density is pronounced. The dependency of these parameters suggests that the final microstructure is thickness-independent above 220 nm. However, it should be noticed that the density shown here takes no account of invisible loops and this is not the real density of existing loops in the sample. A further correction taking into account invisible loops and even escaped loops can be performed with analysis of Burgers vectors, which will be shown in the next subsection.

As mentioned in Section 4.1.3, occasionally in two specimens some perfect loops are found in thin zones which are usually free of defects (Figure 4.13(b)). Figure 4.14 shows the global microstructure in the zone. The thickness is measured by CBED technique and confirmed by EELS. The loop density and size increase with thickness from 50 nm then decrease. The foil normal is [112]. Abnormally large perfect loops are observed at 70-100 nm thickness zones. When the thickness exceeds 160 nm, similar microstructure as previously presented in Figure 4.13(b)(a) is observed. In these thin zones, by analysis of their contrast and their Burgers vectors, majority of large loops in thin zones are perfect loops because no fault contrast was detected in any loop. This transient microstructure seems similar to the bulk sample where a zone with only interstitial perfect loops is detected. This phenomenon is probably related to the foil orientation and will be further discussed in the last chapter.

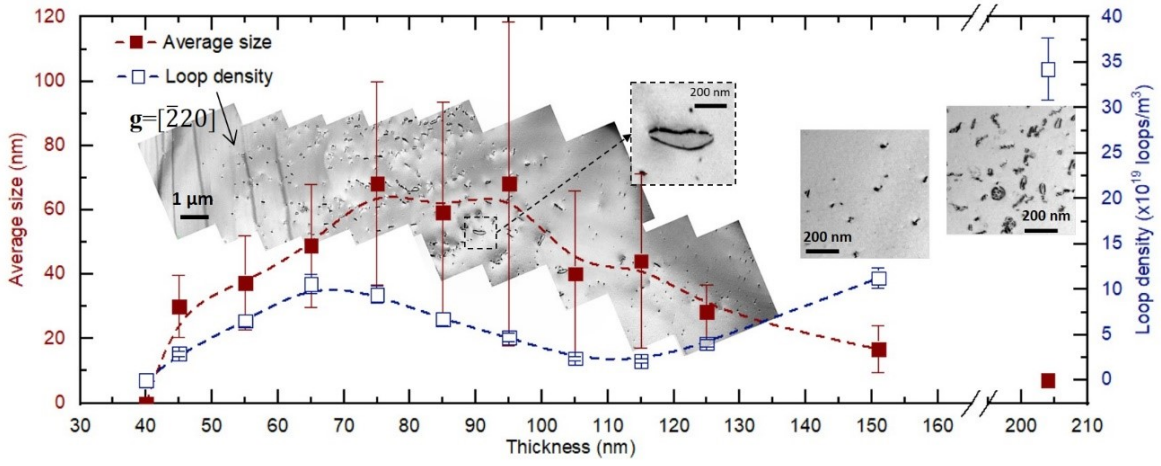

Figure 4.14 Microstructure in very thin zone irradiated to 0.18 dpa at 510°C. TEM micrographs taken under two-beam conditions using g=[220] along zone axis [112]; red curve for average loop size and blue curves for loop density in function of thickness.

4.2.2 Determination of Burgers vectors distribution

4.2.2.1 Loop type analysis in thick zones (>200 nm)

During irradiation, the absorption of mobile loops by surfaces is observed, which may lead to the depletion of some perfect loops. A statistic method presented in (Prokhodtseva et al., 2013) allow us to analyze the density of each loop family. We performed an analysis using this method in the 200 nm thickness zone to study the distribution of Burgers vectors.

First, the same zone is imaged with different **g**. Figure 4.15(a-g) shows seven studied TEM micrographs. According to the authors (Prokhodtseva et al., 2013), at least four **g** vectors should be considered (at least two of them non-coplanar) and the accuracy can statistically-speaking be improved with more **g**. In this work, we selected in total seven different **g**, four along the zone axis [001] and three along [101], which satisfies completely the exigence and provides good accuracy. Then, loop densities are calculated from micrographs taking into account loop-depleted zones (excluding 40 nm for each side). The densities are listed in Table 4.1.

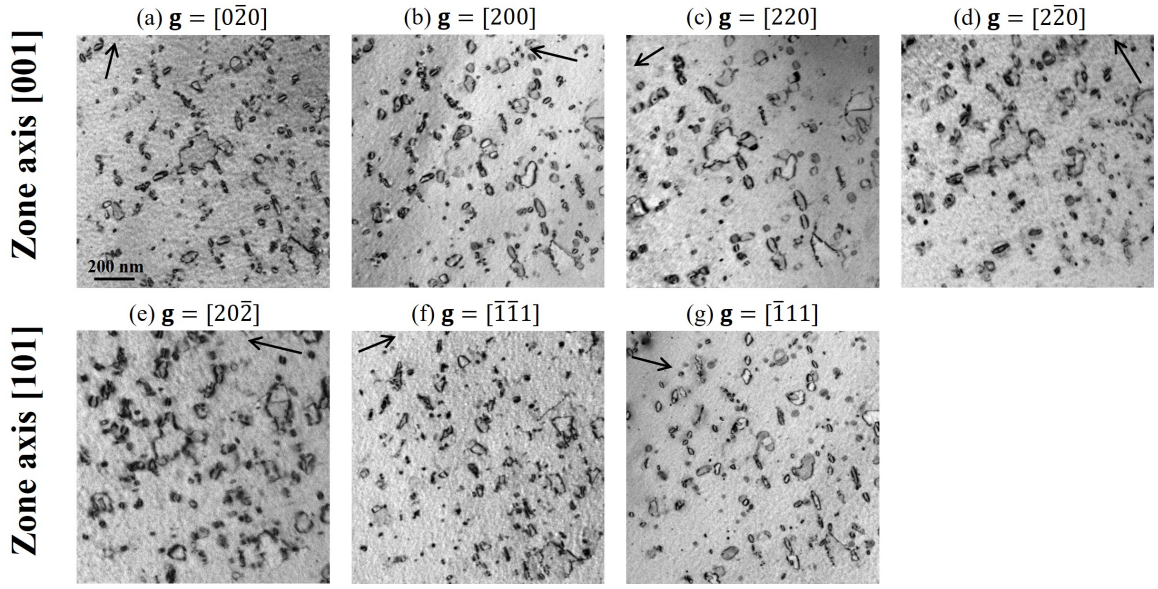

Figure 4.15 TEM micrographs showing the microstructure in the same zones in function of diffraction vectors **g** in a 200 thick zone of Ni irradiated to 0.06 dpa at 510°C.

Table 4.1 Loop density (10^{19} m^{-3}) in function of diffraction vectors **g** Ni in a 200 nm thick zone of Ni irradiated to 0.06 dpa at 510°C.

Zone axis	[001]				[101]		
g investigated	020	200	2$\bar{2}$0	220	$\bar{1}\bar{1}$1	$\bar{1}$11	20$\bar{2}$
Loop density (10^{20} m^{-3})	8.01	7.82	6.13	6.05	7.96	6.24	6.04

The next step is to establish a system of equations which give the number of visible loops for each **g**. Based on the densities in Table 4.1, we performed an individual analysis of loop density for each family using the statistic method(Prokhodtseva et al., 2013). The method is illustrated by the case of the Frank loop family with **b**=1/3[111]. The analysis for other family can be conducted similarly. For **b**=1/3[111] Frank loops, based on the invisibility criteria, the system of equations for achieved diffraction conditions is shown by :

$$\begin{cases} N^{visible}_{\mathbf{g}=020} = \frac{1}{1}N_{\mathbf{b}=\frac{1}{3}[111]} + \frac{3}{3}N_{\mathbf{b}=\frac{1}{3}<111>\ \frac{1}{3}[111]} + \frac{4}{6}N_{\mathbf{b}=\frac{1}{2}<110>} \\ N^{visible}_{\mathbf{g}=200} = \frac{1}{1}N_{\mathbf{b}=\frac{1}{3}[111]} + \frac{3}{3}N_{\mathbf{b}=\frac{1}{3}<111>\ \frac{1}{3}[111]} + \frac{4}{6}N_{\mathbf{b}=\frac{1}{2}<110>} \\ N^{visible}_{\mathbf{g}=2\bar{2}0} = \frac{0}{1}N_{\mathbf{b}=\frac{1}{3}[111]} + \frac{2}{3}N_{\mathbf{b}=\frac{1}{3}<111>\ \frac{1}{3}[111]} + \frac{5}{6}N_{\mathbf{b}=\frac{1}{2}<110>} \\ N^{visible}_{\mathbf{g}=220} = \frac{1}{1}N_{\mathbf{b}=\frac{1}{3}[111]} + \frac{1}{3}N_{\mathbf{b}=\frac{1}{3}<111>\ \frac{1}{3}[111]} + \frac{5}{6}N_{\mathbf{b}=\frac{1}{2}<110>} \\ N^{visible}_{\mathbf{g}=\bar{1}\bar{1}1} = \frac{1}{1}N_{\mathbf{b}=\frac{1}{3}[111]} + \frac{3}{3}N_{\mathbf{b}=\frac{1}{3}<111>\ \frac{1}{3}[111]} + \frac{3}{6}N_{\mathbf{b}=\frac{1}{2}<110>} \\ N^{visible}_{\mathbf{g}=\bar{1}11} = \frac{1}{1}N_{\mathbf{b}=\frac{1}{3}[111]} + \frac{3}{3}N_{\mathbf{b}=\frac{1}{3}<111>\ \frac{1}{3}[111]} + \frac{3}{6}N_{\mathbf{b}=\frac{1}{2}<110>} \\ N^{visible}_{\mathbf{g}=20\bar{2}} = \frac{0}{1}N_{\mathbf{b}=\frac{1}{3}[111]} + \frac{2}{3}N_{\mathbf{b}=\frac{1}{3}<111>\ \frac{1}{3}[111]} + \frac{5}{6}N_{\mathbf{b}=\frac{1}{2}<110>} \end{cases} \tag{4.1}$$

Where $N^{visible}_{\mathbf{g}}$ is the density of visible loops for used g and summarized in Figure 4.16(e), $N_{\mathbf{b}=1/3[111]}$ is the density of 1/3[111] Frank loops, $N_{\mathbf{b}=\frac{1}{3}<111>\ \frac{1}{3}[111]}$ is the sum of three other families of Frank loops, $N_{\mathbf{b}=\frac{1}{2}<110>}$ is the sum of six families of perfect loops. Equation 4.1 can be written in the following way:

$$\begin{bmatrix} 8.01 \\ 7.82 \\ 6.13 \\ 6.05 \\ 7.96 \\ 6.23 \\ 6.04 \end{bmatrix} = \begin{bmatrix} 1 & 1 & \frac{2}{3} \\ 1 & 1 & \frac{2}{3} \\ 0 & \frac{2}{3} & \frac{5}{6} \\ 1 & \frac{1}{3} & \frac{5}{6} \\ 1 & 1 & \frac{1}{2} \\ 1 & 1 & \frac{1}{2} \\ 0 & \frac{2}{3} & \frac{5}{6} \end{bmatrix} \times \begin{bmatrix} N_{\mathbf{b}=1/3[111]} \\ N_{\mathbf{b}=\frac{1}{3}<111>\ \frac{1}{3}[111]} \\ N_{\mathbf{b}=\frac{1}{2}<110>} \end{bmatrix} \tag{4.2}$$

We have to stress the hypothesis when establishing this equation system. The visibility coefficients are calculated based on the assumption that apart from **b**=1/3[111] Frank loops, the three other Frank loop families are equally probable and meanwhile, the six families of perfect loops are equally probable among them.

This matrix equation is solved by the least-squares method using the software Scilab with an error given by the standard deviation from the least-squares. The solution gives the density of three families in Equation 4.2, for instance, $N_{\mathbf{b}=1/3[111]}= 12.3 \pm 5 \times 10^{19}$ m^{-3}. By the same analysis, we can calculate the density of other families. Finally, the density of all Frank loop families and perfect loop families is deduced and presented in Table 4.2.

Table 4.2 Results of loop type analysis family by family in Ni irradiated at 510°C up to 0.06 dpa with all density in 10^{19} m^{-3}

Loop type	Frank loops				perfect loops					
Burgers vectors	111	$\bar{1}11$	$1\bar{1}1$	$11\bar{1}$	110	$1\bar{1}0$	101	$10\bar{1}$	011	$01\bar{1}$
Loop density	12.3	12.7	13.0	11.7	13.0	1.8	7.0	5.7	1.3	14.1
error	5.5	6.2	5.5	6.2	3.9	4	4.6	5.3	3.7	13.3
Frank/perfect loop density	50 ± 10				43 ± 25					
Total density	93 ± 6									
Corrected density	50 ± 10				85 ± 20					
Corrected total density	131 ± 25									

By summing results of each family and are respectively $N_{Frank} = 49.7 \pm 12 \times^{20}$ m^{-3} and $N_{perfect} = 42.9 \pm 10 \times 10^{20}$ m^{-3}.

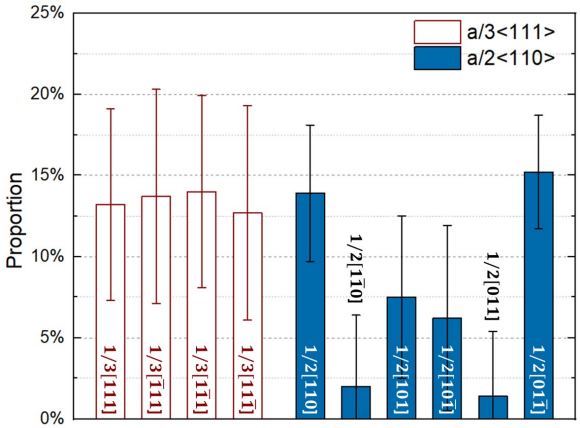

Figure 4.16 Proportion of each family of loops calculated by diving the density of each family by the total density in Ni irradiated at 510°C to 0.06 dpa. White bars for Frank loops and blue bar for perfect loops.

It is worth to note that Frank loops are equally distributed among the 4 families while perfect loops are not. A heterogeneous distribution of perfect loops is clearly shown. The proportion of each family is calculated and plotted in Figure 4.16. As the distribution of perfect loops is not equally probable, the assumption of the method is not satisfied. However, 1/2[110] and 1/2[01$\bar{1}$], 1/2[101] and 1/2[10$\bar{1}$], 1/2[1$\bar{1}$0] and 1/2[011] are respectively equally probable. Therefore, we performed a further analysis by combining perfect loops families two by two using Equation 4.3.

$$\begin{bmatrix} 8.01 \\ 7.82 \\ 6.13 \\ 6.05 \\ 7.96 \\ 6.23 \\ 6.04 \end{bmatrix} = \begin{bmatrix} 1 & 2/2 & 0/2 & 2/2 \\ 1 & 1/2 & 2/2 & 1/2 \\ 1/2 & 1/2 & 2/2 & 2/2 \\ 1/2 & 2/2 & 2/2 & 1/2 \\ 1 & 2/2 & 1/2 & 0/2 \\ 1 & 0/2 & 1/2 & 2/2 \\ 1/2 & 2/2 & 1/2 & 2/2 \end{bmatrix} \times \begin{bmatrix} N_{\mathbf{b}=1/3<111>} \\ N_{\mathbf{b}=1/2[110]+1/2[01\bar{1}]} \\ N_{\mathbf{b}=1/2[101]+1/2[10\bar{1}]} \\ N_{\mathbf{b}=1/2[011]+1/2[1\bar{1}0]} \end{bmatrix} \tag{4.3}$$

The solution of Equation 4.3 are given in Table 4.3. The total density of perfects loops is thus 43±4 m^{-3}. The total density of Frank loops and perfect loops are in good agreement with the previous results (Table 4.2) with an error significantly reduced. The reduced error can be attributed to the increasing number of unknowns and the improved accuracy of the visibility coefficient matrix. Mathematically, when the unknown number increases (maximum to 7 as there are 7 **g**), the equation system becomes more "exact" and the error will be reduced (for example, to 0 for 7 unknowns). The solution is mathematically more accurate using more unknowns but statistically less accurate. With 7 unknowns, a small discrepancy of measured density to the real one in each image could lead to a large discrepancy of the solution to the real density. So, a comprise must be made to obtain a low error keeping the unknowns as few as possible, which is the major advantage of this method. We tested different combinations of perfect loop families for 4 unknowns and the one of Table 4.2 gives the lowest error. Thus, 1/2[110] and 1/2[01$\bar{1}$], 1/2[101] and 1/2[10$\bar{1}$], 1/2[1$\bar{1}$0] and 1/2[011] are indeed respectively equally probable.

Table 4.3 Results of loop type analysis using Equation 4.3 in Ni irradiated at 510°C up to 0.06 dpa with all density in 10^{19} m^{-3}

$N_{\mathbf{b}}$	$1/3<111>$	$1/2[110]+1/2[01\bar{1}]$	$1/2[101]+1/2[10\bar{1}]$	$1/2[011]+1/2[1\bar{1}0]$
Density	51±3	21±3	13±3	9±3

These results show that perfect loops with b=1/2[011] and 1/2[1$\bar{1}$0] have the lowest proportion while perfect loops with b=1/2[110] and 1/2[01$\bar{1}$] have the highest proportion. It is very likely that perfect loops with b=1/2[011] and 1/2[1$\bar{1}$0] are annihilated at surfaces, either by moving towards the surfaces or by intercepting with the surface. This point will be discussed in the last chapter.

With this Burgers vector analysis, the density of loops taking into account of absorbed loops can be estimated. If we consider that loops are formed equally at the beginning and that the depletion of perfect loops results only from their movement to surfaces, the real total density of perfect loops can be estimated by multiplying the highest density by six. The corrected density of perfect loops is 6.2 ± 8 $\times 10^{20}$ m^{-3}. Thus the real density of loops

taking into account of escaped loops at 200 nm thickness is $N_{real} = 11.2 \pm 8 \times 10^{20}$ m^{-3}. The proportion of Frank loops and perfect loops can be also corrected as 45% and 55%.

4.2.2.2 Loop type analysis in thin zones (<90 nm)

Loop type analysis is performed in the Ni sample where perfect loops are detected in thin zones (<150 nm). The thickness of the zone is about 90 nm. As the loop density is low and majority of loops are individual, the analysis is performed by identifying the Burgers vector of each loop. The visibility in function of **g** is shown in Figure 4.17. Three type of perfect loops are identified: 1/2[$\bar{1}$10], 1/2[10$\bar{1}$] and 1/2[0$\bar{1}$1] with proportion shown in Figure 4.14.

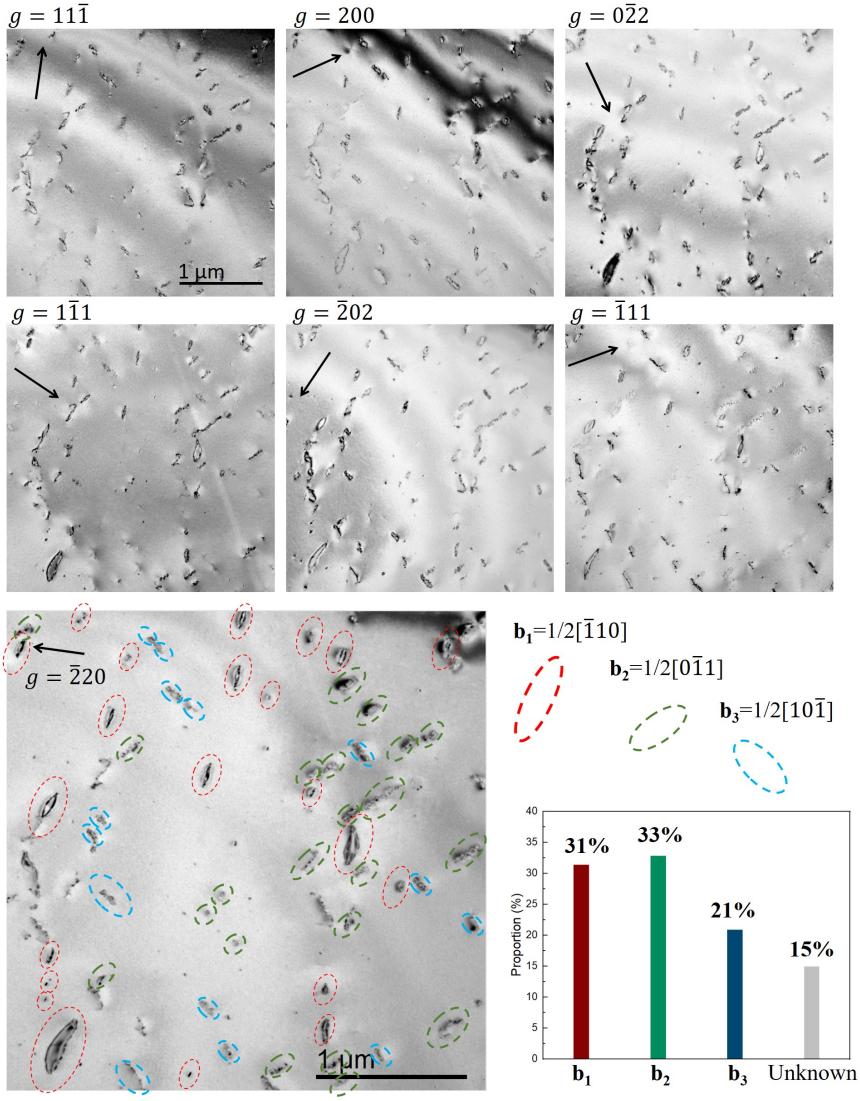

Figure 4.17 Loop type analysis in thin zones (90 nm) of Ni irradiated at 510°C to 0.18 dpa. The analysis performed by manually identifying the Burgers vector of each loops.

4.2.3 Role of temperature on surface effects (critical thickness of saturated microstructure) and defect evolution

The temperature-dependency of surface effects shown in Figure 4.19 is investigated in detail. Figure 4.18(a-b) presents the thickness-dependency of the density and average size of defects respectively at 400, 450 and 510°C. The curves of 510°C has been presented in Figure 4.13(a) and plotted here to compare with the lower temperatures. Microstructures at 400 and 450°C are shown by TEM micrographs in Figure 4.18.

In thin zones of Ni irradiated at 450°C and 400°C, a high density of triangle-form defects is detected as shown in Figure 4.18. These defects are likely stacking fault tetrahedron (SFT) which were observed in neutron or ion irradiated Ni (Kitagawa et al., 1985; Yao et al., 2003; Zinkle and Snead, 1995). When the thickness increases, the irradiated microstructure turns from a SFT-dominated one into a loop-dominated one. This transition leads to a decrease of total defect density at 450/400°C when the thickness increases. The difference between the two temperature is that the loop density increases strongly upon 70 nm thickness at 450°C while a high density of loops is detected upon 50 nm at 400°C. It is worth noting that no SFT is detected in Ni irradiated at 510°C. Finally it leads to the density curves at 450/400°C in Figure 4.18(a) quite different from the one at 510°C in thin zones. In terms of defect size, most SFT remains small (<5 nm). At 400°C, SFT has a similar size to loops in the range of studied thickness so the average size of defects is independent of the thickness. However at 450°C, the average size defects increases with the thickness as the size of loops is larger than SFT at this temperature.

At 400°C and 450°C, the defect density and defect size depend no longer on the thickness when thickness exceeds respectively 90 nm and 110 nm. These values are the critical thickness above which the microstructure is certainly thickness-independent. Based on these observations, a black line is drawn in Figure 4.18(a) dividing approximately thickness-dependent zones and thickness-independent zones.

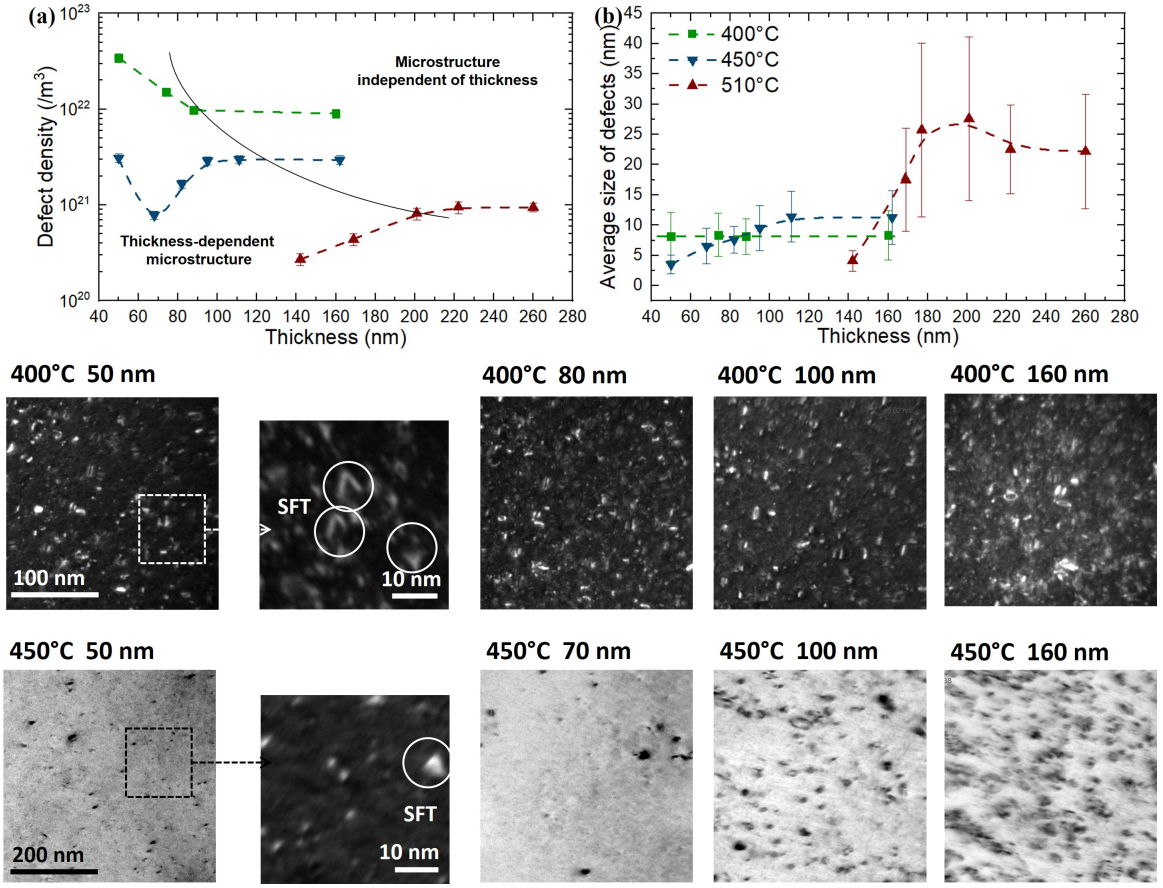

Figure 4.18 Influence of surface effects in function of temperature in pure nickel. Evolution of (a) Loop density and (b) average loop size in function of thickness at 400/450/510°C with selected TEM micrographs showing corresponding microstructure.

4.3 Microstructural evolution in thin foil Ni

In this section, the microstructural evolution and the growth of dislocation loops during irradiation is studied using in-situ irradiations in a TEM. In-situ irradiation is a powerful tool to study real-time microstructural evolution. Comparative in-situ irradiations on Ni and alloys will allow us to study the solute effects on the microstructural evolution and loop growth rate. However, samples of in-situ studies have to be thin foils. Previous results show strong surface effects on the loop density and size and the existence of a critical thickness. This section investigate firstly the maximum temperature where there is a growth of defects. At this temperature, the influence of thickness on the microstructural evolution and loop growth are studied. Then, the microstructural evolution at lower temperatures in "thick" zones (>critical thickness) are also studied.

4.3.1 Influence of temperature on defect formation in Ni for a given thickness

General microstructures after irradiation in zones of 200 nm thickness are shown by TEM micrographs in Figure 4.19 over a large range of temperatures (from 700°C to 400°C). The objective is to find the maximum temperature at which radiation-induced defects can be formed. The thickness of 200 nm is chosen as it is an intermediate value in the range of observable thickness in Ni using a conventional 200 kV TEM. The maximum observable thickness of Ni samples in a 200 kV TEM is around 260 nm (as shown in Figure 4.13). If defects are formed at 200 nm thickness, the thickness marge will be large enough to study the thickness-dependency of the microstructure.

Figure 4.19 present the irradiated microstructure at the same dose (0.06 dpa, 220 s) at respectively 700/600/500/450/400°C. At 700°C and 600°C, pre-existing dislocations move during the irradiation but no newly-created defect is observed. In the literature, dislocation loops have been observed in self-ion irradiated bulk Ni at 575°C (Brimhall and Simonen, 1977) and in He^+ irradiated thin foil Ni up to 700°C at unspecified thickness (Niwase et al., 1993). The fact that no defect is observed in this work at 600°C and 700°C is very likely attributed to the strong absorption of point defects by surfaces at such thickness. When the temperature is reduced to 500°C, visible dislocation loops are formed.

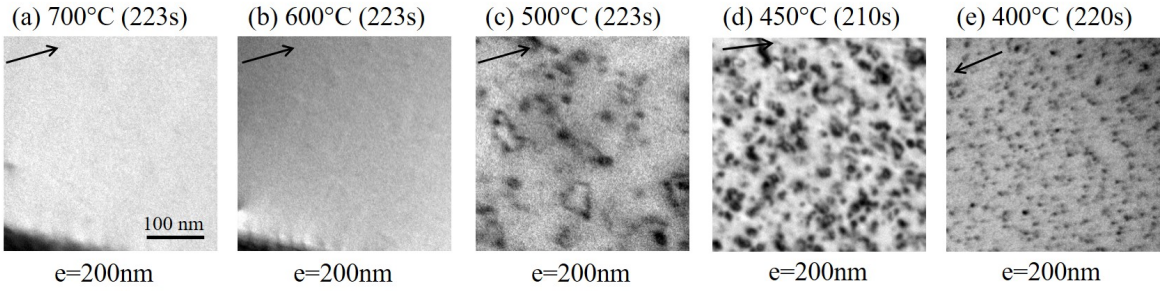

Figure 4.19 TEM micrographs showing microstructure of 200 nm thick zone under irradiation at various temperatures: (a) at 700°C, (b) at 600°C and (c) at 500°C with **g**=<200> close to zone axis <110>; (d) at 450°C with **g**=<200> close to zone axis<103>; (d) at 400°C with **g**=<111> close to zone axis<110>. the dose for 220 seconds of irradiation is 0.06 dpa

Loops grow during the irradiation. The final microstructure at 0.06 dpa (about 220 seconds of irradiation) is shown in Figure 4.19(c). Figure 4.19(d) and Figure 4.19(e) present the final microstructures of two other irradiations at the same dose at respectively 450°C and 400°C. Loops are smaller and show a higher density at lower temperatures. Based on these observations, temperature around 500°C appears to be ideal to study surface effects.

4.3.2 Influence of thickness on defect formation and evolution (density, size and growth rate) at 510°C

The microstructural evolution in thin foil Ni is studied at 510°C in function of thickness (Figure 4.20(a-c)). Figures 4.20(d-e) show respectively the evolution of loop number density and average loop size in function of irradiation duration t. Loop densities and average sizes stabilize at different instants for each thickness. At 150 nm thickness, the loop density and average size are approximately constant when $t > 80$ s i.e. microstructure appears to be in steady-state. At 180 nm and 260 nm, the steady state starts from respectively around 100 s and 130 s. However, the steady state is achieved via different mechanisms. (i) At 150 nm, loops are continuously created during the irradiation. Formed loops grow slightly and most of them quickly disappear, probably to surfaces. An equilibrium of the loop creation and absorption is established and form a steady-state microstructure. (ii) The phenomenon is similar at 180 nm and at 150 nm while loops can grow larger at 180 nm. The interaction mechanism of a dislocation loop with the surface is shown in Figure 4.20(f): a grown Frank loops unfaults, then immediately glides and disappears. (iii) For a thickness of 260 nm, the microstructural evolution is similar at first to the 180 nm one. After 80 s large loops tangle with each other, leading to a dislocation network that reduces slightly the average size.

Figure 4.21(a) presents the typical growth of a Frank loop in function of irradiation time at 510°C. The size of this loop can be approximately considered as linear with time. A similar phenomenon of interstitial Frank loops was extensively studied under electron irradiation experiments (Harbottle and Norris, 1973; Norris, 1970; Urban, 1971; Yoo and Stiegler, 1977). This linear growth rate is verified for many other loops, which allows to calculate an average growth rate for linearly-growing loops. The average growth rate of loops in the steady-state microstructure are indicated in Figure 4.21(b). The loop growth rate increases with thickness as observed intuitively in Figure 4.20.

It is of great interest to notice that the growth rate is close to saturation taking into account of error bar when the thickness exceeds 240 nm. Moreover, the same growth rate is observed in another foil with different grain orientation. The standard deviation of growth rate is quite important because some loops grow very fast while some grow slowly even in thick zones. This should be attributed to the fact that loops are located at different depths inside the foil where the influence of surfaces changes.

Figure 4.22(a) shows the movement of three loops. These TEM micrographs were taken along zone axis <013> with g=<200> during the irradiation. To analyze the direction of their movement, stereo-projection along [013] is shown in Figure 4.22(b). The motion occurs always along <110> directions.

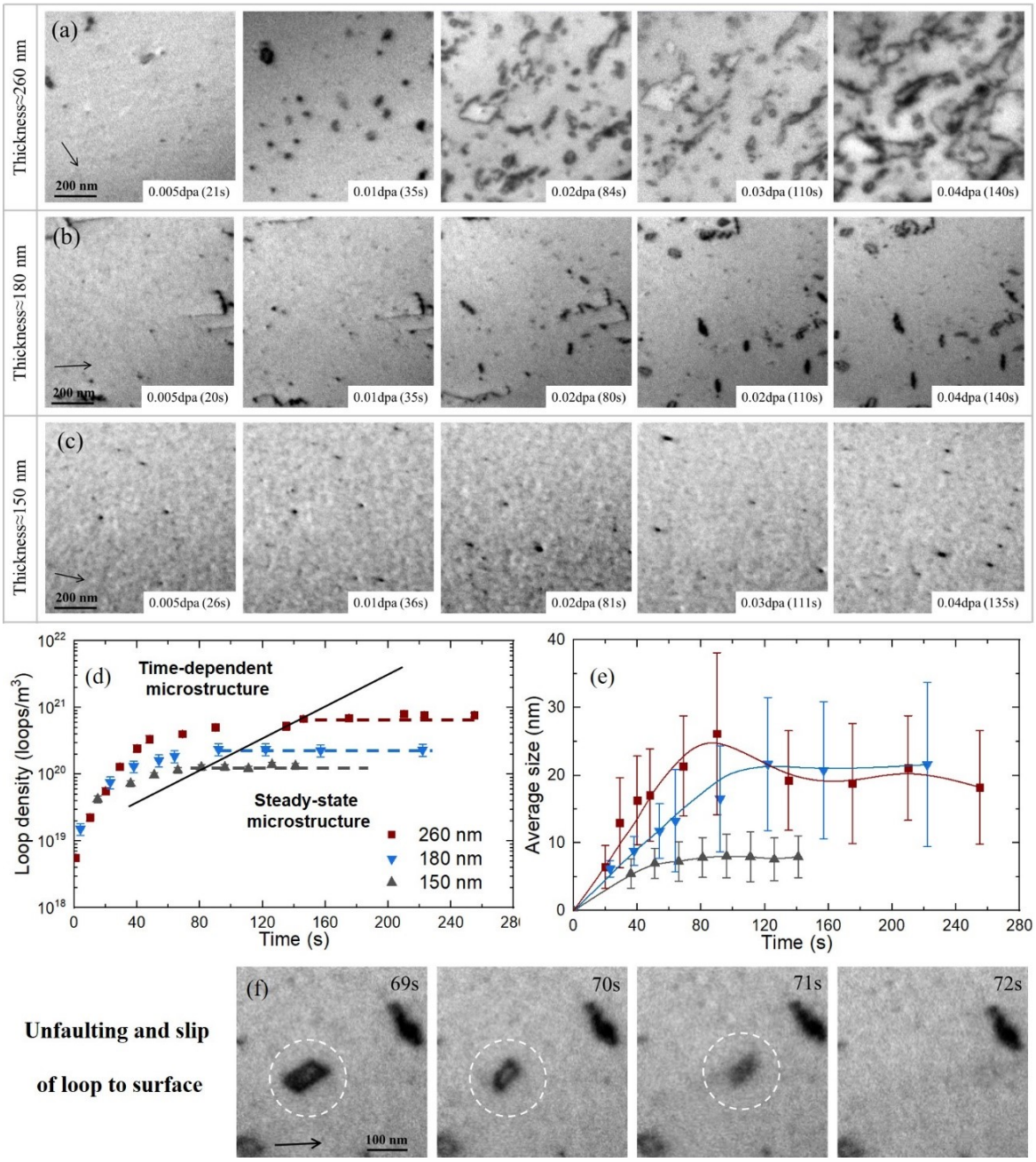

Figure 4.20 Microstructural evolution during in-situ irradiation as a function of irradiation thickness and dose at 510°C. (a-c) Selected micrographs illustrating the microstructure were recorded under two-beam KBF conditions using (a) $\mathbf{g} = <200>$, (b) and (c) $\mathbf{g} = <111>$ with the same scale bar for all micrographs indicated in (a). (d-e) Evolution of loop number density and average size in function of irradiation time.

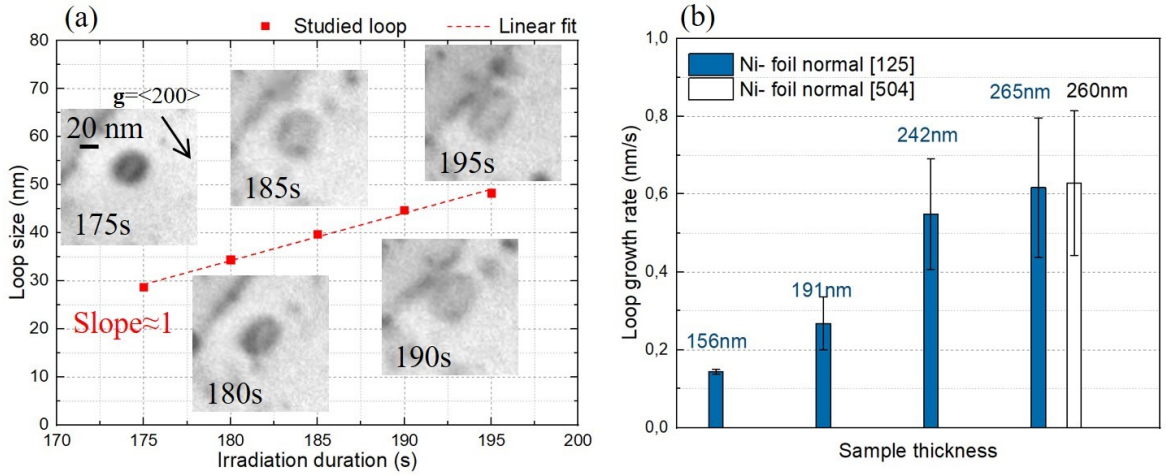

Figure 4.21 Determination of loop growth rate during irradiation at 510°C. (a) selected TEM micrographs of one loop in function of time and linear fitting of loop size v.s. time using Origin 9.0; (b) average loop growth rate in nm/s in function of thickness in two foils.

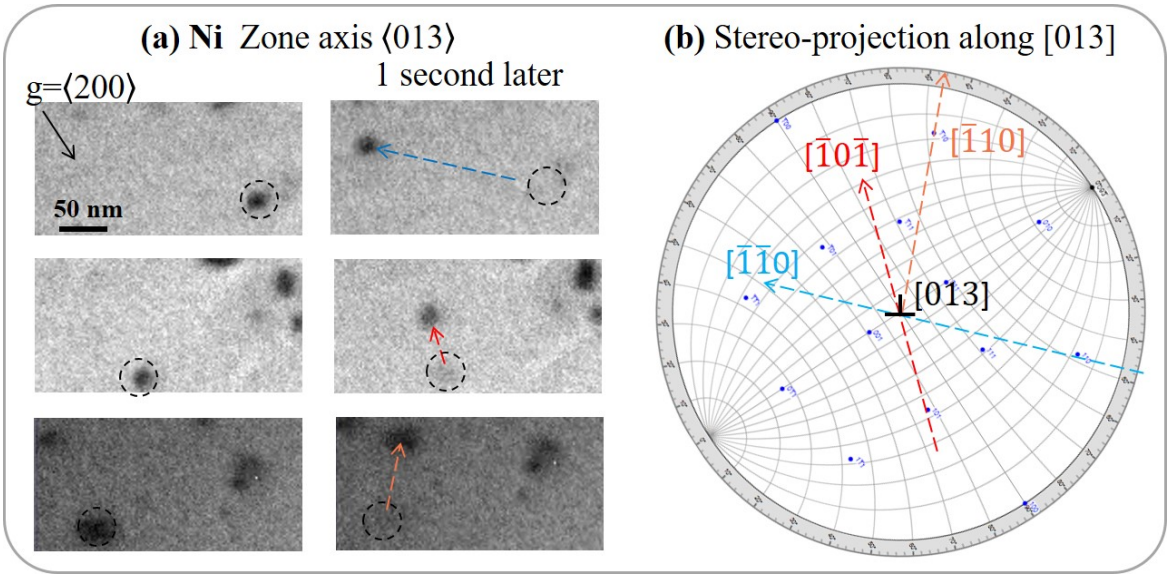

Figure 4.22 Movement direction of dislocation loops in irradiated Ni at 510°C. (a) TEM micrographs showing the movement of three loops with the motion direction indicated by dashed arrows; images taken along zone axis <013> with g=<200>; (b) stereo-projection along [013] with motion directions indicated; the thickness of the zone is 180 nm.

4.3.3 Microstructural evolution at lower temperatures (400°C and 450°C)

Figure 4.18 shows that for each studied temperature, there is a thickness upon which the microstructural evolution is thickness-independent. Microstructural evolution in saturation zones is studied at each temperature, as shown in Figure 4.23(a-b). The number density at 400°C is at a steady-state after 120 seconds while the average size still increases slowly with time. At 450°C, the steady-state of number density is achieved slightly later than 400°C. The average size continuously increases with time after the steady state of loop density. However, this steady state of loop density is temporary. Loop density may finally decrease due to the development of a dislocation network. The irradiation at 450°C is conducted for a high dose in the same foil until 680 seconds (equivalent to 0.18 dpa). This tendency is shown by the two points at t=680 s at 450°C in Figure 4.23(a-b) where loop size and density are both lower than the values at steady state.

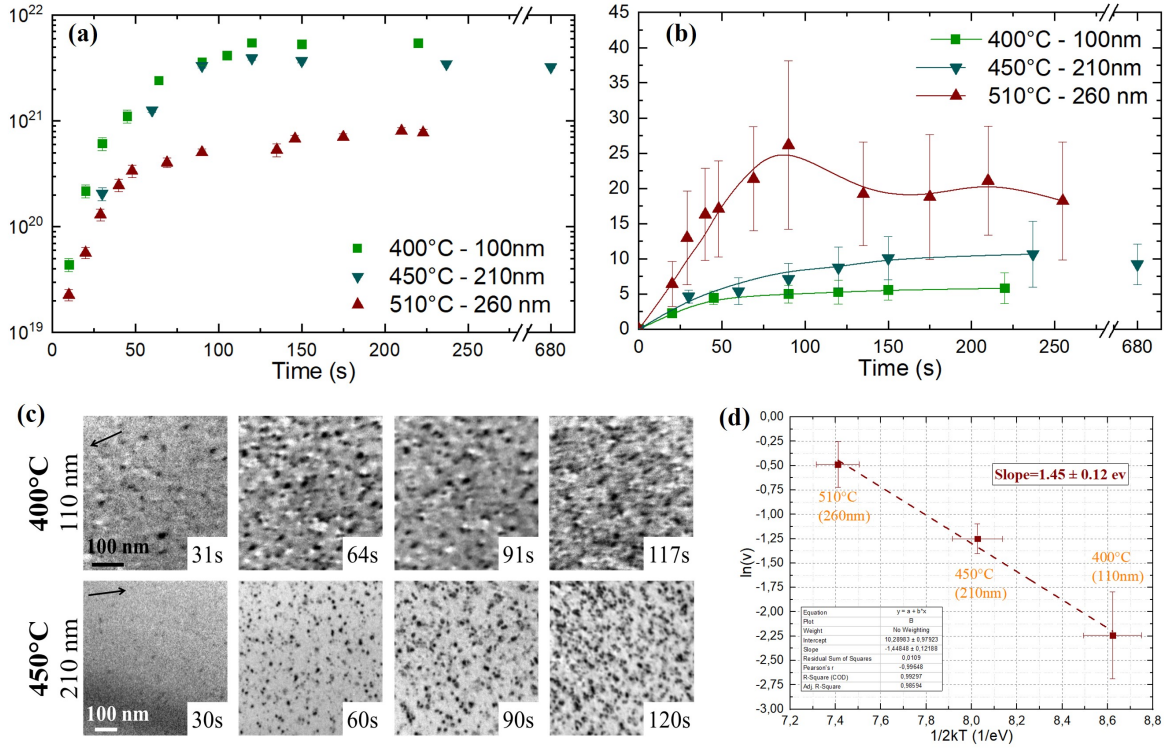

Figure 4.23 Influence of temperature on microstructural evolution in Ni: evolution of (a) loop density and (b) average size in function of time in thickness-independent zones at each temperature; (c) TEM microsgraphs showing the microstructural evolution; (d) logarithm of the average growth rate of loops in Ni in function of $1/(2k_BT)$ with k_B the Boltzmann constant and T the temperature in Kelvin.

The average growth rates of loops are measured at 200 nm thickness at 450°C and 110 nm at 400°C. The results are shown in Figure 4.23(d). The linear fitting between the logarithm

of growth rate and $1/(2k_BT)$ where k_B is Boltzmann constant and T the temperature in Kelvin leads to an Arrhenius slope of 1.45 ± 0.12 eV.

4.4 Summary of chapter

We present here briefly some important conclusions in this chapter:

1. In self-ion irradiated Ni, radiation-induced Frank loops are vacancy-type in the range of our irradiation conditions, independent of the sample form (thin foil v.s. bulk), the dose (0.7 dpa v.s. 0.18 dpa) and the irradiation temperature (450°C v.s. 500°C). It is for the first time that large stable intrinsic Frank loops are identified in irradiated nickel.
2. An eradication mechanism of intrinsic Frank loops by inner extrinsic Frank loops is shown.
3. Interstitial perfect loops are detected in zones distant from the damage production zone in bulk specimen and occasionally in thin zones of thin foils.
4. There is a critical thickness upon which the irradiated microstructure is thickness-independent. The critical thickness depends strongly on the temperature and is respectively 220/100/80 nm at 510/450/400°C.
5. In thick zones, the distribution of Burgers vectors of Frank loops is equally probable but the distribution of perfect loops is not. It is likely attributed to the absorption of mobile perfect loops by surfaces which is observed during irradiation.
6. The microstructural evolution depends also on the thickness. At 510°C, the growth rate of vacancy loops increases with the thickness then reaches a saturation. The critical thickness is also 220 nm.

These results provide a guideline for comparative studies of Ni and its alloys to identify real effects of solutes.

Chapter 5

Influence of an addition of Cr or Ti on irradiation behavior of Ni

This chapter aims to study the influence of solutes on Frank loop nature and the microstructural evolution. In the first part, the influence of a solute addition and the solute content on the Frank loop nature is studied. In the second part, the irradiated microstructure is characterized in Ni-0.4Cr and Ni-xTi (x=0.4, 0.8, 1.2) in order to study solute effects on loop density and size. The last part focuses on the influence of solutes on the microstructural evolution at 510°C in the alloys. The characterization of Frank loop nature and microstructural evolution is performed in zones thicker than the critical thickness determined for each temperature in Section 4.2.3.

5.1 Influence of solute on Frank loop nature

5.1.1 Influence of 0.4% solute addition on Frank loop nature in thin foils irradiated at 450°C

The general microstructure in Ni-0.4Cr and Ni-0.4Ti is shown respectively in Figure 5.1(a) and Figure 5.1(b). TEM micrographs were taken along zone axis <001> with **g**=<200>. Both Frank loops and perfect loops are detected. A low density of voids ($\approx 1O^{18}$ m^{-3}) is detected in Ni-0.4Cr. In Ni-0.4Ti, no large voids are observed while a great number of small defects (<2 nm) exist. The morphology fo Frank loops in function of materials is notable. In Ni-0.4Cr, all the observed Frank loops are segmented (similar to Ni) while Frank loops in Ni-0.4Ti are non-segmented.These observations suggests probably a different Frank loop nature in Ni-0.4Ti compared with Ni and Ni-0.4Cr. Thus the nature of these Frank loops must be determined.

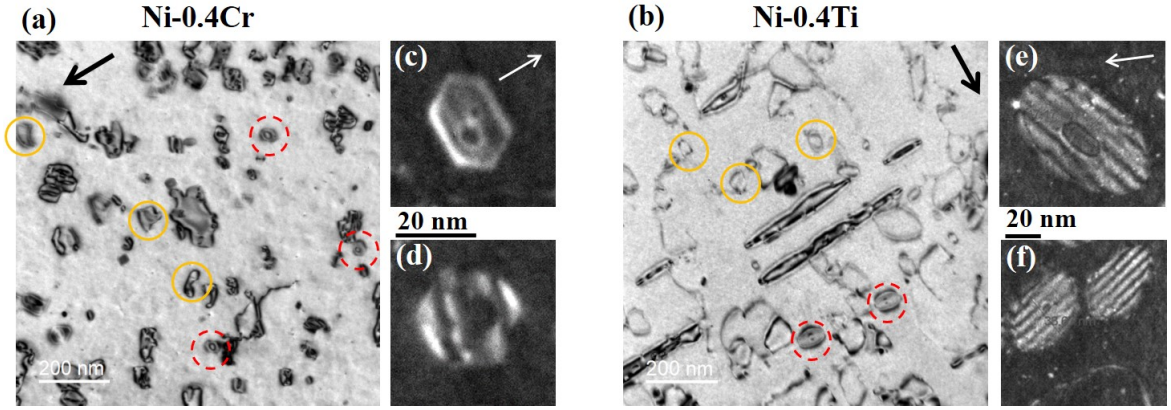

Figure 5.1 General microstructure and Frank loops in thin foil (a) Ni-0.4Cr and (b) Ni-0.4Ti irradiated to 2.3x10^{15} ions.cm^{-2} at 450°C. BF images taken along zone axis <101> with (a) **g**=<111> and (b) **g**=<202> indicated by black arrows; several Frank loops and perfect loops pointed out by respectively red dotted circles and yellow circles; WBDF images showing two typical Frank loops respectively in Ni-0.4Cr (c-d) and Ni-0.4Ti (e-f) with **g**=<200> (white arrows).

5.1.1.1 Frank loops in thin-foil Ni-0.4Cr

Figure 5.2 shows several Frank loops in Ni-0.4Cr. The determination of Frank loop nature is performed using the stereo technique. Figure 5.2(a) and Figure 5.2(b) are a ±**g** pair showing the inside-outside behavior of loops. Images were taken along the zone axis [101] with **g**=±[020]. It is clear that A, B, D and E show an inside contrast and C shows an outside contrast with **g**=[020]. The sample tilt angles are respectively 0° for alpha and -10° for beta. Then sample is tilted in keeping the same diffraction condition **g** to tilt angles of -17° for alpha and 13° for beta. As the diffraction vector **g** is approximately horizontal, the rotation α should be used to determine the loop nature as the rotation axis of α is perpendicular to the **g**. The rotation axis of α is indicated in Figure 5.2. From the variation of their size, the inclination of loops is shown in Figure 5.2(d-e). Therefore, according to Figure 5.2(f), they are all vacancy loops. Loop A, C, D and E are multiple Frank loops. The inner loops show a reverse contrast to the outer loops. Beside, no fault contrast is observed inside the inner loops. They are therefore interstitial-type loops that annihilate the stacking fault of the outer loops. It is similar to Frank loops in pure Ni.

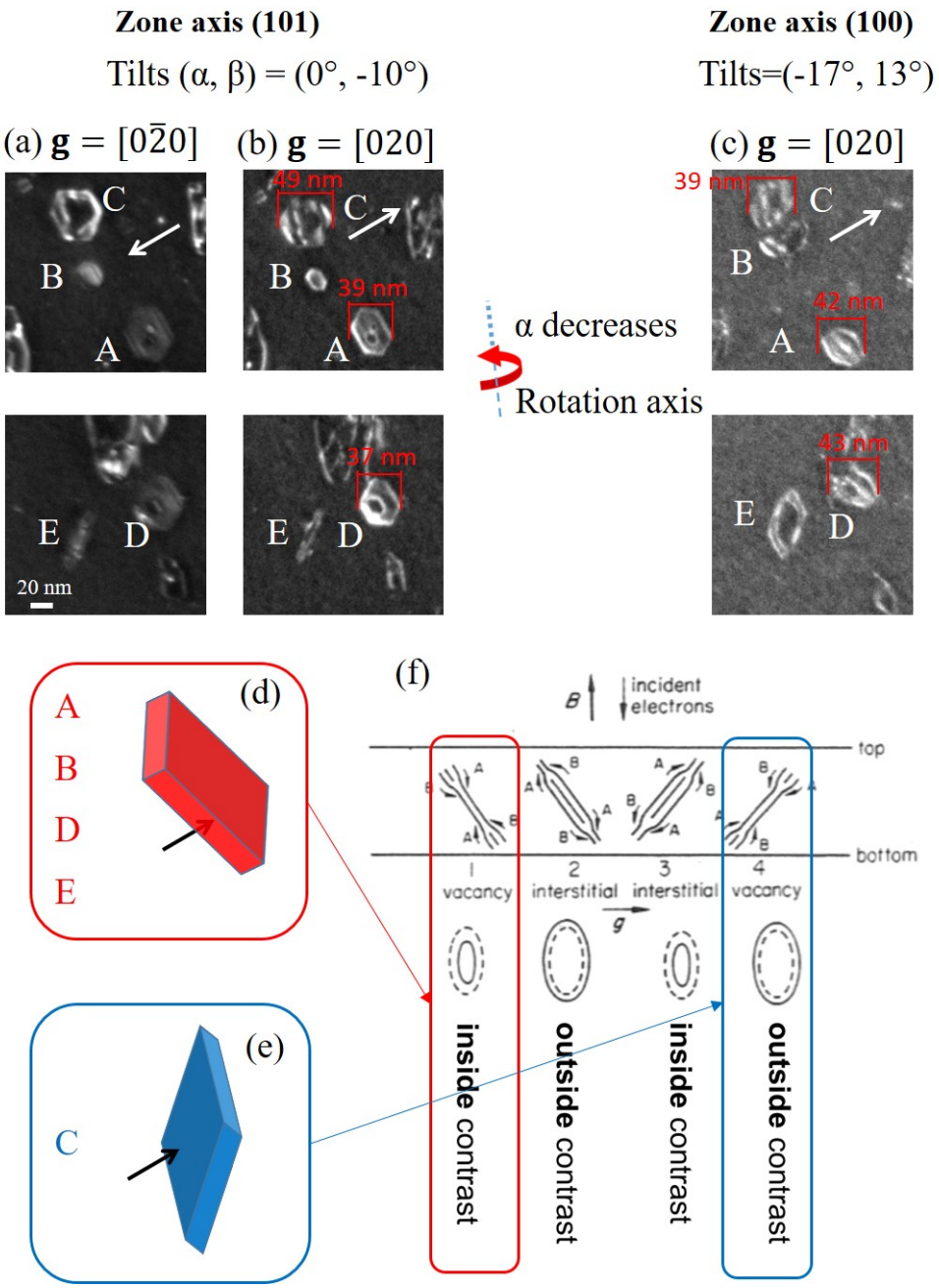

Figure 5.2 Determination of Frank loop nature in thin foil Ni-0.4Cr irradiated 450°C to 0.7 dpa: WBDF TEM images showing contrast of loops A, B, C, D and E with diffraction vector (a) **g**=[0$\bar{2}$0] and (b) **g**=[020] along zone axis [101], and (c) **g**=[020] along zone axis [001] with the same scale bar in (a); loop inclination from stereo images with **g**=[020] in (d) for loops A, B, D, E in (e) for C; (f) determination of loops nature in function of their inclination and inside-outside contrast.

5.1.1.2 Frank loops in thin-foil Ni-0.4Ti

Figure 5.3(a-e) shows Frank loops in Ni-0.4Ti with corresponding Kikuchi map indicating the crystal orientation. In Figure 5.3(f), loops A, B and C have a Burgers vector respectively of $\mathbf{b}=\pm[1\bar{1}1]$, $\pm[11\bar{1}]$ and $\pm[\bar{1}11]$. All these loops are found to be of interstitial-type by the inside-outside method in Figure 5.3(g). Loop A is a multiple loop and the inner loop is of the same Burgers vector as the outer loop. The stacking fault in the inner loop is clearly visible, which is different from the ones in Ni and Ni-0.4Cr.

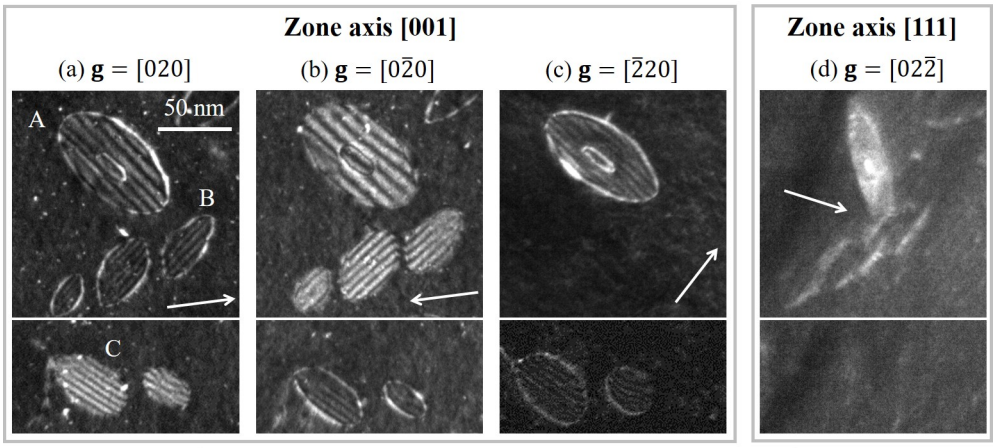

(e)

Table of visibility (V= visible, I= invisible)	Zone axes	[001]		[111]	Loop
	g / Possible b	020	$\bar{2}$20	02$\bar{2}$	/
	$\pm\frac{1}{3}[111]$	V	I	I	
	$\pm\frac{1}{3}[\bar{1}11]$	V	V	I	C
	$\pm\frac{1}{3}[1\bar{1}1]$	V	V	V	A
	$\pm\frac{1}{3}[11\bar{1}]$	V	I	V	B

(f)

Loops	Loop	Contrast of loops: b direction	g = [020]	−g = [0$\bar{2}$0]	g · b for g	b	Nature
A	Outer	$[1\bar{1}1]$	inside	outside	<0	$a_0/3\,[1\bar{1}1]$	interstitial
	Inner	$[1\bar{1}1]$	inside	outside	<0	$a_0/3\,[1\bar{1}1]$	interstitial
B	/	$[11\bar{1}]$	inside	outside	<0	$a_0/3\,[\bar{1}\bar{1}1]$	interstitial
C	/	$[\bar{1}11]$	outside	inside	>0	$a_0/3\,[\bar{1}11]$	interstitial

Figure 5.3 Determination of Frank loop nature in thin foil Ni-0.4Ti irradiated 450°C to 0.7 dpa: (a-d) WBDF TEM images showing visibility and inside-outside behavior of loop A, B and C with diffraction vector **g** indicated by arrows and with the same scale bar in (a); (e) table of visibility for studied loops; (f) determination of Frank loop nature by inside-outside method.

5.1.2 Influence of 0.4% solute addition on Frank loop nature in bulk samples irradiated at 450°C

In this part, alloys on bulk samples are characterized. The depth distribution of radiation damage, morphology of Frank loops and the determination of their nature are presented for each material.

5.1.2.1 Frank loop nature in bulk Ni-0.4Cr

In Ni-0.4Cr, the irradiated microstructure is dominated by dislocation loops with some voids. The damage zone extends to a depth of 2.2 µm and can be divided into:

- Very close to the surface (0-0.2 µm), the density of dislocation lines/loops is very low and no void is detected.
- In deeper zones (0.2-2.2 µm), segmented Frank loops, non-segmented Frank loops and voids coexist in the microstructure as shown in Figure 4.4(b) and Figure 4.4(c). Majority of voids are small (10 nm). Few large voids (50 nm) are cubic in zone axis <001> voids.

The depth distribution of average loop size, loop density and line density is presented in Figure 4.4(e). The depth distribution of average size and density of voids is plotted in Figure 4.4(f).

From previous observations (Section 5.1.1.1 and Section 5.1.1.2), different morphology of Frank loops suggests different nature of these Frank loops. The nature of Frank loops is then determined. We determine firstly the nature of non-segmented loops. Figure 5.5(a-e) shows the analysis of two representative non-segmented Frank loop A and B at two different depths. The Burgers vector of loop A and B are respectively $\pm 1/3[111]$ and $\pm 1/3[\bar{1}11]$. Inside-outside analysis in Figure 5.5(i) results that the Burgers vectors of A and B are respectively $1/3[111]$ and $1/3[\bar{1}11]$. They are thus both interstitial-type. The inner loop in loop A has the same vector de Burgers and nature as A so also interstitial-type. Loop A is thus a multi-layer extrinsic Frank loop.

Three segmented Frank loops (A, B and D) at depth between 300-600 nm are shown in Figure 5.6(a-i). Stereo-imaging is used to determine their nature. The diffraction conditions are presented in Figure 5.6(j). The determination of nature by stereo analysis leads to vacancy-nature for all these segmented loops. Meanwhile, by the same method, the non-segmented Frank loop C is found as interstitial-type, which confirms the previous determination for non-segmented loops. In conclusion, the morphology of Frank loops reveals their nature. Segmented Frank loops are vacancy-type and non-segmented loops are interstitial-type.

Segmented Frank loops are detected at depth between 300-600 nm while non-segmented Frank loops are distributed at all depths. The proportion of vacancy Frank loops is investigated

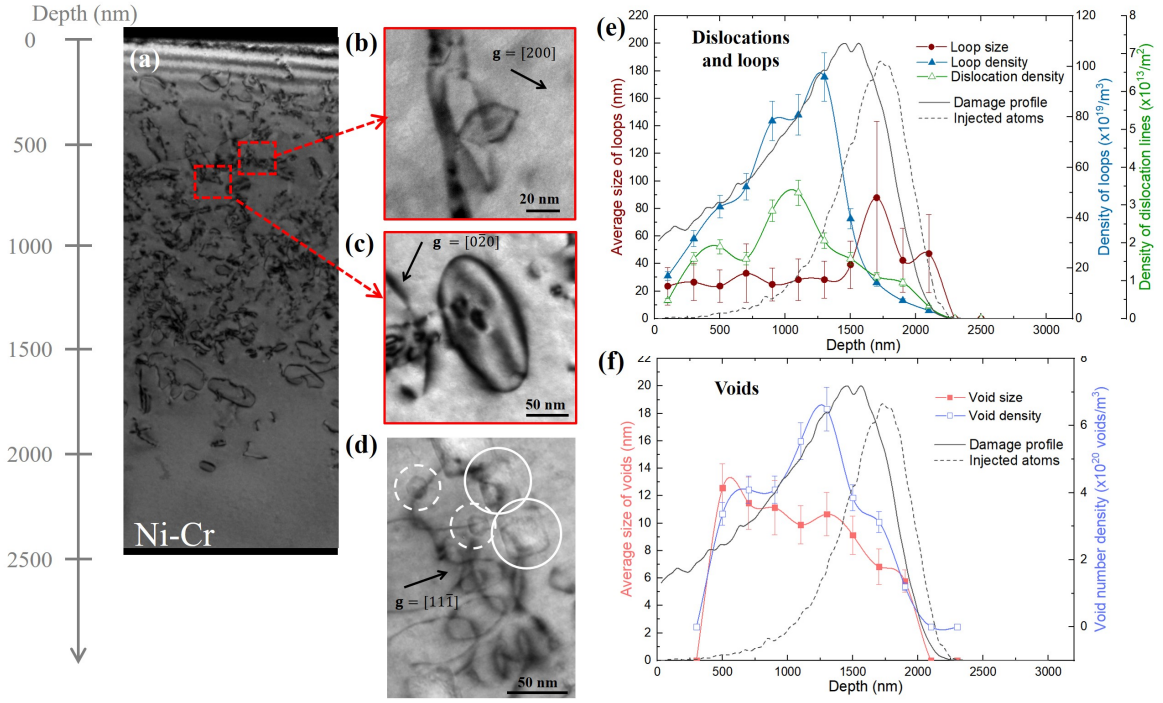

Figure 5.4 General microstructure in Ni-0.4Cr sample irradiated up to 2.3x10^{15} ions.cm^{-2} at 450°C. (a) Low magnification TEM micrograph showing the global microstructure; (b) a segmented Frank loop in the zone relatively close to the surface with diffraction vector **g** indicated by a black arrow; (c) non-segmented Frank loops representing majority of Frank loops at all depths; (d) image under-focus of two types of voids; (e) depth-dependency of the average size and density of loops as well as the density of dislocation lines; (f) depth-dependency of the average size and density of voids.

in function of depth. Figure 5.4(a) shows a zone relatively near the surface with three segmented Frank loops indicated by red dashed circles. In this zone, there is also a large non-segmented Frank loop in yellow dotted circle. Two other Frank loops in blue circles are in edge-on positions and it is difficult to distinguish their form. We studied two other zones at depth between 300-600 nm. The total number of observed Frank loops is 13. 9 of them are segmented so vacancy-type. Three of them are near edge-on position so difficult to tell their morphology. But these edge-on Frank loops are small (blue circles in Figure 5.7(a)). Based on their size, they are probable vacancy-type. Only one loop shown in Figure 5.4(a) is non-segmented. The statistic could be improved by studying more zones but we assume here that the majority (12/13) of Frank loops in near surface zones are segmented. In deeper zones (0.6-2.2 µm), the majority of Frank loops are non-segmented as shown in Figure 5.7(b) and Figure 5.7(c). Small Frank loops are also found in deeper zones but it is difficult to distinguish their form.

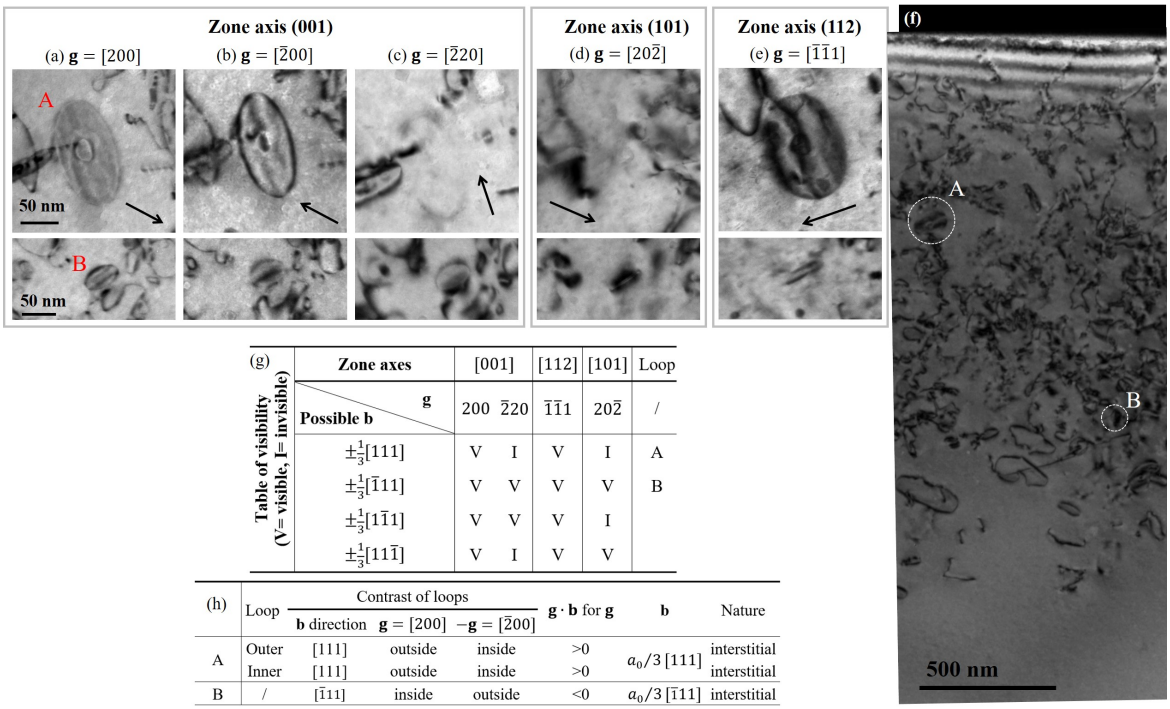

(g) Table of visibility (V= visible, I= invisible)

Zone axes	[001]		[112]	[101]	Loop
Possible b \ g	200	$\bar{2}$20	$\bar{1}\bar{1}$1	20$\bar{2}$	/
$\pm\frac{1}{3}$[111]	V	I	V	I	A
$\pm\frac{1}{3}$[$\bar{1}$11]	V	V	V	V	B
$\pm\frac{1}{3}$[1$\bar{1}$1]	V	V	V	I	
$\pm\frac{1}{3}$[11$\bar{1}$]	V	I	V	V	

(h)

Loop	Contrast of loops: **b** direction	**g** = [200]	−**g** = [$\bar{2}$00]	**g**·**b** for **g**	**b**	Nature
A	Outer	[111]	outside	inside	>0	$a_0/3$ [111]	interstitial
	Inner	[111]	outside	inside	>0		interstitial
B	/	[$\bar{1}$11]	inside	outside	<0	$a_0/3$ [$\bar{1}$11]	interstitial

Figure 5.5 Determination of the nature of two non-segmented Frank loops in Ni-0.4Cr sample irradiated at 450°C: (a-e) Bright-field TEM images under ten two-beam conditions along different zone axis with scale bar for all images indicated in (a); (f) general microstructure of the bulk specimen showing the depth of two Frank loops in (a); (g) table of visibility for both outer and inner loops based on **g**.**b** value; (h) table of determination of loop nature.

It is interesting to note that the observed segmented Frank loops are relatively small compared to non-segmented Frank loops. The maximum size of segmented Frank loops is about 35 nm taking the longest axis while non-segmented loops can be larger than 100 nm.

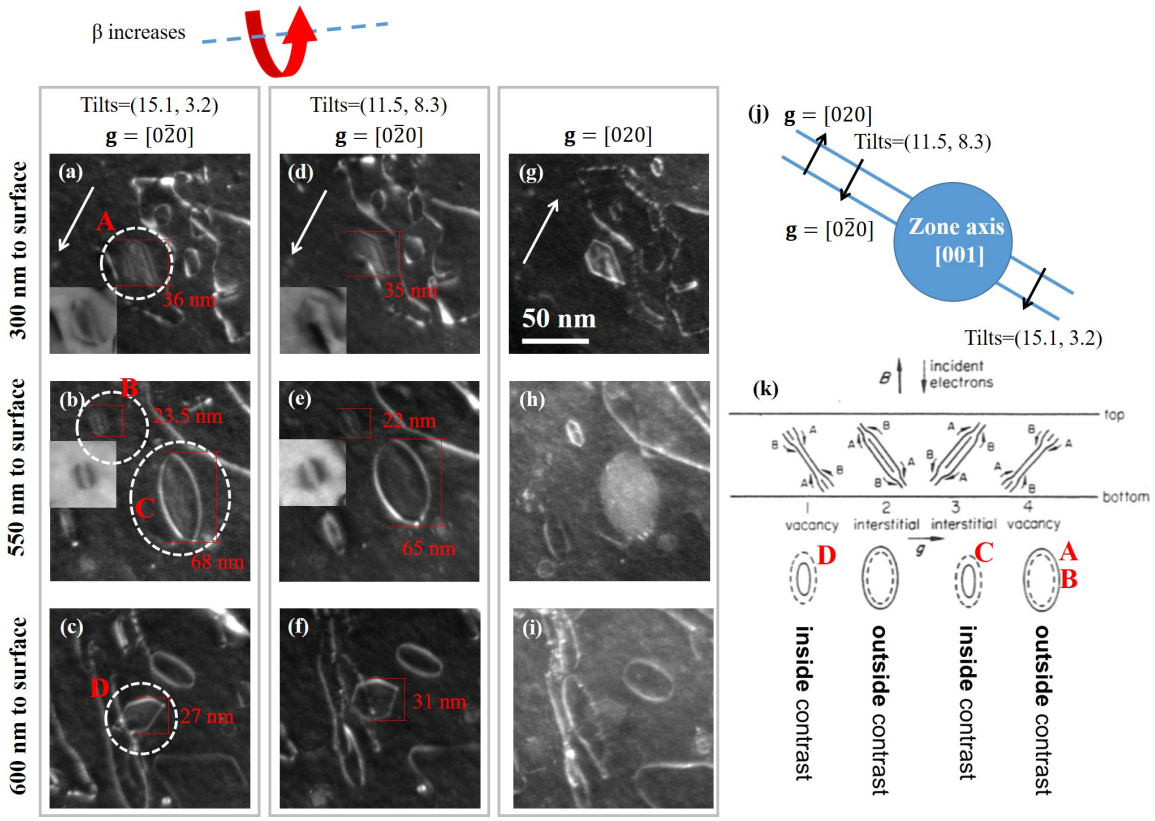

Figure 5.6 Determination of the nature of Frank loops near the surface in Ni-0.4Cr sample irradiated at 450°C: (a-i) WBDF TEM images showing contrast of loops A, B, C and D with diffraction vector **g** indicated by arrows along respectively zone axis [001] using the same scale bar in (g); (j) Kikuchi line indicating diffraction conditions of stereo imaging at different tilts; (k) determination of loops nature in function of their inclination and inside-outside behavior.

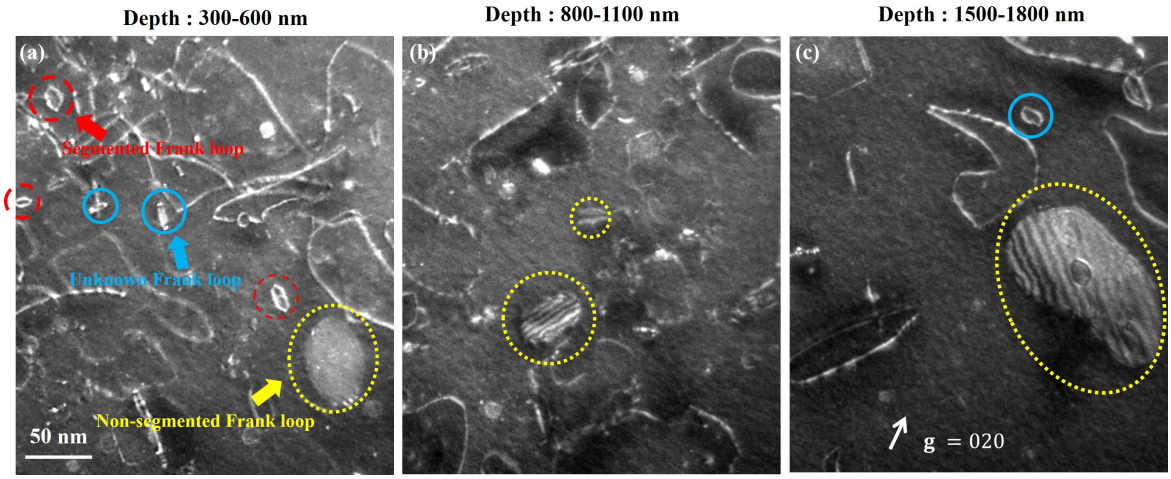

Figure 5.7 Frank loops in function of depth in Ni-0.4Cr sample irradiated up to 2.3x10^{15} ions.cm^{-2} at 450°C : at depth of (a) 300-600 nm; (b) 800-1100 nm; (c) 1500-1800 nm; WBDF images taken along zone axis [001] with diffraction vector g=020 for (g, 3g). Red dashed circles indicating segmented Frank loops, yellow dotted circles indicating non-segmented Frank loops, blue circles indicating edge-on Frank loops which can not be distinguished.

5.1.2.2 Frank loop nature in bulk Ni-0.4Ti

The depth distribution of defects in Ni-0.4Ti is presented in Figure 5.8(a). The microstructure is dominated by a dislocation network along with dislocation loops (Figure 5.8(b)) and voids (Figure 5.8(c)). The damaged zone extends to 1.8 µm depth. For all depths, No large Frank loop is observed, which differs from the observations in thin foil Ni-0.4Ti and bulk Ni-0.4Cr. However, large non-segmented perfect loops as shown in Figure 5.8(b) exist and they are likely formed from the unfaulting process of non-segmented Frank loops. Meanwhile, some Frank loops are detected. Near surface (depth between 0-300 nm), some Frank loops are found segmented (Figure 5.8(b)) while in deeper zones it is difficult to confirm the morphology (such as Figure 5.8(d) and Figure 5.8(e))

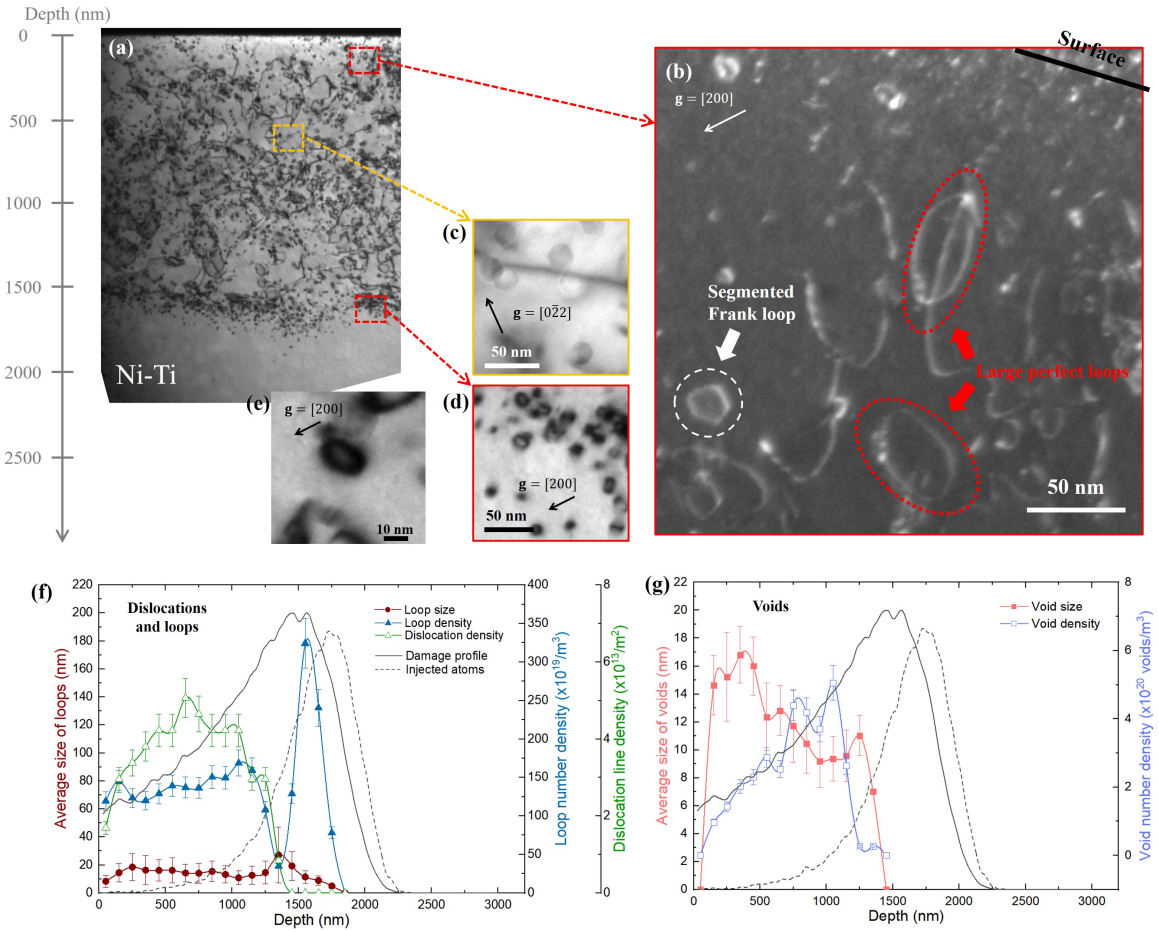

Figure 5.8 General microstructure in the bulk Ni-0.4Ti irradiated up to 2.3x10^{15} ions.cm^{-2} at 450°C. (a) Low magnification TEM micrograph showing the global microstructure; (b) WBDF TEM image showing dislocation loops near the surface with diffraction vectors **g** indicated by black arrows; (c) image over-focus of voids; (d) and (e) dislocation loops in deeper zones; (f) depth-dependency of the average size and density of loops as well as the density of dislocation lines; (g) depth-dependency of the average size and density of voids.

Figure 5.9 presents the determination of three loops using stereo technique. Figure 5.9(a-f) show the inside-outside behavior of these loops. All these loops have an inside contrast with **g**=[200]. Figure 5.9(d-f) and Figure 5.9(d-f) are images before and after tilting keeping the same diffraction conditions (**g**). The rotation direction is indicated by the red arrow. From the variation of loop size, the inclination of loops is deduced and presented in Figure 5.9(j). Finally from the table in Figure 5.9(l), the segmented Frank loop A is a vacancy-type while two perfect loops are interstitial-type.

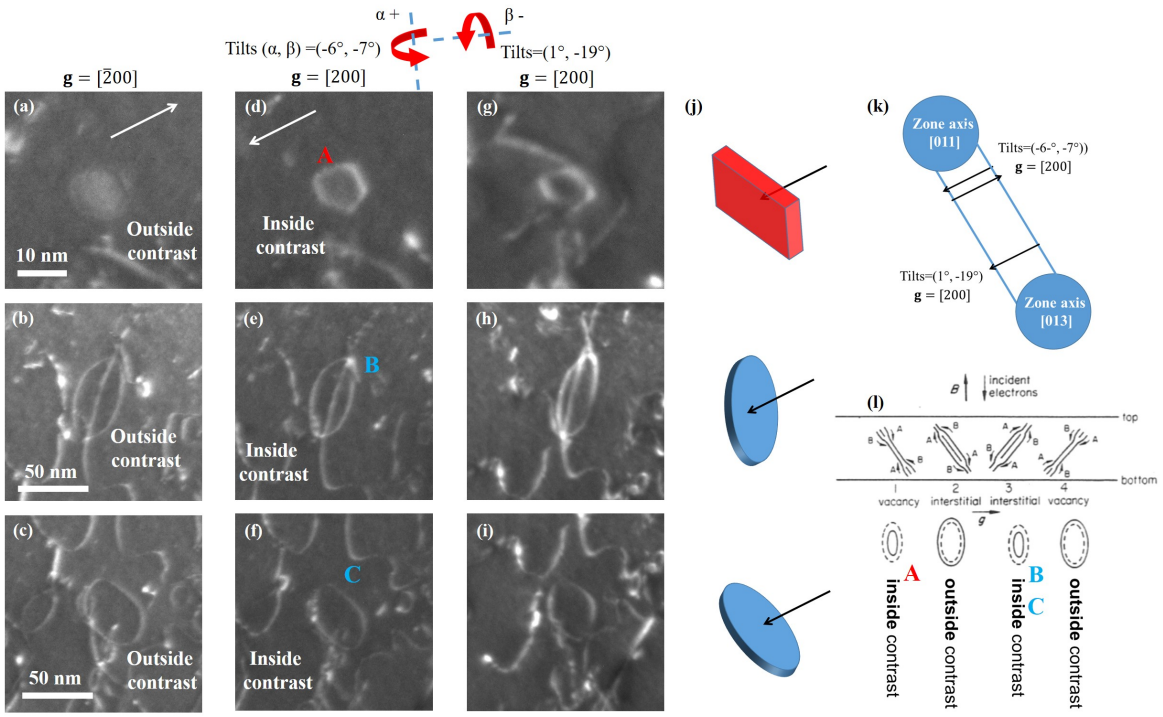

Figure 5.9 General microstructure in the bulk sample of Ni-0.4Ti irradiated up to 2.3x10^{15} ions.cm^{-2} at 450°C. (a) Low magnitude TEM micrograph showing the global microstructure; (b) WBDF TEM image showing dislocation loops near the surface with diffraction vectors **g** indicated by black arrows; (c) image over-focus of voids; (d) and (e) dislocation loops in deeper zones; (f) depth-dependency of the average size and density of loops as well as the density of dislocation lines; (g) depth-dependency of the average size and density of voids.

5.1.3 Influence of temperature on Frank loop nature in the alloys (Ni-0.4Cr and Ni-0.4Ti)

This part aims to study the influence of temperature on Frank loop nature. Irradiations are performed at a higher temperature 510°C. In the previous chapter, a relation between the morphology of Frank loops and their nature is identified: intrinsic (vacancy-type) Frank loops are segmented while extrinsic (interstitial-type) Frank loops are non-segmented. It

provides a very convenient way to determine the Frank loop nature. Here we use directly this criterion to determine the loop nature.

Figure 5.10(a) and Figure 5.10(b) show some Frank loops respectively in Ni-0.4Cr and Ni-0.4Ti. These loops are Frank loops because the contrast of the stacking fault is visible inside the loops. In Ni-0.4Cr, all Frank loops are clearly segmented and we assume that they are vacancy-type. In Ni-0.4Ti, loops are small and very dense. WBDF images show that two loops seems segmented. Non-segmented loops are not detected. To further confirm the nature of loops in Ni-0.4Ti, a thin foils was irradiated at a higher dose (0.18 dpa) in order to have larger loops. However, the loop size does not significantly change. Figure 5.11 shows the determination of loop nature in Ni-0.4Ti irradiated at 510°C to 0.18 dpa. It is very difficult to identify loops due the their changing visibility and relative position in function of used **g** and sample tilts. The analysis is performed on some loops which could be identified. All studied loops are found to be vacancy-type.

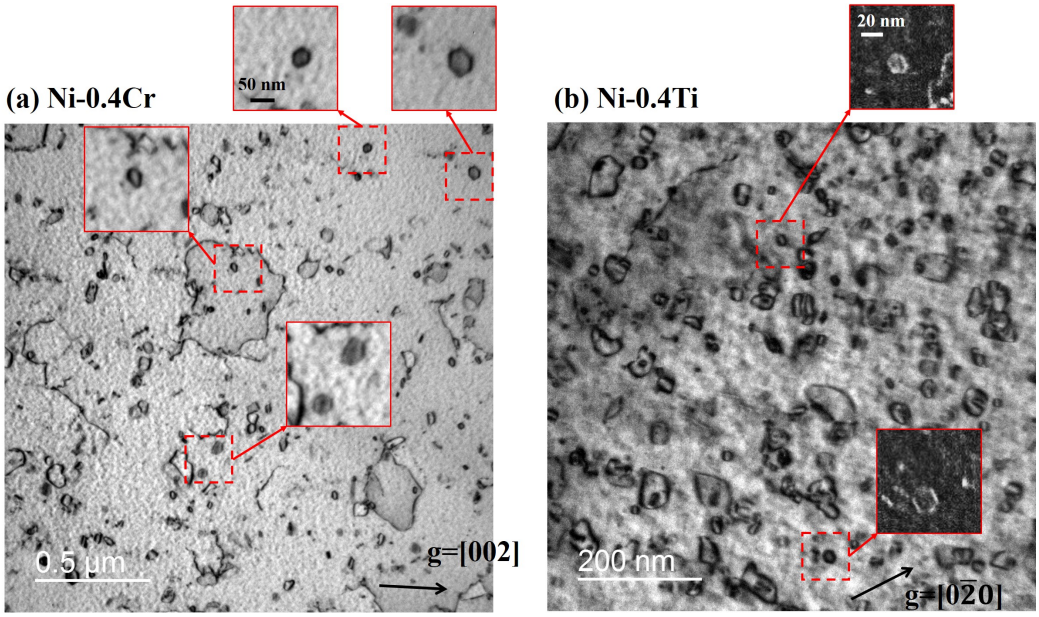

Figure 5.10 TEM micrographs presenting the morphology of Frank loops in (a) Ni-0.4Cr and (b) Ni-0.4Ti: (a) and (b) respectively taken along zone axis [110] and [101] for g=200 and 0$\bar{2}$0; enlargements of small loops in Ni-0.4Ti in WBDF mode for (g,3g)

.

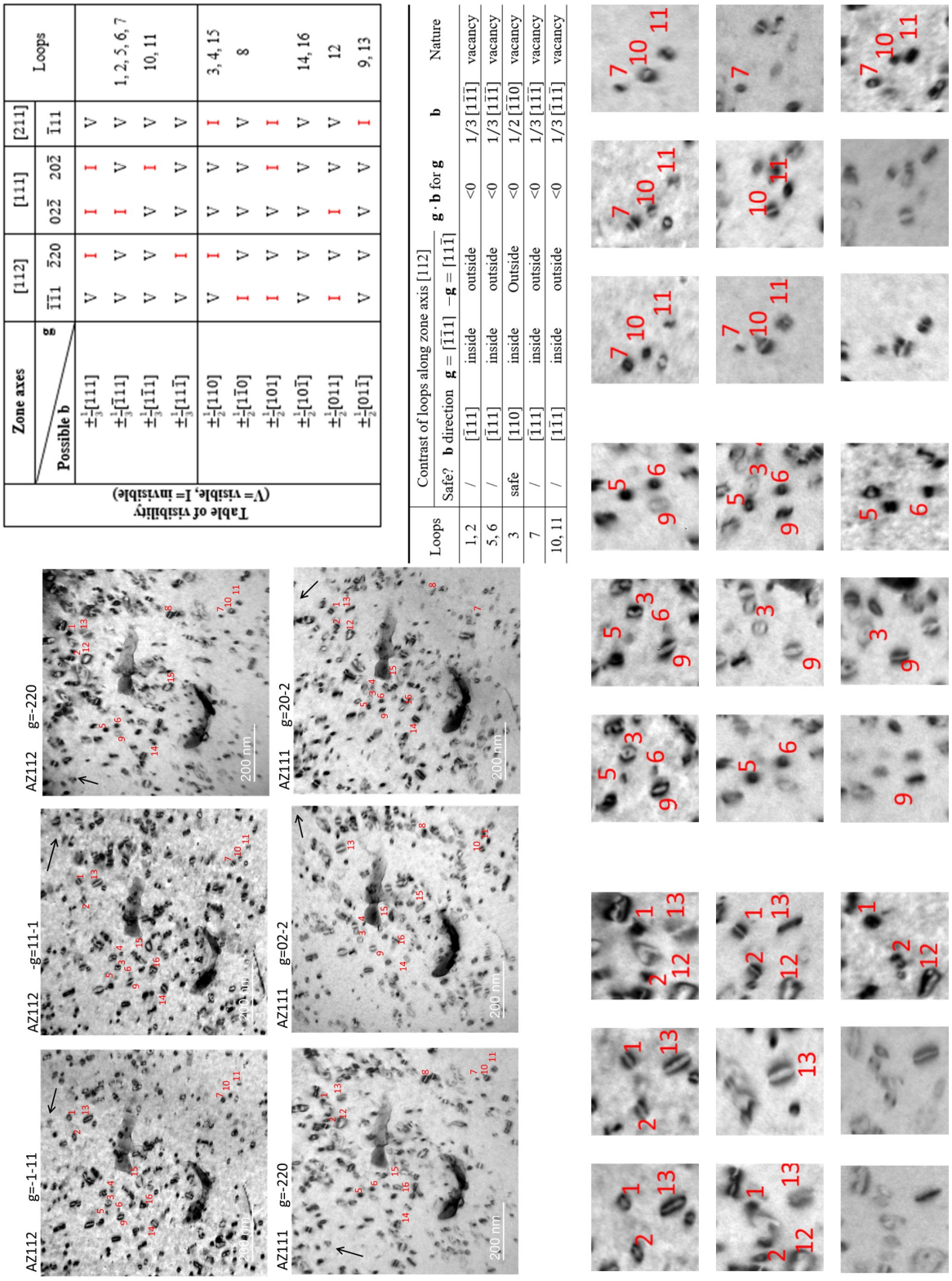

Table of visibility
(V= visible, I= invisible)

Zone axes		[112]		[111]		[211]	Loops
Possible **b**	**g**	$\bar{1}\bar{1}1$	$\bar{2}20$	$02\bar{2}$	$20\bar{2}$	$\bar{1}11$	
$\pm\frac{1}{3}[111]$		V	I	I	I	V	
$\pm\frac{1}{3}[\bar{1}11]$		V	V	I	V	V	1, 2, 5, 6, 7
$\pm\frac{1}{3}[1\bar{1}1]$		V	V	V	I	V	10, 11
$\pm\frac{1}{3}[11\bar{1}]$		V	I	V	V	V	
$\pm\frac{1}{2}[110]$		V	I	V	V	I	3, 4, 15
$\pm\frac{1}{2}[1\bar{1}0]$		I	V	V	V	V	8
$\pm\frac{1}{2}[101]$		I	V	V	I	I	
$\pm\frac{1}{2}[10\bar{1}]$		V	V	V	V	V	14, 16
$\pm\frac{1}{2}[011]$		I	V	I	V	V	12
$\pm\frac{1}{2}[01\bar{1}]$		V	V	V	V	I	9, 13

Loops	Contrast of loops along zone axis [112]				$\mathbf{g}\cdot\mathbf{b}$ for $\mathbf{g}$	$\mathbf{b}$	Nature
	Safe?	**b** direction	$\mathbf{g}=[\bar{1}\bar{1}1]$	$-\mathbf{g}=[11\bar{1}]$			
1, 2	/	$[\bar{1}11]$	inside	outside	<0	$1/3\,[1\bar{1}\bar{1}]$	vacancy
5, 6	/	$[\bar{1}11]$	inside	outside	<0	$1/3\,[1\bar{1}\bar{1}]$	vacancy
3	safe	$[1\bar{1}0]$	inside	Outside	<0	$1/2\,[\bar{1}10]$	vacancy
7	/	$[\bar{1}11]$	inside	outside	<0	$1/3\,[\bar{1}\bar{1}\bar{1}]$	vacancy
10, 11	/	$[\bar{1}\bar{1}1]$	inside	outside	<0	$1/3\,[\bar{1}11]$	vacancy

Figure 5.11 Nature loop Ni04Ti 0.18 dpa

Figure 5.12 summarizes the morphology and nature of Frank loops in the studied thin foil materials in function of solutes and temperatures. It is worth noting that the influence of 0.4%Ti addition is strong enough to change the nature of Frank loop at 450°C but not at 510°C. It is interesting to wonder whether there is a concentration of Ti which can induce the change of nature at 510°C.

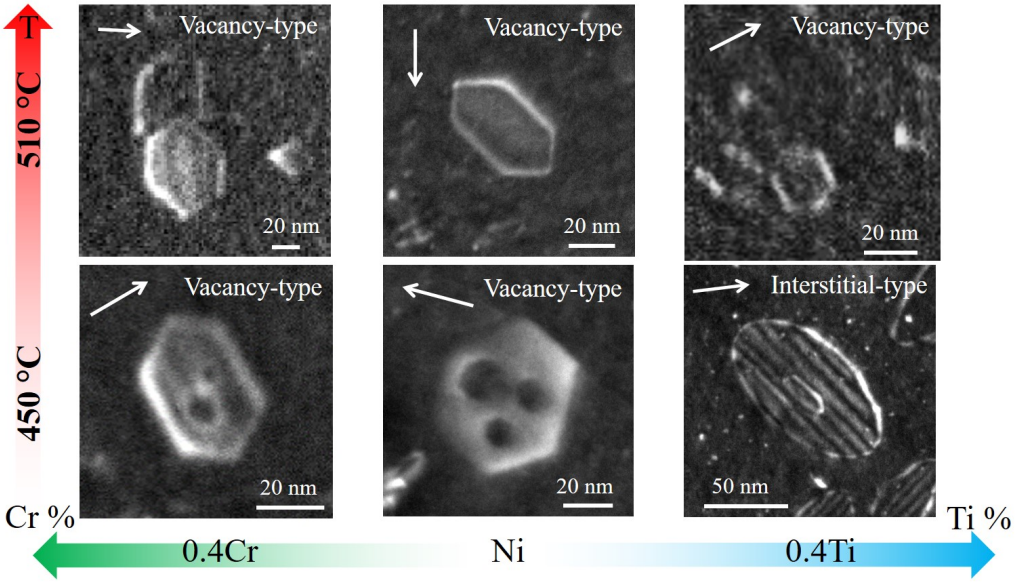

Figure 5.12 Summary of Frank loop nature in function of solute and temperature in thin foils.

5.1.4 Influence of Ti variation on Frank nature (Ni-0.8Ti and Ni-1.2Ti)

The analysis of Frank loop nature is performed in Ni-0.8Ti and Ni-1.2Ti at 0.06 dpa. All Frank loops detected are interstitial-type. Figure 5.13 present the complete analysis in Ni-0.8Ti in a 200 nm thick zone. Four families of Frank loops are detected and are identified as interstitial-type. Moreover, in thinner zones (100 nm), Frank loops with the same morphology are observed. Figure 5.14 shows that Frank loops in thin zones are also interstitial-type.

Frank loops in Ni-1.2Ti show the same morphology as the ones in Ni-0.8Ti (Figure 5.15(a) and Figure 5.15(b)) and they are also interstitial-type, also independent of the thickness.

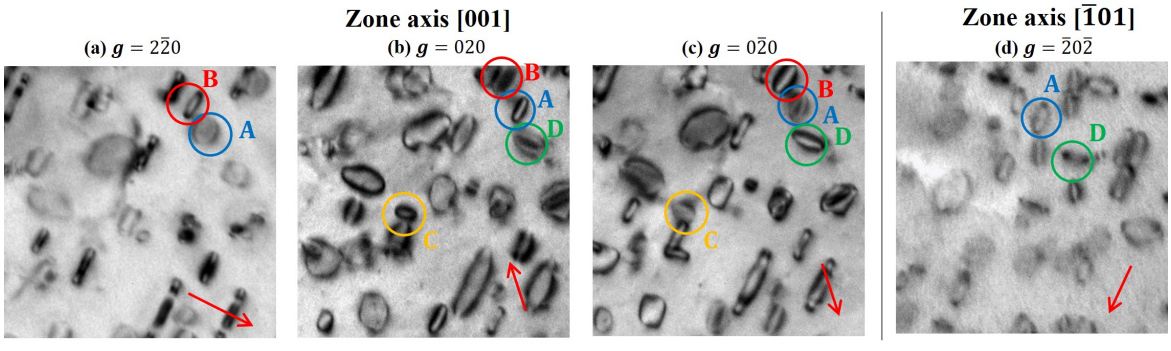

(e)

Loop	Contrast of loops along [001]			$\mathbf{g}\cdot\mathbf{b}$ for $\mathbf{g}$	$\mathbf{b}$	Nature
	$\mathbf{b}$ direction	$\mathbf{g}$ = [020]	$-\mathbf{g}$ = [0$\bar{2}$0]			
A	[1$\bar{1}$1]	inside	outside	>0	$a_0/3$ [1$\bar{1}$1]	interstitial
B	[$\bar{1}$11]	outside	inside	<0	$a_0/3$ [$\bar{1}$11]	interstitial
C	[11$\bar{1}$]	inside	outside	<0	$a_0/3$ [$\bar{1}\bar{1}$1]	interstitial
D	[111]	outside	inside	>0	$a_0/3$ [111]	interstitial

A: 1/3[1$\bar{1}$1]
B: 1/3[$\bar{1}$11]
C: 1/3[$\bar{1}\bar{1}$1]
D: 1/3[111]

Figure 5.13 Determination of Frank loop nature in Ni-0.8Ti irradiated to 0.06 dpa at 510°C in a 100 nm thick zone. (a-d) TEM images under two-beam conditions showing visibility and inside-outside behavior of loop A, B, C and D with diffraction vector **g** indicated by arrows and with the same scale bar in (a); (e) determination of Frank loop nature by inside-outside method (Jenkins, 1994).

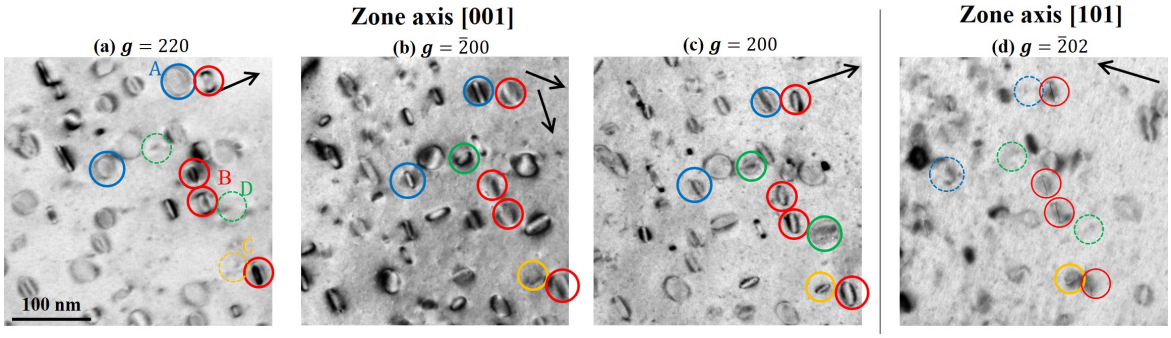

(e)

Loops	Contrast of loops along zone axis [001]			$\mathbf{g}\cdot\mathbf{b}$ for $\mathbf{g}$	$\mathbf{b}$	Nature
	$\mathbf{b}$ direction	$\mathbf{g}$ = [200]	$-\mathbf{g}$ = [$\bar{2}$00]			
A	[111]	outside	inside	>0	1/3 [111]	interstitial
B	[11$\bar{1}$]	inside	outside	<0	1/3 [$\bar{1}\bar{1}$1]	interstitial
C	[$\bar{1}$11]	outside	inside	>0	1/3 [$\bar{1}$11]	interstitial
D	[1$\bar{1}$1]	inside	outside	<0	1/3 [1$\bar{1}$1]	interstitial

A: 1/3[111]
B: 1/3[11$\bar{1}$]
C: 1/3[$\bar{1}$11]
D: 1/3[1$\bar{1}$1]

Figure 5.14 Determination of Frank loop nature in Ni-0.8Ti irradiated to 0.06 dpa at 510°C in a 100 nm thick zone. (a-d) TEM images under two-beam conditions showing visibility and inside-outside behavior of loop A, B, C and D with diffraction vector **g** indicated by arrows and with the same scale bar in (a); (e) determination of Frank loop nature by inside-outside method (Jenkins, 1994).

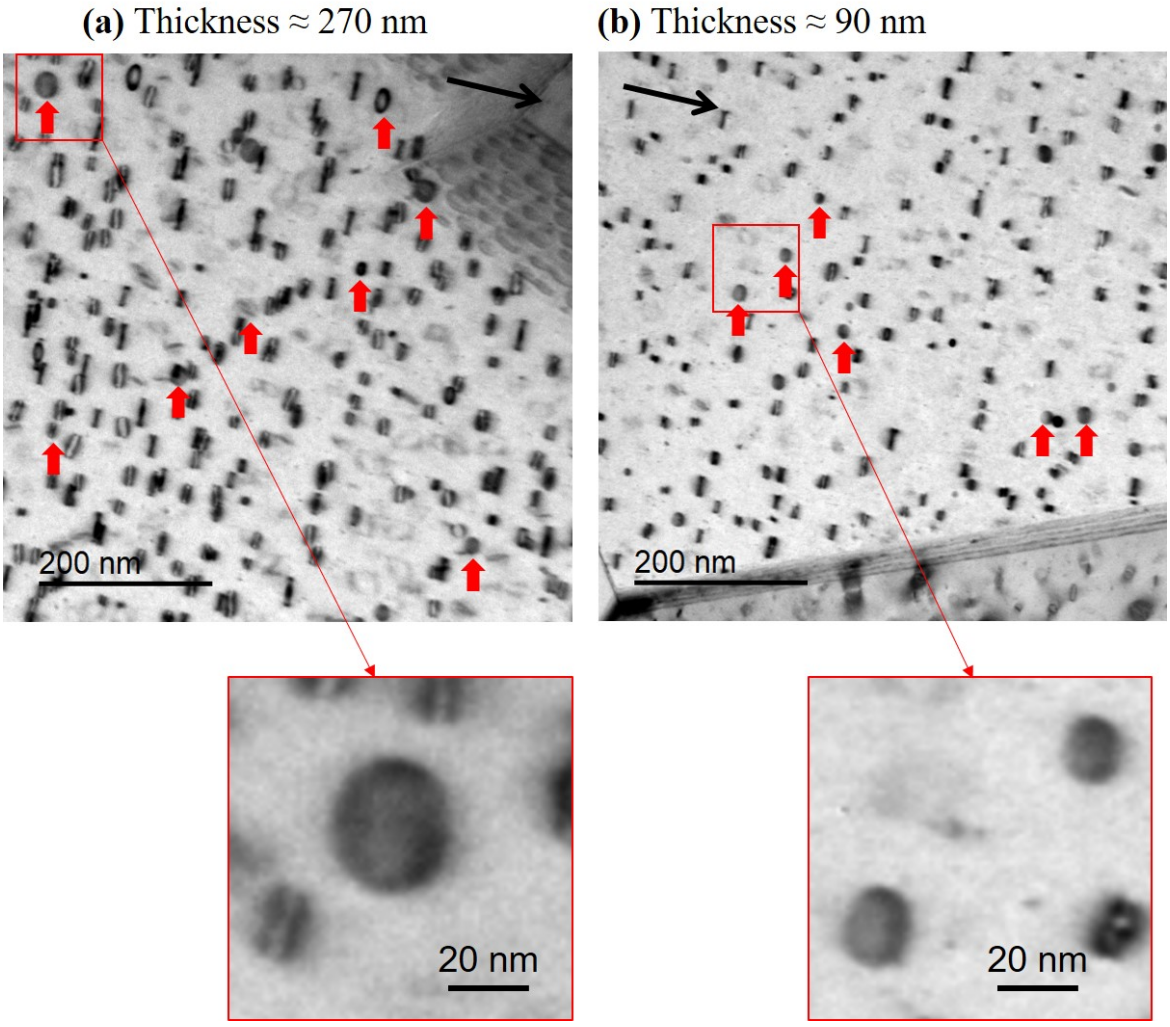

Figure 5.15 Frank loops in Ni-1.2Ti irradiated to 0.06 dpa at 510°C. Images showing the morphology of Frank loops at two thickness (a) 270 nm and (b) 90 nm; images taken along the zone axis [101] with g=$\bar{1}\bar{1}1$ indicated by black arrows.

5.2 Influence of solutes on microstructural evolution at 510°C

This section aims to study the influence of solute on in-situ microstructural evolution of Ni and the loop growth rate. First, we will focus on the effects of an addition of 0.4Cr or 0.4Tiwt.% on the microstructural evolution of Ni. Second, we will study the influence of a progressive addition of Ti (0.4, 0.8, 1.2 Ti wt.%). The irradiation temperature is 510°C as the same nature (vacancy-type) of dislocation loops is observed in Ni, Ni-0.4Cr and Ni-0.4Ti at this temperature.

5.2.1 Influence of an addition of Cr and Ti on microstructural evolution at 510°C

The microstructural evolution at 510°C in 220 nm thick zones of Ni-0.4Cr and Ni-0.4Ti is studied and presented respectively in Figure 5.16(a) and Figure 5.16(b). This thickness is chosen because the microstructure should be independent from the thickness according to the results in Chapter 3. Figure 5.16(c-d) show respectively the evolution of loop number density and average loop size in function of irradiation duration t. During the irradiation in Ni-0.4Ti, the beginning of the video (<84s) is not in good diffraction condition. We can only study the microstructural evolution from 84s to the end of irradiation.

In Ni-0.4Cr, loop density and average size increase with the irradiation time and reach a maximum value at respectively 130 s and 180 s. From TEM micrographs, the saturation of loop size corresponds to the begin of the network formation. In Ni-0.4Ti, loop density increases to a maximum value about 200 s while the average size have not reached a maximum at the end of irradiation. In the TEM image at 214 s (almost the end of irradiation), loops are still small and individual. No dislocation network is formed. The curves of Ni at the thicknesses of 260 nm (Figure 5.16) are also plotted in order to study the influence of solutes. The saturation of microstructure (loop density and average size) is delayed by the addition of solutes. However, the role of Ti and Cr on both parameters is different:

- **Ni-0.4Cr**: The addition of Cr decreases the loop density compared to Ni. The average loop size is lower than the one in Ni in the early stages of irradiation but increases to a higher value in the end. The lower density in Ni-0.4Cr allows loops to grow up to a larger size before tangling into a network. If the irradiation were performed at a higher dose, the network would be more developed and the average size of loops may decrease like in Ni.
- **Ni-0.4Ti**: The addition of Ti on the contrary increases the density of loops but reduce quite strongly the loop size.

The average growth rate of loops in the alloys is presented in Figure 5.17. In Ni and Ni-0.4Cr, the average growth rate is determined before and after the steady state. It is worth

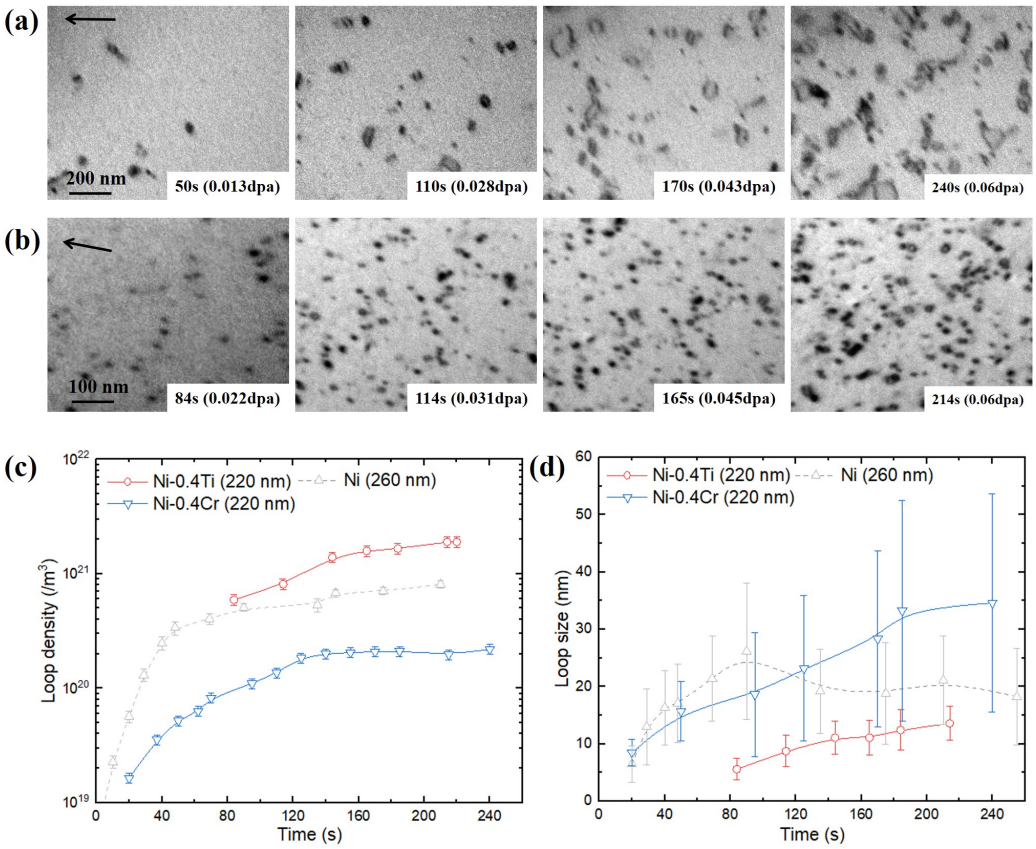

Figure 5.16 Microstructural evolution during in-situ irradiation as a function of irradiation thickness and dose at 510°C. (a-b) Selected micrographs illustrating the microstructure recorded under two-beam KBF conditions using (a) **g** = <200>, (b) **g** = <111> with the same scale bar for all micrographs indicated in the first micrograph. (c-d) Evolution of loop number density and average size in function of irradiation time.

to note that, in these two materials, loops grow fast at the beginning of the irradiation when there are few loops. When the loop density increases and stabilizes, the loop growth rate is slower. One explanation is that the increase of loops increases the number of sinks for PDs. With the same creation rate of PDs, the loop growth rate is therefore reduced.

In terms of the solute effects on loop growth rate:

- **Ni-0.4Cr**: The addition of Cr decreases the loop growth rate at the beginning of irradiation. However, in the steady-state microstructure, the growth is less reduced in Ni-0.4Cr than Ni. It is probably due to the fact that the density of loops and lines in Ni-0.4Cr is lower than the one in Ni.
- **Ni-0.4Ti**: The addition of Ti reduce significantly the loop growth rate.

Moreover, from the in-situ observations, the mobility of loops is reduced in the alloys. To evaluate this phenomenon, we measure the movement distance of loops in each material.

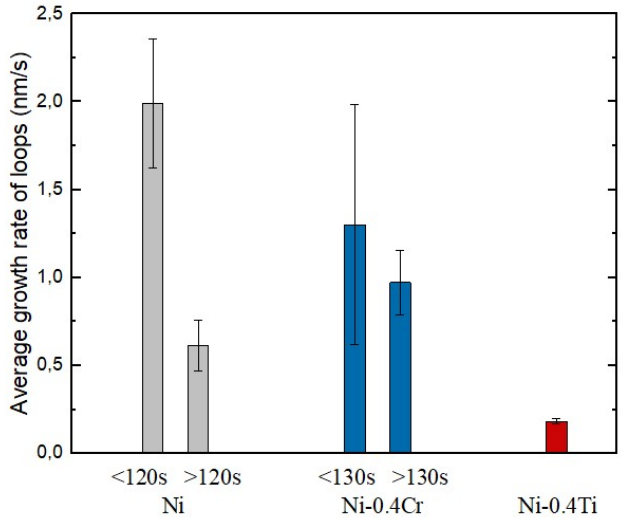

Figure 5.17 Average loop growth rate in Ni and its alloys at 510dC. In Ni and Ni-0.4Cr, loop growth rate is calculated before and after the saturation of loop density.

Figure 5.18(a) and Figure 5.18(b) present the typical movement distance of loops respectively in Ni-0.4Cr and Ni-0.4Ti. The movement is always along the <110> directions as presented in Ni. The distance in which a loop can glide depends clearly on the depth of the loop, its movement distance direction, likely the specimen thickness and the loop density. To obtain comparable data, we measured the average movement distance distance over tens of loops movement distance along different directions before the saturation of loop density in each materials. The influence of other dislocation loops could be minimized as the loop density is still low. The influence of the loop depth and the movement directions are expected to be neglected by calculating the average. Finally, the thickness of the studied zone in Ni (Figure 4.22) is 180 nm, less than 220 nm in Ni-0.4Cr and Ni-0.4Ti. It should lead to a lower movement distance in Ni if the loop mobility is the same for all materials. Results with standard deviation are listed in Table 5.1. The movement distance in Ni is similar to the one in Ni-0.4Cr. However, considering the zone in Ni is thicker than Ni-0.4Cr, the loop mobility in Ni is slightly higher than the one in Ni-0.4Cr. In Ni-0.4Ti, the movement distance is significantly reduced.

Table 5.1 Average movement distance of dislocation loops in Ni, Ni-0.4Cr and Ni-0.4Ti.

Materials	Ni	Ni-0.4Cr	Ni-0.4Ti
Movement distance (nm)	108 ± 39	80 ± 22	18 ± 5

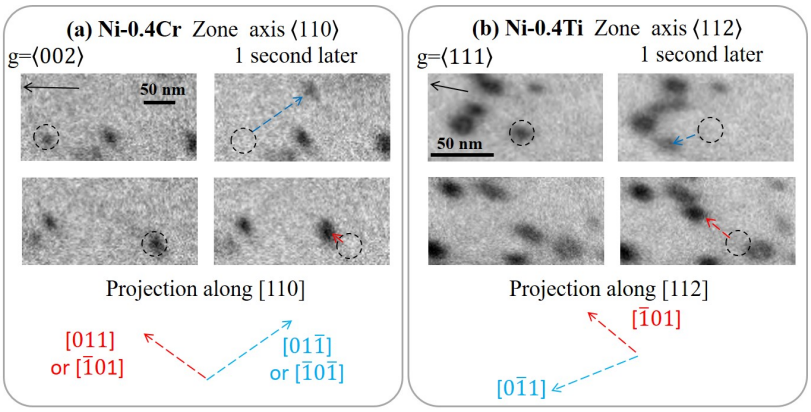

Figure 5.18 Movement of dislocation loops during in-situ irradiations in (a) Ni-0.4Cr and (b) Ni-0.4Ti irradiated at 510°C: movement direction is indicated by blue and red arrows; Projection along the corresponded zone axis showing that the movement directions are <110>; the thickness of the two zones is about 220 nm.

5.2.2 Influence of Ti variation on microstructural evolution at 510°C

Ni-0.8Ti and Ni-1.2Ti are irradiated at 510°C up to 0.18 dpa. During the irradiation, the loop density is too high to distinguish individual defects at 200 nm thickness. Therefore, a lower thickness (120 nm) is chosen to record the microstructural evolution in these higher Ti content alloys. Figure 5.19(a) and Figure 5.19(b) present the microstructural evolution at 120 nm thickness in respectively Ni-0.8Ti and Ni-1.2Ti. Figure 5.19(c) and Figure 5.19(d) show the evolution of loop density and average loop size in both alloys. The curves of Ni and Ni-0.4Ti irradiated at 510°C to 0.06 and 0.18 dpa (Figure 5.16) are also plotted.

In the first phase of irradiation (0-0.06 dpa), the loop density in Ni-0.8Ti and Ni-1.2Ti increases sharply and quickly reach a steady-state. The loop density at the steady state increases with the Ti content. This saturation of loop density in Ni-0.8Ti and Ni-1.2Ti does not result from the formation of a dislocation network like the one in Ni. The saturation of loop density in Ni-Ti alloys is an equilibrium of loop creation and absorption. Meanwhile, the average loop size in Ni-0.8Ti and Ni-1.2Ti continuously increases.

In the second phase of irradiation (0.06-0.18 dpa), the loop density in Ni-0.8Ti and Ni-1.2Ti starts to decrease after 300s. It should be attributed to the agglomeration of large loops. The loop density in the three Ni-Ti alloys finally converge to a similar value at 0.18 dpa. However, loops in Ni-0.8Ti and Ni-1.2Ti are almost immobile and few large loops dissociate into dislocation lines. Even at 0.18 dpa, no dislocation network is formed in Ni-0.8Ti and Ni-1.2Ti. The average loop size thus continuously increases. However in Ni-0.4Ti, the average loop size reach a saturation level at 0.06 dpa and remains the same until the end. The final average loop size is higher for Ni-0.8Ti and Ni-1.2Ti than for Ni-0.4Ti. One reason could be that the average size in Ni-0.8Ti and Ni-1.2Ti seem very similar. On one hand it is because

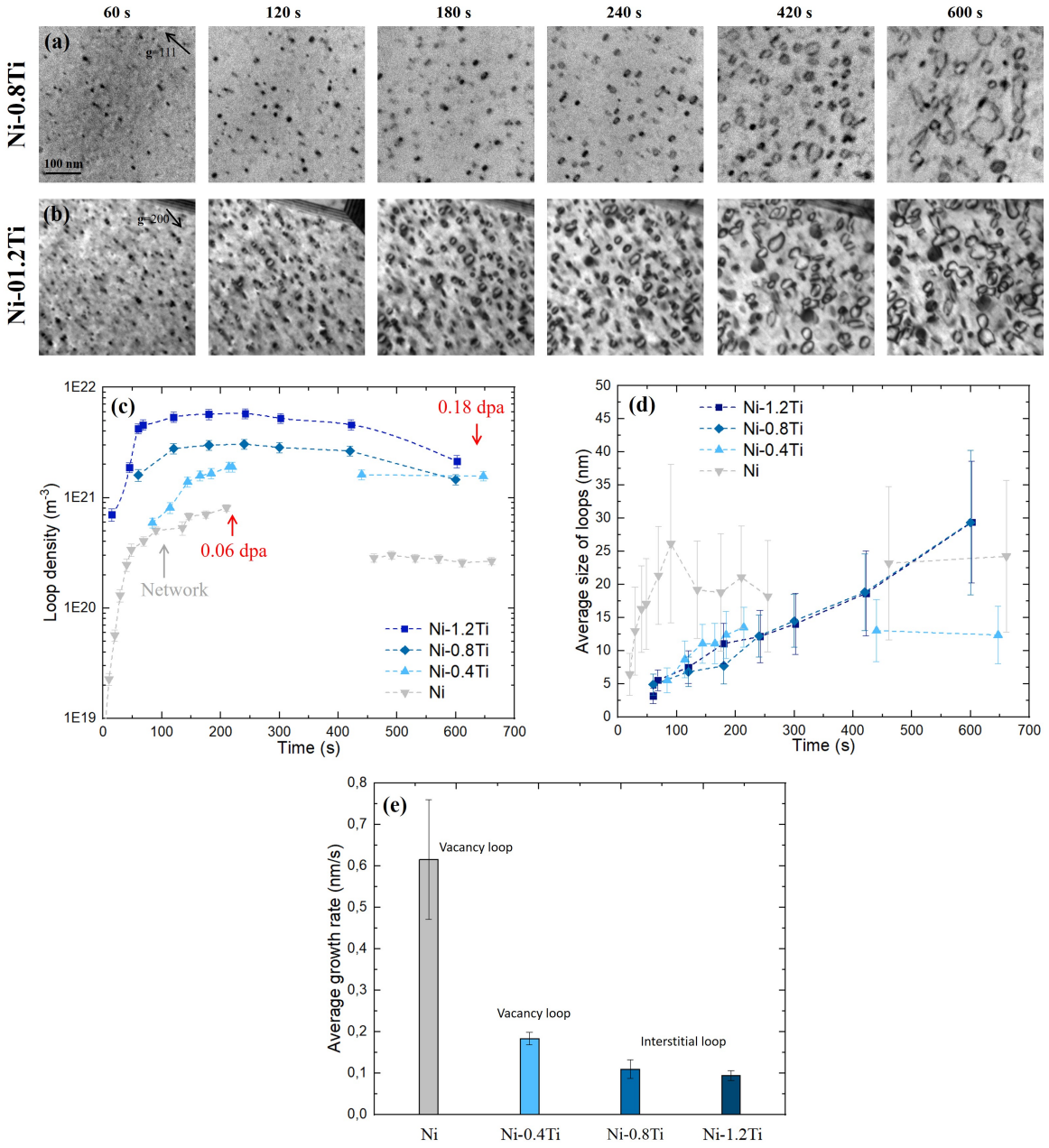

Figure 5.19 Microstructural evolution during in-situ irradiation in Ni-0.8Ti and Ni-1.2Ti in function of time at 510°C. Selected micrographs illustrating the microstructure were recorded under two-beam KBF conditions in (a) Ni-0.8Ti using **g** = <111> and (b) Ni-0.8Ti using (a) **g** = <200> along zone axis <110>; evolution of (c) loop density and (d) average size in function of irradiation time; (e) average loop growth rate in each alloys. The thickness in Ni-0.8Ti and Ni-1.2Ti is about 120 nm.

the growth of loops in both alloys is very slow, which makes the difference small. A second one could be that the loop size depends on the used **g**. In Ni-0.8Ti, **g**=<111> induces usually

a fine contrast while in Ni-1.2Ti **g**=<200> induces a larger contrast. This will make the size difference between the two alloys even smaller and cause an uncertainty to distinguish such a small difference.

The average loop growth rate is determined in both alloys and presented in Figure 5.19(e). The loop growth rates in Ni-0.8Ti and Ni-1.2Ti are lower than the ones in Ni and Ni-0.4Ti. As presented above, it is difficult to really differentiate the loop growth rate between Ni-0.8Ti and Ni-1.2Ti due to the different **g** used. However, the values of average size and growth rate in Ni-0.8Ti are still slightly higher than the ones in Ni-1.2Ti. It tends to suggest that the average loop growth rate decreases with the Ti content.

5.3 Influence of solutes on irradiated microstructure at 510°C

This section investigates firstly the irradiated microstructure (loop density, size and loop type) in Ni-0.4Cr and Ni-0.4Ti at 510°C to 0.06 dpa in order to reveal the influence of a solute addition. In the second part, the final microstructure of Ni-0.8Ti and Ni-1.2Ti is characterized to study the influence of Ti content.

5.3.1 Influence of an addition of solute on irradiated microstructure at 510°C

5.3.1.1 Loop size and density in function of thickness in Ni-0.4Cr and Ni-0.4Ti at 510°C

The final microstructure is characterized in Ni-0.4Cr and Ni-0.4Ti irradiated up to 0.06 dpa at 510°C. Loop average size and dislocation line density in function of thickness are presented in Figure 5.20(a):

- The profile of average loop size in Ni-0.4Cr is similar to the one in Ni but the critical thickness is higher (270 nm).
- The average loop size in Ni-0.4Ti is lower than the other two materials.

It seems that the average size of loops in all materials finally converge to a similar value. The addition of 0.4% solute may not change drastically the loop size in thick zones.

A stereo-imaging is conducted in Ni-0.4Ti and loop-depleted zones are also found with a thickness of about 40 nm like in Ni. We assume that in Ni-0.4Cr the same loop-depleted zones exist. The density of loops taking into account of loop depleted zones are plotted in Figure 5.20(b):

- The profile of loop density in Ni-0.4Cr is similar to the one in Ni but the critical thickness appears in a thicker zone (240 nm). The density of loops in Ni-0.4Cr is quite

lower than Ni. The saturation value in Ni-0.4Cr ($\approx$ 2.7x10^{20} m^{-2}) is about 4 times lower than the one in Ni ($\approx$ 1x10^{21} m^{-2}).

- The profile of loop density in Ni-0.4Ti increases sharply at 180 nm thickness and reaches quickly a high density. It is difficult to correctly measure the density in zones thicker than 250 nm due the superposition of loops. We believe that the density may stabilize to a value of 2.5x10^{21} m^{-2}, which is 2.5 times higher than the one in Ni. The critical size is not in the studied range but it is likely 240 nm.

Unlike the average size, the density of loops is strongly affected by the addition of Ti and Cr. Ti increases significantly the density of loops while Cr reduces it.

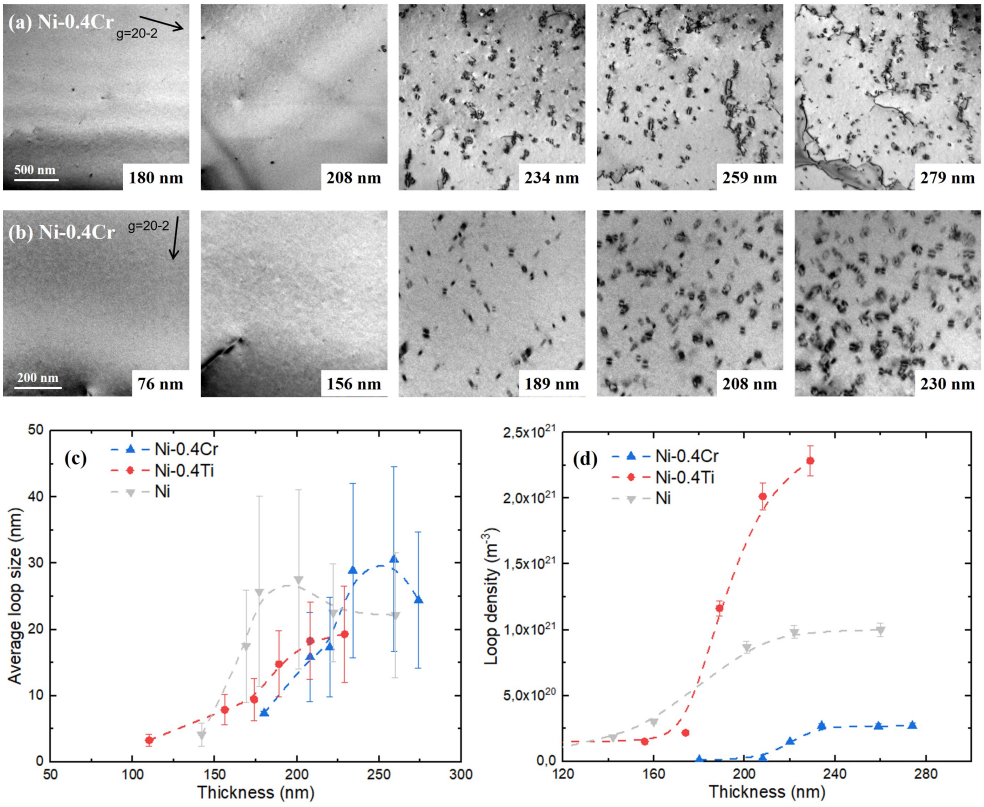

Figure 5.20 Loop size and density in function of thickness in Ni-0.4Cr and Ni-0.4Ti at 510°C to 0.06 dpa. The evolution of loop size and loop density is presented respectively in (c) and (d).

5.3.1.2 Loop type distribution in Ni-0.4Cr and Ni-0.4Ti at 510°C

The statistic method was presented in Section 4.2.2.1 and is applied in the two alloys to study the distribution of Burgers vector. Figure 5.21 presents the TEM micrographs of the same zone under different diffraction conditions with: (a) $\mathbf{g}=[1\bar{1}1]$ along the zone axis [121]; (b) $\mathbf{g}=[\bar{1}1\bar{1}]$, (c) $\mathbf{g}=[002]$, (d) $\mathbf{g}=[\bar{1}11]$ and (e) $\mathbf{g}=[\bar{2}20]$ along the zone axis [110];

$\mathbf{g}=[\bar{1}\bar{1}1]$ along the zone axis [101]. The density of loops in each image is measured and listed in Table 5.2. The same analysis is performed in Ni-0.4Ti thin foil using TEM micrographs shown in Figure 5.22. The diffraction conditions are: (a) $\mathbf{g}=[11\bar{1}]$, (b) $\mathbf{g}=[020]$, (c) $\mathbf{g}=[1\bar{1}\bar{1}]$ along the zone axis [101]; (d) $\mathbf{g}=[20\bar{2}]$, (e) $\mathbf{g}=[\bar{2}\bar{2}0]$, (f) $\mathbf{g}=[022]$ along the zone axis $[1\bar{1}1]$; (g) $\mathbf{g}=[002]$ along the zone axis [100]. The measured loop density are listed in Table 5.3.

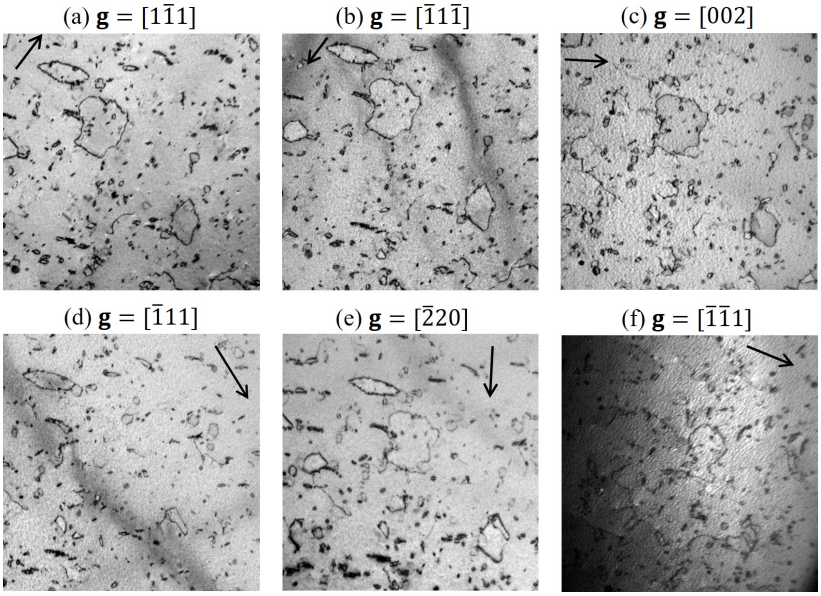

Figure 5.21 TEM micrographs showing the microstructure in the same zones in function of diffraction vectors **g** in a 250 nm thick zone of Ni-0.4Cr irradiated to 0.06 dpa at 510°C.

Table 5.2 Loop density in function of diffraction vectors in Ni-0.4Cr irradiated at 510°C to 0.06 dpa.

Zone axis	[121]	[110]				[011]
g investigated	$1\bar{1}1$	$\bar{1}1\bar{1}$	$\bar{1}11$	002	$\bar{2}20$	$\bar{1}\bar{1}1$
Loop density (10^{20} m^{-3})	2.76	2.73	2.67	3.03	2.34	2.81

Table 5.3 Loop density in function of diffraction vectors in Ni-0.4Ti irradiated at 510°C to 0.06 dpa.

Zone axis	[101]			[1$\bar{1}$1]			[001]
g investigated	$11\bar{1}$	020	$1\bar{1}\bar{1}$	$20\bar{2}$	$\bar{2}0\bar{2}$	022	002
Loop density (10^{21} m^{-3})	1.86	2.05	1.79	1.47	1.52	1.49	1.93

The proportion of each family is calculated and plotted in Figure 5.23(a) for Ni-0.4Cr and Figure 5.23(b) for Ni-0.4Ti. The distribution of Frank loops is equally probable in the alloys. The unequal distribution of perfect loops is less pronounced than the one in Ni. We

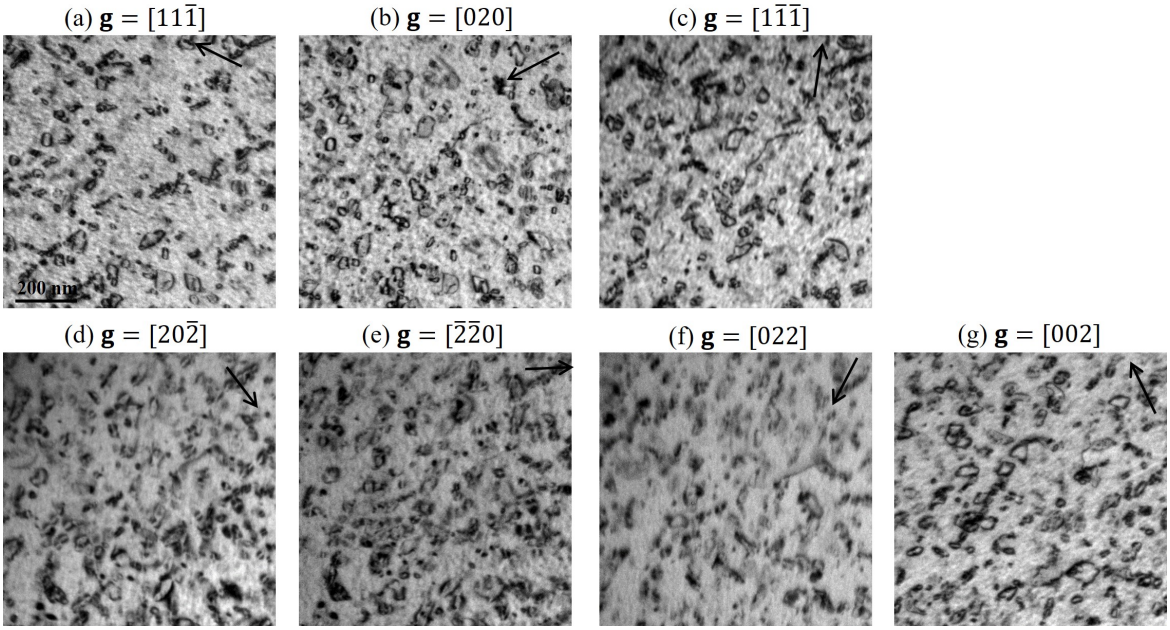

Figure 5.22 TEM micrographs showing the microstructure in the same zones in function of diffraction vectors **g** in a 200 nm thick zone of Ni-0.4Ti irradiated to 0.06 dpa at 510°C.

calculated the average proportion of one perfect loop family in each material: 7.7±4.6 % in Ni, 7.6±2.9% in Ni-0.4Cr and 7.5±2.6% in Ni-0.4Ti.

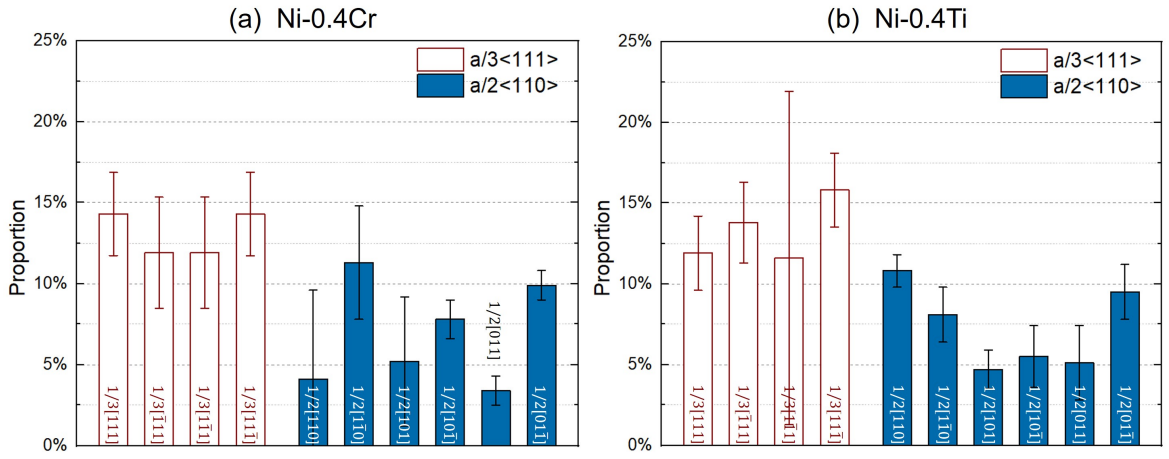

Figure 5.23 Proportion of each family of loops calculated by diving the density of each family by the total density in Ni-0.4Cr and Ni-0.4Ti irradiated at 510°C to 0.06 dpa. White bars for Frank loops and blue bars for perfect loops.

The total density of Frank loops and perfect loops and corresponding proportion in the alloys are calculated by summing up the subfamilies. The total density of perfect loops can be calculated by multiplying the highest family by six. The perfect loop density can thus be corrected taking into account of lost loops. Results are presented in Table 5.4. The

proportion of Ni is also listed. Before the correction, the proportion of Frank loops and perfect loops is almost the same in the three materials. After the correction, the proportion of perfect loops in Ni (63%) is clearly higher than the proportion in the alloys (55% in Ni-0.4Cr and 50 in Ni-0.4Ti). It suggests probably an influence of solute on the stacking fault energy.

Table 5.4 Loop density (10^{19} m^{-3}) in Ni-0.4Cr and Ni-0.4Ti taking into account of invisible loops by statistic method and correction of loop density taking into account loops absorbed by surfaces.

Materials	Loop type	Frank loops	perfect loops	Total
Ni-0.4Cr	Loop density	18.9 ± 2	15.6 ± 1	34.5 ± 3
	Proportion	55%	45%	
	Corrected density	18.9 ± 2	23.4 ± 3	42.3 ± 3
	Corrected proportion	45%	55%	
Ni-0.4Ti	Loop density	137 ± 13	97 ± 9	234 ± 16
	Proportion	59%	41%	
	Corrected density	137 ± 13	136 ± 13	273 ± 18
	Corrected proportion	50%	50%	
Ni	Proportion	46%	54%	
	Corrected proportion	37%	63%	

5.3.2 Influence of Ti variation on irradiated microstructure at 510°C

5.3.2.1 Loop size and density in function of thickness in Ni-0.8Ti and Ni-1.2Ti at 510°C

The post-characterization of irradiated microstructure is performed on Ni-0.8Ti and Ni-1.2Ti irradiated at 510°C to 0.06 dpa. The irradiated microstructure in function of thickness is shown in Figure 5.24. To calculate the density of dislocation loops, stereo-imaging is performed on Ni-1.2Ti at two thickness, 90 nm and 250 nm. The histograms of loop proportion distribution in function of depth are shown in Figure 5.24(c-d). We consider roughly that the total thickness of loop-denuded zones is about 20 nm. We assume the same value for Ni-0.8Ti. Therefore, the loop density taking into account loop-denuded zone can be calculated and plotted in Figure 5.24(e). The average loop size of the two alloys is plotted in Figure 5.24(f).

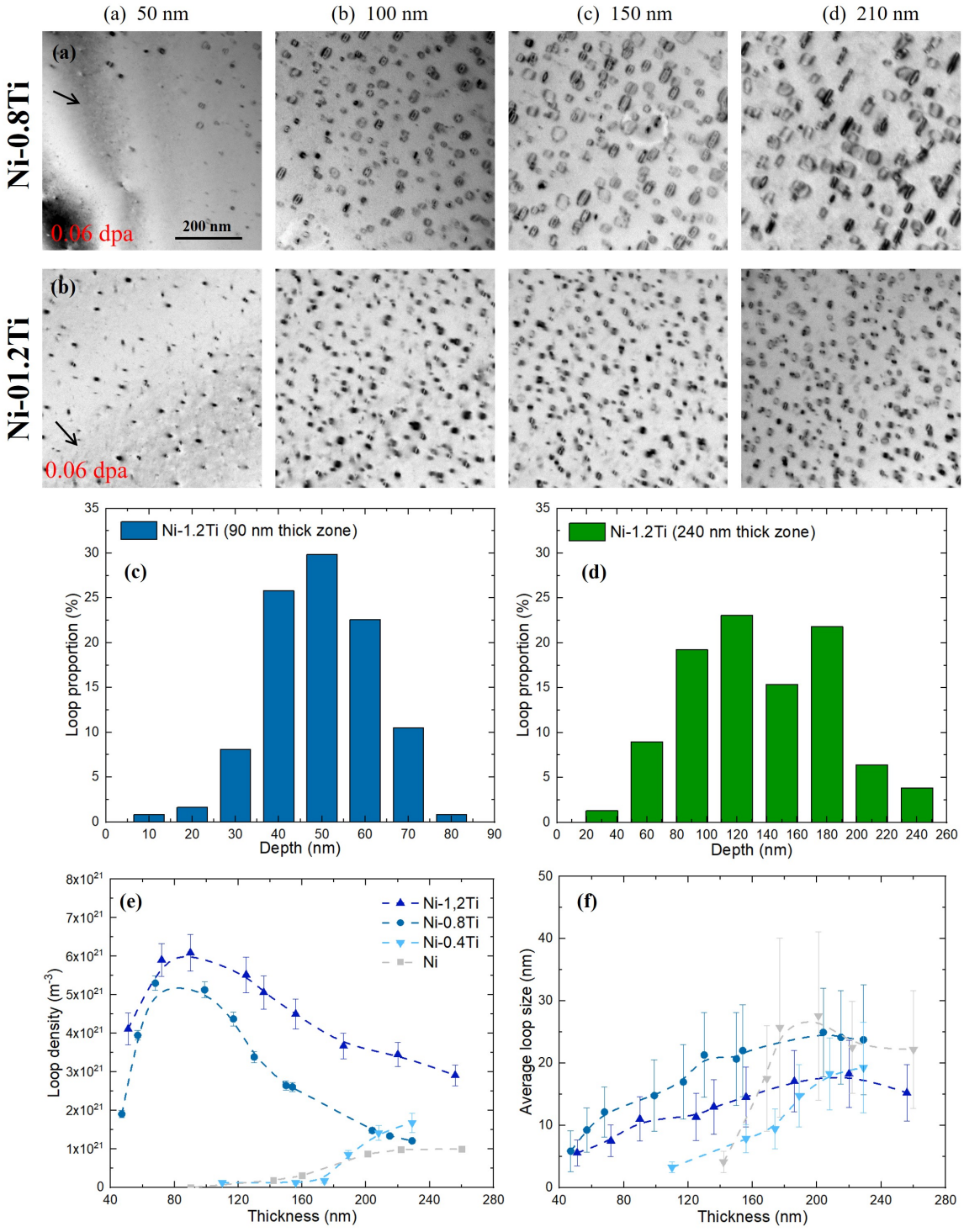

Figure 5.24 Loop size and density in function of thickness in (a) Ni-0.8Ti and (b) Ni-1.2Ti at 510°C to 0.06 dpa. Histograms showing the depth distribution of loops in a (c) 90 nm thick zone and (d) 240 nm thick zone in Ni-1.2Ti. The evolution of loop size and loop density is presented respectively in (e) and (f).

Globally, the thickness dependency of loop density and size in Ni-0.8Ti and Ni-1.2Ti is similar. The density of loops in Ni-1.2Ti is higher than the density in Ni-0.8Ti while the size is the opposite. It can be easily understood that, for the same PD creation rate, when more loops are formed, each loop could absorb less PDs which leads to a smaller growth rate and smaller size. The curves of loop density and size of Ni and Ni-0.4Ti are also plotted in Figure 5.24(e-f). If we compare the behavior of Ni-0/0.4/0.8/1.2Ti, the influence of Ti content on loop density and size has to be divided in two range of thickness: in thin zones <200 nm and in thick zones >200 nm.

- In thin zones (<200 nm), surfaces effects are the controlling factor in Ni and Ni-0.4Ti. When Ti% is higher than 0.8, the effect of solute is sufficiently strong so that interstitial loops can be formed in thin zones;
- In thick zones (>200 nm), the influence of Ti content on loop density and size is not monotonic. The variation of loop density an size in function of Ti content is summarized in Table 5.5.

Table 5.5 Variation of loop density and loop size in function of Ti content (wt.%) at 510°C at 0.06 dpa in thick zones (> 200 nm).

Ti content	0	⇒	0.4	⇒	0.8	⇒	1.2
Loop density		↗		≈		↗	
Loop size		↘		↗		↘	

Combined with the results on Frank loop nature in the previous section, the influence of Ti content on the irradiated microstructure is summarized in Figure 5.25. Under current irradiation conditions (510°C, 0.06 dpa), there is a transition from a vacancy-loop dominated microstructure (low concentration of Ti) to an interstitial-loop dominated microstructure (high concentration of Ti).

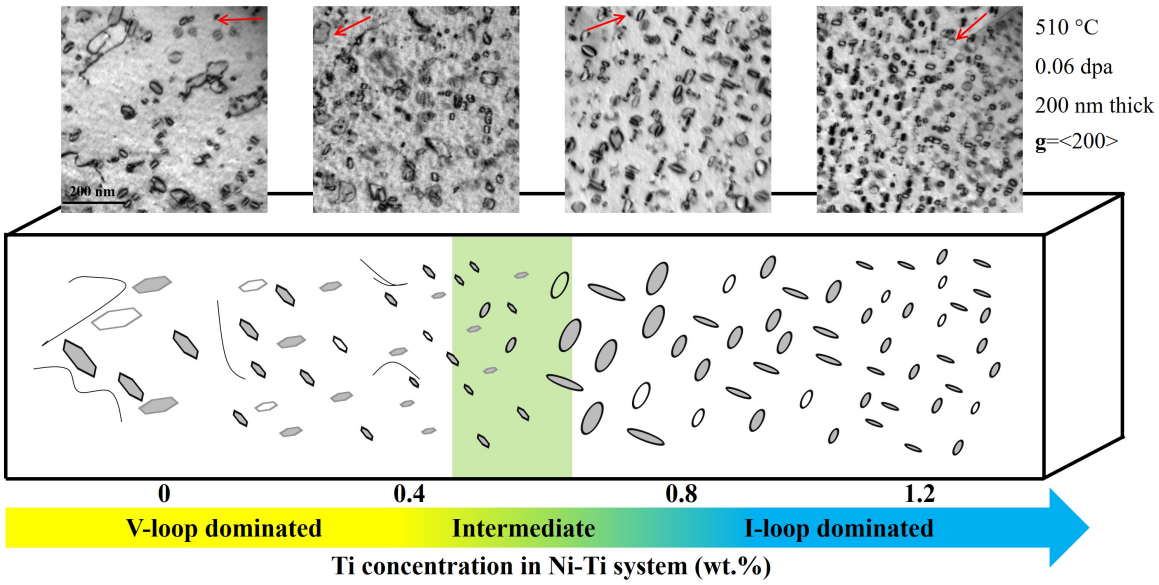

Figure 5.25 Schematic presentation illustrating the evolution of microstructure in function of Ti content in thick zones (>200 nm); **g**=<200> indicated by red arrows in each micrograph.

5.3.2.2 Loop type distribution in Ni-0.8Ti and Ni-1.2Ti at 510°C

We have shown that an addition of 0.4wt.% Ti reduce the mobility of perfect loops. In Ni-Ti alloys with a higher Ti content, perfect loops are found to be almost immobile during the irradiation in Ni-0.8Ti and Ni-1.2Ti. A higher Ti content may further provoke an homogeneous distribution of Burgers vector of perfect loops. The statistic method is used to study the distribution of Burgers vectors in Ni-0.8Ti and Ni-1.2Ti. Figure 5.26 show the TEM micrographs in the two alloys under different **g** used for the statistic analysis. The loop densities in each micrograph are given in Table 5.6 and Table 5.7. We focus on the proportion of each family compared to the total density (Figure 5.27(a) and Figure 5.27(b)). The distribution of perfect loop families can be considered as homogeneous.

Table 5.6 Loop density in function of **g** in a 200 nm thick zone of Ni-0.8Ti irradiated to 0.06 dpa at 510°C.

Zone axis	[001]				$[1\bar{1}2]$
g investigated	$2\bar{2}0$	$0\bar{2}0$	200	$\bar{2}\bar{2}0$	$\bar{1}11$
Loop density (10^{20} m^{-3})	19.15	23.40	23.37	18.82	21.00

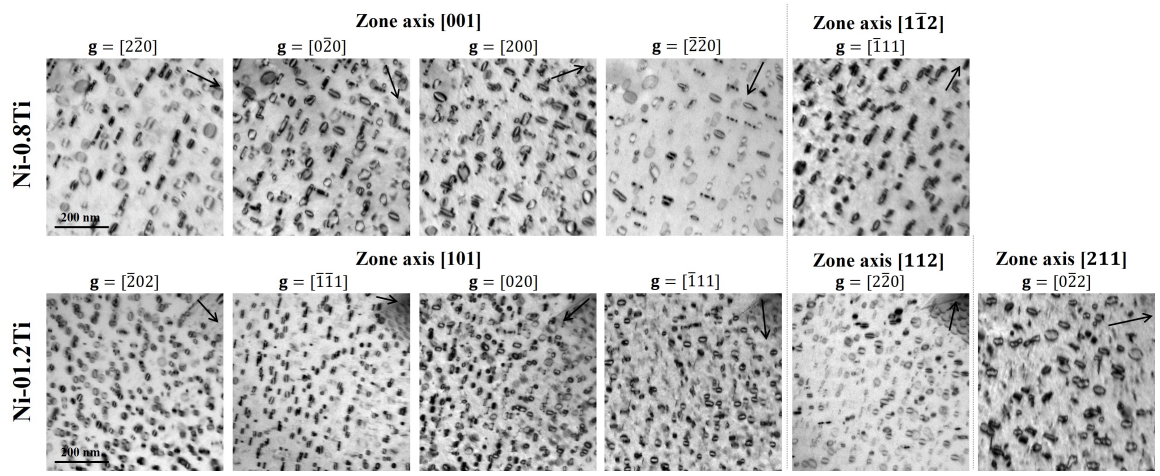

Figure 5.26 TEM micrographs showing the microstructure in the same zones in function of diffraction vectors **g** in 120 nm thick zones of in Ni-0.8Ti and Ni-1.2Ti irradiated at 510°C to 0.06 dpa.

Table 5.7 Loop density in function of **g** in a 200 nm thick zone of Ni-1.2Ti irradiated to 0.06 dpa at 510°C.

Zone axis	[101]				[112]	[211]
g investigated	$\bar{2}02$	$\bar{1}\bar{1}1$	020	$\bar{1}11$	$2\bar{2}0$	$0\bar{2}2$
Loop density (10^{20} m^{-3})	26.35	28.29	31.50	26.32	27.72	25.28

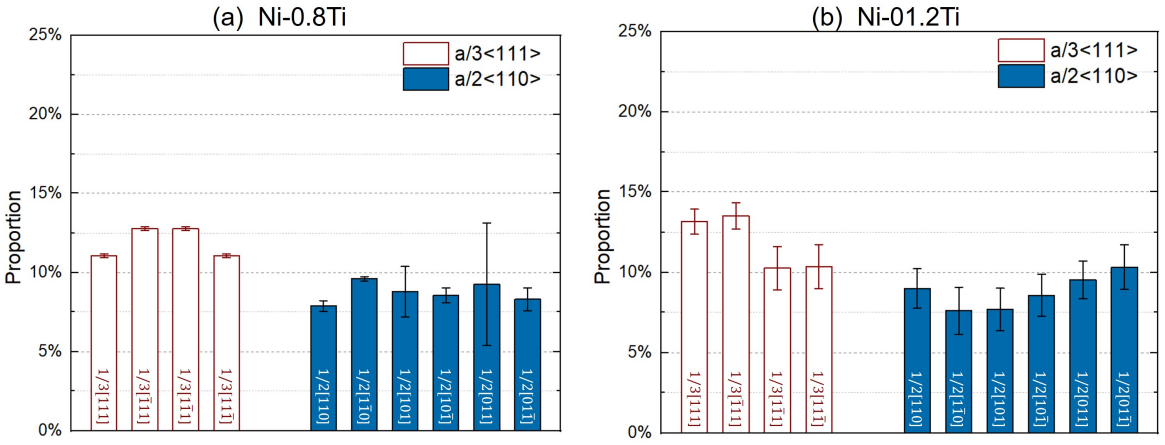

Figure 5.27 Proportion of each family of loops in (a) Ni-0.8Ti and (b) Ni-1.2Ti calculated by dividing the density of each family by the total density. White bars for Frank loops and blue bar for perfect loops.

5.4 Summary of chapter

A drastic influence of micro-alloying on the nature of radiation-induced Frank loops is observed. In Ni, vacancies form intrinsic Frank loops. In thin foils or at depth lower than damage peak, interstitials agglomerate also as Frank loops but only inside existing intrinsic Frank loops and eradicate the stacking fault. In bulk samples of alloys, vacancies form voids while interstitials agglomerate as single or multi-layer extrinsic Frank loops. For the first time, (i) the real impact of micro-alloying on Frank loop nature and fine microstructure is shown; (ii) the morphology of Frank loops is shown to be a characteristic feature of their nature. The influence of Ti is much stronger than Cr on reducing the mobility of defects (PDs and dislocation loops) and loop growth rate. Very low concentration of Ti can induce a strong increase of loop density as well as a change of Frank loop nature in thin foils. There is a critical concentration of Ti above which the nature of Frank loops in thin foil samples changes from vacancy-type to interstitial-type. The critical content depends on the temperature: lower than 0.4% at 450°C; between 0.4% and 0.8% at 510°C.

These observations of fundamental properties of radiation-induced defects introduce new considerations in theoretical calculations, which will contribute significantly to a better understanding of the elementary mechanisms of radiation damage and solute effects in fcc structure.

Chapter 6

Influence of a carbon addition on microstructure evolution in Ni-0.4Ti alloy

6.1 Influence of a carbon addition on Frank loop nature in Ni-0.4Ti

6.1.1 Frank loop nature in Ni-Ti-C irradiated at 510°C

Figure 6.1 presents the determination of Frank loop nature in Ni-Ti-C. In the studied zone, three families of Frank loops are detected. From their visibility in Figure 6.1(c) and Figure 6.1(d), their Burgers vectors are obtained. Their inside-outside behavior with $\mathbf{g}=\pm[020]$ is listed in Figure 6.1(e) and shows that they are all interstitial-type.

Inner loops are frequently observed in interstitial Frank loops in Ni-Ti-C. Detailed characterization is conducted to study the structure of these Frank loops. Figure 6.2 shows the analysis of a typical Frank loop with a Burgers vector $1/3[1\bar{1}1]$. Inside the interstitial Frank loop, there is an inner loop. As the stacking fault inside the inner loop is not observed, the fault was eliminated by the inner loop. Therefore, this inner dislocation can be either a Frank loop of an opposite nature with the outer loop or a Shockley partial 1/6<112>. As the inner loop is in the same plane as the outer loop, the possible Burgers vectors is listed in Figure 6.2(g). The possible Burgers vectors are $1/3[\bar{1}1\bar{1}]$ or 1/6[121] from its visibility. The visibility of the inner loop with $\mathbf{g}=\bar{1}1\bar{1}$ should have been able to determine the Burgers vector but the loop is in edge-on position. However, the contrast of inner loop is always the opposite to the outer loop. Therefore the inner loop is an intrinsic (vacancy-type) Frank loop. Moreover, the projection of the three segments of the inner loops is superposed with the three

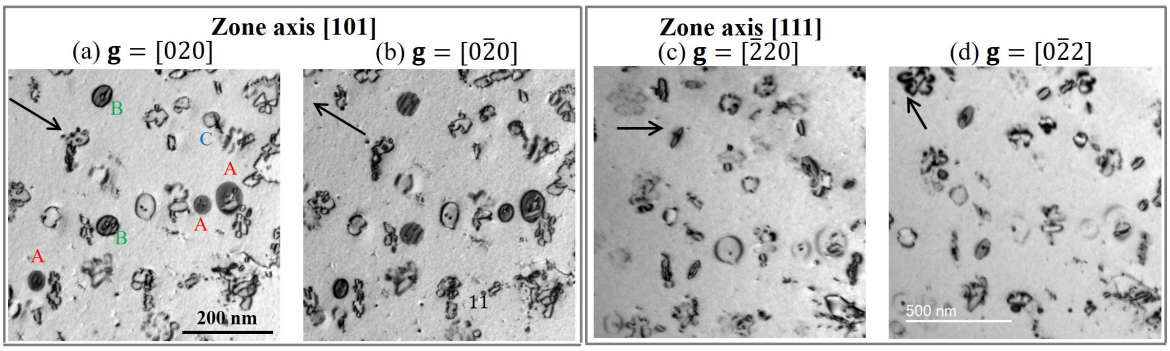

A: 1/3[111]
B: 1/3[1$\bar{1}$1]
C: 1/3[$\bar{1}$11]

(e)

Loops	Contrast of loops along zone axis [001]			g · b for g	b	Nature
	b direction	g = [020]	−g = [0$\bar{2}$0]			
A	[111]	outside	inside	>0	1/3 [111]	interstitial
B	[1$\bar{1}$1]	inside	outside	>0	1/3 [1$\bar{1}$1]	interstitial
C	[$\bar{1}$11]	outside	inside	<0	1/3 [$\bar{1}$11]	interstitial

Figure 6.1 Determination of Frank loop nature in Ni-Ti-C irradiated to 0.06 dpa at 510°C.

<110> directions ($\bar{1}$10, 110 and 011) contained in the (1$\bar{1}$1) plane. This is a characteristic feature of segmented vacancy Frank loops (Edington and Smallman, 1965; Humble et al., 1967), suggesting also that this loop is a vacancy loop instead of Shockley partial. This phenomenon is also an eradication mechanism of Frank loops but by in the opposite way to the one in Ni.

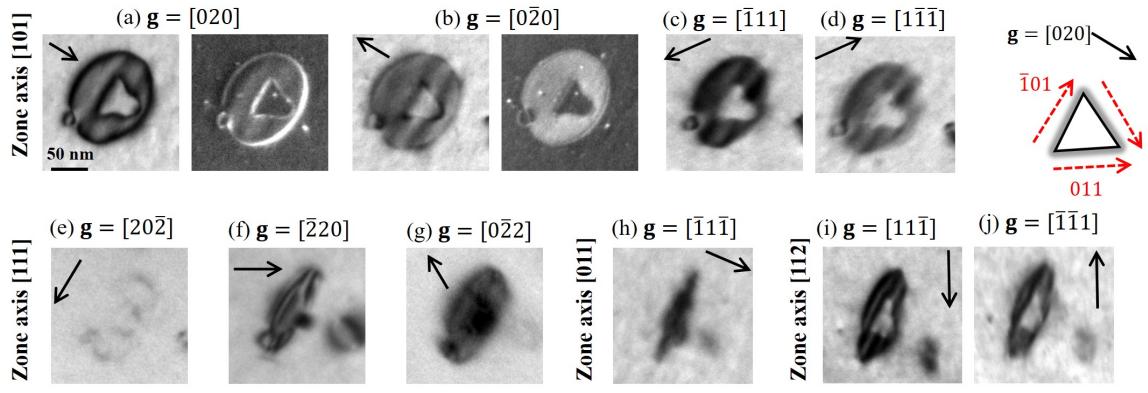

(k)

Table of visibility (V= visible, I= invisible)	Zone axes	[101]		[111]			011]	[112]
	g / Possible b	020	$\bar{1}$11	20$\bar{2}$	$\bar{2}$20	0$\bar{2}\bar{2}$	$\bar{1}$1$\bar{1}$	11$\bar{1}$
	$\pm\frac{1}{3}[\bar{1}1\bar{1}]$	V	V	I	V	V	V	V
	$\pm\frac{1}{6}[121]$	V	V	I	V	V	I	V
	$\pm\frac{1}{6}[1\bar{1}\bar{2}]$	V	V	V	V	V	I	V
	$\pm\frac{1}{6}[\bar{2}\bar{1}1]$	V	V	V	V	V	V	V

(l)

Inside-outside behvior	Zone axes	[101]				[112]	
	g / Possible b	020	0$\bar{2}$0	$\bar{1}$11	1$\bar{1}\bar{1}$	11$\bar{1}$	$\bar{1}\bar{1}$1
	$\pm\frac{1}{3}[1\bar{1}1]$	in	out	in	out	in	out
	$\pm\frac{1}{3}[\bar{1}1\bar{1}]$	out	in	out	in	out	in
	$\pm\frac{1}{6}[121]$	out	in	in	out	in	out

Figure 6.2 Determination of Frank loop nature in Ni-Ti-C irradiated to 0.06 dpa at 510°C.

6.1.2 Frank loop nature in Ni-Ti-C irradiated at different temperatures

The irradiation temperature has an effect on the Frank loop nature in Ni-0.4Ti (Figure 5.12). It is interesting to investigate the nature of Frank loops at different temperatures in Ni-Ti-C. The morphology of Frank loops irradiated at 450°C (Figure 6.3(a)) and 560°C (Figure 6.3(b)) is shown in Ni-Ti-C. It is very likely that Frank loops formed at 450°C and 560°C are interstitial-type.

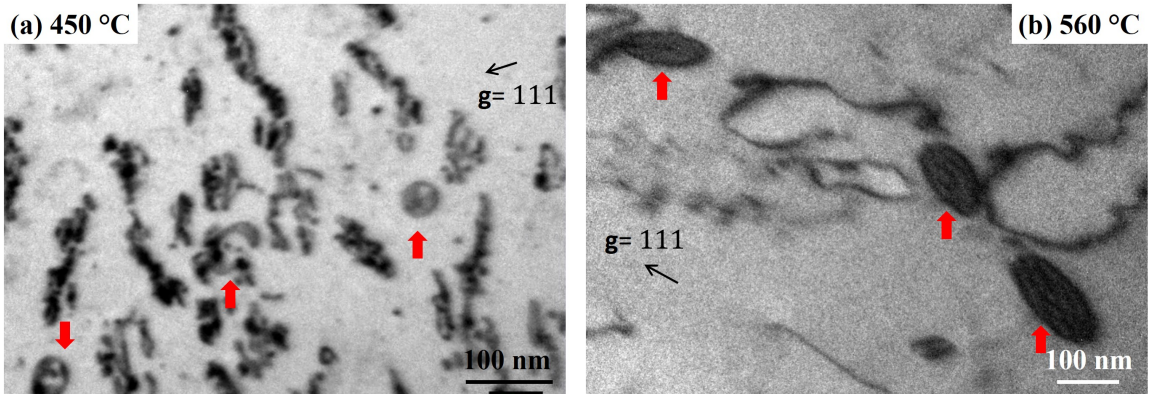

Figure 6.3 Frank loops in Ni-Ti-C irradiated at (a) 450°C and (b) 560°C.

Figure 6.4 shows the determination of the structure of a typical Frank loop in Ni-Ti-C at 560°C. The large Frank loop is interstitial-type (Figure 6.4(b)). There are four small loops (1/2/3/4) inside the projection of the large Frank loop. These loops are on the same plane as the outer loops (or on very close planes) as the outer and inner loops are all close to the edge-on position in the TEM micrograph with $\mathbf{g}=[\bar{1}\bar{1}\bar{1}]$ along the zone axis $[0\bar{1}1]$. The inner loops 1/2/3 has the same Burgers vector (Figure 6.4(a)) and nature (Figure 6.4(b)) as the outer loop. For the inner loop 4, the visibility with actual $\mathbf{g}$ suggests that it is a Shockley partial with two possible Burgers vectors. The inside-outside contrast (Figure 6.4(c)) with $\mathbf{g}=\pm[020]$, $\pm[220]$ and $\pm[111]$ shows that its Burgers vector is $1/6[211]$. Thus, the Frank loop is partially multi-layer and unfaulted by a Shockley partial.

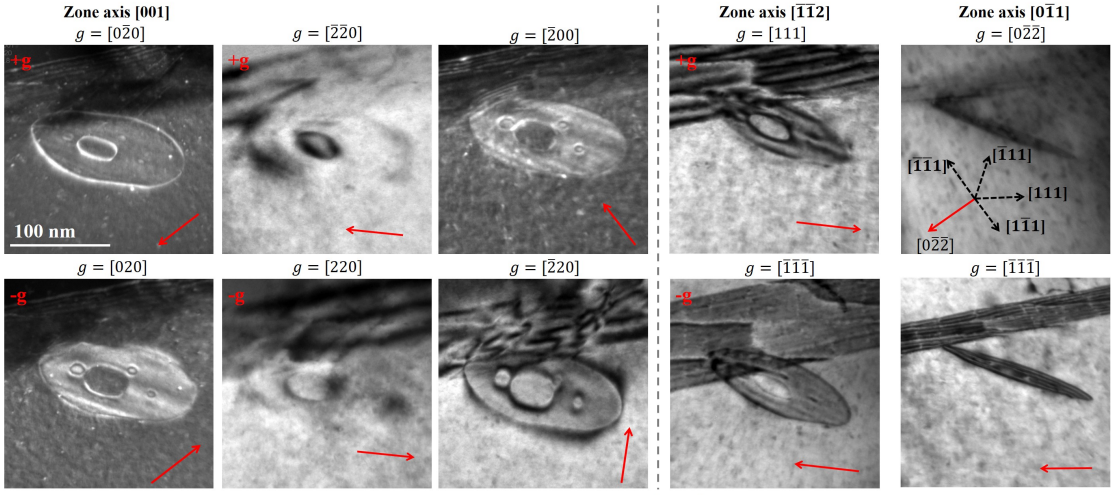

(a)

Table of visibility (V= visible, I= invisible)	Loop type	Zone axes / g / Possible b	0$\bar{2}$0	$\bar{2}$00	$\bar{2}\bar{2}$0	$\bar{2}$20	111	0$\bar{2}\bar{2}$	Loops
			[001]				[$\bar{1}\bar{1}$2]	[0$\bar{1}$1]	
	Frank loops	$\pm\frac{1}{3}$[111]	V	V	I	V	V	I	Outer loop Inner loops 1/2/3
		$\pm\frac{1}{3}$[$\bar{1}$11]	V	V	V	I	V	I	
		$\pm\frac{1}{3}$[1$\bar{1}$1]	V	V	V	I	V	V	
		$\pm\frac{1}{3}$[11$\bar{1}$]	V	V	I	V	V	V	
	Perfect loops	$\pm\frac{1}{2}$[110]	V	V	V	I	V	V	
		$\pm\frac{1}{2}$[1$\bar{1}$0]	V	V	I	V	I	V	
		$\pm\frac{1}{2}$[101]	I	V	V	V	V	V	
		$\pm\frac{1}{2}$[10$\bar{1}$]	I	V	V	V	I	V	
		$\pm\frac{1}{2}$[011]	V	I	V	V	V	I	
		$\pm\frac{1}{2}$[01$\bar{1}$]	V	I	V	V	I	V	
	Shockley partials on ($\bar{1}$11) plane	$\pm\frac{1}{6}$[211]	V	V	V	V	V	V	Inner loop 4
		$\pm\frac{1}{6}$[$\bar{1}\bar{2}$1]	V	V	V	V	V	V	Inner loop 4
		$\pm\frac{1}{6}$[$\bar{1}$1$\bar{2}$]	V	V	I	V	V	V	

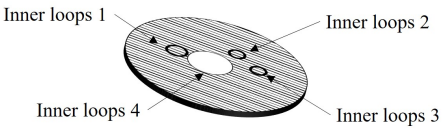

(b)

Loops	Contrast of loops along zone axis [001]		g · b for g	b	Nature
	b direction	g = [0$\bar{2}$0] / −g = [020]			
Outer loop	[$\bar{1}$11]	inside / outside	>0	1/3 [$\bar{1}$11]	interstitial
Inner loops 1/2/3	[$\bar{1}$11]	inside / outside	>0	1/3 [$\bar{1}$11]	interstitial

(c)

Inside-outside behvior	Zone axes / g / Possible b	[001] 0$\bar{2}$0	[001] $\bar{2}\bar{2}$0	[$\bar{1}\bar{1}$2] 111	Loops
	$\frac{1}{3}$[$\bar{1}$11]	in	/	out	Outer loop
	$\frac{1}{6}$[$\bar{1}\bar{2}$1]	out	out	in	
	$\frac{1}{6}$[211]	in	in	out	Inner loop 4

Figure 6.4 Determination of the structure of an interstitial Frank loop in Ni-Ti-C irradiated to 0.18 dpa at 560°C. (a) Visibility table including all possibilities of Frank loop families, perfect loop families and 3 Shockley partials laying on the ($\bar{1}$11) plane. (b) Determination of loop nature. (c) Table of inside-outside contrast to determine the Burgers vector of the inner loop 4.

6.2 Growth rate of interstitial Frank loops in Ni-Ti-C in function of temperature

In-situ irradiations were performed on Ni-Ti-C alloys at 510°C. Figure 6.5 presents the microstructural evolution of Ni-Ti-C at 510°C. The thickness of the zone is about 200 nm. Globally, the evolution in Ni-Ti-C is similar to the one in Ni-0.4Ti. However, there are still some differences. the loop density in Ni-Ti-C quickly reach a steady state at about 30s, earlier than Ni and Ni-0.4Ti. Moreover, the loop size in Ni-Ti-C is larger than the one in Ni-0.4Ti. The loop growth rate in Ni-Ti-C at 510°C is shown in Figure 6.5(c) and compared with the growth rate in Ni and Ni-0.4Ti. The loop growth rate is "intermediate" between the other two materials but the different loop nature has to be noted. Mechanisms of the loop

growth in Ni-Ti-C may differ from th ones in Ni/Ni-0.4Ti. These observations suggest that the presence of C favor the nucleation of loops but the influence of Ti on loop growth rate is reduced. Moreover, the mobility of perfect loops is extremely low in Ni-Ti-C from the in-situ observations. This may also be attributed to the precipitation.

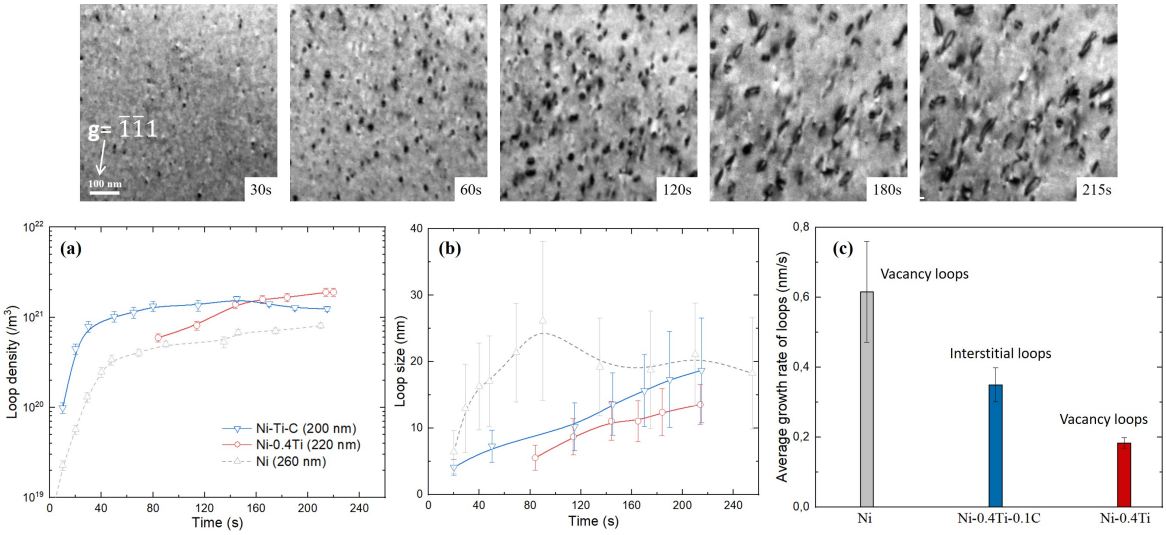

Figure 6.5 Microstructural evolution during in-situ irradiation in Ni-Ti-C in function of time at 510°C. Selected micrographs illustrating the microstructure were recorded under two-beam KBF conditions in using $\mathbf{g} = [111]$ along zone axis [112]; evolution of (a) loop density and (b) average size in function of irradiation time; (c) average loop growth rate in Ni, Ni-Ti-C and Ni-0.4Ti. The thickness of the zone is about 200 nm.

The relation between the growth rate of interstitial Frank loops and the temperature can give an estimation of the migration energy of vacancies based on the rate theory (Kiritani et al., 1975). As only interstitial loops are detected in Ni-Ti-C irradiated from 450°C to 560°C, it is interesting to study the their growth rate in function of temperature. The logarithm of growth rates of interstitial Frank loops in Ni-Ti-C at 450/510/560°C in function of the temperature ($\frac{1}{2k_BT}$ in eV^{-1}) are plotted in Figure 6.6. It shows a good linear regression fitting. Based on the rate theory (Equation), the slope is 1.27±0.01 eV which should correspond to the vacancy migration energy in Ni-Ti-C.

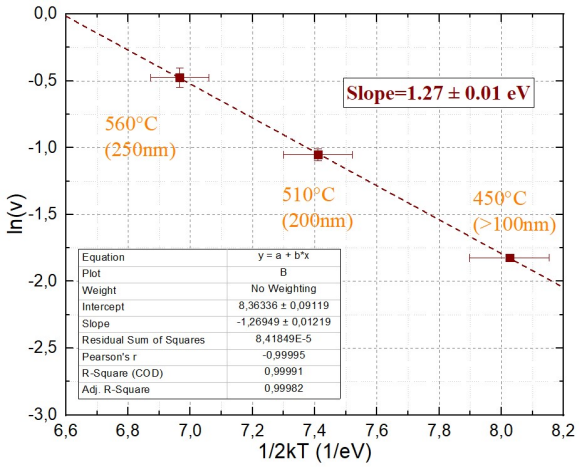

Figure 6.6 Growth rate of interstitial Frank loops in Ni-Ti-C in function of temperature.

6.2.1 Evolution of interstitial Frank loops in Ni-Ti-C in function of temperature

Another point of interest during the in-situ irradiation is the formation of large Frank loops in Ni-Ti-C which are not observed in Ni and Ni-0.4Ti. Moreover, the formation of complex Frank loops and their evolution is observed during the in-situ irradiation. The evolution of Frank loops in Ni-Ti-C can be summarized to two cases:

- The first case in shown in Figure 6.7(a). A black point is formed at +8s close to a single large Frank loop. The black point grows with the time. At +60s, the black point seems to be absorbed by the large Frank loop. Then the stacking fault in the center of the Frank loop is very likely removed since no contrast of stacking fault is visible. When the irradiation proceeds, the inner perfect zone grow with the out loop. Finally at +168s, the large Frank loop disappears. It is either eliminated due to the interaction with the surface, or unfaulted into a perfect loop and becomes invisible with the used **g**.
- The second case is shown in Figure 6.7(b). A black point is formed close to a large Frank loop but there is no absorption along the irradiation. Finally; when the large Frank loop disappears, the contrast of black point remains and gradually disappear with the irradiation time.

Based on the in-situ observations and the determination of Frank loop nature, we tend to suggest that the black point in Figure 6.7 should be an intrinsic Frank loop with an opposite **b** to the outer extrinsic loop. The absorption of this opposite-nature Frank loop could eliminate a part of the stacking fault in the large loop. However, since Frank loops are immobile, the absorption may be due to the fluctuation of the lattice and depends strongly on the distance of two loops. When the large loop disappears, the small vacancy loop can not

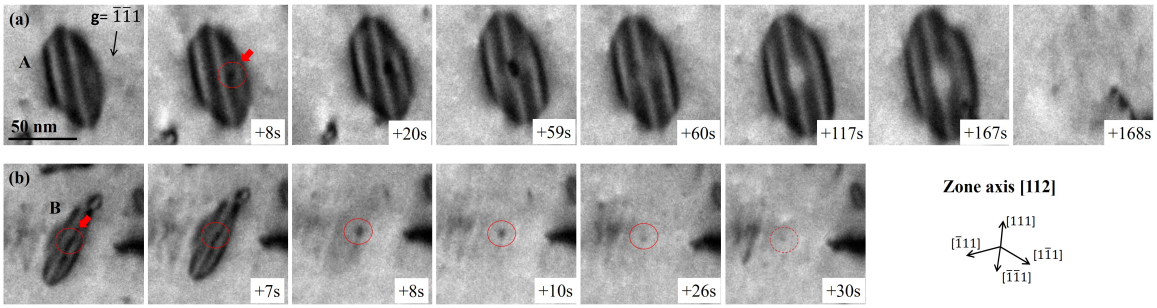

Figure 6.7 Evolution of two typical Frank loops in Ni-Ti-C at 510°C. TEM micrographs taken along zone axis [112] with $\mathbf{g}=\bar{1}\bar{1}1$.

exist alone since the actual microstructure is dominated by interstitials. Thus the shrinkage of these vacancy loops occurs.

The evolution of Frank loops are studied at 450°C and 560°C as well. Figure 6.8(a-b) shows the evolution of Frank loops at 450°C. In Figure 6.8(a) and Figure 6.8(b), the growth of the inner loop tends to reshape the outer interstitial Frank loops. The triangle form of the inner loop is clearly observed in Figure 6.8(b). It should be a vacancy Frank loop which eliminates the stacking fault. In Figure 6.8(a), the interstitial Frank loops evacuates the inner loop and return to a single Frank loop to minimize its periphery (related to the energy of dislocation line). In Figure 6.8(b), the outer loop is unfaulted during the reshaping (+8s). These observations suggest also the coexistence of two elimination mechanisms of Frank loops: the eradication by vacancy loops and the unfaulting by Shockley partials.

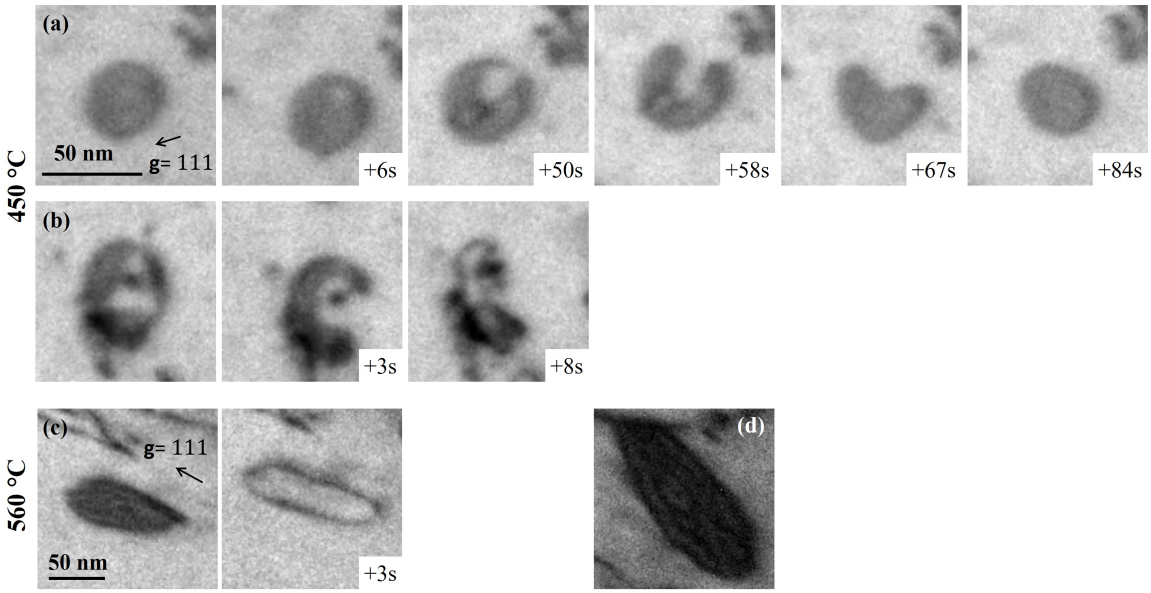

Figure 6.8 Frank loops and their evolution in Ni-Ti-C at (a-b) 450°C as well as (c-d) 560°C. In both samples, TEM images are taken along zone axis <112> with $\mathbf{g}=<111>$.

At 560°C, Frank loops tend to directly unfault into perfect loops (Figure 6.8(c)) or develop to multi-layer loops (Figure 6.8(d)). This is in agreement with the characterization in Figure 6.4. Meanwhile, no vacancy loop is detected within large interstitial Frank loops. It seems that the size of vacancy loops is reduced when the irradiation temperature increases. It is also worth to remind that the perfect loops are still almost immobile even at 560°C. When the unfaulting occurs, the perfect loops even at 560°C remains in the same position. This phenomenon is also observed at lower temperatures (510°C and 450°C). The mobility of perfect loops is extremely low in the studied range of irradiation temperature.

6.3 Investigation of precipitation under irradiation in Ni-Ti-C system

The structure of Frank loops in Ni-0.4Ti changes drastically with the addition of carbon. In Ni-0.4Ti, multi-layer interstitial Frank loops are formed at 450°C while, in Ni-Ti-C, vacancy Frank loops are formed within the interstitial Frank loops and tend to eliminate the stacking fault. It is important to understand how this carbon addition affects the microstructure: it can induce the precipitation of TiC or it plays a role alone in solid solution. In this work, we focuses on the possible precipitation of TiC in a Ni-Ti-C sample irradiated at 510°C up to a high dose (0.54 dpa).

6.3.1 Supplementary spots on the diffraction pattern in TEM

The irradiated sample is studied under several zone axes with different **g**. No visible large size precipitates is detected after irradiation. Thus, they are either very small or not even formed. Diffraction mode is firstly used to reveal the existence of secondary phases. Diffraction patterns close to the zone axis [112] is recorded at different thickness as shown in Figure 6.9(a). Figure 6.9(b-c) show the corresponding diffraction patterns in each zone. This zone axis is chosen because it was reported that the $[011]_{TiC}$ and $[112]_{Ni}$ zone axis are privileged (Strzeciwilk et al., 2003) to study the TiC precipitation.

In very the thin zone (zone A), strong signal of supplementary spots are detected (Figure 6.9(b)). The yellow circles and lines indicate the Ni matrix along [112]. The blue circles point out supplementary spots. The angle AOB is 35.53°. It is very close to 35.26°, the angle of (220)-(000)-(111) along zone axis <110> for a fcc structure. The ratio AO/BO is 6.16/4.08=1.63, which is the same ratio of d_{220}/d_{111} for a fcc structure. Therefore, a secondary phase indeed exists and it has very likely the fcc structure. Spot A should correspond to the (220) reflection and Spot B and C correspond to the [111] reflection. It should be noticed

that the (200) reflection of secondary phase is very close but not exact superposed at [111] reflection of Ni matrix.

Possible candidate of the secondary phase in this case is NiO and TiC. Both of them have fcc structure. Table 6.1 presents the lattice parameters of Ni, NiO and TiC. The inter-planar distances of NiO and TiC are similar due to their close lattice parameters. The measured distances of AO and OB are close to both candidates. The diffusion of the spot makes it difficult to tell the exact distance. However, the oxidation of the matrix is usually amorphous and its diffraction consists of several bands. If re-crystallization of nickel dioxide is induced by the irradiation, the same phenomenons should have been observed in other materials. However, it is not the case. Consequently, we believe that these supplementary spots are caused by the formation of TiC precipitates.

The diffraction in thicker zones shown in Figure 6.9(c) reveals that the intensity of the TIC signal decreases gradually when the thickness increases. Finally the supplementary spots are completely invisible. It is very likely due to the stronger diffraction of the matrix which conceals the diffraction of TiC.

Table 6.1 Lattice parameter a_0 (nm) and inter-planar distance d_{hkl} (nm^{-1}) in reciprocal lattice of Ni, NiO and TiC.

Materials	a_0	d_{200}	d_{220}	d_{111}
Ni	0.352 (Hermann, 2011)	5.68	8.03	4.92
NiO	0.417 (Rooksby, 1943)	4.80	6.78	4.15
TiC	0.432 (Yang et al., 2008)	4.63	6.54	4.01

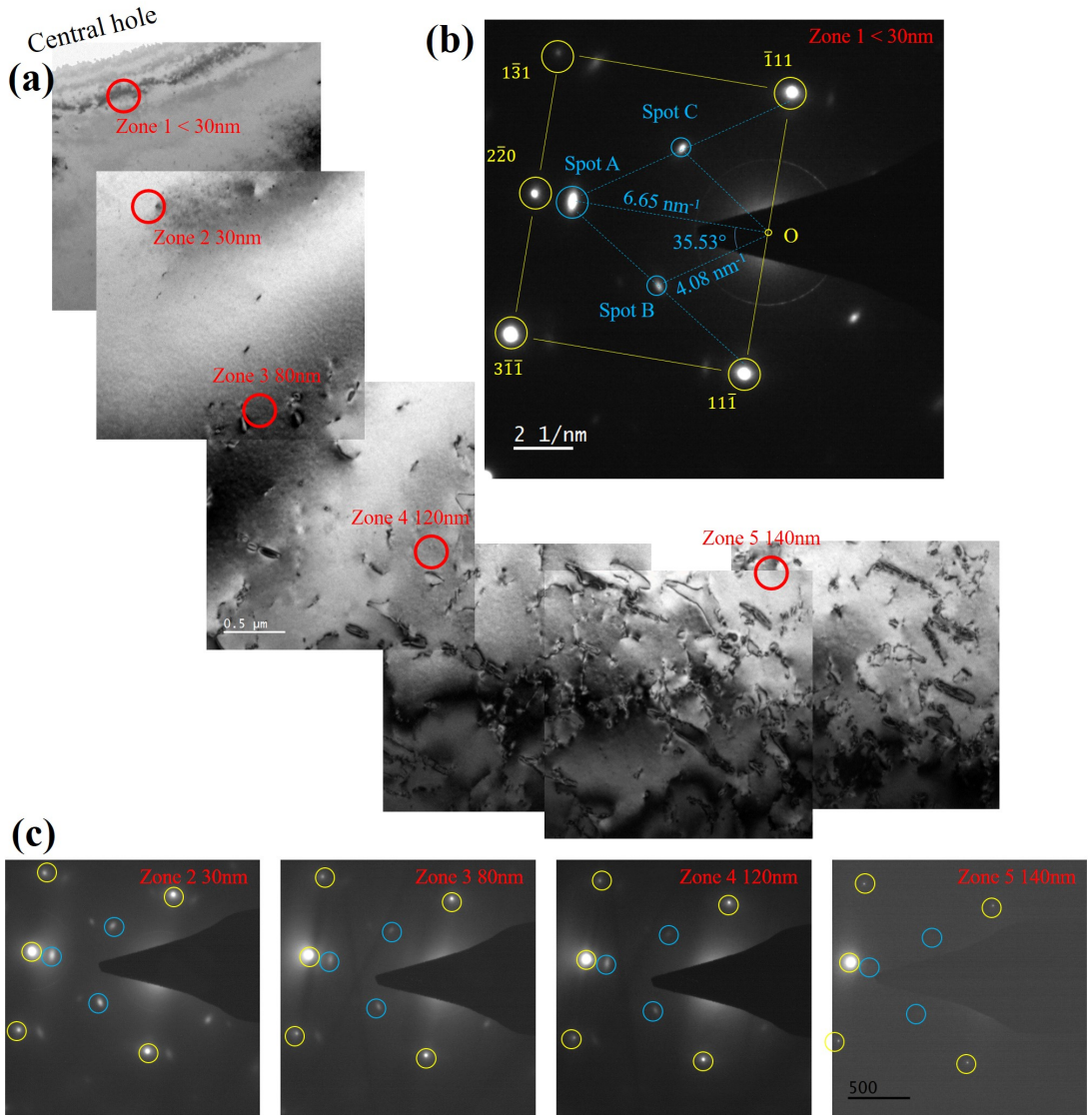

Figure 6.9 Diffraction in function of thickness in Ni-Ti-C irradiated at 510°C to 0.54 dpa. (a) TEM images showing the overview of microstructure; (b) diffraction patterns of a zone close to the hole thinner than 30 nm; (c) diffraction in thicker zones.

6.3.2 Nano-precipitates enriched in Ti by TEM-EDS

The diffraction suggest a possible precipitation of TiC. TEM-EDS analysis is performed to study existence of TiC. Figure 6.10(a) shows the HAADF image in a 150 nm thick zone. Figure 6.10(b) is the Ti mapping in this zone. Some small clusters of Ti are detected. Two 1D plots of Ti concentration across the Ti clusters are presented in Figure 6.10(c) and Figure 6.10(d). We could fairly conclude that this atmosphere is rich in Ti. Combined with the previous results of diffraction, these Ti clusters are probably TiC. Their size is about 2

nm. However, it is difficult to tell whether these precipitates are at surfaces or in the matrix. We tend to suggest that the precipitates are located inside the matrix considering their form because the precipitation at surfaces usually shows an extended, planar and irregular form. Moreover, precipitates at surfaces should not affect the loop mobility and Frank loop evolution under irradiation.

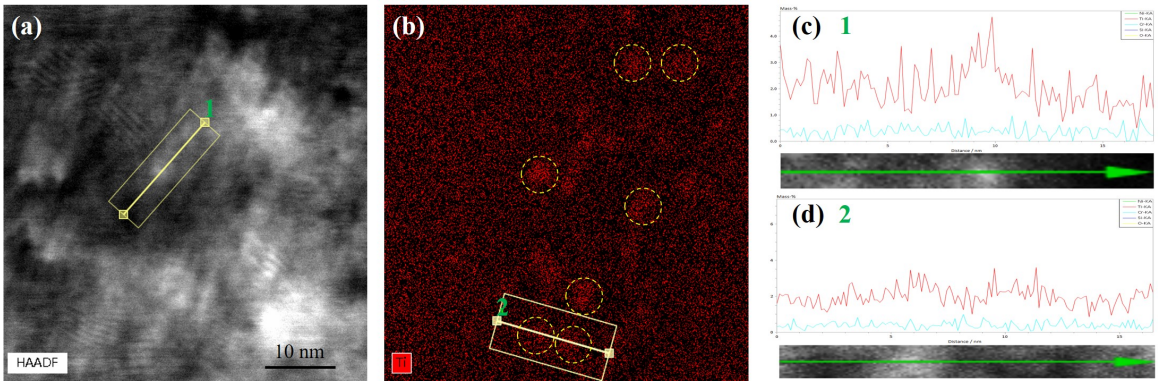

Figure 6.10 TEM-EDS analysis of Ni-Ti-C irradiated at 510°C to 0.54 dpa. (a) STEM-HAADF image of a 150 nm thick zone; (b) Ti concentration in the zone; 1D profile of Ti concentration along (c) line 1 across a Ti cluster and (d) line 2 across two Ti clusters; dotted circles showing the position of Ti-rich clusters. EDS analysis is performed in collaboration with ETH-Zurich by Dr. R. Schäublin.

6.4 Summary of the chapter

The influence of carbon addition in Ni-0.4Ti on Frank loop nature is first investigated at different temperatures. In Ni-Ti-C, Frank loops are always interstitial-type in the range of our irradiation conditions (450-560°C). The addition of carbon changes the structure of interstitial Frank loops at 450°C and 510°C. Compared with Ni-0.4Ti where multi-layer extrinsic Frank loops are observed, interstitial Frank loops in Ni-Ti-C are frequently found to be partially unfaulted. Two mechanisms of Frank loop elimination are identified. The extrinsic stacking fault can be eradicated by an inner intrinsic Frank loop with an opposite Burgers vector or by the nucleation of Shockley partial at 450°C and 510°C. Such phenomenon is not observed at 560°C. At 560°C, small interstitial Frank loops and Shockley partial can be formed inside large interstitial Frank loops.

The growth of interstitial Frank loops are studied in function of temperature. In Ni-Ti-C, the migration energy of vacancies is estimated as 1.27±0.01 eV by the correlation of interstitial loop growth rate and temperature. This value is lower than the estimated value in Ni. The mobility of vacancies should be increased.

Finally, the diffraction patterns and TEM-EDS analysis suggest the precipitation of small TiC during the irradiation. This could be the key point understand the combining effects of Ti and C.

Chapter 7

Discussions of results

7.1 Influence of surfaces on the irradiated microstructure of Ni

7.1.1 Absorption of point defects by surfaces

In Section 4.2.1 (Figure 4.13), we showed that the loop size and density in irradiated Ni are affected by the thickness of the zone i.e. there is an influence of surfaces on the irradiated microstructure. To evaluate surface effects, the absorption of point defects by surfaces should be considered. We consider here a system without internal sinks (dislocation lines and loops) to maximize the influence of surfaces. The concentration profile of point defects along depth direction can be described by one-dimensional steady-state diffusion equations for a given thickness and a given temperature (Foreman, 1972):

$$D_v \frac{\partial^2 C_v}{\partial z^2} = \phi - K_r C_v C_i (D_v + D_i) \tag{7.1}$$

$$D_i \frac{\partial^2 C_i}{\partial z^2} = \phi - K_r C_v C_i (D_v + D_i) \tag{7.2}$$

Where C_v and C_i are atomic fraction of vacancies and interstitials, D_v and D_i are diffusion coefficients of vacancies and interstitials, ϕ production rate of point defects in dpa/s, $K_r = 4\pi r_c/\Omega$ the recombination coefficient deduced from Waite's theory (Waite, 1957) with r_c the recombination radium assumed to be the lattice parameter (0.352 nm) and Ω the volume of Ni atom.

Equation 7.1 and 7.2 lead to D_vC_v=D_iC_i. For a given temperature, $D_i \gg D_v$ (Tucker et al., 2010). Thus, Equation 7.1 can be normalized and rewritten as:

$$\frac{\partial^2 Y}{\partial X^2} = \frac{t^2\phi}{D_v C_{v,\infty}}(Y^2 - 1) \tag{7.3}$$

Where $Y = C_v/C_{v,\infty}$ with $C_{v,\infty} = \sqrt{\frac{\phi}{K_r D_v}}$ the vacancy concentration in bulk materials without surface effects and $X = z/t$ with t the thickness of specimen. Equation 7.3 gives the profile of vacancy concentration. The form of the profile depends on the thickness, irradiation flux, and the temperature. To solve Equation 7.3, the diffusion coefficient is calculated by Arrhenius law with parameters as given in (Tucker et al., 2010) and boundary conditions $C_v(z = 0) = 0$ ($C_(v, eq)$ at thermal equilibrium negligible to $C_{v,\infty}$ and $C'_v(z = 0.5) = 0$ (by symmetry). The equation is finally solved numerically using MATHEMATICA.

Profiles of vacancies are calculated numerically for thickness of 50/100/150/180/220/260 nm at 400/450/500/600°C. Based on the solution, we can calculate the normalized profile (Y/Y_{max} for each thickness) and the profile of concentration of vacancies ($C_v = YC_{v,\infty}$). Results are presented in Figure 7.1(a-h). For a given temperature, for instance 510°C (Figure 7.1(b) and Figure 7.1(f)), the profile expand from a typical surface-dominated one to a recombination-dominated one with increasing thickness. This could explain the thickness-dependency of irradiation microstructure shown in Figure 4.13(a) and Figure 4.13(b). At 510°C, a recombination-dominated zones occurs in the center of the foil when t=150 nm. It correspond to the beginning of loop growth in thick zones experimentally observed. The fraction of volume which is less affected by surface increases with thickness. Finally in thick zones (220 nm), the vacancy concentration is stabilized and become thickness-independent in the center of the foil, which could lead to the observed thickness-independent microstructure. The same tendency is shown at lower temperatures. However, surface effects remains strong at 600°C in this thickness range. When temperature decreases, the profile expands more quickly with increasing thickness from surface-dominated profiles to recombination profile. This could be related to the temperature dependency of critical thickness for saturated microstructure.

To further evaluate the absorption by free surfaces, the vacancy flux to surface $J_{v,surf}$ and to the recombination $J_{v,recomb}$ are calculated as follwowing:

$$J_{v,recomb} = K_r C_v C_i (D_v + D_i) \approx K_r C_v C_i D_i = K_r D_v C_v^2 \tag{7.4}$$

$$J_{v,surf} = \phi - J_{v,recomb} \tag{7.5}$$

The ratio of $J_{v,surf}$ to $J_{v,recomb}$ is calculated for the center of a foil with different thickness in function temperature and shown in Figure 7.2. The lower dashed line correspond to a ratio

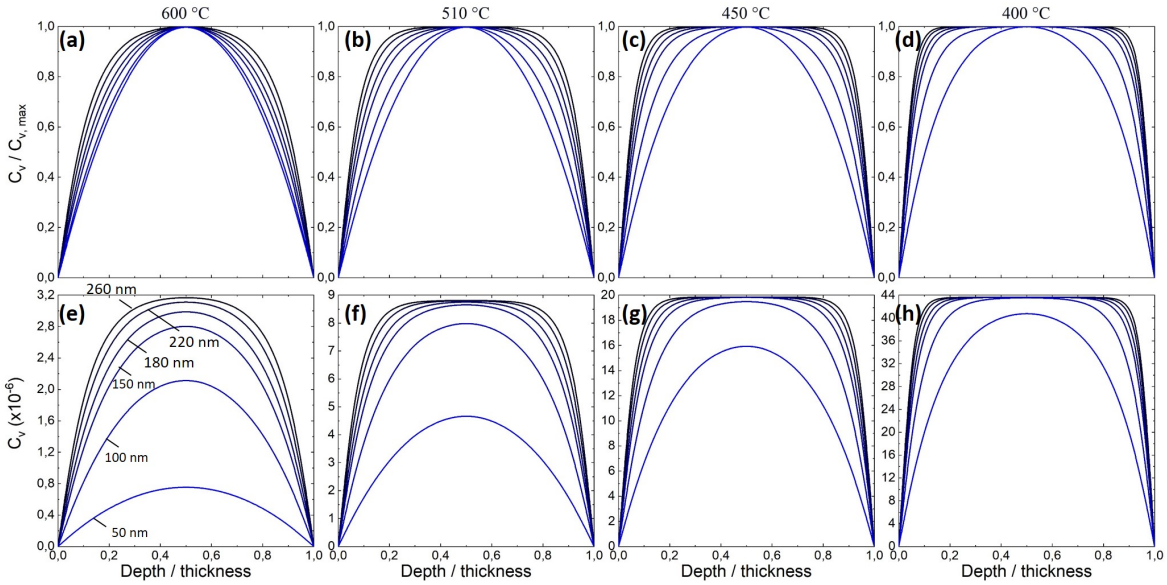

Figure 7.1 Profiles of (a-d) normalized and calculated (e-f) vacancy concentrations and (i) ratio of vacancy flux towards surfaces and to recombination in the center of the foil in function of thickness (50/100/150/180/220/260 nm) and temperature: concentration profiles at (a,e) 600°C; (b,d) 510°C; (c,g) 450°C; (d,h) 400°C.

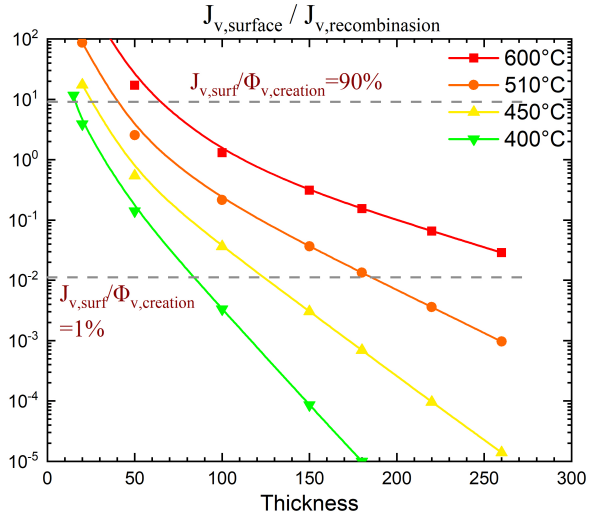

Figure 7.2 Ratio of $J_{v,surf}$ to $J_{v,recomb}$ in function of thickness and temperature for the center of a foil.

of 0.01 i.e. approximately 1% of PDs are absorbed by surfaces. The corresponding thicknesses for each temperature are 80/120/190 nm respectively for 400/450/500°C. Considering the simplicity of the model without effects of internal sinks (ignoring radiation-induce loops during the irradiation and thermal vacancies as recombination site (Foreman, 1972), this estimation is fairly in good agreement with our experiment observations (90/220 nm respectively for

450/510°C) in Figure 4.18(a). The upper dashed line in Figure 7.2 corresponds to 90% absorption of PDs by surfaces. It is worth noting that the results in Figure 7.2 is for the very center of the foil, where the surface absorption is the lowest across the entire depth. The surface absorption in the rest of the volume is higher than 90%. Thus, it suggests a critical thickness under which the sample will be completely free of defects. It reads respectively 18/25/40/70 nm for 400/450/510/600°C. This is in fairly good agreement with our observations at 510°C (40 nm from Figure 4.14) and with others at lower temperatures (24 nm at 300°C and 40 nm at 400°C in Ni under Ar^+ irradiation (Ishino et al., 1984)).

7.1.2 Surface effects on loop localization

In thick zones, the free surfaces still have an impact on the microstructure even if the loop density and size become independent of thickness. Surfaces can still absorb PDs near surfaces and also absorb mobile dislocation loops in the whole volume, leading to a non-uniform distribution of defects density along the depth direction of thin foils as shown in Figure 4.22. The depth distribution of radiation-induced defects in thin foils has been investigated in several materials (Chen and Ardell, 1976; Hasanzadeh et al., 2018; Ishino, 1997; Li et al., 2012; Yoo and Stiegler, 1977). In the literature, the thickness of depleted zones for each side of the foil was found to be

- 12 nm at 300°C under Ar^+ irradiation (Ishino, 1997);
- 20 nm at 400°C under Ar^+ irradiation (Ishino, 1997);
- 50 nm at 550°C under He^+ irradiation (Niwase et al., 1993);

In the present work, a loop-depleted zone is indeed shown in Figure 4.13(d) and is roughly 40 nm in each side of the foil in self-ion irradiated Ni at 510°C. Moreover, the thickness of loop-denuded zones in Ni at 450°C is also investigated by stereo-imaging and it is about 25 nm on each side (Figure 7.3).

Although the amount of data is limited and irradiation conditions are different, these data at least are in reasonable agreement and suggest that the surface denuded zones depends on temperature. The width of surface denuded zones L is described by a similar formula from the work of Foreman (Foreman, 1972) and of Huang (Huang et al.):

$$L = \sqrt{\frac{D_v C_{v,\infty}}{\phi}} = (\frac{D_v K_r}{\phi})^{\frac{1}{4}} \tag{7.6}$$

All these parameters are the same as the ones in Equation 7.1.

L is thus proportional to $D_v^{1/4}$ so proportional to $exp(-Ev,m/(4k_BT))$. Experimental results of $ln(L)$ (L=12/20/25/40/50 nm) in function of $(4k_BT)^{-1}$ for 400/450/510/550°C are plotted in Figure 7.4. Error bars are plotted only for our experiment data since the

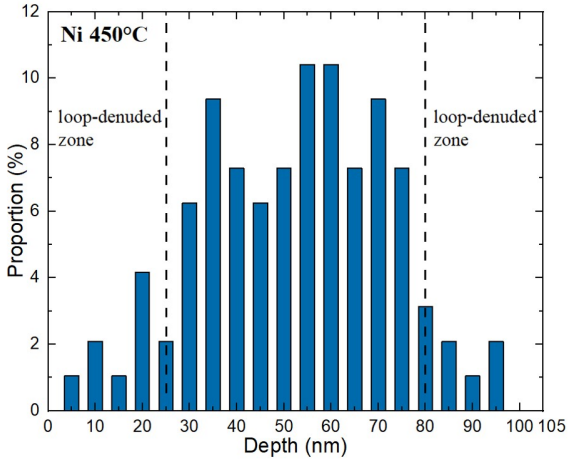

Figure 7.3 Depth distribution of loops in Ni irradiated at 450°C to 0.18 dpa. The width of loop denuded zones is about 25 nm on each side of the foil.

uncertainty of L is not given in the literature. Data at T>400°C leads to a fairly good linear fitting considering the error bar. The fitted slope reads 1.2 ± 0.1 eV, which gives a good estimation of migration energy of vacancy from self-diffusion experiments (1.24 eV (Tucker et al., 2010) and by some simulations (1.32 eV (Lu et al., 2016b), 0.92-1.46 eV (Poletaev and Starostenkov, 2010)) in the literature.

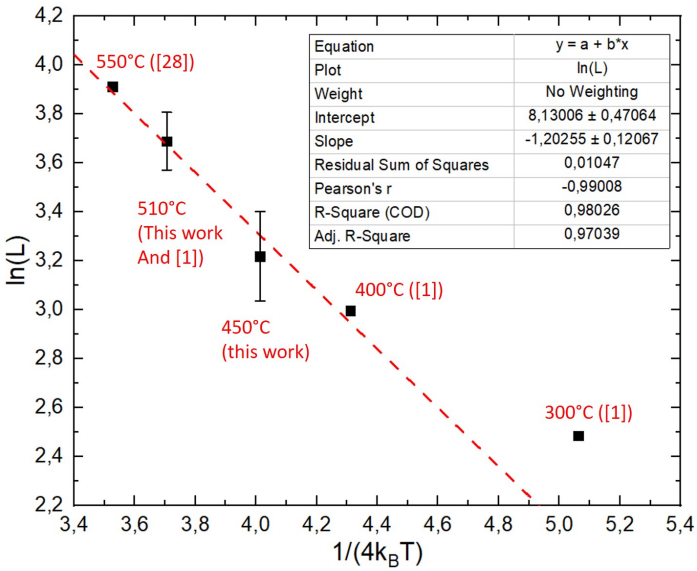

Figure 7.4 Plot of $(4k_BT)^{-1}$ v.s. $ln(L)$. T is the irradiation temperature in K, L is the thickness of loop depleted zone at each side of the foil, k_B=8.617x10^{-5} ev/K is the Boltzmann constant. Error bar of y axis results from the uncertainty of depleted zone thickness (±5 nm).

Yet, the data at 300°C deviates from the fitting line. There are three possible explanations. The first explanation is related to the uncertainty of the loop-denuded thickness determination. The uncertainty and the error bar increase significantly at lower temperatures. The fact that error bars were not given at 300°C and 400°C in (Ishino, 1997) and at 550°C in (Niwase et al., 1993) could induce a slight discrepancy of the plotted slope. The second reason might be a potential influence of injected gaseous impurities (Ar^+ irradiations at 300/400°C in (Ishino, 1997)) on the mobility of vacancies since it is known that impurities can impact the migration of PDs (Baskes et al., 1979). The third one is the applicability of Equation 7.6 at low temperatures. At T<400°C, the nature of loops nucleated at 300°C could change. Foreman suggested that the denuded zone of interstitial defects should be a measure of the interstitial mobility instead of the vacancy mobility (Foreman, 1972). Therefore, the correlation between $ln(L)$ and $(4kBT)^{-1}$ might no longer be related to the diffusion coefficient of vacancies but the one of interstitials. This will lead to a much smaller slope ($E_{i,m}$ ≈0.15eV (Tucker et al., 2010)), which consists with the reduction of slope towards lower temperatures shown in Figure 7.4.

7.1.3 Surface effects on the proportion of Burgers vectors of perfect loops

In Figure 4.16, unequal distribution of Burger vectors of perfect loops is observed in irradiated Ni. A plausible mechanism to explain this phenomenon is the preferential absorption of some loops by surfaces. During in situ experiments, many loops move along <110> directions and disappear probably at surfaces as shown in Figure 4.22(a).The loop displacements and absorption might be influenced by its Burgers vector. To understand this point, it is thus interesting to wonder firstly whether the movement of a perfect loop with **b**=1/2<110> is along the direction of its Burgers vector <110>.

During in-situ irradiation at high temperatures, it is difficult to analyze the Burgers vector and the loop habit plane. Thus, a post-characterization was performed in irradiated Ni (510°C/0.06 dpa). Figure 7.5(a) shows a representative rhombus-shape perfect loop (no fault contrast inside the loop). Its Burgers vector is $1/2[01\bar{1}]$ (Figure 7.5(b-c)). The two segments of the rhombus (D1 and D2) are respectively [321] and $[\bar{3}21]$. Detailed determination of the segment directions is presented in Appendix A. The loop plane normal $\mathbf{n}_{loop}$ is obtained by $\mathbf{n}_{loop}=[321]\wedge[\bar{3}21]=[0\bar{1}2]$ with the convention $\mathbf{n}_{loop}$ pointing always upward. Perfect loops with similar segment directions and loop planes were detected in Al-based alloys in the literature (Makin and Hudson, 1963).

Figure 7.5(d) shows schematically the loop structure. The two segments [321] and $[\bar{3}21]$ are respectively in $(\bar{1}11)$ and (111) planes which are slip planes in fcc structure. The intersection of the two planes is $[0\bar{1}1]$, therefore the common slip direction of the two segments is collinear with the loop Burgers vector $1/2[01\bar{1}]$. Since the loop keeps its form during the

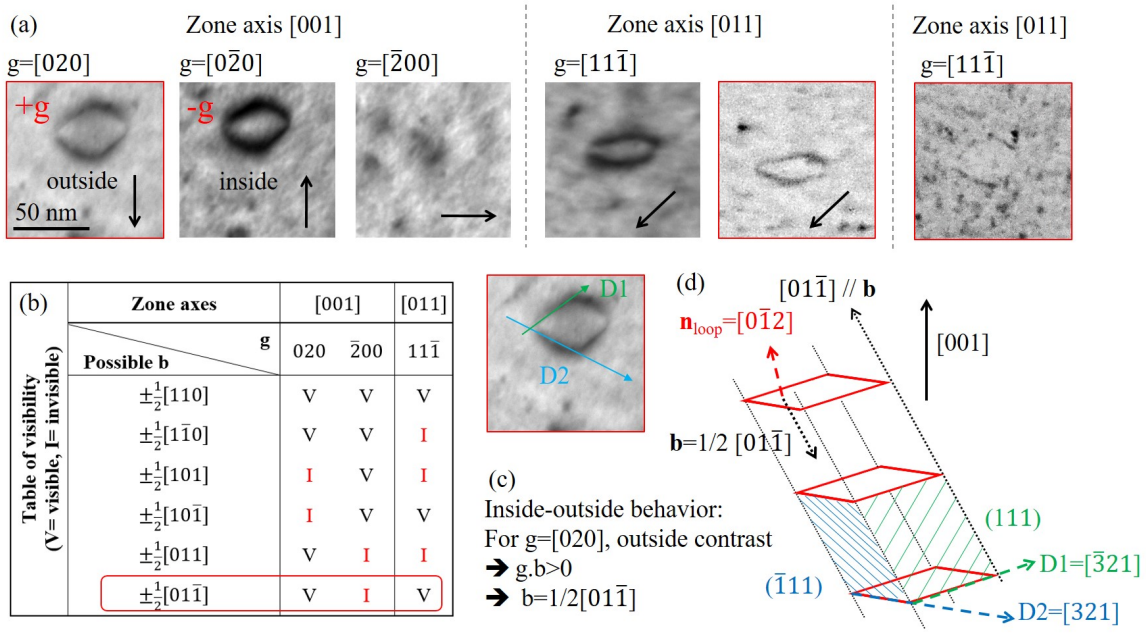

Figure 7.5 Analysis of Burgers vector and habit plane of an rhombus perfect loop in Ni irradiated at 510°C up to 0.06 dpa. (a) TEM micrographs showing the visibility of the loop with the same scale bar in the first one. (b) Table of visibility showing the Burgers vector. (c) Inside-outside contrast analysis determining the sign of the Burgers vector. (d) Directions of line segments and the habit plane of the rhombus loop; the segment directions are determined from TEM micrographs with red frame. (See Appendix A for more details.)

movement (Figure 4.22(a)), the loop segments move together and should slip along a common direction. From this post-characterization of loop structure, we reasonably assume that the motion of a perfect loop is along the common slip direction of its segments thus its Burgers vector. This movement of rhombus perfect loops consists perfectly with the slip systems (on 111 planes in <110> directions (Hull and Bacon, 2011)) of the fcc structure.

It is noted that the loop habit plane is not exactly in pure edge position (deviation of 18°) in Ni (this work) and Al alloys (Makin and Hudson, 1963). Calculations in Al and copper showed that the position of the minimum elastic energy of a rhombus-shaped loop depends on its size in the fcc structure (Bacon et al., 1970). For an infinite large loop ($L = \infty$), the elastic energy reaches a minimum at pure edge position. For a real loop with a finite radius (typically $L = 100$ nm as shown in (Makin and Hudson, 1963)), the minimum position is deviated from the edge position. In Ni, further calculations would be interesting to confirm this point.

To understand the unequal distribution of perfect loops (Figure 7.6(a)), the normal of the studied foil and the Burgers vectors of perfect loops are plotted in Figure 7.6(b). The angle between the foil normal and each Burgers vector is shown. The direction [011]

is the closest direction to the foil normal while $[01\bar{1}]$ and [110] are far from it. We could expect that families of loops having shorter path lengths along the motion direction to the foil surface would be depleted compared to other families. This is in agreement with the experimental observations for most families except $1/2[1\bar{1}0]$ perfect loops. One possible explanation could be an easier interception of these loops by surfaces due to their habit plane, which is approximately perpendicular to the Burgers vector. As the $[1\bar{1}0]$ direction is almost parallel to the surfaces (Figure 7.6), the habit plane of $1/2[1\bar{1}0]$ loops is almost perpendicular to the surfaces. Therefore, when $1/2[1\bar{1}0]$ loops grow and rotate to near/pure edge position, they can easily intercept surfaces and disappear. These interceptions result in a depletion of this family. It is worth noting that the influence of surfaces remains strong for a 180 nm thick zone where the absorption of PDs by surfaces is moderate. It shows that surfaces affect not only primary defects like PDs but also larger defects like dislocation loops. For a further investigation, it would be of great interest to study thicker zones and bulk material to investigate if a critical thickness exists above which the proportion of Frank loops and perfect loops is no longer affected by the surfaces.

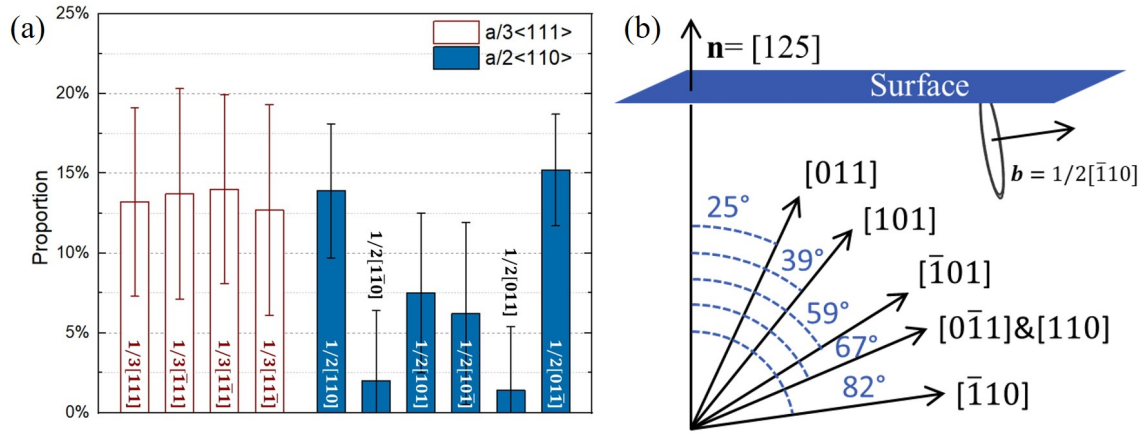

Figure 7.6 Distribution of Burgers vectors in a [125] foil and the angle between each Burgers vector and the surface. (a) Distribution of Burgers vector presented in Figure 4.16; (b) angle of each **b** to the foil normal [125].

7.2 On the origin of vacancy loop growth in Ni: the formation of I-clusters

For the first time, large stable vacancy Frank loops are observed in thin foils and in bulk Ni after high-temperature irradiation. These observations seem to contrast with most previous studies where large stable loops were reported as interstitial-type (Chen and Ardell, 1976; Ishino et al., 1984; Mazey and Hudson, 1970; Norris, 1970). Vacancy loops were only

reported as meta-stable (Ishino et al., 1984; Robinson and Jenkins, 1981) or either near other dislocations (Urban, 1971).

The mechanism of the growth of dislocation loops was explained by dislocation bias model based on rate theory (Brailsford and Bullough, 1972; Yoo and Stiegler, 1977). The concentrations of PDs are described by rate equations:

$$\frac{dC_v}{dt} = \phi - K_R(D_i + D_v)C_iC_v - k_v^2 D_v C_v \tag{7.7}$$

$$\frac{dC_i}{dt} = \phi - K_R(D_i + D_v)C_iC_v - k_i^2 D_i C_i \tag{7.8}$$

where ϕ is the creation rate by irradiation in dpa/s, K_R is the recombination coefficient with r_c the recombination radius and k_α^2 is the sink strength for species α (i or v). The sink strength is the sum over the different objects (dislocation lines, loops, surfaces, and etc.). In steady-state, Eqs 7.7 minus Eqs 7.8 gives:

$$k_i^2 D_i C_i = k_v^2 D_v C_v \tag{7.9}$$

Without the emission of PDs from loops, the growth rate of a loop is given by (Yoo, 1977):

$$\frac{dR}{dt} = \frac{\Omega}{b}(Z_{l,i} D_{l,i} C_i - Z_{l,v} D_{l,v} C_v) \tag{7.10}$$

where R is the loop radius, t is the time, b is the Burgers vector, Ω the atomic volume, D_α and C_α the diffusion coefficient and concentration of species α (α=i for interstitials or v vacancies). The constant $Z_{l,\alpha}$ is an absorption efficiency which depends on the elastic interaction between a PD and the loop. This formula is the opposite for a vacancy loop. Therefore, if the growth rate $\frac{dR}{dt}$ is positive, the loop accumulates interstitials. If $\frac{dR}{dt}$ is negative, the loop accumulates vacancies.

With Equation 7.9, Equation 7.10 can be rewritten as:

$$\frac{dR}{dt} = \frac{\Omega}{b} Z_{l,i}(B_l - \bar{B}) D_v C_v \tag{7.11}$$

where $B_l = \frac{Z_{l,i} - Z_{l,v}}{Z_{l,i}}$ is the bias of the dislocation loop and $\bar{B} = \frac{k_i^2 - k_v^2}{k_i^2}$ is the average bias of the medium. If the average bias in the medium is stronger than the bias of dislocation loops, the growth rate of dislocation loops will be negative i.e. loops will absorb more vacancies than interstitials. It will lead to a growth of vacancy loops and the shrinkage of interstitial ones.

In the conventional dislocation bias model, dislocation lines/loops and voids are two major defects considered. Both vacancy loops and interstitial loops have both a positive bias (Carpentier, 2018; Woo, 1982). Voids are usually considered as a neutral sink. Thus, it leads

to $B_l > \bar{B}$ i.e. interstitial loops can grow while vacancy loops would shrink under irradiation. The origin of the growth of vacancy loops is thus not theoretically understood within the conventional rate theory. To further understand the mechanism, two factors should be taken into account:

1) **Production bias** (Figure 7.7(a)): The conventional rate theory assumes a homogeneous production of isolated vacancies and interstitials at an equal rate. Some studies showed that this assumption may not be appropriate with the presence of cascades. Self-interstitials partially form clusters within the cascade to a greater extent than vacancies (Woo and Singh, 1992; Zinkle and Singh, 1993). Moreover, interstitial clusters were found to migrate in long-distance 1D motion in Ni (Lu et al., 2016b), they could quickly escape the production zone. Thus, in the damage production zone, very few interstitials or interstitial clusters remain accessible for dislocation loops, leading to the growth of vacancy loops.

2) **Medium bias** (Figure 7.7(b)): Recently, a DFT study in fcc metals (Cu and Al) (to be published by A.M. Goryaeva, M.C. Marinica et al.) shows a possible existence of a strong sink for interstitials. They identify a stable configuration of interstitial clusters consisting of 15 self-interstitials atoms (SIAs), called A15. By molecular dynamics (MD) simulation, this type of clusters can be formed under irradiation. Moreover, it attracts strongly SIAs, in another word, it has a strong bias. The size of this cluster increases by absorbing SIAs. From DFT calculations, when the cluster size increases, most A15 clusters could transform into 1/3<111> Frank loops (case of Al) or 1/2<110> perfect loops (case of Cu). Data in Ni will be studied in further work. Here, we tend to believe that A15 clusters are very likely formed in Ni. The presence of A15 clusters could strongly increase the medium bias $\bar{B}$. The growth of vacancy loops could thus be favored.

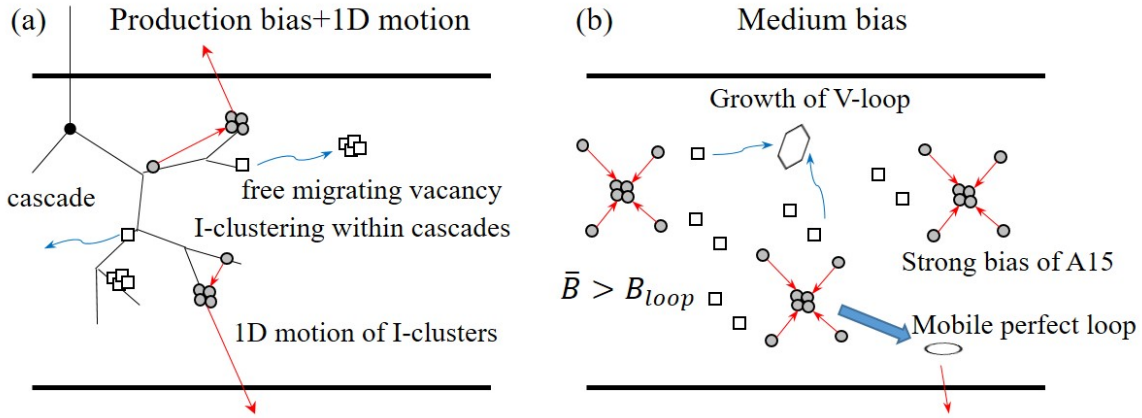

Figure 7.7 Schematic illustration of production bias hypothesis and medium bias hypothesis.

Under ion irradiation, it is difficult to study separately these mechanisms. It is thus interesting to focus on electron irradiations or high-energy light-ion irradiations where no or very few cascades should be created. We remind that the microstructural evolution of Ni under electron irradiation at high temperatures has been extensively studied. The nature of large Frank loops was only reported to be interstitial but was rarely demonstrated. Within the framework of this thesis, we performed a series of electron irradiation experiments at 450°C using a 1 MeV EM7 High Voltage Electron Microscope (HVEM) located at CEA-Saclay. Detailed results are presented in Appendix B and summarized in Table 7.1.

Table 7.1 Summary of HVEM experiments at 450°C in Appendix B.

No.	Materials	Flux (µA)	Pre-irradiation	Microstructural evolution at 450°C
(I)	Ni	0.017	/	Rare nucleation of loops
(II)	Ni	0.05	/	Rare nucleation of loops
(III)	Ni	0.017	30 s at T_{room}	Growth of interstitial Frank loops, rare nucleation at 450°C
(IV)	Ni-0.4Ti	0.017	/	Very low density of loops, growth of perfect loops

At 450°C (Experiments (I) and (II)), the nucleation and growth of visible loops is scarce. Only three radiation-induced loops are detected during several hours of irradiation. The nature of these loops can not be determined as they disappeared during the experiment. It is thus difficult to discuss these results due to a lack of post-characterization and statistics. However, these observations still suggest two possible mechanisms:

(1) it may be hard to nucleate defects with only mono-interstitials or mono-vacancies due to their high mobility at a high temperature in our conditions (450°C, 0.017 µA);

(2) small clusters may form but migrate fast to the surfaces and disappear.

To investigate the mechanism (1), we increased the electron flux to a much higher value than 0.05 µA, which induces a higher production rate of PDs and may increase the nucleation probability. Still there was no visible growing loops for an irradiation of 20 minutes. The nucleation density is not visibly increased. The flux may be still too low. Otherwise, it may be related to the second mechanism.

There are two explanations for Mechanism (2). The first one is the 1D motion of I-clusters. Once I-clusters are formed, they quickly migrate to the surface along a long-distance 1D motion. The second one is the transformation of I-clusters into mobile perfect loops. When I-clusters grow by agglomerating interstitials, a majority of them transform into perfect loops and slip to surfaces when they are small. Some I-clusters could turn into Frank loops.

The only visible loops would be these Frank loops if they can grow (the interstitial depletion due to the elimination of perfect loops might cause a super-saturation of vacancies).

As it is difficult to create loops, it is essential to increase the nucleation density in order to improve the statistics and to determine the nature of loops induced by electron irradiation.

To increase the loop density, the first method employed is a pre-irradiation at room temperature (Experiments (III)). This time, we observed much more loops and their growth during the irradiation. We still note that no loop was newly created during the irradiation. All grown Frank loops are found to be interstitial-type (Appendix B.2). They remain non-segmented even up to an enormous size with a diameter > 0.5 µm (Figure 7.8(a)). One explanation is that, at room temperature, as the surface sink is reduced and interstitials can agglomerate, they can turn into either Frank loops and perfect loops. When the temperature increases, some perfect loops may slip to the surfaces while all Frank loops could remain and grow, as they are sessile. However, it is worth to note that loops formed directly at 450°C (Figure 7.8(b-c)) seem to be segmented. It is also worth noting that, in most studies on electron irradiated Ni (Harbottle and Norris, 1973; Norris, 1970; Urban, 1971), no loops were newly created during high temperature irradiations from their TEM images, except one loop in the paper of (Norris, 1970) as shown in Figure 2.15(a). This loop is also presented in Figure 7.8(d) and claimed as interstitial-type. However, the loop is clearly segmented. These observations raise question about the nature of Frank loops directly created during the high temperature electron irradiation. It becomes thus essential to unambiguously determine the nature of loops directly formed at a high temperature in order to further discuss these results.

The second method to increase the loop density is an addition of Ti (Experiment IV), which is shown to reduce significantly the mobility of perfect loops under ion irradiations. Under electron irradiations, the nucleation density increased slightly (Appendix B.3). The growth of several perfect loops is observed. By a post-characterization, the nature of a perfect loop is interstitial-type. We assume that some perfect loops indeed could form directly at the high temperature and be trapped by Ti. These observations do not contrast with the A15 model. However, it will be crucial to prove directly the existence of A15 and perform further calculations showing how A15 can transform into loops in function of flux and temperature in Ni.

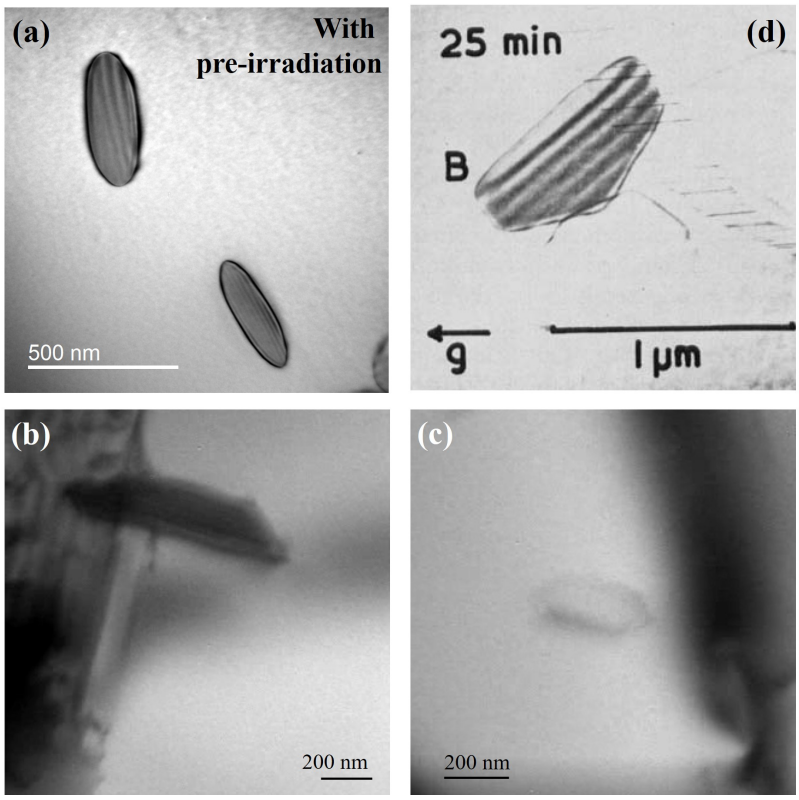

Figure 7.8 Morphology of Frank loops created under electron irradiation. (a) Interstitial Frank loops in pre-irradiated Ni (Experiment III); (b-c) Frank loops in Experiment II; (d) a Frank loop, noted B, created at high temperature irradiation in (Norris, 1970).

7.3 Drastic effects of solute on Frank loop nature and microstructural evolution

7.3.1 Solute effects on point defect mobility affecting Frank loop nature and defect distribution

By molecular dynamics (MD) calculations, Lu et al. reported that solutes like Fe and Co can increase the migration energy barrier of I-clusters, resulting in a short-distance complex migration trajectory (Lu et al., 2016b). The reduced mobility of I-clusters can change drastically the nature and distribution of defects in irradiated Ni (Lu et al., 2017).

In this study, the nature of Frank loops in thin foils and bulk specimens of Ni is the same (vacancy-type). In the alloys, interstitial Frank loops are detected. However, Frank loop nature in the alloys depends on the form of specimens, the irradiation depth in bulk and irradiation temperature. This point have to be understood before discussing solutes effects on Frank loop nature and their mechanisms.

Ni-0.4Cr

In Ni-0.4Cr irradiated at 450°C, Frank loops are vacancy-type and segmented in the thin foil and in zones near surface (<600 nm) of bulk specimens. In these regions, microstructural evolution should be dominated by the vacancies. In deeper zones of the bulk sample, a dislocation network is present and Frank loops at this depth are non-segmented and of interstitial nature, suggesting a super-saturation of interstitials under these irradiation conditions. We suppose that Cr reduces te 1D motion of I-clusters that occur in Ni. I-clusters can migrate from their production zone but most of them remain in the global damage production zone. This phenomenon would explain the existence of vacancy Frank loops close to surfaces and the formation of irradiation-induced defects slightly after the injected ion depth predicted by SRIM.

Ni-0.4Ti

The case of Ni-Ti irradiated at 450°C seems to be the opposite case of Ni-0.4Cr. Large interstitial Frank loops exist in Ni-0.4Ti thin foils. However, in the bulk specimen, no large interstitial Frank loop is detected while a strong dislocation network with large interstitial perfect loops and small segmented Frank loops (supposed to be vacancy-type) are found.

Firstly, it is important to understand the change of nature in Ni-0.4Ti thin-foils compared with the two other materials. A plausible mechanism which explains the interstitial nature in thin-foil Ni-0.4Ti could still be the reduction of the mobility of interstitial defects by the addition of alloying element. The mobility of interstitials and clusters in Ni-0.4Ti may be strongly reduced compared to Ni and Ni-0.4Cr. The surface absorption becomes weak in thin foil so that interstitial defects could remain within the thin foil and grow by absorbing near-by interstitials. From the microstructure in bulk Ni-0.4Ti (Figure 5.8(a)), dislocation loops and lines are detected in zones very close to surfaces. It suggests indeed a weak surface effect thus a low mobility of PDs or clusters.

Apart from effects on PD and cluster mobility, another possible mechanism to explain solute effects is the modification of perfect loop mobility As observed in in-situ experiments, all loops are immobile. Perfect loops form from A15 transformations stay in the damage production zone and therefore suppress the super-saturation of vacancies. Moreover, the mobility reduction of loops and probably I-clusters with the increase of Ti content, may explain the difference of loop nature at 510°C between Ni-0.4Ti and Ni-0.8Ti. The elevation of Ti may be enough to activate the I-clusters in Ni-0.4Ti but not enough in Ni-0.8Ti and Ni-1.2Ti.

Secondly, it is interesting to wonder why no large interstitial loop is detected in bulk Ni-0.4Ti. The dislocation network in bulk may be an important factor to be considered. A dislocation network is developed from the agglomeration of perfect dislocation lines/loops.

We tend to believe that interstitial loops are formed in the early stages of irradiation, grow and agglomerate into a network. The presence of a strong dislocation network induces a super-saturation of vacancies and inhibit the growth of newly-created interstitial loops.

A plausible mechanism to explain the presence of a strong network in bulk but not in thin foil may be the surface absorption of loops. Although the absorption of defects by surfaces is expected to be weak, the PD concentration should be always suppressed in thin foils due to the surface absorption. The thickness of the studied zone in Figure 5.3(c) where many large interstitial Frank loops are detected is about 80 nm. The zone is quite thin, and surface absorption could still play a role. Figure 7.9 presents the irradiated microstructure at different thicknesses in thin-foil Ni-0.4Ti. The dislocation line density increases with the thickness from Figure 7.9(a) to Figure 7.9(c). Meanwhile, the density of visible large non-segmented Frank loops (which are supposed to be interstitial loops) decreases with the development of network. In 250 nm thickness zones (see Figure 7.9(c)), no large Frank loop is detected with a measured dislocation line density about 1.3x10^{13} m^{-2}, which is close to the line density (1.8x10^{13} m^{-2}) at 100 nm depth in bulk. It means that the microstructure in zones thicker than 250 nm in thin foil is representative for bulk. Since in bulk and in thick zones of thin foil, the concentration of PDs is very weakly even not suppressed by the surface, most free interstitials remain in the volume and contribute to the microstructural evolution. Moreover, large loops in thin zones intercept easier with the surface than thick zones, which hinder the formation and development of dislocation network. It is thus reasonable to have a well developed network in bulk samples. In thin zones of thin foils, it seems to be irradiated to a "lower" dose than thick zones and bulk sample.

To further confirm this point, FIB specimens irradiated at 450°C to a lower dose (0.06 dpa near the surface) were prepared. At this lower dose, the network should be less develop. It is interesting to see whether large Frank loops exist. Figure 7.10 shows the global microstructure in the lower dose FIB sample of Ni-0.4Ti. A dislocation network has already been formed. The maximum dislocation line density is about 2x10^{12} m^{-2} at 800 nm depth. The depth of the maximum dislocation density is the same for the higher dose sample (0.7 dpa) in Figure 5.8(f). But the density for lower dose sample is 25 times lower. With the diffraction condition $\mathbf{g}=<200>$, all families of Frank loop should be visible if they exist. However, by searching carefully in different zones, no large Frank loop is detected. Since a network has been formed, this dose may be still too high to confirm our assumption. Otherwise, other factors must play role. We might suppose that Frank loops unfault easily in deep zones of Ni-0.4Ti bulk foil than in Ni-0.4Ti thin zones. It would explain a quick formation of network even at such a very low dose because of a strongly reduced mobility of interstitials and I-clusters.

Thirdly, the presence of segmented vacancy Frank loops in bulk Ni-0.4Ti may be attributed to the strong network. The super-saturation of vacancies produced by the network

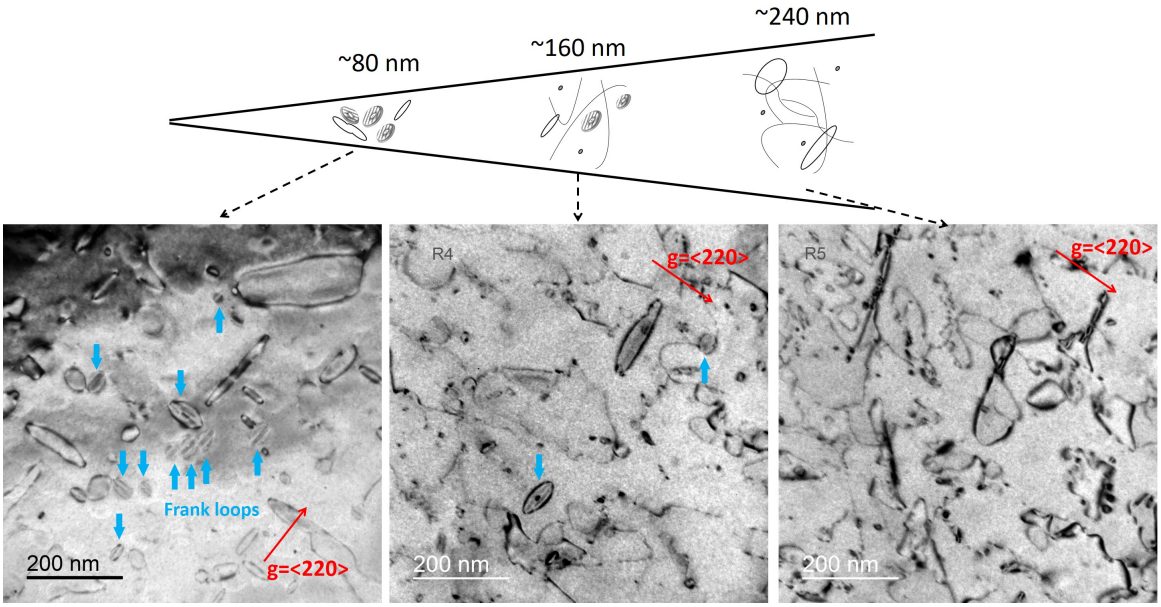

Figure 7.9 Microstructure in thin foil Ni-0.4Ti in function of foil thickness. TEM micrographs taken along zone axis <001> with **g**=<220>.

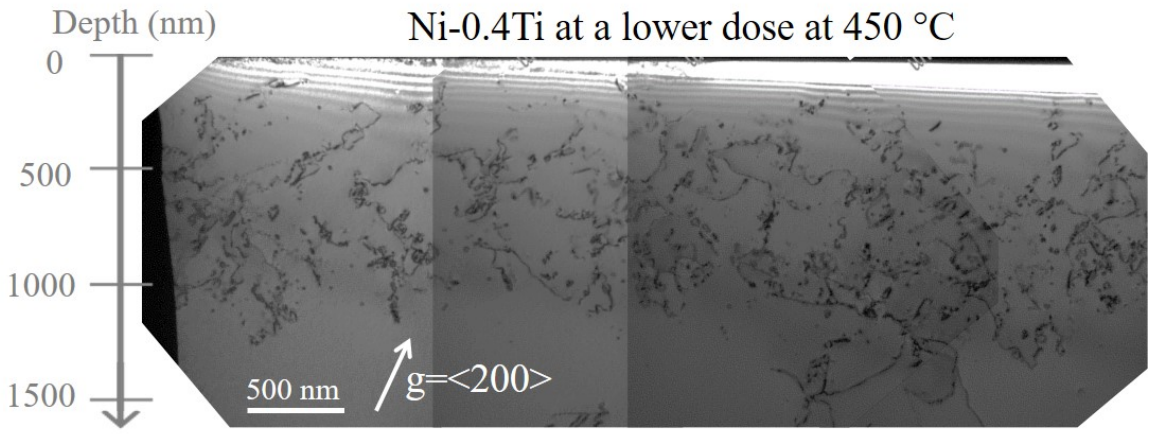

Figure 7.10 Microstructure of bulk Ni-0.4Ti irradiated at 450°C up to 2x10^{14} ions.cm−2. TEM microsgraphs are taken along zone axis <001> with **g**=<200>.

lead to the formation of vacancy defects. Larger vacancy clusters can form voids or small loops. This point will be discussed in the following subsection.

To summarize the solute effects on the nature and form of defects in Ni and alloys:

1) vacancies form intrinsic Frank loops in Ni while majority of them form voids in the alloys;

2) interstitials in Ni agglomerate as Frank loops within intrinsic Frank loops and eradicate the stacking fault. The growth of inner extrinsic Frank loops will lead to the total

eradication of the intrinsic Frank loops. Considering that loops in Ni are vacancy-type and partially eradicated, interstitials may be depleted in the damage production zone by migrating far away.

3) Contrarily to Ni, interstitials in the alloys agglomerate as single or multi-layer Frank loops.

The drastic difference of the defect nature between Ni and the alloys should be related to the reduced mobility of interstitials or I-clusters. In the alloys, interstitials atoms, I-clusters, and interstitial loops remain in irradiated zones leading to the growth of interstitial loops and the nucleation of a multi-layer structure as observed in our case. Such complex Frank loops were observed in irradiated nickel and alloys (Chen and Ardell, 1976; Das and Mitchell, 1975). As the content of solute in our alloys is very low, a minor addition of Ti or Cr modifies drastically the migration of interstitial-type defects. However, the data on the transformation of I-clusters into dislocation loops is too limited. Further studies are expected.

7.3.2 Solute effects on the formation of vacancy defects (vacancy loops v.s. voids

The nucleation and growth of vacancy defects occurs both in Ni (vacancy loops) and in the alloys (stable voids). Due to the much higher migration energy of vacancies compared to interstitials, the vacancy diffusion path is quite short (Lu et al., 2016b). Thus, vacancy clusters created in cascades can absorb nearby free vacancies and grow into larger defect in irradiated regions. It is interesting to wonder why vacancies agglomerate into different forms in Ni and in the alloys.

Some calculations in Ni demonstrate that the stable form of vacancy defects depends mostly on the number of vacancies N_v, the stacking fault energy (SFE) and the surface energy of voids (SEV) (Zinkle et al., 1987). Under a critical value of N_v, the vacancy defect should be a vacancy loop. Otherwise, it should be a void. Using the values of SFE and SEV for pure nickel (Figure 7.11(a)), the critical value is $N_{v,c}$=3.2x10^4. In this study, the average number of vacancies present in loops for Ni (≈20 nm in diameter) is ≈ 6x10^3 vacancies. This value is lower than the theoretical critical value in (Zinkle et al., 1987). Therefore those single vacancy Frank loops are energetically favorable compared to voids. However, some vacancy Frank loops are much larger than 20 nm (even >100 nm) (Figure 4.2 and Figure 4.4(c)). We believe that these large loops are stabilized by the inside interstitial loops and their energy should be much lower than a single vacancy Frank loop of the same size.

In the alloys, vacancies agglomerate mostly as voids.With a strong network in the alloys (0.7 dpa), the formation of voids is reasonable because the dislocation network provides a significant bias and create a strong super-saturation of vacancies. To understand the stability of voids compared with vacancy loops, we calculate the number of vacancies present in the

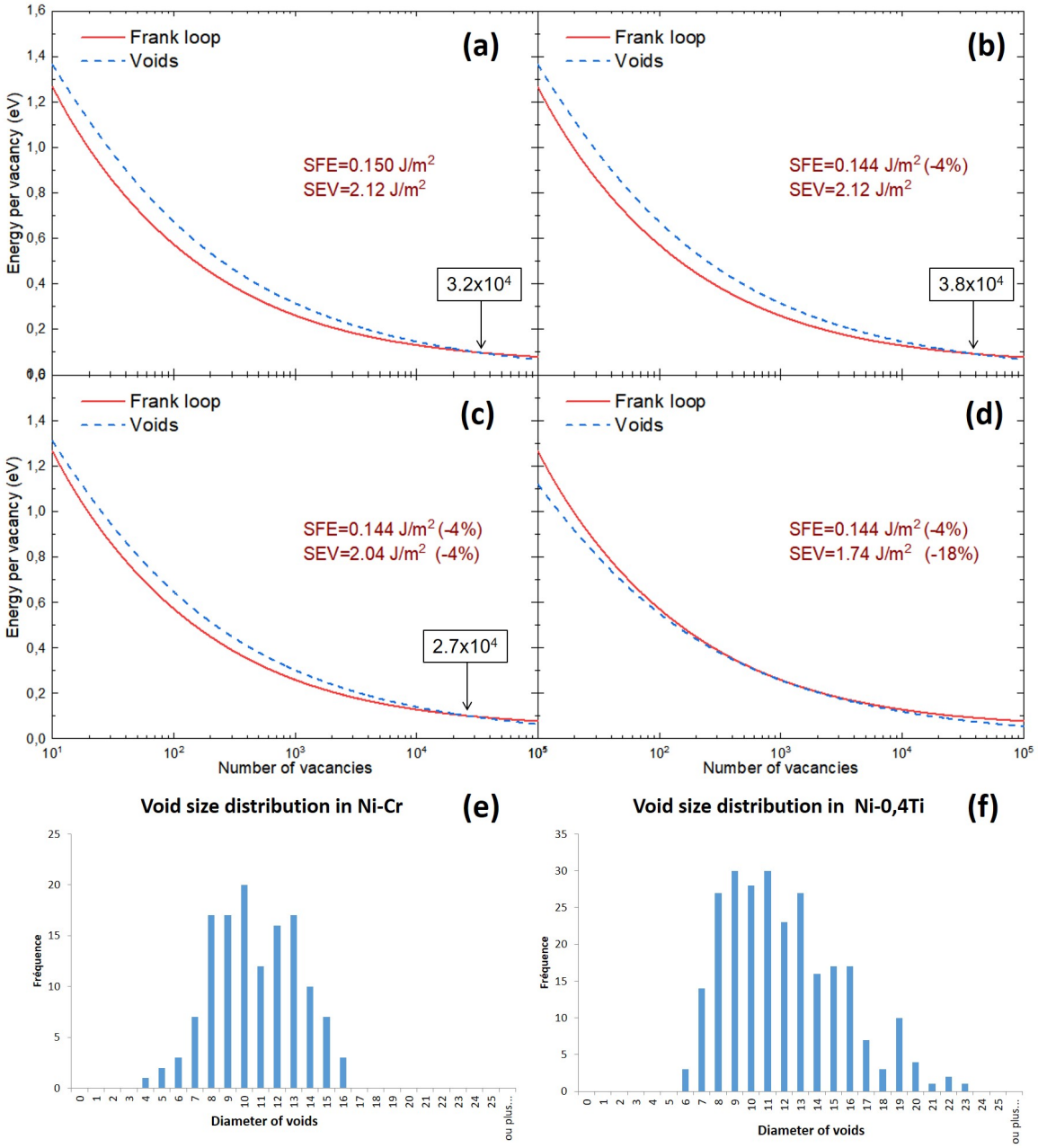

Figure 7.11 Energy of vacancy defects in function of stacking fault energy, surface energy of voids, and number of vacancies. (a) with the SFE and SEV values extracted from (Zinkle et al., 1987).

smallest voids. Figure 7.11(e) and Figure 7.11(f) present the size distribution of all voids detected respectively in Ni-0.4Cr and Ni-0.4Ti. The minimum size of voids is ≈4 nm, which corresponds to $3x10^4$ vacancies. This number of vacancies can be considered fairly of the same level of the one in vacancy Frank loops in Ni and is lower than the calculated critical value for Ni. It is interesting to wonder why, in the alloys, vacancies prefer to agglomerate into voids instead of vacancy loops.

One explanation is that the critical size could be lowered by the addition of solute, either by increasing the SFE or by reducing the surface energy of voids (SEV). The literature suggests that the addition of Ti and Cr reduces the SFE of Ni (Deléhouzée and Deruyttere, 1967; Kumar et al., 2018). Ti is very effective to reduce the SFE in Ni system. An addition of 1% at. of Ti reduces the SFE by a factor of 0.1 (Kumar et al., 2018). Figure 7.11(b) shows the energy of vacancy Frank loops and voids assuming that the SFE in Ni-0.4Ti is reduced by 4%. The critical size increases for granted, which is opposite to our assumption. Therefore, these solutes affect necessarily the SEV. Two cases with a reduced SEV are plotted in Figure 7.11(c-d) (reduction of SEV by 4% and by 18%).

- A reduction of 4% of the SEV compensates the influence on SFE. In this case, the critical value is slightly lower than the case of pure nickel. This value fits with the stability of voids in the alloys because it is lower than the number of vacancies contained in the smallest voids;
- The reduction of 18% of the SEV is an extreme case. Voids become stable for any size of vacancy cluster. As vacancy Frank loops are seen in thin foils, this case is not likely in our alloys because the solute content is only 0.4%. However, it is worth noting that, in the literature, Ni-based binary alloys contained usually >1% of solute (Chen and Ardell, 1976; Lu et al., 2016b). With high concentration of solute, a permanent stability of voids may be achieved so that vacancy loop would rarely be reported in the irradiated Ni alloys.

It would be of great interest to study the mechanism of solute effects on surface energy of voids. Experimentally, the local composition around a voids would be helpful to study a potential segregation near the voids surface. Ti atom (atomic radius 215 pm) and Cr atom (atomic radius 200 pm) are both larger than Ni atom (atomic radius 163 pm). From a thermodynamic view, these solutes would segregate to the surface of voids where the compression around solute atoms could be released. However, under irradiation, flux-coupled diffusion should also be considered. Therefore, related diffusion process and energy of voids coupled with solute would be important to better understand these solute effects.

7.4 Redistribution of solute at sinks in irradiated microstructure

The influence of solute on the dislocation loop dominated microstructure depends on the nature of solute. The radiation-induced segregation may be a key factor to understand the different role of Cr and Ti. In this section, we firstly study the theoretical RIS in Ni-0.4Ti and Ni-0.4Cr using an analytical model (Huang et al.). Then, the chemical composition is characterized using TEM-EDS and APT techniques. Experiment and simulation results are coupled.

7.4.1 Prediction of segregation in function of irradiation conditions in NiTi and NiCr

An analytical model based on a mean-field theory is developed by Huang (Huang et al.) to study the RIS in function of irradiation conditions : the point defect creation rate (dpa/s), irradiation temperature (K) and sink strengths of existing sinks. The principal of model is presented in Section 3.4. Here we apply the model in our study to predict whether RIS could take place under the present irradiation conditions. The flux and irradiation temperature was given in Chapter 3. The sink strength is estimated from the defect size and density in the microstructure.

7.4.1.1 Determination of sink strength from defect density and size in irradiated microstructure

The sink strengths of surfaces, dislocation loops, dislocation lines and voids are respectively calculated using the following formulas (Carpentier, 2018):

$$k^2_{surf} = \frac{12}{h^2} \tag{7.12}$$

$$k^2_{loop} = \frac{4\pi^2 \rho_{loop} \bar{r}}{ln(\frac{8\bar{r}}{r_{c,loop}})} \tag{7.13}$$

$$k^2_{line} = \frac{2\pi \rho_{line}(1-(\frac{r_c}{R_L})^2)}{ln(\frac{R_L}{r_c}) - \frac{3}{4} + (\frac{r_c}{R_L})^2 - \frac{1}{4}(\frac{r_c}{R_L})^4} \tag{7.14}$$

$$k^2_{void} = \frac{4\pi \bar{r}_v \rho_{void}(1-(\frac{\bar{r}_v}{R_v})^3}{1 - \frac{9}{5}\frac{\bar{r}_v}{R_v} + (\frac{\bar{r}_v}{R_v})^3 + \frac{1}{5}(\frac{\bar{r}_v}{R_v})^6} \tag{7.15}$$

where

- h is the depth for bulk samples or the thickness of thin foils

- ρ_{loop} is the loop density;
- $\bar{r}$ is the average size of loops;
- $r_{c,loop}$ is the the theoretical cross-section radius of dislocation taken as the $\frac{1}{2}|\mathbf{b}|$ with $\mathbf{b}$ the Burgers vector of the loop;
- ρ_{line} is the dislocation line density;
- $R_L = \sqrt{\frac{1}{\pi\rho_{line}}}$ is the outer radium of a dislocation line;
- ρ_{void} is the void density;
- $\bar{r}_v$ is the average radium of voids;
- $R_v = \sqrt[3]{\frac{3}{4\pi\rho_{void}}}$ is the outer radium of voids;

Experimentally, each irradiation conditions (flux and temperature) will lead to one irradiated microstructure where the defect density and size are different from one to another. With these three factors as input parameters (flux, temperature, sink strength in the irradiated microstructure: thickness + density/size of loops, lines and voids), the model can estimate the RIS in the system. Ideally, the sink strength for each flux and temperature has to be recalculated. However, as a first application of the model, we assume a constant sink strength for a given system in the range of interest of irradiation conditions (the flux and irradiation temperature of our ex-situ and in-situ experiments). In this way, the model can produce a 2D map to predict the RIS in function of flux and temperature. This assumption is not too bad because the total sink strength in thin foil Ni irradiated in-situ at 400/450/510°C are in the same magnitude (10^{14} m^{-2}) although their loop-dominated microstructure is different from one to another.

The objective is to study the RIS around dislocation loops in Ni-0.4Cr and Ni-0.4Ti. We consider bulk samples for this simulation. We choose the bulk samples to minimize the surface effects in thin foils on the RIS. Moreover, grain boundaries are far away (>100 µm) from the zone where we lift out bulk samples so the influence of grain boundaries on solute content during the irradiation can be neglected as well. The RIS depends thus mainly on the nature and density of the radiation-induced defects (loops, dislocations, voids). The depth distribution of average loop size, loop density, dislocation line density, average voids size and void density in function of the depth has been given in Figure 5.4 and Figure 5.8. We take the data at 500 nm depth to estimate the sink strength in the two alloys. Since Equation 7.12 is for a foil, here in bulk we consider roughly h as two times of the depth as a very rough approximation. Experiment data used for the calculations of sink strength are listed in Table 7.2 and results are given in Table 7.3. It is worth to mention that the absorption of PDs by surface is indeed lower than the other terms.

Table 7.2 Experiment data used for the calculations of sink strength.

	Depth	Loop density	Loop size	Line density	Void density	Void size
	(nm)	(m^{-3})	(nm)	(m^{-2})	(m^{-3})	(nm)
Ni-0.4Cr	500	5x10^{20}	20	2x10^{13}	4x10^{20}	10
Ni-0.4Ti	500	15x10^{20}	18	4x10^{13}	3x10^{20}	12

Table 7.3 Sink strength (m^{-2}) of each sink for the calculation of RIS.

Sinks	Surface	Dislocation loops	Dislocation lines	Voids
Ni-0.4Cr	1.2x10^{13}	1.7x10^{13}	5.6x10^{13}	6.3x10^{13}
Ni-0.4Ti	1.2x10^{13}	4.5x10^{13}	11.9x10^{13}	5.8x10^{13}

7.4.1.2 Theoretical map of RIS in function of flux and temperature

Using the sink strength in Table 7.3, the model of Huang (Huang et al.) allows to calculate the amount of solute atoms B segregated at dislocation loops S_B in function of damage flux ϕ and irradiation temperature T. The sign of S_B describe the nature of RIS:

- S_B=0: there is no RIS;
- S_B>0: there is an enrichment of solute B at the sink;
- S_B<0: there is a depletion of B at the sink.

Results of S_B in function of damage flux ϕ and irradiation temperature T is presented as maps in Figure 7.12(a) and Figure 7.12(b) respectively for Ni-0.4Ti and Ni-0.4Cr. The two maps both consist of three zones: (i) a vacancy-diffusion dominant zone, (ii) a RIS zone where majority of PDs are eliminated at sinks and (iii) a SIA-vacancy recombination dominated zone. In the zone (i) and (iii), there is no RIS. Outside these two zones, S_B is no longer zero and RIS could occur. The nature of RIS is different between Ni-Ti and Ni-Cr systems. In Ni-0.4Ti, S_B is negative i.e. Ti is depleted at the sink. On the contrary, in Ni-0.4Cr, S_B is positive so Cr is enriched at the sink.

However, when RIS is too weak (corresponding to a small $|S_B|$), it is difficult to detect experimentally the RIS phenomenon, especially when the solute content is very low in this thesis. Therefore, RIS is only expected to be detected in the green zone of Ni-0.4Ti map and in red zone of Ni-0.4Cr. In Figure 7.12, the irradiation conditions of ex-situ experiments (6x10^{-5} dpa/s and 723 K) and in-situ experiments (3x10^{-4} dpa/s and 773 K) are indicated respectively by the orange point and the grey point. In Ni-0.4Ti, the condition of both ex-situ and in-situ experiments are in RIS zone. The RIS is expected to be more pronounced in ex-situ irradiated specimens. In Ni-0.4Cr, both experiments are in the intermediate zone between the RIS zone and the recombination zone. If the RIS occurs, it should be weak. Therefore, in the following part, we focus on the investigation of RIS in the Ni-0.4Ti alloy.

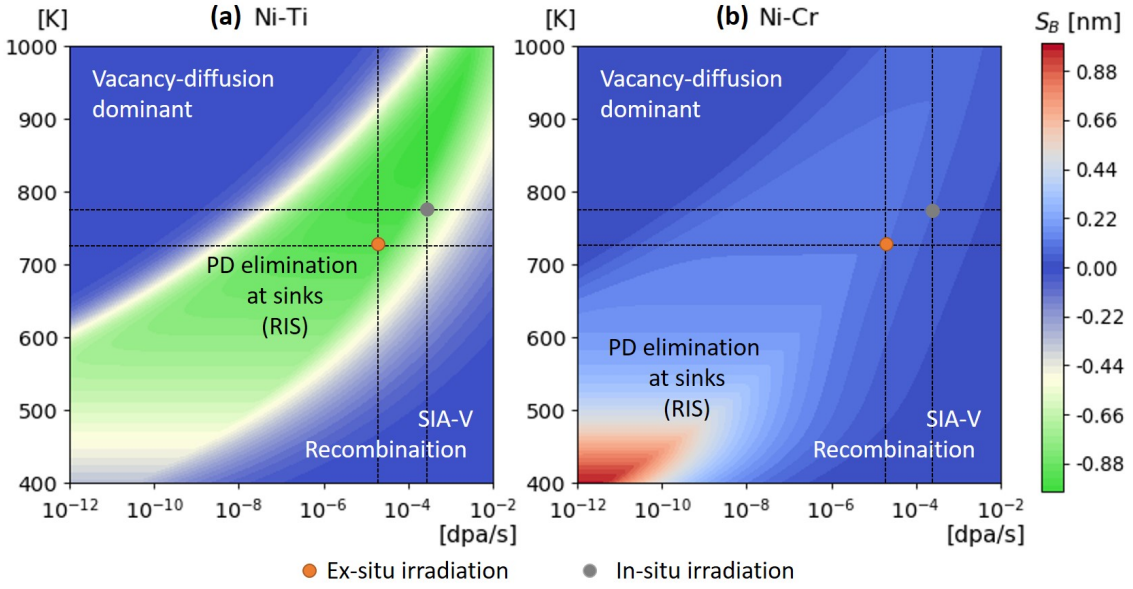

Figure 7.12 RIS simulation

Table 7.4 Content of Ti before unirradiated Ni-0.4Ti samples by APT analysis.

Materials	Unirradiated samples			Unirradiated side		Average
Specimen No.	1	2	3	4	5	
Ti% at.	0.36% ±0.003%	0.38% ±0.003%	0.38% ±0.005%	0.35% ±0.008%	0.34% ±0.008%	0.36% ±0.01%

7.4.2 Solute distribution before irradiation

Unirradiated samples are analyzed by APT to confirm the homogeneity of Ti distribution before irradiation. Specimens were prepared by FIB from unirradiated Ni-0.4Ti specimens and unirradiated side of irradiated Ni-0.4Ti foils. The content of Ti is shown in Table 7.4. We remind that the initial content of Ti in the raw material is 0.39% wt. corresponding to 0.48% at.. The Ti content in prepared samples (0.36%at.) is lower than the expected value. It might result from a heterogeneity of the Ti concentration along the raw materials (30 cm long metal bars). As all our samples were taking around the same location along the bar (1 cm max), the Ti content is homogeneous among them.

7.4.3 Radiation-induced segregation in Ni-Ti at 450°C

This section focuses on the experimental investigation of RIS in irradiated Ni-0.4Ti. Firstly TEM-EDS was performed on the as-irradiated Ni-0.4Ti thin foil to investigate the

RIS at dislocation loops. Secondly, APT analysis was conducted on needle-shape specimen lifted from the bulk sample at depth and near surface to study the Ti content in the bulk material.

7.4.3.1 Characterization by TEM-EDS around dislocation loops in Ni-Ti

EDS measurements were performed in STEM mode on the dislocation loops in irradiated Ni-0.4Ti sample irradiated at 450°C up to 0.7 dpa by 5 MeV Ni^{2+} ions. To optimize the signals, the habit plane of dislocation loops has to be exactly perpendicular to the electron beam direction i.e. loops are in edge-on position. STEM mode was used to image the loops in High Angle Annular Dark Field (HAADF) imaging modes (CARTER et al., 1996). The HAADF image in Figure 7.13(a) shows a perfect loop in edge-on position. The spectroscopy measurement in Figure 7.13 reveals that there is a depletion of Ti and an enrichment of Ni at the dislocation loop.

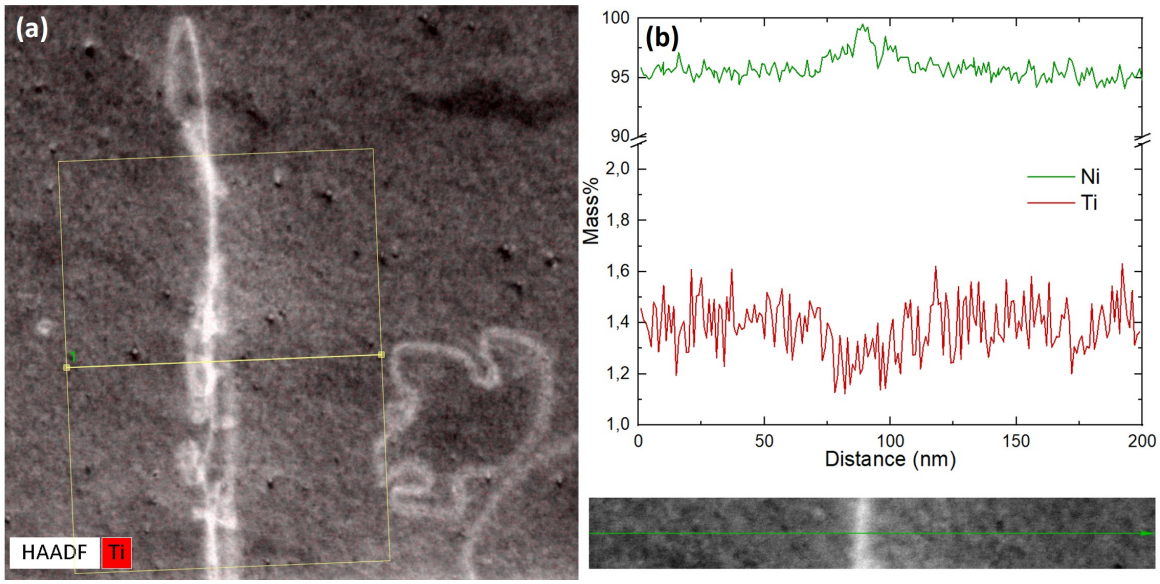

Figure 7.13 Characterization of Ni-0.4Ti irradiated at 450°C to 0.7 dpa. (a) STEM-HAADF of a dislocation loop in edge-on position; the yellow line represents the trace of the line scan for EDS measurement; (b) concentration of Ti and Ni in weight percent on the dislocation loops; EDS analysis performed in a 200 kV FEI Talos F200X TEM equipped with four EDS detectors in collaboration with ETH-Zurich by Dr. R. Schäublin.

7.4.3.2 APT analysis of irradiated Ni-0.4Ti at depth

APT experiments were performed to quantitatively investigate the Ti distribution within the dislocation loops. APT needles were lifted at depth between 200 nm - 500 nm in order to intercept dislocation loops. The distribution of Ti in most APT needles is homogeneous.

In two needles, Ti depleted zones were detected. A 3D reconstruction of a needle is shown in the middle of Figure 7.14. Two zones (a) and (b) in which Ti% is lower than the matrix are observed and their 1D concentration profiles along Z-axis on the two sides of Figure 7.14 indeed show the Ti-depletion and Ni-enrichment. In the TEM bulk sample of Ni-0.4Ti, only dislocation loops, lines and voids are currently detected. These two zones could not be a dislocation line, or a void since the Ni content increases. Considering the Ti-depletion at a loop by EDS, these Ti-depleted zones correspond very likely to two dislocation loops.

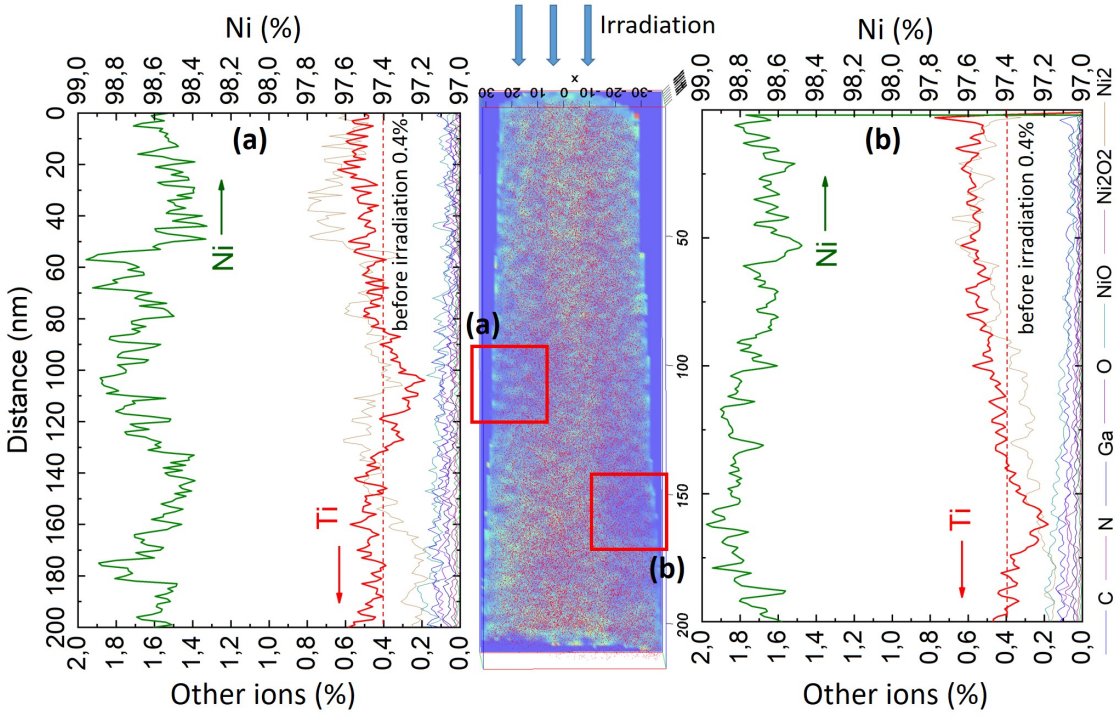

Figure 7.14 RIS simulation

Out of these two depletion zones, Ti is homogeneously distributed in the whole volume and the content is around 0.5%at.. The Ti content in the matrix is clearly higher than the initial Ti content of unirradiated samples (0.36 at.%, Table 7.4). Table present the average Ti content in other APT needles after irradiation. No segregation is detected in these sample but the Ti content varies from one volume to another. The average Ti content is 0.49%at.. The increase of Ti concentration in the matrix could might from the depletion of Ti around radiation-induced defects.

Figure 7.15 shows the comparison between the experimentally measured profiles of Ti content within the two Ti-depleted zones (Figure 7.14) and the calculated profile using the model of Huang (Huang et al.). The coupling of the experiment and the modeling is fairly good. The increase of Ti concentration in the matrix and the "V" profile at loops are in good agreement within the results. The calculated Ti concentration at sink is reduced to 0 in the

Table 7.5 Content of Ti of in irradiated Ni-0.4Ti samples by APT analysis (Ti content in %at. and volume in 10^4 nm^3).

Specimen	Electric mode				Laser mode				Average
No.	1	2	3	4	5	6	7	8	
Ti content	0.46	0.58	0.58	0.52	0.40	0.29	0.40	0.65	0.49
	0.004	0.004	0.003	0.002	0.003	0.004	0.002	0.009	0.004
Volume	16	12	61	34	9	9	56	12	/

model as the equilibrium concentration at sink is unknown. Taking in into account would change the simulated profile and would better fit with experimental results.

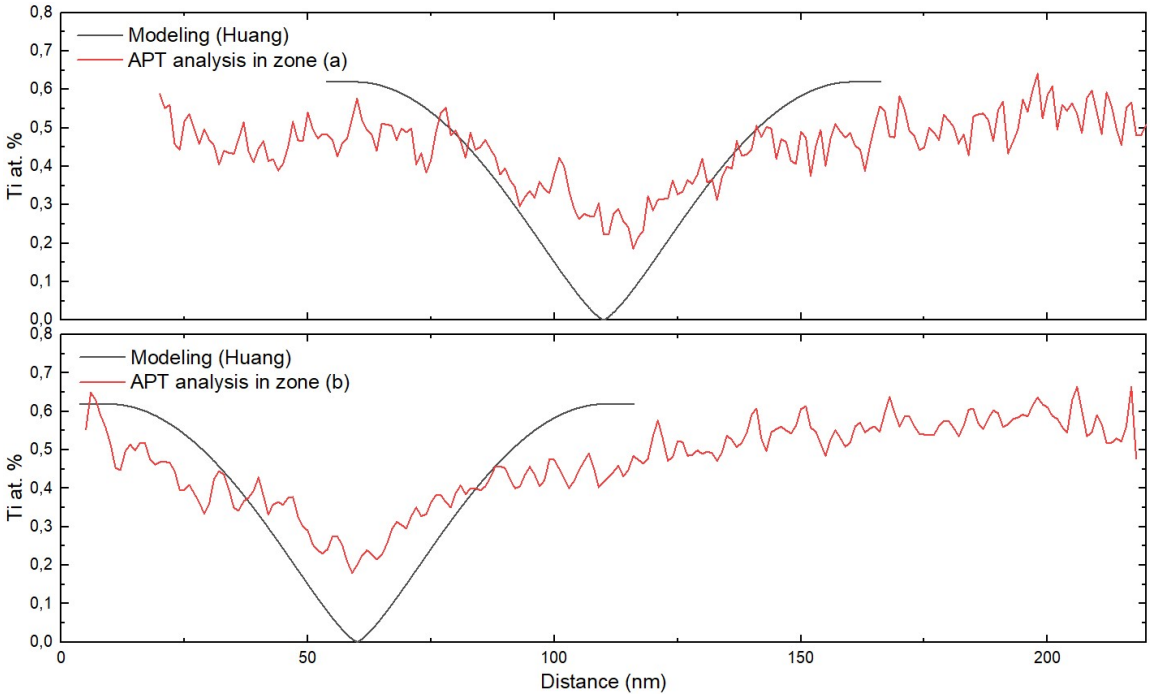

Figure 7.15 Comparison of experiment and simulation results on Ti depletion profile in Ni.

7.5 Combining effect of Ti and C on the irradiation behavior of Ni

In this section, we first remind the main result in the NiTiC system (Table 7.6) summarize the effects of carbon addition in Ni-0.4Ti: (i) interstitial nature of Frank loops independent of temperature; (ii) a decrease of the perfect loop mobility compared to Ni-0.4Ti; (iii)

formation of vacancy loops within interstitial loops. These effects could be understood with the formation of TiC precipitates.

To explain the effect (i), two factors should be taken into account. The first is the effect of Ti in solid solution. Ti in solid solution reduces the mobility of interstitials. However, the expected concentration of Ti should be lower than 0.4% due to the TiC precipitation. At 450°C the real Ti concentration in solid solution can still higher than the critical concentration (<0.4%) to form interstitial loops. However, at 510°C and 560°C, loops should be vacancy-type at 510°C and 560°C since the critical concentration at these temperatures are expected to be higher than 0.4%. This point could be attributed to the second factor: the precipitation. We remind that vacancy loops can growth only when the medium bias is stronger than the dislocation bias according to the rate theory (Equation 7.11). The presence of I-clusters like A15 could indeed provide such a strong medium bias. However, TiC must be a strong sink for vacancies as the lattice of TiC ($a_{0,TiC}$=0.432 nm) is dilated compared with the one of Ni ($a_{0,Ni}$=0.352 nm). The formation of TiC requires to dilate the lattice. Therefore, the absorption of vacancies by TiC could reduce the medium bias and the growth rate returns to be positive, which favors the growth of interstitial loops.

Table 7.6 Effects of a carbon addition on the nature of Frank loops in Ni-0.4Ti

Materials	450°C		510°C		560°C	
	Outer	Inner	Outer	Inner	Outer	Inner
Ni-0.4Ti	interstitial	interstitial	vacancy	/	/	/
Ni-0.4Ti-0.1C	interstitial	vacancy	interstitial	vacancy	interstitial	vacancy

The decrease of perfect loop mobility in NiTiC (effect (ii)) should be related to a direct interaction of loop with TiC. The lowered Ti concentration should have increases the mobility of loops. However the mobility is even further reduced with the carbon addition. A plausible mechanism to explain this effect is that TiC precipitates hinder the movement of dislocation loops, as mentioned in the literature (Yvon et al., 2015). However, we have to admit that the effect of carbon in solid solution on loop mobility is not known. It is less likely that such a low carbon concentration (<0.1 wt.% due to the precipitation) could induce such a strong reduction of the loop mobility.

The addition of carbon drastically change the evolution of interstitial Frank loops (effect (iii))). Instead of forming multi-layer interstitial Frank loops (case of Ni-0.4Ti at 450°C), vacancy loops are frequently formed close to or within interstitial Frank loops at 450°C. The formation of TiC gives a natural explanation that the Ti in solid solution is reduced thus its effect in stabilizing stacking fault is lessened. However, this mechanism can not explain why the nature of Frank loops in Ni-Ti-C at higher temperatures (510°C and 560°C) remains the

same as 450°C. Further studies are required to better understand the distribution of Ti in solid solution and TiC in the matrix.

It is worth noting that the absorption of vacancies by TiC and the elimination of vacancy loops by interstitial loops may suppress the vacancy concentration thus suppress the void formation. Voids are detected in bulk Ni-0.4Ti irradiated at 450°C at 0.18 and 0.7 dpa. It would be interesting to study the void distribution in the bulk sample of Ni-Ti-C irradiated at 450°C at the same doses.

Chapter 8

General conclusions and perspectives

8.1 General conclusions

This thesis is devoted to better understand the solute effects on the irradiation behavior of fcc structure in the early stages of irradiation. Ultra-high purity Ni and Ni-based alloys (Ni-Cr, Ni-Ti and Ni-Ti-C) are used as fcc model materials. Self-ion irradiation experiments were performed at the JANNuS facilities. Post-characterization were conducted on as-irradiated thin foils (by in-situ irradiations or ex-situ irradiations at JANNuS-Saclay) and FIB-lifted bulk specimens to study the nature of dislocation loops and the global microstructure (loop density and average size). The real-time microstructural evolution and loop growth rate under irradiation at various temperature were studied during the in-situ irradiations. Comparative studies on Ni and its alloys are conducted to investigate the influence of solutes. EDS in STEM mode and APT were also employed mainly to see the depletion of Ti near dislocation loops in Ni-0.4Ti and the precipitation of TiC in Ni-Ti-C. A part of work was complimented by simulation using ab-initio calculations (to be published by A.M. Goryaeva, M.C. Marinica et al.) and an original diffusion model (Huang et al.) to obtain insight into the mechanisms of radiation damage.

8.1.1 Irradiation behavior of Ni

Influence of I-cluster formation on irradiated microstructure of Ni

The nature of Frank loops in self-ions (Ni^{2+}) irradiated Ni are unambiguously determined. Large Frank loops were identified as vacancy-type independent of the sample form (thin foil or bulk), the temperature (450-510°C) and the dose (<0.7 dpa). Interstitial Frank loops are

found only within large vacancy loops and eliminate the stacking fault. It is for the first time that (i) large stable intrinsic Frank loops are identified in nickel; (ii) an eradication mechanism of intrinsic Frank loops by inner extrinsic Frank loops is clearly shown. Zones with only interstitial perfect loops are detected in some circumstances: distant regions out of the damage production zone in bulk samples and thin zones of thin foils.

The growth of vacancy loops in Ni may be explained by two mechanisms: the 1D motion of some small I-clusters and the formation of I-clusters (A15) predicted by (to be published). The long-distance 1D motion of I-clusters can induce a "loss" of interstitials in the production zone thus provoke a super-saturation of vacancies. The growth of vacancy loops is thus possible. The same result can also be obtained using medium bias model combined with the formation of A15 clusters.As I-clusters A15 are strong sinks for interstitials, the medium bias becomes stronger than the dislocation bias, which favors the growth of vacancy loops. Moreover, A15 clusters can transform into perfect loops who glide in long-distance 1D motion. They escape either to surface(s) or distant regions out of the damage zone. This could explain the super-saturation of vacancies in the damage production zone and also and some zones with only interstitial perfect loops. From now, it is hard to determine which mechanism dominates in Ni.

Surface effects on irradiated microstructure of Ni

The influence of free surfaces on microstructural evolution is studied in Ni at different temperatures. The loop growth rate, loop density and average size strongly depends on the thickness. However, there is a critical thickness above which these parameters is no longer dependent on the thickness. The critical thickness strongly depends on the irradiation temperature: 220 nm for 510°C, 100 nm for 450°C and <80 nm for 400 nm. These surface effects should be attributed to the PD absorption by surfaces. The concentration profile of PDs is significantly affected by the thickness. When the thickness exceeds a critical value, the PD concentration could reach a saturation. The growth rate of vacancy loops in "thick" zones (>critical thickness) in function of temperature gives an estimation of the migration energy of vacancies, which is 1.45±0.12 eV. It is the first time that the migration energy of vacancies is estimated by the temperature-dependency of the growth rate of vacancy loops.

The loop type analysis using the statistic method (Prokhodtseva et al., 2013) shows that the microstructure in thick zones is still affected by the surfaces. A depletion of some perfect loops is due to the surface absorption of mobile loops which glide probably along the direction of their Burgers vector.

8.1.2 Irradiation behavior of the alloys

Effects of Ti and Cr in solid solution on irradiated microstructure of Ni

A drastic influence of micro-alloying on the nature of radiation-induced Frank loops is observed. In Ni, vacancies form intrinsic Frank loops. In thin foils or at depth lower than damage peak, interstitials agglomerate also as Frank loops but only inside existing intrinsic Frank loops and eradicate the stacking fault. In bulk samples of alloys, vacancies form voids while interstitials agglomerate as single or multi-layer extrinsic Frank loops.

Drastic effects of Cr and Ti in solid solution are shown on :

i) the Frank loop nature (vacancy loops in Ni while interstitial loops in the alloys);

ii) loop density/size (Ti increases drastically loop density and reduce loop size);

iii) loop types (more Frank loops and lower depletion of perfect loops in the alloys);

iv) loop mobility and growth rate (the mobility and growth rate of loops are lower in the alloys than in Ni).

These effects of solute should be considered from two aspects: kinetic and energy. Kinetically, solutes can reduce the mobility of interstitials and I-clusters, turning the 1D long-distance motion into complex short-distance motion (Lu et al., 2016b). In bulk specimens, the microstructure is thus dominated by interstitial defects. In thin foil samples of alloys, the microstructure could still be dominated by vacancies due to a strong surface absorption of interstitials and I-clusters. However, the growth rate of vacancy loops is reduced as a result of the reduction of interstitial mobility. Moreover, the mobility of interstitials and I-clusters should be further reduced with the increasing concentration of solute. It then leads to a critical concentration for the transition from a vacancy-dominated microstructure to an interstitial-dominated one in thin foils. The solute addition reduces not only the mobility of PDs but also of dislocation loops. The in-situ observations and loo type analysis show that the mobility of perfect loops is reduced in the alloys.

From an energetic point of view, solute can affect the formation energy of defects (loops compared with voids). The corrected loop proportion shows that there are more Frank loops in Ni-0.4Ti and Ni-0.4Cr than Ni. It suggests that the addition of Ti or Cr may stabilize stacking fault thus reduce the SFE, which is in agreement with the literature (Deléhouzée and Deruyttere, 1967; Kumar et al., 2018). The presence of solutes may also reduce the surface energy of voids as vacancies agglomerate into voids in the alloys instead of vacancy loops in Ni.

However, the influence of Ti and Cr is different. It could be attributed to a different interaction between the solute and defects. The RIS in Ni-Ti and Ni-Cr is studied as a crucial phenomenon to evaluate the difference of Ti and Cr. The RIS is firstly calculated by an analytical model (Harbottle and Norris, 1973) using our experiment results as input

parameters. Simulation suggests a depletion of Ti and an enrichment of Cr near dislocations. Experimentally, TEM-EDS and APT analysis reveal that Ti is depleted around dislocation loops. Moreover, the Ti concentration in the matrix increases after irradiation, which also suggests implicitly a depletion of Ti near radiation-induced defects. The depletion of Ti near dislocation loops shows a fairly good agreement with the simulation.

Finally, the comparative studies on Frank loops in Ni and its alloys shows that the morphology of Frank loops is a characteristic feature of their nature.The correlation between the morphology of Frank loops and their nature provides a new and simple TEM characterization method for the analysis of Frank loops in nickel systems.

Combining effects of Ti and C on irradiated microstructure of Ni

The addition of Ti and C changes drastically the nature, evolution and mobility of defects of dislocation loops in Ni. Frank loops are always interstitial-type in the range of our irradiation conditions (450-560°C). Two mechanisms of the elimination of Frank loops are identified: the eradication of extrinsic stacking faults by inner vacancy loops and the unfaulting process by Shockley partials. The perfect loops are almost immobile. Diffraction and TEM-EDS analysis reveals a possible formation of small TiC precipitates in the matrix, which should be the key point to explain the combining effects of Ti and C. TiC precipitates could act as a strong sink for vacancies and thus decreases the medium bias. It results in an interstitial-dominated microstructure and therefore in the formation of interstitial loops. Moreover, the distribution of TiC in matrix can act as obstacles for the dislocation movements.

8.2 Perspectives

Experiments

The formation of I-clusters (A15) could be a crucial factor controlling the irradiated microstructure of Ni. Firstly, it will be interesting to prove experimentally the existence of A15 using High-Resolution TEM. Then, the influence of temperature and solutes on the transformation of A15 into perfect/Frank loops should be studied in order to verify our hypotheses in this work. One way to do so is the electron irradiation experiments. The nucleation time and density of interstitial Frank loops could be related to the transformation of A15. Moreover, it is interesting to investigate by simulation the mobility of A15 in pure nickel and in the alloys.

The measurement of the SFE in Ni and its alloys will be interesting. It is difficult to measure the SFE by conventional methods as the SFE of Ni is high. In the literature, the

in-situ annealing was used to measure the SFE of Al which has also a high value of SFE (Dobson et al., 1967). It will be interesting to perform in-situ annealing in irradiated Ni and deduce the SFE from the shrinkage of vacancy Frank/perfect loops. Then, comparative studies could be performed on the alloys to investigate the solutes effects on SFE.

It would also be of great interest to study the mechanisms of solute effects on surface energy of voids. Experimentally, the local composition around a voids would be helpful to study a potential segregation near the voids surface. Ti atom (atomic radius 215 pm) and Cr atom (atomic radius 200 pm) are both larger than Ni atom (atomic radius 163 pm). From a thermodynamic view, these solutes would segregate to the surface of voids where the compression around solute atoms could be released. However, under irradiation, flux-coupled diffusion should also be considered. Therefore, related diffusion process and energy of voids coupled with solute would be important to better understand these solute effects.

In this work, the addition of Ti draws more attention than Cr as the effects of Ti are stronger than Cr at current solute content. In the future, it will be interesting to study the effects of Cr at higher contents and investigate the enrichment of Cr on dislocation loops. A detailed study in Ni-Ti-C is also desired to further reveal the conditions and kinetic of the formation of TiC.

Simulation

It is difficult to study numerically the growth of vacancy loops under ion irradiations by conventional rate theory. The 1D motion of interstitials and I-clusters and strong medium bias must be introduced into the calculations. The studies on A15 will be helpful to further develop the rate theory. Thanks to these mechanisms, the growth of vacancy loops could be numerically studied by rate theory using cluster dynamics code.

The correlation of Frank loop morphology and their should be attributed to the dislocation energy. Further calculations of dislocation line energy in function of the SFE (intrinsic or extrinsic) and line orientation could theoretically prove this correlation. It will be very helpful to provide a solid method for the determination of loop nature. It is also interesting to examine whether such a characteristic feature exists in other materials like austenitic steels.

Chapitre 9

Résumé du manuscrit

Introduction et étude bibliographique

Le développement des réacteurs rapides à caloporteur sodium (RNR-Na) requiert des matériaux de structure, notamment pour la gaine du combustible, résistants à des conditions extrêmes de service : hautes températures (>500°C) et fortes doses d'irradiation. Parmi les nombreux candidats, les matériaux les plus avancés pour constituer la future gaine combustible sont les aciers austénitiques : leur procédé de fabrication est éprouvé et leur comportement sous irradiation aux neutrons rapides est bien connu (retour d'expériences des réacteurs Phénix et SuperPhénix) (Garner, 2012; Was, 2016; Yvon, 2016). Le principal inconvénient des aciers austénitiques est leur déformation macroscopique sous irradiation, appelé gonflement. Ce gonflement gène la circulation du caloporteur et de fait limite la durée d'utilisation du combustible nucléaire.

Le gonflement des aciers austénitiques est un phénomène compliqué. Il se décompose en deux régimes : (i) un régime d'incubation où il n'y a pas de changement macroscopique mais une évolution microstructurale ; et au-delà d'une dose dite d'incubation (ii) un régime stationnaire où les aciers gonflent linéairement avec la dose (Dubuisson, 2011). De nombreuses études ont montré que le taux de gonflement en régime stationnaire était indépendamment de la composition et de la microstructure initiale (Garner et al., 1997; J.L. Seran, 2015; Johnston et al., 1974). Le seuil du régime d'incubation est, quant à lui, fortement impacté par ces deux facteurs. Afin d'améliorer leur tenue sous irradiation, la composition des aciers austénitiques a été optimisée en modulant le ratio des éléments majors (Ni/Cr) et en ajoutant certains éléments mineurs comme le titane et le carbone. Ces deux éléments sont connus pour prolonger le régime d'incubation mais leurs mécanismes restent encore incertains.

L'objectif de cette thèse est de mieux comprendre les effets du Cr et Ti (seul ou avec du C) sur le comportement sous irradiation des aciers austénitiques pendant la période

d'incubation (faible dose). La complexité chimique (>12 éléments) et microstructurale des aciers industriels rend difficile d'isoler les effets d'un soluté en particulier et les mécanismes associés. Nous utilisons ici des matériaux modèles, à base de nickel, de même structure cristalline (cubique à faces centrées, CFC) que les aciers austénitiques. Le nickel a été choisi car c'est un élément majoritaire des aciers austénitiques.

L'évolution microstructurale du nickel et ses alliages a été étudiée dans la littérature. Différents points et certaines limitations sont mis en évidence :

1. Les défauts d'irradiation prédominants à faible dose dans le nickel et ses alliages sont des boucles de dislocation. Il en existe deux types : les boucles de Frank (vecteur de Burgers $\mathbf{b}=1/3<111>$) et les boucles parfaites ($\mathbf{b}=1/2<110>$). Elles ont été observées après irradiations aux neutrons (Kojima et al., 1988), aux électrons (Norris, 1970; Urban, 1971; Yoo and Stiegler, 1977) et aux ions (Chen and Ardell, 1976; Lu et al., 2016b; Mazey and Hudson, 1970) sur une large gamme de conditions d'irradiation. Dans la littérature, les boucles de Frank sont systématiquement considérées comme interstitielles sans que la détermination soit prouvée. Des boucles lacunaires ont néanmoins été rapportées dans quelques études mais elles étaient soient métastables (Ishino et al., 1984; Robinson and Jenkins, 1981; Wakai et al., 2002) soit associées à dislocation ou une boucle interstitielle (Urban, 1971).
2. L'étude de l'évolution microstructurale du Ni lors d'irradiations aux électrons dans un Microscopie Electronique à Transmission (MET) à haute tension (THT) met en évidence une croissance linéaire des boucles de Frank interstitielles. Cette croissance se comprend par des modèles de type « Rate Theory ». Néanmoins, comme les électrons ne créent que des paires de Frenkel (une lacune + un interstitiel), l'évolution décrite est probablement différente lors d'irradiations aux neutrons ou ions.
3. Les irradiation in-situ (ions et électrons) dans des MET sont couramment utilisées pour étudier les évolutions microstructurales des matériaux. Lors de ces irradiations, les échantillons sont irradiés sous la forme de lames minces où les surfaces peuvent influencer les mécanismes observés. Cependant, les effets de surfaces ne sont pas clairement caractérisés.
4. Le titane et le chrome ont un effet sur la formation des boucles et des cavités. Le titane et le chrome (au-delà de 2% mass.) diminue la taille et la densité des cavités formées sous irradiation (Pinizzotto et al., 1978; Porollo et al., 2013). Deux effets en compétition sont avancés. Le premier est la stabilisation des cavités par les solutés et le second est la modification des énergies de migration des défauts ponctuels. En plus des modifications microstructurales, l'irradiation modifie la distribution des solutés dans la matrice (ségrégation induite par l'irradiation). Du Ti et Cr ont été détectés à la surface de Ni irradié aux ions (Marwick et al., 1979).

5. Différents modèles sont proposés pour comprendre le comportement sous irradiation du Ni et décrire les mécanismes des solutés sur la structure CFC. Le premier repose sur le biais des dislocations (absorption préférentielle des interstitiels par les dislocations). Couplé avec la Rate Theory, il permet de comprendre la croissance linéaire des boucles de dislocation interstitielles lors des irradiations aux électrons (Kiritani et al., 1975; Urban, 1971; Yoo and Stiegler, 1977). Un second modèle, basé sur l'interaction défauts ponctuels (PDs)-soluté, explique la réduction de la taille des cavités induite par l'ajout de soluté dans le Ni. Dans le Ni, les interstitiels et ses amas migrent sur des longues distances grâce à une migration en ligne droite soit 1 dimension (1D). Dans les alliages, cette migration 1D est inhibée et devient un parcours 3D (Lu et al., 2016b). Enfin, des modèles basés sur la modification de l'énergie de faute d'empilement (SFE) et de l'énergie de surface des cavités par des solutés sont également utiles pour comprendre les stabilité des défauts (boucles et cavités) (Pinizzotto et al., 1978; Seitzman et al., 1986).

Malgré une littérature relativement dense, la base de données actuelle sur les systèmes à base de Ni est encore insuffisante pour décrire sans ambiguïté les mécanismes fondamentaux des effets d'irradiation et des solutés. Premièrement, aucune étude systématique sur l'évolution microstructurale n'a été rapportée pour l'irradiation aux ions qui est plus représentative de l'irradiation aux neutrons au niveau des défauts primaires (cascades de déplacement). Deuxièmement, les expériences comparatives des systèmes Ni, Ni-Ti et Ni-Cr sont très limitées pour bien élucider l'effet du Ti et du Cr sur les défauts induits par l'irradiation. La ségrégation de ces solutés sur des boucles de dislocation ou des cavités n'a pas été expérimentalement rapportée dans les alliages du Ni. Des études comparatives de ces matériaux sont donc fortement souhaitées.

Matériaux et méthodes

Dans cette thèse, des matériaux ultra purs (Ni, Ni-xCr, Ni-xTi et Ni-xTi-yC) sont utilisés comme des matériaux modèles. Le Ni, Ni-0,4Cr, Ni-0,4Ti et Ni-0,4Ti-0,1C (% massique) ont été élaborés à l'Ecole des Mines de Saint Etienne (EMSE). L'analyse de leur composition chimique montre de faibles teneurs (<15 ppm) en impuretés (C, S, O et N). Deux autres alliages Ni-0,8Ti et Ni-1,2Ti ont été fabriqués dans un four à induction au Service de Recherches Métallurgiques Physiques (SRMP) au CEA-Saclay en utilisant du nickel et du titane de haute pureté (99.99%wt.). Les matériaux ont été tronçonnés, amincis mécaniquement, recuits puis électro-polis afin de préparer les lames minces pour l'observation MET et l'irradiation. La microstructure a été contrôlé par MET avant irradiation. La densité de dislocation initiale était très faible ($<10^{10}$ m^{-2}) dans tous les échantillons.

Des irradiations aux ions lourds (Ni^{2+}) ont été effectuées sur la plateforme d'irradiation JANNuS (Saclay et Orsay). Après irradiation, des échantillons de différentes formes ont été préparés. Des lames transversales (lames bulk ou FIB) ont été prélevées par Focus Ion Beam (FIB) pour comparer avec les lames minces. La technique de flash-electropolishing a été utilisé sur les lames FIB pour éliminer les défauts induits par la préparation. Des pointes de Sonde Atomique Tomographique (SAT) ont aussi été préparées par FIB avant et après irradiation pour étudier la modification de composition induite par l'irradiation (ségrégation). La post-caractérisation des défauts structuraux (principalement les boucles de dislocation) a été effectuée par microscopie électronique en transmission (MET) conventionnelle. Elle se concentre sur trois paramètres : **la nature des boucles de dislocation** et **la microstructure irradiée** (densité et taille moyenne des boucles) et **l'évolution microstructurale** (vitesse de montée des dislocations). L'évolution microstructurale en temps réel sous irradiation à différentes températures est étudiée pendant les irradiations in-situ. Des études comparatives sur le Ni et ses alliages sont menées pour étudier l'influence des solutés. La MET couplée à l'analyse de la dispersion en Energie des Rayons-X (STEM-EDS) à ETH Zurich et la Sonde Atomique Tomographique (SAT) au CEA-Saclay ont également été utilisées pour caractériser la déplétion en Ti sur les boucles de dislocation dans Ni-0,4Ti et la précipitation du TiC dans Ni-Ti-C. Une partie du travail est complétée par les études ab-initio (to be published) et la simulation avec un modèle de diffusion (Huang et al.).

Les résultats expérimentaux sont résumés dans les trois parties suivantes. Nous nous intéressons tout d'abord au comportement du Ni comme matériau de référence. Ensuite, nous traitons le cas des alliages puis nous discutons les résultats pour mieux comprendre les mécanismes impliqués.

Comportement sous irradiation du Ni

La nature des boucles de Frank dans le Ni est d'abord étudiée en fonction de plusieurs paramètres : la forme de l'échantillon (lame mince v.s. lame bulk), la dose (0.7 v.s. 0.18) et la température d'irradiation (450 °C v.s. 500 °C). Les grandes boucles de Frank sont toujours de type lacunaire (boucles de Frank intriséques) dans la gamme de nos conditions d'irradiation. Ces boucles de Frank intrinsèques sont toujours segmentées. Les boucles de Frank de type interstitielles (boucles de Frank extrinséques) sont observées à l'intérieur des boucles de Frank lacunaires. Les fautes d'emmpilement intrinséque dans la boucles lacunaire est éradiquée par les boucles interstitielles.

Les boucles parfaites interstitielles sone aussi détectées dans deux situations. Elles sont observées des zones hors du pic d'implantation, loin de la zone irradiée. Dans un autre cas

particulier, elles sont detectées dans des zones à faible épaisseur (<130 nm) dans les lames minces. Dans les deux cas, il existe seulement des boucles parfaites interstitielles.

La microstructure irradiée est étudiée à 510/450/400°C en fonction de l'épaisseur. A une température donnée, la densité de la boucle, la taille moyenne augmentent avec l'épaisseur. Il existe une épaisseur critique au dela duquel ces parameters sont stabilisés. Cette épaisseur critique augmente drastiquement avec la température. À 510 °C, ces paramètres sont indépendants de l'épaisseur lorsque l'épaisseur dépasse 220 nm. À 450 °C et 400 °C, l'épaisseur critique est respectivement 90 nm et <80 nm.

La microstructure irradiée à 510°C est caractérisée en détailles. Des zones dénudées des boucles sont détectées à chaque côté de la lame par le technique stéréo-imaging. De plus, une analyse des types de boucle par une méthode statistique basée sur la critère d'invisibilité montre que certaines familles des boucles sont déplétées. L'absorption des boucles parfaites par les surface donc existe toujours même dans les zones épaisses. Ce résultat est cohérent avec les observations in-situ où les boucles parfaites glissent et disparaissent en surface. Mais cette analyse nous permet de corriger la densité des boucles mesurée en rendu compte des boucles absorbées par la surface.

L'évolution microstructurale est étudiée pendent les irradiations in-situ. A 510°C, la vitesse de montée des dislocations (vitesse de croissance des boucles) augmente avec l'épaisseur et sature vers 220 nm. Les boucles sont hautement mobiles et elles glissent probablement le long des directions <110> par l'analyse de stéréogramme. De plus, les irradiations à basses temperatures (450/400°C) montrent que la vitesse de montée des boucles diminue drastiquement avec la temperature.

Comportement sous irradiation du Ni-0.4Cr et Ni-xTi

La nature des boucles de Frank est d'abord étudiée dans les alliages de Ni-0,4Cr et Ni-0,4Ti (%mass.) en lames minces et en lames FIB après irradiation à 450°C. Dans les lames minces de Ni-0,4Cr, les boucles de Frank sont lacunaires et segmentées. Elles sont interstitielles et non-segmentées dans Ni-0,4Ti. Dans les lames FIB, des boucles de Frank lacunaires et segmentées sont détectées proche de la surface pour le Ni-0,4Cr. Loin de la surface, la majorité des boucles de Frank et des boucles parfaites sont interstitielles. Dans les deux alliages, des boucles de Frank interstitielles multi-fautées sont observées. Les boucles de Frank interstitielles sont non-segmentées et des cavités sont détectées dans les lames FIB des deux alliages.

La nature des boucles est ensuite déterminée dans les lames minces à une température plus haute, 510 °C. Les boucles de Frank sont alors toutes de nature lacunaire. Dans l'alliage Ni-0,4Ti, la nature des boucles de Frank détectées en lame mince change entre 450°C et 510°C.

Afin de savoir si un taux supérieur de Ti permettrait de conserver des boucles interstitielles en lame mince, les nuances Ni-0,8Ti et Ni-1,2Ti sont étudiées après irradiation à 510°C. Dans ces deux alliages, les boucles de Frank sont de nature interstitielle et non-segmentées.

Des irradiations in-situ à 510°C montrent que l'ajout de titane ou de chrome dans du nickel réduit la vitesse de montée et la mobilité des boucles de dislocation sous irradiation. L'effet du Ti sur la réduction de la vitesse de montée et la mobilité des boucles augmente avec la concentration.

Les caractérisations des microstructures irradiées montrent que la taille moyenne des boucles est réduite par un ajout du soluté et que leur densité augmente fortement avec la tenue en Ti. Un ajout de Cr n'a que peu d'effet sur ces paramètres. L'analyse des vecteurs de Burgers des boucles ne met pas en évidence une forte déplétion d'un type de boucles contrairement au cas du nickel. Ces observations sont cohérentes avec la réduction de la mobilité des boucles dans les alliages. Après correction de leur densité, il apparait que la proportion de boucles de Frank augmente avec l'addition croissante de soluté.

Comportement sous irradiation du Ni-Ti-C

L'influence de l'ajout du carbone dans Ni-0,4Ti sur la nature de la boucle de Frank est étudiée à différentes températures. Dans Ni-Ti-C, les boucles de Frank sont toujours de nature interstitielle dans la gamme de nos conditions d'irradiation (450-560 °C). L'ajout de carbone modifie aussi la structure des boucles de Frank interstitielles. Par rapport à Ni-0,4Ti où des boucles de Frank extrinsèques multicouches sont observées, les boucles de Frank interstitielles dans Ni-Ti-C sont souvent partiellement défautées. Deux mécanismes d'élimination des boucles de Frank interstitielles sont identifiés. Les fautes d'empilement extrinsèques peuvent être éradiquées par la nucléation de boucles de Frank intrinsèques ou par la nucléation d'une dislocation partielle de Shockley.

L'étude de la croissance des boucles de Frank interstitielles dans Ni-Ti-C en fonction de la température permet d'estimer l'énergie de migration des lacunes à $1{,}27 \pm 0{,}01$ eV.

Pour comprendre l'effet combiné du Ti et du C, nous cherchons à caractériser la potentielle précipitation de carbures de titane (TiC) sous irradiation. Les clichés de diffraction en axe de zone, dans des lames minces irradiées de faible épaisseur, mettent en évidence une structure cristalline différente de celle du nickel. Elle pourrait correspondre à une structure TiC. Des analyses STEM-EDS révèlent des enrichissements de titane localisés (<2 nm). Nous supposons qu'il s'agit de précipités TiC. Leur formation est un point essentiel pour comprendre les effets combinés du Ti et du C.

Discussions

Dans cette section, nous allons d'abord discuter le comportement du Ni, y compris l'influence de la surface sur la microstructure irradiée et l'origine des boucles lacunaires. Après, nous discuterons de l'effet du Cr ou Ti en solution solide et puis l'effet combiné du Ti avec du C.

Effet de surface sur la microstructure irradiée du Ni

L'effet des surfaces dans les lames minces sur la microstructure irradiée est d'abord attribué à l'absorption des défauts ponctuels (PDs). Les concentrations normalisées des lacunes sont calculées en fonction de l'épaisseur et de la température par un modèle de Rate Theory en régime stationnaire. A une température donnée, la concentration de PDs peut atteindre une saturation au milieu de la lame si l'épaisseur dépasse une valeur critique. Les épaisseurs critiques calculées correspondent à celles déterminées expérimentalement pour la saturation de la densité et la taille des boucles.

L'énergie de migration de la lacune est estimée par 2 moyens : l'analyse de la variation de l'épaisseur de la zone dénudée en fonction de la température et celle de la vitesse de croissance des boucles lacunaires dans les zones "épaisses" (> épaisseur critique).

La comparaison de l'épaisseur de la zone dénudée en boucles proche des surfaces avec la littérature (Ishino, 1997; Niwase et al., 1993; Yoo and Stiegler, 1977) et son couplage avec un modèle simple (Foreman, 1972), donne une première estimation de 1 eV. Cette estimation est légèrement plus faible que les valeurs de la littérature (1.32 eV (Lu et al., 2016b), 0,92-1,46 eV Poletaev and Starostenkov (2010), 1.2 eV (Yoo and Stiegler, 1977)). La vitesse de croissance des boucles lacunaires en fonction de la température donne une estimation de 1,45 $\pm$ 0,12 eV. C'est la première fois que l'énergie de migration des lacunes est estimée par la dépendance en température de la vitesse de croissance des boucles lacunaires.

Origine des boucles lacunaires due à la formation des amas interstitiels dans Ni irradié aux ions lourds

Pour la première fois, (i) de grandes boucles de Frank intrinsèques stables sont identifiées dans le nickel ; (ii) un mécanisme d'éradication des boucles de Frank intrinsèques par des boucles de Frank extrinsèques est clairement montré ; (iii) des boucles parfaites interstitielles sont détectées dans des zones non irradiées en lames FIB et occasionnellement des zones de faible épaisseur, habituellement sans défauts, dans les lames minces.

Dans la littérature, la croissance des boucles interstitielles sous irradiation aux électrons est expliquée par la Rate Theory conventionnelle (Kiritani et al., 1975; Urban, 1971; Yoo and Stiegler, 1977). Comme les boucles de dislocation, indépendamment de leur nature,

ont un biais positif (absorption préférentielle des interstitiels (Bullough et al., 1981)), les boucles interstitielles peuvent donc croître pendant que les boucles lacunaires rétrécissent sous irradiation. La Rate Theory est donc insuffisante pour expliquer nos observations.

Pour comprendre nos observations dans le Ni irradié aux ions lourds, deux hypothèses supplémentaires sont intéressantes à considérer : (I) le biais de production dû aux cascades + migration des amas interstiels en 1D et (II) le biais du milieu.

Hypothèse (I) : les ions lourds créent des cascades dans lesquels les amas interstitiels et lacunaires sont formés. Si les amas interstitiels migrent en 1D à distance longue (Lu et al., 2016b), ils partent soit aux surfaces soit loin de leur zone de production, en laissant localement une sur-saturation de lacunes.

Hypothèse (II) : selon la Rate Theory et le bilan des PDs d'une boucles, la variation du rayon d'une boucles peut être exprimé suivant :

$$\frac{dR}{dt} = \frac{\Omega}{b} Z_{l,i}(B_l - \bar{B}) D_v C_v$$

où B_l est le biais d'une boucle de dislocation, $\bar{B}$ est le biais de milieu, Ω le volume atomique, b le vecteur de Burgers, D_α and C_α les coefficients de diffusion et concentrations d'espèces α (α=i pour les interstitiels ou v pour les lacunes), $Z_{l,i}$ l'efficacité d'absorption des interstitiels par une boucle. Si le biais de milieu est supérieur au biais de la boucle de dislocation, autrement-dit d'autres puits absorbent plus fortement les interstitiels que les boucles, la croissance des boucles interstitielles peut être favorisée. Une étude théorique récente prédit l'existence d'un amas d'interstitiels de type A15 dans la structure CFC . Les amas interstitiels A15 sont des puits efficaces pour les interstitiels et donc augmentent fortement le biais de l'environnement. De plus, ces amas peuvent se transformer en boucles parfaites ou en boucles de Frank. La probabilité de transformation d'un amas A15 en un type de boucle dépend fortement du matériau . Nous supposons que dans le cas du Ni la proportion d'amas A15 qui se transforme en boucles parfaites n'est pas nulle. Etant donné que les boucles parfaites peuvent glisser le long de leur vecteur de Burger, ie en 1D, elles migrent sur de longue distance et sont donc rapidement loin de leur zone de nucléation. Par ce biais, les défauts interstitiels sont continûment éliminés de leurs zones de production. Ce mécanisme équivaut à un biais de production.

Ces mécanismes permettent d'expliquer à la fois la microstructure dominée par les défauts lacunaires et l'existence des zones avec uniquement des boucles parfaites interstitielles. Pour étudier le mécanisme (II), nous avons effectué des irradiations aux électrons où seules des paires de Frenkel sont créées sans cascades. Les résultats actuels ne sont pas contradictoires avec les mécanismes ci-dessus mais ils ne permettent pas encore de les démontrer.

Effet drastique du soluté sur la nature des boucles et la microstructure irradiée

Un effet drastique du Cr et du Ti en solution solide sur la nature des boucles de Frank est mis en évidence. Les effets du soluté sur les défauts peuvent être expliqués en deux aspects : cinétique et énergétique.

Au niveau cinétique, les solutés peuvent réduire la mobilité des interstitiels et des I-clusters en changeant leur parcours de migration. Dans le Ni, les défauts interstitiels migreraient en 1D sur des longues distances mais lorsque le Ni est fortement allié, les défauts migreraient sur des courtes distances en 3D (Lu et al., 2016b). Dans les alliages, le biais de production serait donc réduit et la microstructure serait dominée par des boucles interstitielles. Dans les lames minces des alliages, bien que la mobilité des interstitiels et leurs amas soient réduites, la microstructure pourrait toujours être contrôlée par les lacunes à cause d'une absorption préférentielle des interstitiels par les surfaces. L'efficacité de réduction de la mobilité des interstitiels et leur amas dépendraient non seulement de la nature du soluté mais de sa teneur. L'ensemble de ces hypothèses expliqueraient la vitesse de croissance des boucles lacunaires réduite par l'ajout du Cr et du Ti (sursaturation en lacunes moins importante) et le changement de nature de boucles de Frank au-delà d'une certaine teneur en soluté. Nos observations lors des irradiations in-situ et l'analyse des vecteurs de Burgers des boucles montrent que l'ajout de soluté réduit non seulement la mobilité des défauts ponctuels et des amas mais aussi celles des boucles de dislocation.

Un autre mécanisme pour comprendre les effets du soluté est son impact sur l'énergie des défauts (boucles et cavités). La proportion corrigée des boucles montre qu'il y a plus de boucles de Frank dans le Ni-0,4Ti et le Ni-0,4Cr que dans le Ni. Cela suggère que Ti et Cr pourraient réduire l'énergie de faute d'empilement (SFE). Cette tendance est en accord avec la littérature (Deléhouzée and Deruyttere, 1967; Kumar et al., 2018). Cet effet augmenterait la stabilité des boucles de Frank. De plus, la SFE est peut-être impliquée dans la transformation des amas de type A15 vers les boucles. Une diminution de la SFE pourrait favoriser la transformation des amas A15 en boucles de Frank au lieu de boucles parfaites. Comme les boucles de Frank sont sessiles, elles resteraient dans la zone de production diminuant ainsi le biais de production. La présence de solutés impacte non seulement la formation et l'évolution des boucles de dislocation mais aussi celles des cavités. Etant donné que les lacunes s'agglomèrent en cavités dans les alliages (et pas sous la forme de boucles de Frank), nous supposons que l'ajout de soluté pourrait également réduire l'énergie de surface des cavités, ce qui les stabiliserait.

Cependant, l'influence du Ti et du Cr est différente. Elle pourrait être attribuée à une interaction différente entre le soluté et les défauts. Une conséquence directe est la ségrégation induite par l'irradiation (RIS). La RIS est étudiée dans Ni-0,4Ti et Ni-0,4Cr. La RIS est d'abord calculée par un modèle de diffusion analytique (Huang et al.) utilisant nos résultats

expérimentaux comme paramètres d'entrée. La simulation suggère un appauvrissement en Ti et un enrichissement en Cr sur les dislocations. La déplétion du Ti doit être plus visible expérimentalement étant donné nos conditions d'irradiation. Nous nous intéressons donc à la caractérisation de RIS dans Ni-0,4Ti avant et après l'irradiation à 450 °C. Des analyses par STEM-EDS et SAT sont effectuées. Des déplétions en Ti, probablement sur les boucles de dislocation, sont détectées. De plus, les analyses SAT montrent que la concentration en Ti dans la matrice est hétérogène et augmente après irradiation. Ces observations suggèrent également des déplétions locales en Ti . Les profils de déplétion du Ti par SAT sont en bon accord avec la simulation de profils de déplétion sur des boucles de dislocation, ce qui valide la précision du modèle.

Enfin, les études comparatives sur les boucles de Frank dans le Ni et les alliages montrent que la morphologie des boucles de Frank dépend drastiquement de leur nature. La corrélation entre la morphologie des boucles de Frank et leur nature fournit une nouvelle méthode de caractérisation simple pour déterminer la nature des boucles de Frank dans les systèmes au nickel et plus généralement les systèmes de structure cubique à faces centrées (CFC).

Effet combiné du Ti et du C sur la microstructure irradiée

L'ajout du Ti et du C change radicalement la nature, l'évolution et la mobilité des défauts des boucles de dislocation dans le Ni. La formation de précipités TiC peut expliquer ces phénomènes. Le paramètre de maille des TiC étant inférieur à celui du Ni, la formation des précipités dilate la matrice et absorbe des lacunes. Ainsi, TiC diminue le biais de l'environnement, ce qui favorisera la croissance des boucles interstitielles. En plus d'un changement du biais du milieu, les précipités peuvent être des obstacles aux mouvements des dislocations et réduiraient la mobilité des boucles parfaites. La formation des boucles lacunaires à l'intérieur des boucles interstitielles est probablement liée à la formation de précipités proche des boucles. Ces précipités pourraient être des sites de nucléation pour des boucles lacunaires ou inversement.

Conclusion générale

Dans cette thèse, nous nous intéressons à l'influence du titane et du chrome sur la nature des boucles, la microstructure irradiée et l'évolution microstructurale dans le nickel et ses alliages. Les résultats principaux sont les suivants :

1. Les surfaces de l'échantillons jouent un rôle important sur la microstructure irradiée dû à l'absorption des défauts ponctuels et des boucles mobiles par la surface. Pour s'affranchir de l'effet de surface sur la densité et la taille des boucles, il faut que l'épaisseur dépasse une valeur critique qui dépend fortement de la température. Néanmoins, il

existe toujours une déplétion de certaines familles des boucles parfaites à cause de leur glissement vers les surfaces.

2. Nous rapportons pour la première fois l'existence des grandes boucles de Frank lacunaires dans le Ni irradié au-delà de 450°C. Des modifications des modèles actuels doivent être considérées pour comprendre l'origine des boucles lacunaires. Un biais de production dû à la migration 1D d'amas d'interstitiels ou de boucles parfaites directement formées à partir d'amas de type A15 sont des hypothèses intéressantes pour expliquer nos observations.
3. Nos études montrent un effet drastique d'une faible concentration de soluté sur la nature, la densité, la taille, la vitesse de montée et la mobilité des boucles de dislocation sous irradiation. Les mécanismes associés peuvent être le piégeage des amas interstitiels ou des boucles de type 1/2<110> par les solutés, un changement de l'énergie de faute d'empilement ou une modification de l'énergie de surface des cavités. De plus, l'effet du soluté dépend de sa chimie probablement via des mécanismes de ségrégation.
4. L'effet combiné du Ti et du C est différent de celui du Ti en solution solide. L'ajout du C dans Ni-Ti change drastiquement la nature des boucles de Frank et réduit considérablement la mobilité des boucles parfaites. Cet effet combiné est peut-être attribué à la formation des nano-précipités TiC.

Ces résultats nous permettent de mieux comprendre le comportement sous irradiation du Ni et de ses alliages. Les observations des défauts au niveau fondamental introduisent de nouvelles considérations pour les calculs théoriques, ce qui contribue à une meilleure compréhension des mécanismes fondamentaux du dommage induit par l'irradiation et des effets du soluté dans la structure CFC.

Perspectives

La formation d'amas interstitiels (A15) est un facteur crucial contrôlant la microstructure irradiée du Ni. Il serait intéressant de prouver expérimentalement son existence par MET Haute Résolution. Les études comparatives entre le Ni et les alliages sur la proportion d'amas A15 se transformant en boucles de Frank ou parfaites seront utiles pour mieux comprendre les mécanismes impliqués. Il serait aussi important de mesurer de l'énergie de faute d'empilement en fonction de la composition et de quantifier la ségrégation autour des cavités dans les alliages pour évaluer l'impact du soluté sur l'énergie de surface des cavités.

Si l'effet du titane seul en solution solide semble donc avéré, il est important de s'intéresser désormais à l'effet combiné du titane et du carbone en détails. La prochaine étape sera ainsi d'évaluer la cinétique de précipitation/stabilité des carbures de titane sous irradiation et voir leur impact sur l'évolution microstructurale des aciers austénitiques modèles.

Au niveau de la modélisation, il serait intéressant d'introduire l'hypothèse de la formation d'amas A15 en dynamique d'amas pour évaluer son impact sur la nature des boucles formées sous irradiation.

Table des figures

Liste des tableaux

Bibliographie

Hiroaki Abe, Naoto Sekimura, and Yunmin Yang. Stability and mobility of defect clusters in copper under displacement cascade conditions. *Proceedings of the Second IEA Fusion Materials Agreement Workshop on Modeling and Experimental Validation*, 323(2) :220–228, December 2003. ISSN 0022-3115. doi : 10.1016/j.jnucmat.2003.08.006. URL http://www.sciencedirect.com/science/article/pii/S0022311503003660.

Samuel M Allen and Ernest L Hall. Foil thickness measurements from convergent-beam diffraction patterns an experimental assessment of errors. *Philosophical Magazine A*, 46 (2) :243–253, 1982.

Peter M Anderson, John P Hirth, and Jens Lothe. *Theory of dislocations*. Cambridge University Press, 2017.

Kazumi Aoto, Philippe Dufour, Yang Hongyi, Jean Paul Glatz, Yeong-il Kim, Yury Ashurko, Robert Hill, and Nariaki Uto. A summary of sodium-cooled fast reactor development. *Progress in Nuclear Energy*, 77 :247–265, 2014.

DJ Bacon, R Bullough, and JR Willis. The anisotropic elastic energy of a rhombus-shaped dislocation loop. *Philosophical Magazine*, 22(175) :31–45, 1970.

Alexander Barashev, Yuri Osetsky, Hongbin Bei, Chenyang Lu, Lumin Wang, and Yanwen Zhang. Chemically-biased diffusion and segregation impede void growth in irradiated ni-fe alloys. *Current Opinion in Solid State and Materials Science*, 23(2) :92–100, 2019.

Christopher M. Barr, Leland Barnard, James E. Nathaniel, Khalid Hattar, Kinga A. Unocic, Izabela Szlurfarska, Dane Morgan, and Mitra L. Taheri. Grain boundary character dependence of radiation-induced segregation in a model Ni–Cr alloy. *Journal of Materials Research*, 30(9) :1290–1299, 2015.

M.I. Baskes, C.L. Bisson, and W.D. Wilson. Calculations of the trapping and migration of vacancies and nickel self-interstitials in the presence of rare gases and dislocations. *Journal of Nuclear Materials*, 83(1) :139–146, August 1979. ISSN 0022-3115. doi : 10.1016/0022-3115(79)90599-3. URL http://www.sciencedirect.com/science/article/pii/0022311579905993.

J.F. Bates and R.W. Powell. Irradiation-induced swelling in commercial alloys. *Journal of Nuclear Materials*, 102(1) :200–213, November 1981. ISSN 0022-3115. doi : 10.1016/0022-3115(81)90560-2. URL http://www.sciencedirect.com/science/article/pii/0022311581905602.

A. Bhattacharya, E. Meslin, J. Henry, A. Barbu, S. Poissonnet, and B. Décamps. Effect of chromium on void swelling in ion irradiated high purity Fe–Cr alloys. *Acta Materialia*,

108 :241–251, April 2016. ISSN 13596454. doi : 10.1016/j.actamat.2016.02.027. URL https://linkinghub.elsevier.com/retrieve/pii/S135964541630101X.

Arunodaya Bhattacharya. *Ion irradiation effects on high purity bcc Fe and model FeCr alloys*. Theses, Université Paris Sud - Paris XI, December 2014. URL https://tel.archives-ouvertes.fr/tel-01252243.

R.C. Birtcher, M.A. Kirk, K. Furuya, G.R. Lumpkin, and M-O. Ruault. In situ Transmission Electron Microscopy Investigation of Radiation Effects. *Journal of Materials Research*, 20(7) :1654–1683, 2005. ISSN 0884-2914. doi : 10.1557/JMR.2005.0242. URL https://www.cambridge.org/core/article/in-situ-transmission-electron-microscopy-investigation-of-radiation-effects/E069AFF5F038062296A07D83C0DA7BB7.

R.M. Boothby and T.M. Williams. The effects of silicon and titanium on void swelling and phase transformations in neutron irradiated 12Cr-15Ni steels. *Journal of Nuclear Materials*, 152(2) :123–138, May 1988. ISSN 0022-3115. doi : 10.1016/0022-3115(88)90318-2. URL http://www.sciencedirect.com/science/article/pii/0022311588903182.

H. R. Brager, J. L. Straalsund, J. J. Holmes, and J. F. Bates. IRRADIATION PRODUCED DEFECTS IN AUSTENITIC STAINLESS STEEL. Technical Report WHAN-FR–16, 4039123, January 1970. URL http://www.osti.gov/servlets/purl/4039123/.

H.R. Brager. The effects of cold working and pre-irradiation heat treatment on void formation in neutron-irradiated type 316 stainless steel. *Journal of Nuclear Materials*, 57(1) : 103–118, July 1975. ISSN 00223115. doi : 10.1016/0022-3115(75)90184-1. URL http://linkinghub.elsevier.com/retrieve/pii/0022311575901841.

A.D. Brailsford and R. Bullough. The rate theory of swelling due to void growth in irradiated metals. *Journal of Nuclear Materials*, 44(2) :121–135, August 1972. ISSN 00223115. doi : 10.1016/0022-3115(72)90091-8. URL http://linkinghub.elsevier.com/retrieve/pii/0022311572900918.

A.D. Brailsford and L.K. Mansur. Effect of self-ion injection in simulation studies of void swelling. *Journal of Nuclear Materials*, 71(1) :110–116, December 1977. ISSN 0022-3115. doi : 10.1016/0022-3115(77)90194-5. URL http://www.sciencedirect.com/science/article/pii/0022311577901945.

Samuel A. Briggs, Christopher M. Barr, Janne Pakarinen, Mahmood Mamivand, Khalid Hattar, Dane D. Morgan, Mitra Taheri, and Kumar Sridharan. Observations of defect structure evolution in proton and Ni ion irradiated Ni-Cr binary alloys. *Journal of Nuclear Materials*, 479 :48–58, October 2016. ISSN 0022-3115. doi : 10.1016/j.jnucmat.2016.06.046. URL http://www.sciencedirect.com/science/article/pii/S0022311516303002.

J.L. Brimhall and B. Mastel. Stability of voids in neutron irradiated nickel. *Journal of Nuclear Materials*, 33(2) :186–194, November 1969a. ISSN 00223115. doi : 10.1016/0022-3115(69)90059-2. URL https://linkinghub.elsevier.com/retrieve/pii/0022311569900592.

J.L. Brimhall and B. Mastel. Voids in neutron irradiated face centered cubic metals. *Journal of Nuclear Materials*, 29(1) :123–125, January 1969b. ISSN 00223115. doi : 10.1016/0022-3115(69)90132-9. URL https://linkinghub.elsevier.com/retrieve/pii/0022311569901329.

JL Brimhall and EP Simonen. Effect of helium on void formation in nickel. *Journal of Nuclear Materials*, 68(2) :235–243, 1977.

S. M. Bruemmer, E. P. Simonen, P. M. Scott, P. L. Andresen, G. S. Was, and J. L. Nelson. Radiation-induced material changes and susceptibility to intergranular failure of light-water-reactor core internals. *Journal of Nuclear Materials*, 274(3) :299 – 314, 1999. ISSN 0022-3115. doi : https://doi.org/10.1016/S0022-3115(99)00075-6. URL http://www.sciencedirect.com/science/article/pii/S0022311599000756.

R. Bullough, M.H. Wood, D.W. Wells, and J.R. Willis. THE INTERACTION ENERGY BETWEEN INTERSTITIAL ATOMS AND DISLOCATIONS AND ITS RELEVANCE TO IRRADIATION DAMAGE PROCESSES. In M.F. ASHBY, R. BULLOUGH, C.S. HARTLEY, and J.P. HIRTH, editors, *Dislocation Modelling of Physical Systems*, pages 116–141. Pergamon, January 1981. ISBN 978-0-08-026724-1. doi : 10.1016/B978-0-08-026724-1.50017-0. URL http://www.sciencedirect.com/science/article/pii/B9780080267241500170.

Denise Carpentier. *Simulation de la cinétique d'absorption des défauts ponctuels par les dislocations et amas de défauts*. Ph.D. thesis, Université Paris-Saclay, Paris, 2018. URL https://pastel.archives-ouvertes.fr/tel-01915303/document.

BARRY AUTOR CARTER, David Brian Williams, David Bernard Williams, and C Barry Carter. *Transmission Electron Microscopy : A Textbook for Materials Science. Diffraction. II*, volume 1. Springer Science & Business Media, 1996.

C. B. Carter and S. M. Holmes. The stacking-fault energy of nickel. *The Philosophical Magazine : A Journal of Theoretical Experimental and Applied Physics*, 35(5) :1161–1172, May 1977. ISSN 0031-8086. doi : 10.1080/14786437708232942. URL https://www.tandfonline.com/doi/full/10.1080/14786437708232942.

C Cawthorne and EJ Fulton. Voids in irradiated stainless steel. *Nature*, 216(5115) :575–576, 1967.

Dongyue Chen, Kenta Murakami, Hiroaki Abe, Zhengcao Li, and Naoto Sekimura. Investigation of interactions between defect clusters in stainless steels by in situ irradiation at elevated temperatures. *Acta Materialia*, 163 :78–90, January 2019. ISSN 1359-6454. doi : 10.1016/j.actamat.2018.10.011. URL http://www.sciencedirect.com/science/article/pii/S1359645418308036.

H. C. Chen, R. D. Lui, C. L. Ren, H. F. Huang, J. J. Li, G. H. Lei, W. D. Xue, W. X. Wang, Q. Huang, D. H. Li, L. Yan, and X. T. Zhou. Evolution of dislocation loops in He ion irradiated nickel under different temperature. *Journal of Applied Physics*, 120 (12) :125303, September 2016. ISSN 0021-8979, 1089-7550. doi : 10.1063/1.4963344. URL http://aip.scitation.org/doi/10.1063/1.4963344.

L. J. Chen and A. J. Ardell. The observation of multiple-layer loops in nickel base alloys under ion bombardment. *Physica Status Solidi (a)*, 34(2) :679–690, April 1976. ISSN 00318965, 1521396X. doi : 10.1002/pssa.2210340232. URL http://doi.wiley.com/10.1002/pssa.2210340232.

D. J. H. Cockayne, M. L. Jenkins, and I. L. F. Ray. The measurement of stacking-fault energies of pure face-centred cubic metals. *Philosophical Magazine*, 24(192) :1383–1392, December 1971. ISSN 0031-8086. doi : 10.1080/14786437108217419. URL http://www.tandfonline.com/doi/abs/10.1080/14786437108217419.

Jean-Paul Crocombette and Christian Van Wambeke. Quick calculation of damage for ion irradiation : implementation in Iradina and comparisons to SRIM. *EPJ Nuclear Sciences & Technologies*, 5 :7, 2019. ISSN 2491-9292. doi : 10.1051/epjn/2019003. URL https://www.epj-n.org/10.1051/epjn/2019003.

Gopal Das and T. E. Mitchell. Irradiation damage of nickel in a high-voltage electron microscope. *Journal of Nuclear Materials*, 56(3) :297–306, 1975.

C. David, B.K. Panigrahi, S. Balaji, A.K. Balamurugan, K.G.M. Nair, G. Amarendra, C.S. Sundar, and Baldev Raj. A study of the effect of titanium on the void swelling behavior of D9 steels by ion beam simulation. *Journal of Nuclear Materials*, 383(1-2) : 132–136, December 2008. ISSN 00223115. doi : 10.1016/j.jnucmat.2008.08.049. URL http://linkinghub.elsevier.com/retrieve/pii/S0022311508004881.

L Deléhouzée and A Deruyttere. The stacking fault density in solid solutions based on copper, silver, nickel, aluminium and lead. *Acta Metallurgica*, 15(5) :727–734, May 1967. ISSN 0001-6160. doi : 10.1016/0001-6160(67)90353-7. URL http://www.sciencedirect.com/science/article/pii/0001616067903537.

P. S. Dobson, P. J. Goodhew, and R. E. Smallman. Climb kinetics of dislocation loops in aluminium. *Philosophical Magazine*, 16(139) :9–22, July 1967. ISSN 0031-8086. doi : 10.1080/14786436708229253. URL http://www.tandfonline.com/doi/abs/10.1080/14786436708229253.

P. Dubuisson. Le gonflement des aciers austénitiques. *Revue de Métallurgie–International Journal of Metallurgy*, 108(1) :33–37, 2011.

P. Dubuisson and D. Gilbon. Behaviour and microstructure of stainless steels irradiated in the french fast breeder reactors. Technical report, France, 1991. URL http://inis.iaea.org/search/search.aspx?orig_q=RN:23010805. CEA-CONF–10539.

J. W. Edington. Interpretation of Transmission Electron Micrographs. In *Interpretation of Transmission Electron Micrographs*, page 27. Macmillan Education UK, London, 1975. ISBN 978-1-349-02658-6. doi : 10.1007/978-1-349-02658-6_1. URL https://doi.org/10.1007/978-1-349-02658-6_1.

J. W. Edington and R. E. Smallman. Faulted dislocation loops in quenched aluminium. *The Philosophical Magazine : A Journal of Theoretical Experimental and Applied Physics*, 11 (114) :1109–1123, June 1965. ISSN 0031-8086. doi : 10.1080/14786436508224922. URL https://www.tandfonline.com/doi/full/10.1080/14786436508224922.

D.J Edwards, E.P Simonen, F.A Garner, L.R Greenwood, B.M Oliver, and S.M Bruemmer. Influence of irradiation temperature and dose gradients on the microstructural evolution in neutron-irradiated 316SS. *Journal of Nuclear Materials*, 317(1) :32–45, April 2003. ISSN 00223115. doi : 10.1016/S0022-3115(03)00003-5. URL https://linkinghub.elsevier.com/retrieve/pii/S0022311503000035.

A. K. Eikum and D. M. Maher. Electron microscope image contrast from multiple Frank dislocation loops. *Physica Status Solidi (a)*, 29(1) :281–292, May 1975. ISSN 00318965, 1521396X. doi : 10.1002/pssa.2210290131. URL http://doi.wiley.com/10.1002/pssa.2210290131.

A. Etienne, M. Hernández-Mayoral, C. Genevois, B. Radiguet, and P. Pareige. Dislocation loop evolution under ion irradiation in austenitic stainless steels. *Journal of Nuclear Materials*, 400(1) :56–63, May 2010. ISSN 0022-3115. doi : 10.1016/j.jnucmat.2010.02.009. URL http://www.sciencedirect.com/science/article/pii/S0022311510000486.

H. Föll and M. Wilkens. A simple method for the analysis of dislocation loops by means of the inside-outside contrast on transmission electron micrographs. *physica status solidi (a)*, 31(2) :519–524, 1975.

S. B. Fisher, P. K. Madden, and K. M. Miller. The role of silicon in the void swelling of stainless steel. I. Effects on loop growth. *Physica Status Solidi (a)*, 57(1) :281–290, January 1980. ISSN 00318965, 1521396X. doi : 10.1002/pssa.2210570131. URL http://doi.wiley.com/10.1002/pssa.2210570131.

A. J. E. Foreman. The diffusion of point defects to the foil surface during irradiation damage experiments in the high voltage electron microscope. *Radiation Effects*, 14(3-4) : 175–179, June 1972. ISSN 0033-7579. doi : 10.1080/00337577208231197. URL https://doi.org/10.1080/00337577208231197.

F.A. Garner. Impact of the injected interstitial on the correlation of charged particle and neutron-induced radiation damage. *Journal of Nuclear Materials*, 117 :177–197, July 1983. ISSN 0022-3115. doi : 10.1016/0022-3115(83)90023-5. URL http://www.sciencedirect.com/science/article/pii/0022311583900235.

F.A. Garner. Radiation Damage in Austenitic Steels. In *Comprehensive Nuclear Materials*, pages 33–95. Elsevier, 2012. ISBN 978-0-08-056033-5. doi : 10.1016/B978-0-08-056033-5.00065-3. URL http://linkinghub.elsevier.com/retrieve/pii/B9780080560335000653.

Fa Garner and Hr Brager. Swelling of Austenitic Iron-Nickel-Chromium Ternary Alloys During Fast Neutron Irradiation. In Fa Garner and Js Perrin, editors, *Effects of Radiation on Materials : Twelfth International Symposium*, pages 187–187–15. ASTM International, 100 Barr Harbor Drive, PO Box C700, West Conshohocken, PA 19428-2959, January 1985. ISBN 978-0-8031-0450-1. doi : 10.1520/STP37361S. URL http://www.astm.org/doiLink.cgi?STP37361S.

F.A. Garner and W.G. Wolfer. Factors which determine the swelling behavior of austenitic stainless steels. *Journal of Nuclear Materials*, 122(1-3) :201–206, May 1984. ISSN 00223115. doi : 10.1016/0022-3115(84)90596-8. URL http://linkinghub.elsevier.com/retrieve/pii/0022311584905968.

F.A. Garner, H.R. Brager, and R.J. Puigh. Swelling behavior of titanium-modified alloys in EBR-II. *Journal of Nuclear Materials*, 133-134 :535–539, August 1985. ISSN 0022-3115. doi : 10.1016/0022-3115(85)90205-3. URL http://www.sciencedirect.com/science/article/pii/0022311585902053.

F.A. Garner, C.A. Black, and D.J. Edwards. Factors which control the swelling of Fe-Cr-Ni ternary austenitic alloys. *Journal of Nuclear Materials*, 245(2-3) :124–130, June 1997. ISSN 00223115. doi : 10.1016/S0022-3115(97)00016-0. URL http://linkinghub.elsevier.com/retrieve/pii/S0022311597000160.

Baptiste Gault. A brief overview of atom probe tomography research. *Applied Microscopy*, 46(3) :117–126, 2016.

Didier Gilbon, Lucien le Naour, Gérard Didout, and Viviane Levy. Influence de la concentration en silicium et en titane sur le gonflement d'aciers du type 316 Ti irradiés par des électrons de 1 MeV. *Journal of Nuclear Materials*, 100 :253–265, 1981.

G.W. Greenwood, A.J.E. Foreman, and D.E. Rimmer. The role of vacancies and dislocations in the nucleation and growth of gas bubbles in irradiated fissile material. *Journal of Nuclear Materials*, 1(4) :305–324, December 1959. ISSN 00223115. doi : 10.1016/0022-3115(59)90030-3. URL http://linkinghub.elsevier.com/retrieve/pii/0022311559900303.

K. P. Gupta. The Cr-Ni-Hf (Chromium-Nickel-Hafnium) System. *Journal of Phase Equilibria and Diffusion*, 31(5) :472–474, October 2010. ISSN 1863-7345. doi : 10.1007/s11669-010-9689-5. URL https://doi.org/10.1007/s11669-010-9689-5.

J. E. Harbottle and D. I. R. Norris. High voltage electron microscope studies of void nucleation in nickel. *Journal of Microscopy*, 97(1-2) :129–138, January 1973. ISSN 00222720. doi : 10.1111/j.1365-2818.1973.tb03767.x. URL http://doi.wiley.com/10.1111/j.1365-2818.1973.tb03767.x.

S. Hasanzadeh, R. Schäublin, B. Décamps, V. Rousson, E. Autissier, M. F. Barthe, and C. Hébert. Three-dimensional scanning transmission electron microscopy of dislocation loops in tungsten. *Micron*, 113 :24 – 33, 2018. ISSN 0968-4328. doi : https://doi.org/10.1016/j.micron.2018.05.010. URL http://www.sciencedirect.com/science/article/pii/S0968432818301057.

K Hermann. Appendix e : Parameter tables of crystals. *Crystallography and Surface Structure : An Introduction for Surface Scientists and Nanoscientists*, pages 265–266, 2011.

J.A. Hinks. A review of transmission electron microscopes with in situ ion irradiation. *Nuclear Instruments and Methods in Physics Research Section B : Beam Interactions with Materials and Atoms*, 267(23) :3652–3662, December 2009. ISSN 0168-583X. doi : 10.1016/j.nimb.2009.09.014. URL http://www.sciencedirect.com/science/article/pii/S0168583X09009811.

Peter Bernhard Hirsch. *Electron microscopy of thin crystals*. Plenum Press, 1967.

Akimichi Hishinuma and Katsumaro Fukai. Effect of Solute Titanium on Void Swelling in 316 Stainless Steel. *Journal of Nuclear Science and Technology*, 20(8) :668–673, August 1983. ISSN 0022-3131, 1881-1248. doi : 10.1080/18811248.1983.9733448. URL http://www.tandfonline.com/doi/abs/10.1080/18811248.1983.9733448.

J.J. Holmes, R.E. Robbins, J.L. Brimhall, and B. Mastel. Elevated temperature irradiation hardening in austenitic stainless steel. *Acta Metallurgica*, 16(7) :955–967, July 1968. ISSN 0001-6160. doi : 10.1016/0001-6160(68)90062-X. URL http://www.sciencedirect.com/science/article/pii/000161606890062X.

M. Horiki and M. Kiritani. Microstructural evolution in low-dose neutron-irradiated Fe-16Ni-15Cr alloy. *Journal of Nuclear Materials*, 212-215 :246–251, September 1994. ISSN 00223115. doi : 10.1016/0022-3115(94)90065-5. URL http://linkinghub.elsevier.com/retrieve/pii/0022311594900655.

Barbara Horváth, Robin Schäublin, and Yong Dai. Flash electropolishing of TEM lamellas of irradiated tungsten. *Nuclear Instruments and Methods in Physics Research Section B : Beam Interactions with Materials and Atoms*, 449 :29–34, June 2019. ISSN 0168583X. doi : 10.1016/j.nimb.2019.04.047. URL https://linkinghub.elsevier.com/retrieve/pii/S0168583X19302320.

A. Howie and P. R. Swann. Direct measurements of stacking-fault energies from observations of dislocation nodes. *Philosophical Magazine*, 6(70) :1215–1226, October 1961. ISSN 0031-8086. doi : 10.1080/14786436108243372. URL http://www.tandfonline.com/doi/abs/10.1080/14786436108243372.

Archibald Howie and Michael John Whelan. Diffraction contrast of electron microscope images of crystal lattice defects-ii. the development of a dynamical theory. *Proceedings of the Royal Society of London. Series A. Mathematical and Physical Sciences*, 263(1313) : 217–237, 1961.

Archibald Howie and Michael John Whelan. Diffraction contrast of electron microscope images of crystal lattice defects. iii. results and experimental confirmation of the dynamical theory of dislocation image contrast. *Proceedings of the Royal Society of London. Series A. Mathematical and Physical Sciences*, 267(1329) :206–230, 1962.

Liangzhao Huang, Nastar Maylise, Schuler Thomas, and Messina. Luca. Multi-scale modeling of the effects of temperature, radiation flux and sink strength on point-defect and solute redistribution in dilute fe-based alloys. unpublished.

Derek Hull and David J. Bacon. *Introduction to dislocations*. Elsevier/Butterworth-Heinemann, Amsterdam, 5. ed edition, 2011. ISBN 978-0-08-096672-4 978-0-08-096673-1. OCLC : 704891549.

P. Humble, M. H. Loretto, and L. M. Clarebrough. The nature of defects in quenched nickel. *Philosophical Magazine*, 15(134) :297–303, February 1967. ISSN 0031-8086. doi : 10.1080/14786436708227702. URL http://www.tandfonline.com/doi/abs/10.1080/14786436708227702.

S. Ishino, N. Sekimura, H. Sakaida, and Y. Kanzaki. In Situ Observation of Heavy Ion Radiation Damage in some FCC Metals. *Materials Science Forum*, 97-99 :165–182, January 1992. ISSN 1662-9752. doi : 10.4028/www.scientific.net/MSF.97-99.165. URL https://www.scientific.net/MSF.97-99.165.

Shiori Ishino. A review of in situ observation of defect production with energetic heavy ions. *Proceedings of the International Workshop on Defect Production, Accumulation and Materials Performance in an Irradiation Environment*, 251 :225–236, November 1997. ISSN 0022-3115. doi : 10.1016/S0022-3115(97)00247-X. URL http://www.sciencedirect.com/science/article/pii/S002231159700247X.

Shiori Ishino, Koji Fukuya, Takeo Muroga, Naoto Skinura, and Hiroshi Kawanishi. In-situ microstructural observation of radiation damage in nickel produced by energetic heavy particles. *Journal of Nuclear Materials*, 122&123 :597–601, 1984.

M.L. Jenkins. Characterisation of radiation-damage microstructures by TEM. *Journal of Nuclear Materials*, 216 :124–156, October 1994. ISSN 0022-3115. doi : 10.1016/0022-3115(94)90010-8. URL http://www.sciencedirect.com/science/article/pii/0022311594900108.

J.L. Seran. NT DMN : synthese des études sur le gonflement des alliages austénitiques développées au CEA pour le gainage du combustible RNR-Na in Sodium-Cooled Nuclear Reactors. In *A Nuclear Energy Division Monograph*, pages 135–142. 2015.

W.G. Johnston, J.H. Rosolowski, A.M. Turkalo, and T. Lauritzen. An experimental survey of swelling in commercial Fe-Cr-Ni alloys bombarded with 5 MeV Ni Ions. *Journal of Nuclear Materials*, 54(1) :24–40, November 1974. ISSN 00223115. doi : 10.1016/0022-3115(74)90073-7. URL http://linkinghub.elsevier.com/retrieve/pii/0022311574900737.

PM Kelly, A Jostsons, RG Blake, and JG Napier. The determination of foil thickness by scanning transmission electron microscopy. *Physica status solidi (a)*, 31(2) :771–780, 1975.

H. W. King. Quantitative size-factors for metallic solid solutions. *Journal of Materials Science*, 1(1) :79–90, February 1966. ISSN 0022-2461, 1573-4803. doi : 10.1007/BF00549722. URL http://link.springer.com/10.1007/BF00549722.

M. Kiritani, T. Yoshiie, S. Kojima, Y. Satoh, and K. Hamada. Fission-fusion correlation by fission reactor irradiation with improved control. *Journal of Nuclear Materials*, 174 (2) :327–351, November 1990. ISSN 0022-3115. doi : 10.1016/0022-3115(90)90245-I. URL http://www.sciencedirect.com/science/article/pii/002231159090245I.

Michio Kiritani, Naoaki Yoshida, Hiroshi Takata, and Yasuhiro Maehara. Growth of Interstitial Type Dislocation Loops and Vacancy Mobility in Electron Irradiated Metals. *Journal of the Physical Society of Japan*, 38(6) :1677–1686, 1975. doi : 10.1143/JPSJ.38.1677.

K. Kitagawa, K. Yamakawa, H. Fukushima, T. Yoshiie, Y. Hayashi, H. Yoshida, Y. Shimomura, and M. Kiritani. Ion-irradiation experiment for the fundamental studies of damage evolution of fusion materials. *Journal of Nuclear Materials*, 133-134 :395–399, August 1985. ISSN 0022-3115. doi : 10.1016/0022-3115(85)90175-8. URL http://www.sciencedirect.com/science/article/pii/0022311585901758.

R.L. Klueh and D.R. Harries. *High-chromium Ferritic and Martensitic Steels for Nuclear Applications*. ASTM's monograph series. ASTM, 2001. ISBN 978-0-8031-2090-7. URL https://books.google.fr/books?id=e51rngEACAAJ.

S. Kojima, T. Yoshiie, and M. Kiritani. Defect structure evolution from cascade damage in 14 Mev neutron irradiated nickel and nickel alloys. *Journal of Nuclear Materials*, 155 : 1249–1253, 1988.

Doris Kuhlmann-wilsdorf. On the origin of dislocations. *Philosophical Magazine*, 3(26) : 125–139, February 1958. ISSN 0031-8086. doi : 10.1080/14786435808244398. URL http://www.tandfonline.com/doi/abs/10.1080/14786435808244398.

Kaushlendra Kumar, R. Sankarasubramanian, and Umesh V. Waghmare. Influence of dilute solute substitutions in Ni on its generalized stacking fault energies and ductility. *Computational Materials Science*, 150 :424–431, July 2018. ISSN 0927-0256. doi : 10.1016/j.commatsci.2018.04.043. URL http://www.sciencedirect.com/science/article/pii/S0927025618302842.

T. Lauritzen, A. Withop, and U.E. Wolff. Swelling of austenitic stainless steels under fast neutron irradiation at elevated temperatures. *Nuclear Engineering and Design*, 9(2) : 265–268, February 1969. ISSN 0029-5493. doi : 10.1016/0029-5493(69)90063-6. URL http://www.sciencedirect.com/science/article/pii/0029549369900636.

E.H. Lee, A.F. Rowcliffe, and E.A. Kenik. Effects of Si and Ti on the phase stability and swelling behavior of AISI 316 stainless steel. *Journal of Nuclear Materials*, 83(1) : 79–89, August 1979. ISSN 00223115. doi : 10.1016/0022-3115(79)90594-4. URL http://linkinghub.elsevier.com/retrieve/pii/0022311579905944.

E.H. Lee, A.F. Rowcliffe, and L.K. Mansur. Precipitation and cavity formation in austenitic stainless steels during irradiation. *Journal of Nuclear Materials*, 104 :1475–1480, January 1981. ISSN 00223115. doi : 10.1016/0022-3115(82)90808-X. URL http://linkinghub.elsevier.com/retrieve/pii/002231158290808X.

Clément Lemaignan. *Science des matériaux pour le nucléaire*. EDP Sciences, December 2012. ISBN 978-2-7598-0164-0. Google-Books-ID : ACfX9vQ28PsC.

Meimei Li, M.A. Kirk, P.M. Baldo, Donghua Xu, and B.D. Wirth. Study of defect evolution by TEM with in situ ion irradiation and coordinated modeling. *Philosophical Magazine*, 92(16) :2048–2078, June 2012. ISSN 1478-6435. doi : 10.1080/14786435.2012.662601. URL https://doi.org/10.1080/14786435.2012.662601.

Mike H. Loretto and Raymond Edward Smallman. *Defect analysis in electron microscopy*. Chapman and Hall, New York, 1975. ISBN 0-412-13760-7.

Chenyang Lu, Ke Jin, Laurent K. Béland, Feifei Zhang, Taini Yang, Liang Qiao, Yanwen Zhang, Hongbin Bei, Hans M. Christen, Roger E. Stoller, and Lumin Wang. Direct Observation of Defect Range and Evolution in Ion-Irradiated Single Crystalline Ni and Ni Binary Alloys. *Scientific Reports*, 6(1), April 2016a. ISSN 2045-2322. doi : 10.1038/srep19994. URL http://www.nature.com/articles/srep19994.

Chenyang Lu, Liangliang Niu, Nanjun Chen, Ke Jin, Taini Yang, Pengyuan Xiu, Yanwen Zhang, Fei Gao, Hongbin Bei, Shi Shi, Mo-Rigen He, Ian M. Robertson, William J. Weber, and Lumin Wang. Enhancing radiation tolerance by controlling defect mobility and migration pathways in multicomponent single-phase alloys. *Nature Communications*, 7 :13564, December 2016b. ISSN 2041-1723. doi : 10.1038/ncomms13564. URL http://www.nature.com/doifinder/10.1038/ncomms13564.

Chenyang Lu, Taini Yang, Ke Jin, Ning Gao, Pengyuan Xiu, Yanwen Zhang, Fei Gao, Hongbin Bei, William J Weber, Kai Sun, et al. Radiation-induced segregation on defect clusters in single-phase concentrated solid-solution alloys. *Acta Materialia*, 127 :98–107, 2017.

DM Maher and BL Eyre. Neutron irradiation damage in molybdenum. part i. characterization of small perfect dislocation loops by transmission electron microscopy. Technical report, Atomic Energy Research Establishment, Harwell, Eng., 1971.

M. J. Makin. Electron displacement damage in copper and aluminium in a high voltage electron microscope. *The Philosophical Magazine : A Journal of Theoretical Experimental and Applied Physics*, 18(153) :637–653, 1968. doi : 10.1080/14786436808227466. URL https://doi.org/10.1080/14786436808227466.

MJ Makin and B Hudson. {012} loops in face-centred cubic metals. *Philosophical Magazine*, 8(87) :447–460, 1963.

L.K. Mansur and M.H. Yoo. The effects of impurity trapping on irradiation-induced swelling and creep. *Journal of Nuclear Materials*, 74(2) :228–241, June 1978. ISSN 00223115. doi : 10.1016/0022-3115(78)90362-8. URL http://linkinghub.elsevier.com/retrieve/pii/0022311578903628.

A. D. Marwick and R. C. Filler. The effect of point defect fluxes on radiation-enhanced diffusion in nickel. *Radiation Effects*, 33(4) :245–250, January 1977. ISSN 0033-7579. doi : 10.1080/00337577708233113. URL https://doi.org/10.1080/00337577708233113.

A.D. Marwick, R.C. Piller, and P.M. Sivell. Mechanisms of radiation-induced segregation in dilute nickel alloys. *Journal of Nuclear Materials*, 83(1) :35–41, August 1979. ISSN 00223115. doi : 10.1016/0022-3115(79)90589-0. URL https://linkinghub.elsevier.com/retrieve/pii/0022311579905890.

B. Mastel and J.L. Brimhall. Voids produced in high purity nickel by neutron irradiation. *Journal of Nuclear Materials*, 28(1) :115–117, October 1968. ISSN 00223115. doi : 10.1016/0022-3115(68)90063-9. URL http://linkinghub.elsevier.com/retrieve/pii/0022311568900639.

D. J. Mazey and J. A. Hudson. Observation of large faulted interstitial loops in proton-irradiated nickel. *Journal of Nuclear Materials*, 37(1) :13–17, 1970.

D.J. Mazey, D.R. Harries, and J.A. Hudson. The effects of silicon and titanium on void swelling and phase stability in 12Cr-15Ni austenitic alloys irradiated with 46 MeV nickel ions. *Journal of Nuclear Materials*, 89(1) :155–181, March 1980. ISSN 00223115. doi : 10.1016/0022-3115(80)90020-3. URL http://linkinghub.elsevier.com/retrieve/pii/0022311580900203.

P. J. Maziasz and C. J. McHargue. Microstructural evolution in annealed austenitic steels during neutron irradiation. *International Materials Reviews*, 32(1) :190–219, January 1987. ISSN 0950-6608, 1743-2804. doi : 10.1179/095066087790150331. URL http://www.tandfonline.com/doi/full/10.1179/095066087790150331.

P.J. Maziasz. Formation and stability of radiation-induced phases in neutron-irradiated austenitic and ferritic steels. *Journal of Nuclear Materials*, 169 :95–115, December 1989. ISSN 0022-3115. doi : 10.1016/0022-3115(89)90525-4. URL http://www.sciencedirect.com/science/article/pii/0022311589905254.

P.J. Maziasz. Overview of microstructural evolution in neutron-irradiated austenitic stainless steels. *Journal of Nuclear Materials*, 205 :118–145, October 1993. ISSN 00223115. doi : 10.1016/0022-3115(93)90077-C. URL http://linkinghub.elsevier.com/retrieve/pii/002231159390077C.

Bertrand Michaut. *Caractérisation et modélisation de l'évolution de la microstructure et du gonflement d'aciers austénitiques représentatifs des internes inférieurs de Réacteur à Eau Pressurisée sous irradiations aux ions.* PhD thesis, Paris Saclay, 2017.

Kiritani Michio, Yoshida Naoaki, and Takata Hiroshi. Growth of intersitital type dislocation loops and vacancy mobility in electron irradiated metals. *Journal of physical society of Japan*, 38(6) :1677–1686, 1975.

K.M. Miller. Interstitial loop growth in hvem-irradiated nickel foils. *Journal of Nuclear Materials*, 115(2) :216–222, April 1983. ISSN 0022-3115. doi : 10.1016/0022-3115(83)90313-6. URL http://www.sciencedirect.com/science/article/pii/0022311583903136.

K.M. Miller, S.B. Fisher, and R.J. White. Interstitial loop growth in irradiated thin foils. *Journal of Nuclear Materials*, 110(2-3) :265–276, October 1982. ISSN 00223115. doi : 10.1016/0022-3115(82)90155-6. URL http://linkinghub.elsevier.com/retrieve/pii/0022311582901556.

T. Muroga and N. Yoshida. The influence of isotopically controlled boron addition on void swelling of nickel irradiated in FFTF. *Journal of Nuclear Materials*, 191-194 : 1254–1258, September 1992. ISSN 00223115. doi : 10.1016/0022-3115(92)90675-B. URL https://linkinghub.elsevier.com/retrieve/pii/002231159290675B.

L.E. Murr. Stacking-fault anomalies and the measurement of stacking-fault free energy in f.c.c. thin films. *Thin Solid Films*, 4(6) :389–412, December 1969. ISSN 00406090. doi : 10.1016/0040-6090(69)90089-3. URL http://linkinghub.elsevier.com/retrieve/pii/0040609069900893.

I. M. Neklyudov and V. N. Voyevodin. Radiation swelling of modified austenitic steels. *Russian Physics Journal*, 51(4) :400–413, April 2008. ISSN 1064-8887, 1573-9228. doi : 10.1007/s11182-008-9063-9. URL http://link.springer.com/10.1007/s11182-008-9063-9.

K. Niwase, T. Ezawa, T. Tanabe, M. Kiritani, and F.E. Fujita. Dislocation loops and their depth profiles in He+ and D+ ion irradiated nickel. *Journal of Nuclear Materials*, 203(1) :56–66, July 1993. ISSN 00223115. doi : 10.1016/0022-3115(93)90430-7. URL http://linkinghub.elsevier.com/retrieve/pii/0022311593904307.

Kai Nordlund, Andrea E. Sand, Fredric Granberg, Steven J. Zinkle, Roger Stoller, Robert S. Averback, Tomoaki Suzudo, Lorenzo Malerba, Florian Banhart, and William J. Weber. Primary radiation damage in materials. *Report prepared by the OECD/NEA Working Party on Multiscale Modelling of Fuels and Structural Materials for Nuclear Systems, Expert Group on Primary Radiation Damage Nuclear Science NEA/NSC/DOC*, 9, 2015.

D. I. R. Norris. Dislocation loop growth in an electron irradiated thin foil. *Philosophical Magazine*, 22(180) :1273–1278, December 1970. ISSN 0031-8086. doi : 10.1080/14786437008226935. URL http://www.tandfonline.com/doi/abs/10.1080/14786437008226935.

Okamoto Hiroaki, Massalski T.B., Subramanian P.R., and Kacprzak L. *Binary alloy phase diagrams*, volume 3. ASM International, Materials Park, Ohio, 2nd edition, 1990. ISBN 978-0-87170-403-0.

R. F. Pinizzotto, L. J. Chen, and A. J. Ardell. Nickel and nitrogen ion irradiation induced void swelling and defect microstructures in Ni-Al, Ni-Cr and Ni-Ti solid solutions. *Metallurgical Transactions A*, 9(12) :1715–1727, December 1978. ISSN 0360-2133, 1543-1940. doi : 10.1007/BF02663401. URL http://link.springer.com/10.1007/BF02663401.

Igor Pioro. *Handbook of generation IV nuclear reactors*. Woodhead Publishing, 2016. ISBN 0-08-100162-2.

C Pokor, Y Brechet, P Dubuisson, J.-P Massoud, and A Barbu. Irradiation damage in 304 and 316 stainless steels : experimental investigation and modeling. Part I : Evolution of the microstructure. *Journal of Nuclear Materials*, 326(1) :19–29, March 2004. ISSN 00223115. doi : 10.1016/j.jnucmat.2003.11.007. URL http://linkinghub.elsevier.com/retrieve/pii/S0022311503005129.

G. M. Poletaev and M. D. Starostenkov. Contributions of different mechanisms of self-diffusion in face-centered cubic metals under equilibrium conditions. *Physics of the Solid State*, 52(6) :1146–1154, June 2010. ISSN 1090-6460. doi : 10.1134/S1063783410060065. URL https://doi.org/10.1134/S1063783410060065.

S.I Porollo, A.M Dvoriashin, A.N Vorobyev, and Yu.V Konobeev. The microstructure and tensile properties of fe–cr alloys after neutron irradiation at 400°C to 5.5–7.1 dpa. *Journal of Nuclear Materials*, 256(2-3) :247–253, August 1998. ISSN 00223115. doi : 10.1016/S0022-3115(98)00043-9. URL http://linkinghub.elsevier.com/retrieve/pii/S0022311598000439.

S.I. Porollo, A.M. Dvoriashin, Yu.V. Konobeev, and F.A. Garner. Microstructure and swelling of neutron irradiated nickel and binary nickel alloys. *Journal of Nuclear Materials*, 442 (1-3) :S809–S812, November 2013. ISSN 00223115. doi : 10.1016/j.jnucmat.2013.05.019. URL http://linkinghub.elsevier.com/retrieve/pii/S0022311513007587.

A. Prokhodtseva, B. Décamps, A. Ramar, and R. Schäublin. Impact of He and Cr on defect accumulation in ion-irradiated ultrahigh-purity Fe(Cr) alloys. *Acta Materialia*, 61(18) : 6958–6971, October 2013. ISSN 13596454. doi : 10.1016/j.actamat.2013.08.007. URL http://linkinghub.elsevier.com/retrieve/pii/S1359645413005934.

I. M. Robertson, J. S. Vetrano, M. A. Kirk, and M. L. Jenkins. On the formation of vacancy type dislocation loops from displacement cascades in nickel. *Philosophical Magazine A*, 63 (2) :299–318, February 1991. ISSN 0141-8610, 1460-6992. doi : 10.1080/01418619108204851. URL http://www.tandfonline.com/doi/abs/10.1080/01418619108204851.

T. M. Robinson and M. L. Jenkins. Heavy-ion irradiation of nickel and nickel alloys. *Philosophical Magazine A*, 43(4) :999–1015, April 1981. ISSN 0141-8610, 1460-6992. doi : 10.1080/01418618108239507. URL http://www.tandfonline.com/doi/abs/10.1080/01418618108239507.

HP Rooksby. Structure of nickel oxide. *Nature*, 152(3854) :304–304, 1943.

Baptiste Rouxel, Caroline Bisor, Yann De Carlan, Arnaud Courcelle, and Alexandre Legris. Influence of the austenitic stainless steel microstructure on the void swelling under ion irradiation. *EPJ Nuclear Sciences & Technologies*, 2 :30, 2016. ISSN 2491-9292. doi : 10.1051/epjn/2016023. URL http://www.epj-n.org/10.1051/epjn/2016023.

Raluca Schibli and Robin Schäublin. On the formation of stacking fault tetrahedra in irradiated austenitic stainless steels – A literature review. *Journal of Nuclear Materials*, 442(1-3) :S761–S767, November 2013. ISSN 00223115. doi : 10.1016/j.jnucmat.2013.05.077. URL http://linkinghub.elsevier.com/retrieve/pii/S0022311513008416.

L.E. Seitzman, L.M. Wang, G.L. Kulcinski, and R.A. Dodd. The effect of oxygen on void stability in nickel and austenitic steel. *Journal of Nuclear Materials*, 141-143 : 738–742, November 1986. ISSN 00223115. doi : 10.1016/0022-3115(86)90083-8. URL https://linkinghub.elsevier.com/retrieve/pii/0022311586900838.

N. Sekimura and S. Ishino. The effect of titanium addition on microstructural evolution in austenitic steel irradiated with fast neutrons in FFTF. *Journal of Nuclear Materials*, 179-181 :542–545, March 1991. ISSN 00223115. doi : 10.1016/0022-3115(91)90145-W. URL http://linkinghub.elsevier.com/retrieve/pii/002231159190145W.

J. Silcox and P. B. Hirsch. Direct observations of defects in quenched gold. *Philosophical Magazine*, 4(37) :72–89, January 1959. ISSN 0031-8086. doi : 10.1080/14786435908238228. URL http://www.tandfonline.com/doi/abs/10.1080/14786435908238228.

B. N. Singh, T. Leffers, M. J. Makin, G. P. Walters, and A. J. E. Foreman. Effects of implanted helium on void nucleation during hvem irradiation of stainless steel containing silicon. *Journal of Nuclear Materials*, 104 :1041–1045, 1981.

R.E. Smallman and K.H. Westmacott. Invited review : The nature and behaviour of vacancy clusters in close-packed metals. *Materials Science and Engineering*, 9 :249–272, January 1972. ISSN 00255416. doi : 10.1016/0025-5416(72)90042-0. URL http://linkinghub.elsevier.com/retrieve/pii/0025541672900420.

P. A. Stadelmann. JEMS-EMS java version. *CIME-EPFL, Lausanne, Switzerland*, 2004.

R.E. Stoller, M.B. Toloczko, G.S. Was, A.G. Certain, S. Dwaraknath, and F.A. Garner. On the use of SRIM for computing radiation damage exposure. *Nuclear Instruments and Methods in Physics Research Section B : Beam Interactions with Materials and Atoms*, 310 :75–80, September 2013. ISSN 0168-583X. doi : 10.1016/j.nimb.2013.05.008. URL http://www.sciencedirect.com/science/article/pii/S0168583X13005053.

J.L. Straalsund, R.W. Powell, and B.A. Chin. An overview of neutron irradiation effects in LMFBR materials. *Journal of Nuclear Materials*, 108&109 :299–305, 1982. ISSN 0022-3115.

D Strzeciwilk, Z Wokulski, and P Tkacz. Growth and tem and hrem characterisation of tic crystals grown from high-temperature solutions. *Crystal Research and Technology : Journal of Experimental and Industrial Crystallography*, 38(3-5) :283–287, 2003.

James F. Stubbins and F. A. Garner. Swelling and microstructure of high purity nickel irradiated with fast neutrons in EBR-II. *Journal of nuclear materials*, 191 :1295–1299, 1992.

Masayoshi Suzuki, A. Sato, T. Mori, J. Nagakawa, N. Yamamoto, and H. Shiraishi. In situ deformation and unfaulting of interstitial loops in proton-irradiated steels. *Philosophical Magazine A*, 65(6) :1309–1326, June 1992. ISSN 0141-8610, 1460-6992. doi : 10.1080/01418619208205606. URL http://www.tandfonline.com/doi/abs/10.1080/01418619208205606.

J.D. Tucker, R. Najafabadi, T.R. Allen, and D. Morgan. Ab initio-based diffusion theory and tracer diffusion in Ni–Cr and Ni–Fe alloys. *Journal of Nuclear Materials*, 405(3) : 216–234, October 2010. ISSN 00223115. doi : 10.1016/j.jnucmat.2010.08.003. URL http://linkinghub.elsevier.com/retrieve/pii/S0022311510003715.

K. Urban. Growth of defect clusters in thin nickel foils during electron irradiation (I). *Physica Status Solidi (a)*, 4(3) :761–772, March 1971. ISSN 00318965, 1521396X. doi : 10.1002/pssa.2210040321. URL http://doi.wiley.com/10.1002/pssa.2210040321.

T. R. Waite. Theoretical Treatment of the Kinetics of Diffusion-Limited Reactions. *Phys. Rev.*, 107(2) :463–470, July 1957. doi : 10.1103/PhysRev.107.463. URL https://link.aps.org/doi/10.1103/PhysRev.107.463.

E. Wakai, N. Hashimoto, J.P. Robertson, T. Sawai, and A. Hishinuma. Swelling of cold-worked austenitic stainless steels irradiated in HFIR under spectrally tailored conditions. *Journal of Nuclear Materials*, 307-311 :352–356, December 2002. ISSN 00223115. doi : 10.1016/S0022-3115(02)01189-3. URL http://linkinghub.elsevier.com/retrieve/pii/S0022311502011893.

L.M. Wang, R.A. Dodd, and G.L. Kulcinski. Gas effects on void formation in 14 MeV nickel ion irradiated pure nickel. *Journal of Nuclear Materials*, 141-143 :713–717, November 1986. ISSN 00223115. doi : 10.1016/0022-3115(86)90078-4. URL https://linkinghub.elsevier.com/retrieve/pii/0022311586900784.

Gary S. Was. *Fundamentals of Radiation Materials Science : Metals and Alloys*. Springer, July 2016. ISBN 978-1-4939-3438-6. Google-Books-ID : yDGmDAAAQBAJ.

G.S. Was and T. Allen. Intercomparison of microchemical evolution under various types of particle irradiation. *Journal of Nuclear Materials*, 205 :332–338, October 1993. ISSN 00223115. doi : 10.1016/0022-3115(93)90097-I. URL http://linkinghub.elsevier.com/retrieve/pii/002231159390097I.

H. Watanabe, A. Aoki, T. Muroga, and N. Yoshida. Effect of combined addition of phosphorus and titanium on microstructural evolution in Fe-Cr-Ni alloys. *Journal of Nuclear Materials*, 179-181 :529–533, March 1991. ISSN 00223115. doi : 10.1016/0022-3115(91)90142-T. URL http://linkinghub.elsevier.com/retrieve/pii/002231159190142T.

J Weertman and WV Green. Void Growth Suppression by Dislocation Impurity Atmospheres. In FR Shober, editor, *Irradiation Effects on The Microstructure and Properties of Metals*, pages 256–269. ASTM International, West Conshohocken, PA, January 1976. ISBN 978-0-8031-5543-5. doi : 10.1520/STP38053S. URL https://www.astm.org/DIGITAL_LIBRARY/STP/PAGES/STP38053S.htm.

C. H. Woo and B. N. Singh. Production bias due to clustering of point defects in irradiation-induced cascades. *Philosophical Magazine A*, 65(4) :889–912, April 1992. ISSN 0141-8610. doi : 10.1080/01418619208205596. URL https://doi.org/10.1080/01418619208205596.

C.H. Woo. Intrinsic bias differential between vacancy loops and interstitial loops. *Journal of Nuclear Materials*, 107(1) :20–30, May 1982. ISSN 0022-3115. doi : 10.1016/0022-3115(82)90555-4. URL http://www.sciencedirect.com/science/article/pii/0022311582905554.

Ya-Feng Yang, Hui-Yuan Wang, Jun Zhang, Ru-Yi Zhao, Yun-Hong Liang, and Qi-Chuan Jiang. Lattice parameter and stoichiometry of ticx produced in the ti–c and ni–ti–c systems by self-propagating high-temperature synthesis. *Journal of the American Ceramic Society*, 91(8) :2736–2739, 2008.

Z. Yao, R. Schäublin, and M. Victoria. Irradiation induced behavior of pure Ni single crystal irradiated with high energy protons. *Journal of Nuclear Materials*, 323(2-3) : 388–393, December 2003. ISSN 00223115. doi : 10.1016/j.jnucmat.2003.08.015. URL http://linkinghub.elsevier.com/retrieve/pii/S0022311503003829.

M. H. Yoo and J. O. Stiegler. Growth kinetics and 'preference factor' of Frank loops in nickel during electron irradiation. *Philosophical Magazine*, 36(6) :1305–1315, December 1977. ISSN 0031-8086. doi : 10.1080/14786437708238518. URL http://www.tandfonline.com/doi/abs/10.1080/14786437708238518.

MH Yoo. Dislocation loop growth and void swelling in bounded media by charged particle damage. *Journal of Nuclear Materials*, 68(2) :193–204, 1977.

T Yoshiie, Q Xu, Y Satoh, H Ohkubo, and M Kiritani. The effect of alloying elements on the defect structural evolution in neutron irradiated Ni alloys. *Journal of Nuclear Materials*, page 5, 2000.

Pascal Yvon. *Structural Materials for Generation IV Nuclear Reactors*. Woodhead Publishing, 1 edition, 2016. ISBN 978-0-08-100906-2.

Pascal Yvon, Marion Le Flem, Céline Cabet, and Jean Louis Seran. Structural materials for next generation nuclear systems : Challenges and the path forward. *Nuclear Engineering and Design*, 294 :161–169, December 2015. ISSN 00295493. doi : 10.1016/j.nucengdes.2015.09.015. URL http://linkinghub.elsevier.com/retrieve/pii/S0029549315004173.

James F. Ziegler. SRIM-2003. *Proceedings of the Sixteenth International Conference on Ion Beam Analysis*, 219-220 :1027–1036, June 2004. ISSN 0168-583X. doi : 10.1016/j.nimb.2004.01.208. URL http://www.sciencedirect.com/science/article/pii/S0168583X04002587.

S. J. Zinkle and B. N. Singh. Analysis of displacement damage and defect production under cascade damage conditions. *Journal of Nuclear Materials*, 199(3) :173 – 191, 1993. ISSN 0022-3115. doi : https://doi.org/10.1016/0022-3115(93)90140-T. URL http://www.sciencedirect.com/science/article/pii/002231159390140T.

S. J. Zinkle, L. E. Seitzman, and W. G. Wolfer. I. Energy calculations for pure metals. *Philosophical Magazine A*, 55(1) :111–125, 1987.

S. J. Zinkle, P. J. Maziasz, and R. E. Stoller. Dose dependence of the microstructural evolution in neutron-irradiated austenitic stainless steel. *Journal of Nuclear materials*, 206 (2-3) :266–286, 1993.

S.J. Zinkle and L.L. Snead. Microstructure of copper and nickel irradiated with fission neutrons near 230°C. *Journal of Nuclear Materials*, 225 :123–131, August 1995. ISSN 00223115. doi : 10.1016/0022-3115(94)00670-9. URL http://linkinghub.elsevier.com/retrieve/pii/0022311594006709.

S.J. Zinkle and L.L. Snead. Opportunities and limitations for ion beams in radiation effects studies : Bridging critical gaps between charged particle and neutron irradiations. *Scripta Materialia*, 143 :154–160, January 2018. ISSN 1359-6462. doi : 10.1016/j.scriptamat.2017.06.041. URL http://www.sciencedirect.com/science/article/pii/S1359646217303548.

Steven J. Zinkle and Jeremy T. Busby. Structural materials for fission & fusion energy. *Materials Today*, 12(11) :12–19, November 2009. ISSN 13697021. doi : 10.1016/S1369-7021(09)70294-9. URL http://linkinghub.elsevier.com/retrieve/pii/S1369702109702949.

Annexe A

Determination of the habit plane of a polygon loop

In this part, we show the method to determine the habit plane of the rhombus-shaped perfect loop in Figure 7.5 of Section 7.1.3.

Determination of projected directions of loop segments

Figure A.1 shows the loop along three zone axes. The projection of segments D1 and D2 along the zone axes are noted as (p1, p2), (p'1, p'2) and (p"1, p"2). In each image, two reference directions are shown using the diffraction patterns and the Kikuchi map (Loretto and Smallman, 1975). Thus, the projection directions are determined and shown in Figure A.1.

The vector product of the zone axis direction (for example Z1=[001]) with the projection direction of a segment (for example p1) gives a plane with the plane normal k1=[-70 89 0] which contains the segment D1. By the same way, the projection along the second zone axis gives another non-linear planes (for example, k'1) which also contain D1. Theoretically, the D1 is the intersection of these two plane. However, due to the error of measurements, a third plane (for example, k"1) is usually required to exam the collinearity.

All the vector products are shown in Figure A.2. Two groups of planes (k1, k'1, k"1) and (k2, k'2, k"2) are drawn in a stereo-gram. Each group of planes form a small intersection triangle. The direction of the segment should thus be contained of close to the triangle. All the directions with usual indices in fcc structure <001>, <011>, <111>, <112> and <123> are shown. Therefore, D1 and D2 should be respectively [321] and $[\bar{3}21]$. The two other segments are parallel to D1 and D2 thus should has the same direction. Finally, the loop habit plane is obtained by the vector product of D1 and D2 which gives $[0\bar{1}2]$.

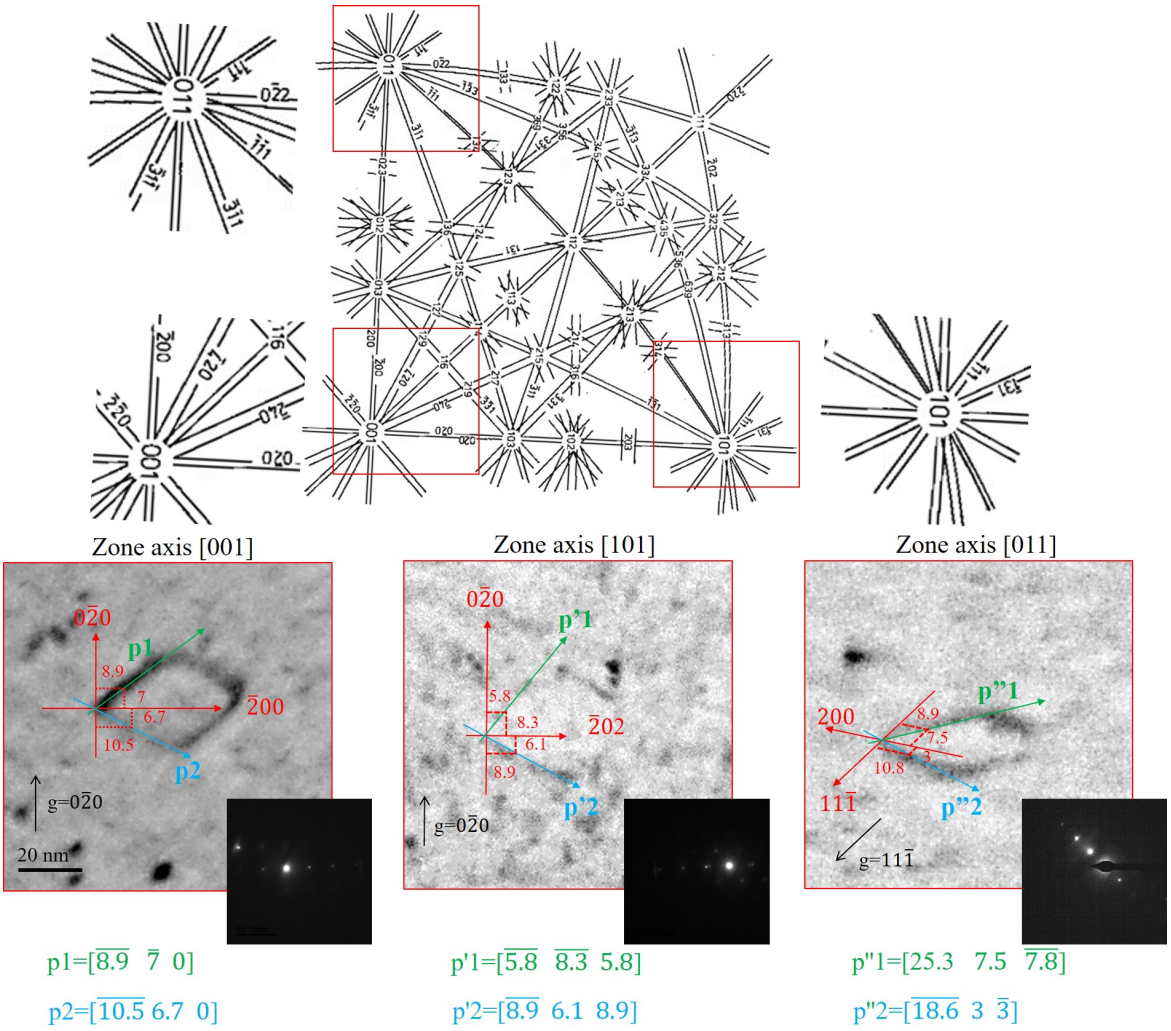

FIGURE A.1 TEM micrographs showing the projection of loop segments along three zone axes with crystal orientation shown by the Kikuchi map (Loretto and Smallman, 1975).

(a)

Projection dans Z1 001				Projection dans Z2 101				Projection dans Z3 011		
p1	p2	Z1		p'1	p'2	Z2		p''1	p''2	Z3
-8,9	-10,5	0		-5,8	-8,9	1		25,3	-19	0
-7	6,8	0		-8,3	6,1	0		7,5	3	1
0	0	1		5,8	8,9	1		-7,8	-3	1
Produit vectoriel avec Z1				Produit vectoriel avec Z2				Produit vectoriel avec Z3		
k1=p1∧Z1	k2=p2∧Z1			k'1=p'1∧Z2	k'2=p'2∧Z2			k''1=p''1∧Z3	k''2=p''2∧Z3	
-7	6,8			-8,3	6,1			15,3	6	
8,9	10,5			11,6	17,8			-25,3	19	
0	0			8,3	-6,1			25,3	-19	

(b)

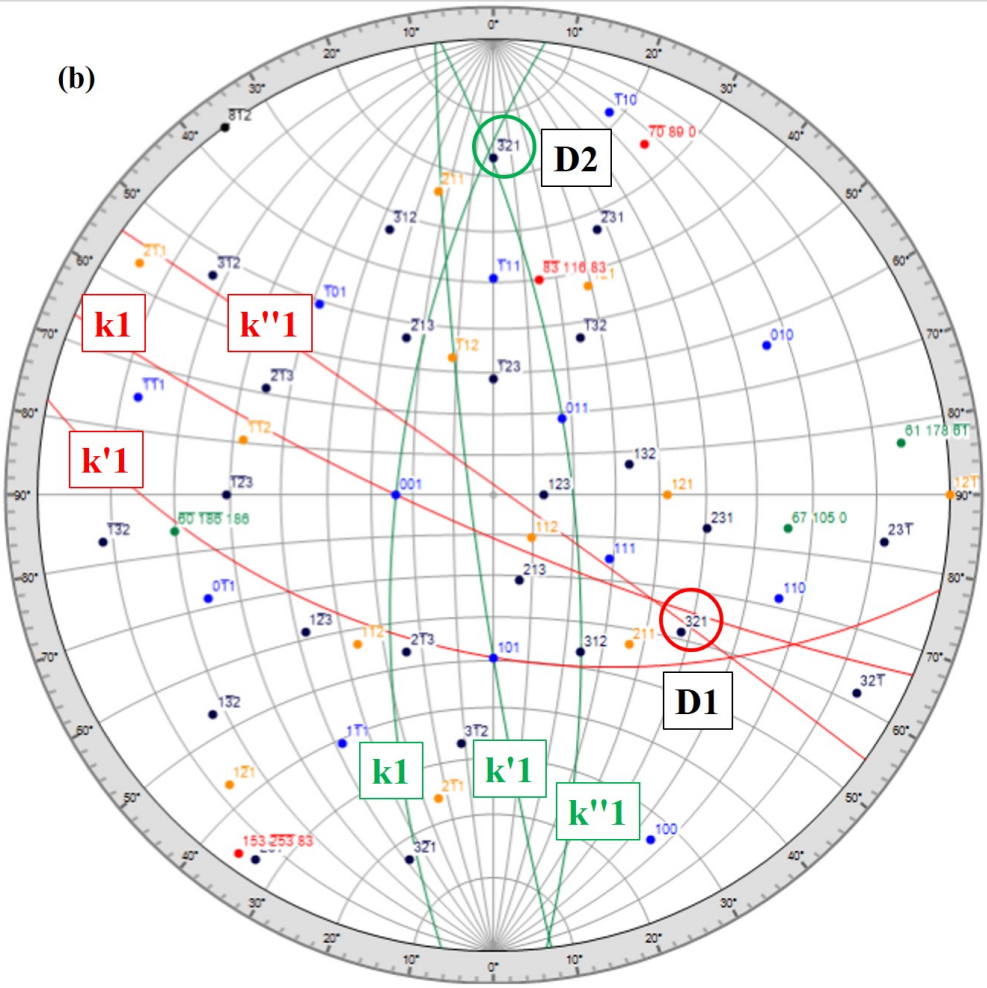

FIGURE A.2 Determination of segments directions using stereo-gram. (a) Calculations of vector products between segment projections and zone axes. (b) Stereo-gram showing the intersection of each group of planes.

Annexe B

Electron irradiation experiments on Ni and Ni-0.4Ti

The objective of this part is to investigate the origin of interstitial loops. Since electron bombardments create no or few cascade, electron irradiation experiments allow us to avoid the formation of clusters within cascades and to focus on the formation of clusters and loops due to free-migrating PDs i.e. to investigate the mechanism of medium bias and the possible existence of I-clusters A15. In this part, the electron irradiation experiments performed in this thesis are described and results are presented.

We remind that, in high voltage electron microscope (HVEM), when the sample is under observation, it is being irradiated. In the facility, it is impossible to record the diffraction pattern. However, when we record the microstructural evolution, the two-beam condition was verified on the screen to correctly image loops.

B.1 Electron irradiations on Ni at 450°C

Electron irradiation experiments were firstly performed on Ni. The temperature was increased up to 450°C without any observation on the sample. Then, the current intensity was measure to be 0.017 µA in the central hole. A zone of interest is chosen and maintained.

Figure B.1(a-b) shows the microstructural evolution at 450°C with a flux of 0.017 µA. During a long irradiation duration, no visible defect was detected. Then, in a second experiments, the flux was increased to a higher value 0.05 µA. The nucleation of visible defects was still extremely difficult. During several hours' HVEM experiments on Ni in several zones, we have only detected 3 loops which are presented in Figure B.2. The nucleation of these loops were out of the camera. The loop in Figure B.2(a) is a perfect loop while the

one in Figure B.2(b) is a Frank loop due to the stacking fault contrast. These loops both disappeared in the end. Their nature remains undetermined.

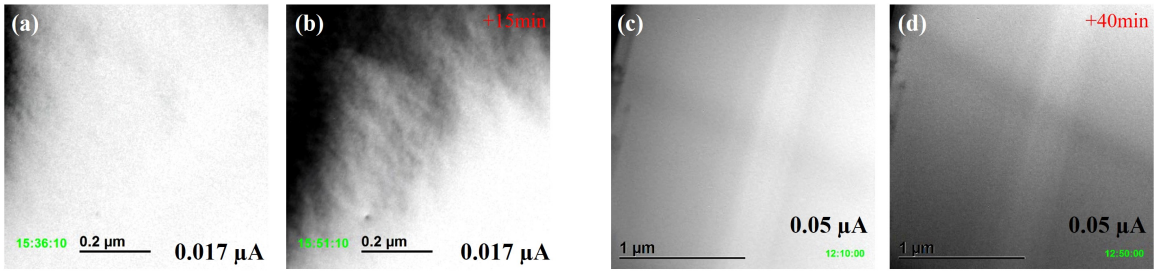

FIGURE B.1 Microstructural evolution of Ni under electron at 450°C with a flux of (a-b) 0.017 µA and (c-d) 0.05 µA.

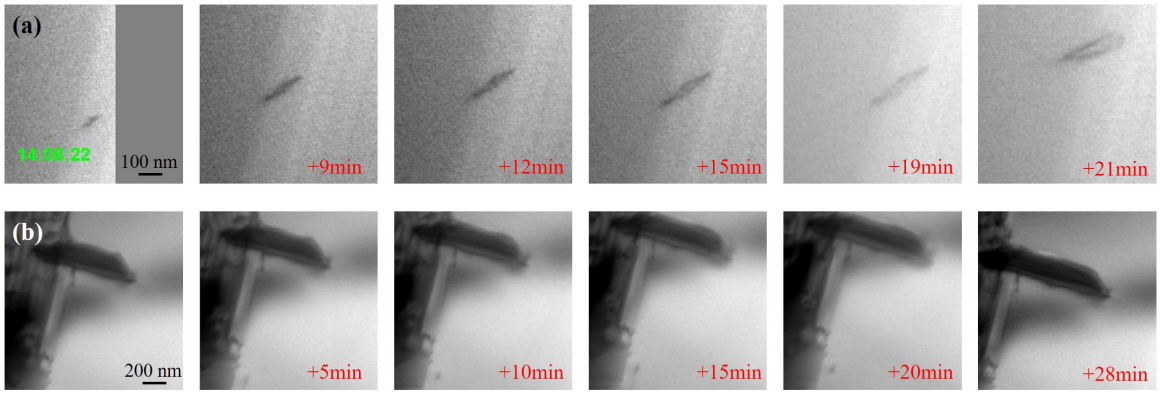

FIGURE B.2 Growth of two dislocation loops in Ni under electron at 450°C with a flux of 0.05 µA.

B.2 Electron irradiations on Ni at 450°C with a pre-irradiation at room temperature

The scarce nucleation of loops in Ni at high temperature makes the studies of radiation-induced defects (loops) difficult. To increase the nucleation density, Ni was pre-irradiated in HVEM at room temperature for 30 seconds since the mobility of PDs are much lower at room temperature than 450°C. Then, the temperature was increased to 450°C without irradiation. The pre-irradiated zone was identified and irradiated at 450°C. It is worth noting that no visible defect was observed during the pre-irradiation at room temperature.

Figure B.3 presents the microstructural evolution of pre-irradiated Ni at 450°C. At the beginning of irradiation (450°C), many visible loops have already existed in the pre-irradiated

zone. During the irradiation, some Frank loops grew into a large size. Some perfect loops grew and dissociated into dislocation lines. No loop was newly created at 450°C.

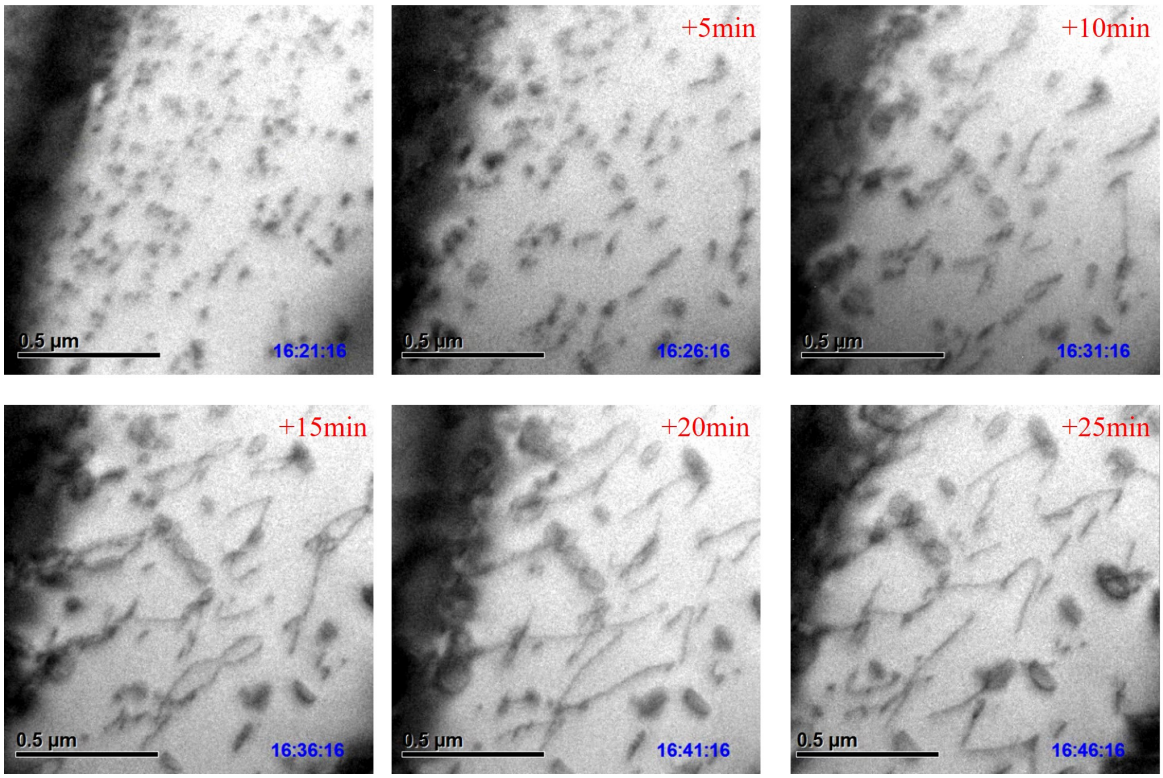

FIGURE B.3 Microstructural evolution of pre-irradiated Ni under electron at 450°C with a flux of 0.017 µA.

During the in-situ irradiation, observed Frank loops are non-segmented. We perform a post-characterization to determine their nature and results are shown in Figure B.4. Four families of Frank loops are identified. The inside-outside behavior is shown for $\mathbf{g}=\pm[200]$. When the contrast of dislocation line around the loop is diffused ($\mathbf{g}=[200]$), it shows an outside contrast. When the dislocation line is well defined ($\mathbf{g}=[\bar{2}00]$), it shows an inside contrast. The determination of loop nature in Figure B.4 demonstrates that these loops are interstitial-type.

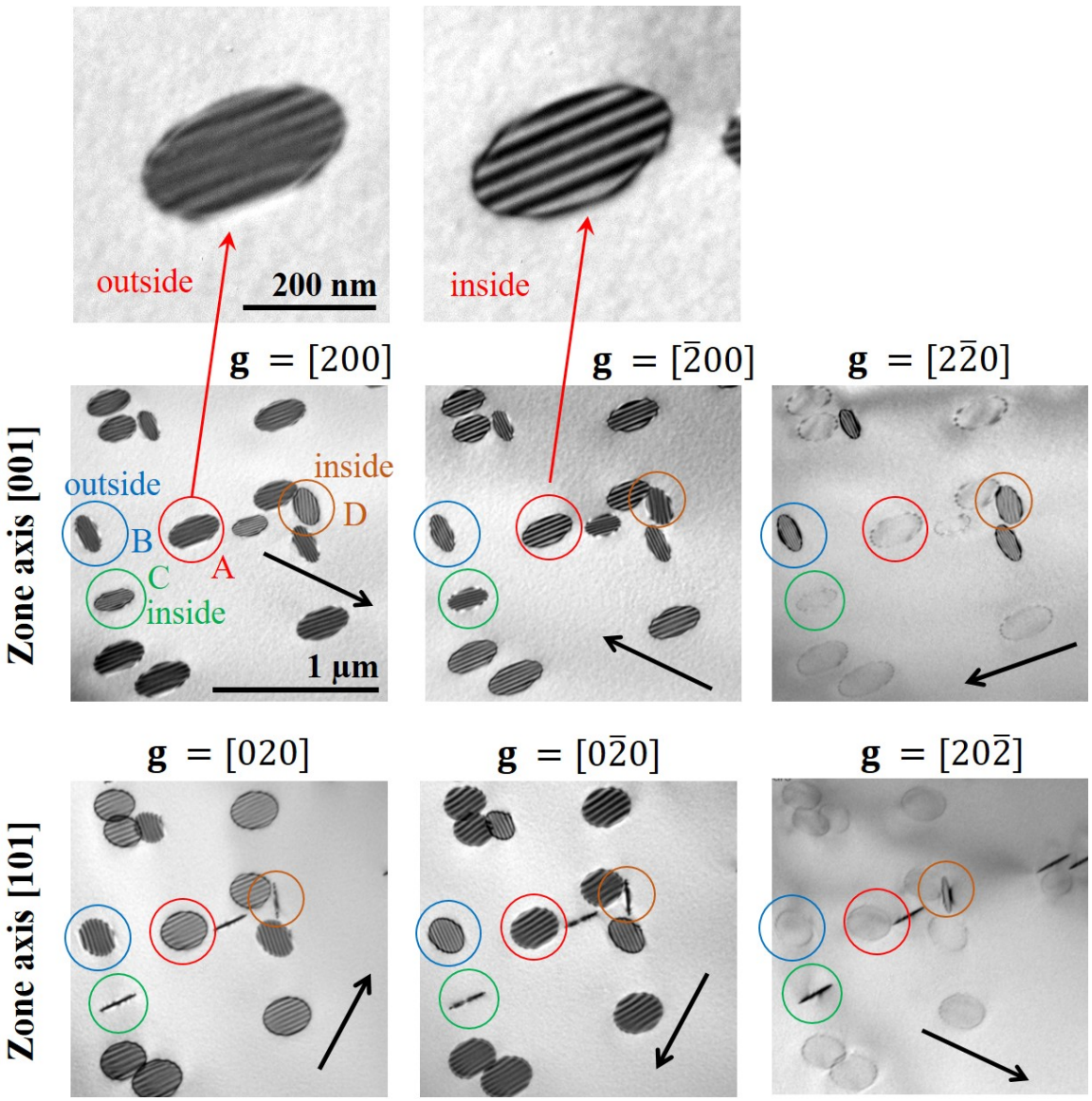

Loop	Contrast of loops along [001]			$\mathbf{g}\cdot\mathbf{b}$ for $\mathbf{g}$	$\mathbf{b}$	Nature
	$\mathbf{b}$ direction	$\mathbf{g}=[200]$	$-\mathbf{g}=[\bar{2}00]$			
A	$[1\bar{1}1]$	outside	inside	>0	$a_0/3\,[1\bar{1}1]$	interstitial
B	[111]	outside	inside	>0	$a_0/3\,[111]$	interstitial
C	$[\bar{1}11]$	inside	outside	<0	$a_0/3\,[\bar{1}11]$	interstitial
D	$[11\bar{1}]$	inside	outside	<0	$a_0/3\,[\bar{1}\bar{1}1]$	interstitial

FIGURE B.4 Determination of Frank loop nature in electron-irradiated Ni at 450°C. TEM micrographs taken along zone axis [001] with $\mathbf{g}=\pm200$, ±020, $2\bar{2}0$ and along zone axis [101] with $\mathbf{g}=20\bar{2}$; table showing the determination of Frank loop by inside-outside method.

B.3 Electron irradiations on Ni-0.4Ti at 450°C

To avoid the temperature variation, another way to increase the nucleation density could be an addition of Ti given that the loop density in Ni-0.4Ti is much higher than the one in Ni. Thus, irradiations were performed on Ni-0.4Ti at 450°C.

During the irradiation, in spite of a sparse nucleation, there were more loops in Ni-0.4Ti than Ni. Figure B.5 shows the growth of several perfect loops in Ni-0.4Ti. Figure B.6 presents a post-characterization of a perfect loop in Ni-0.4Ti and this loops is interstitial-type.

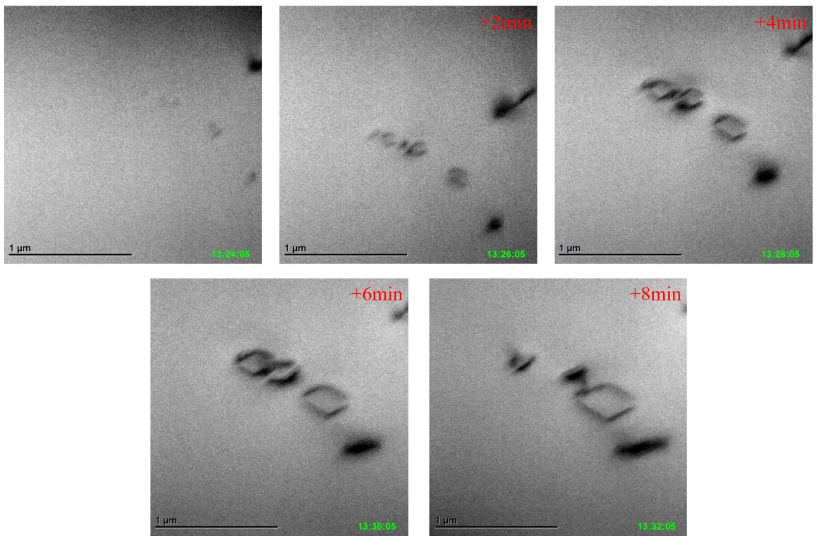

FIGURE B.5 Microstructural evolution of Ni-0.4Ti under electron at 450°C with a flux of 0.017 µA.

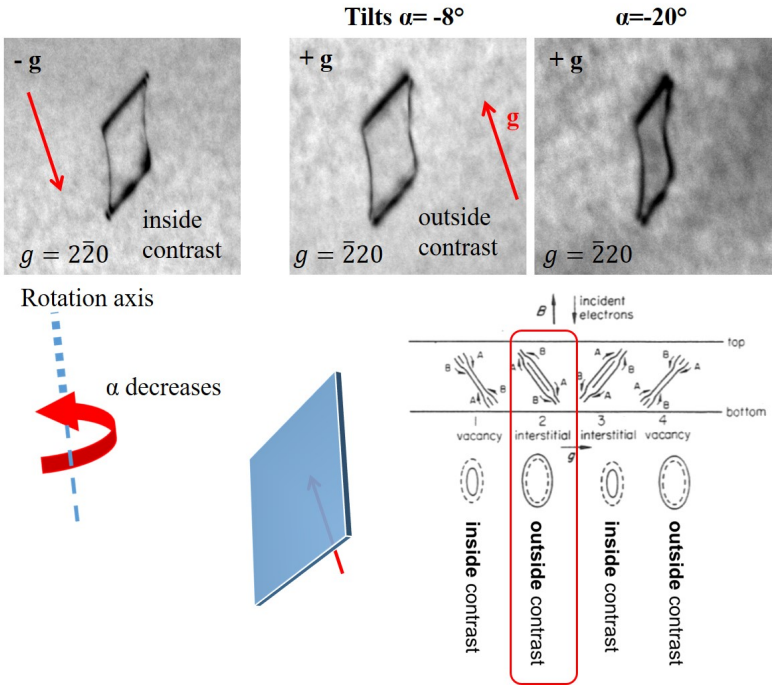

FIGURE B.6 Determination of Frank loop nature in electron-irradiated Ni-0.4Ti at 450°C.

Annexe C

Determination of specimen thickness using Convergent Beam Electron Diffusion (CBED) technique

In this part, we present in details how to apply CBED to measure thickness in our samples.

C.1 Measurement method

We take the CBED pattern in Chapter 3 (Figure 3.15) as example. The zone of interest is put in the two-beam condition with s=0, shown in Figure 3.15(a). Then the electron beam is focalized on the zone of interest and the diffraction is recorded. Then the fringe spacing $\Delta\theta_i$ and the separation spacing $2\theta_B$ of two diffraction patterns 000/2-20 are measured. $2\theta_B$ corresponds to Bragg's angle for diffracting (hkl) plane shown in Figure 3.15(b). The interplanar spacing d_{hkl} can be calculated by Eq. C.1 with known lattice constant a. The final parameter is the deviation parameter s_i that can be determined by Eq. C.2 with λ the wave-length of electrons in TEM. Based on these parameters, according to Eq. C.3, with the correct integers n_k, the plot of $\frac{s_i}{n_k}^2 = f(\frac{1}{n_k}^2)$ should be a line with the intercept of $\frac{1}{t^2}$ and the slope of $\frac{1}{\psi_g^2 n_k^2}$ where t is the thickness and ξ_g the extinction distance. n_k is a group of continuous integers that allows to have a linear correlation between $\frac{s_i^2}{n_k^2}$ and $\frac{1}{\xi_g^2 n_k^2}$.

$$d_{hkl}^2 = \frac{a^2}{h^2+k^2+l^2} \tag{C.1}$$

$$s_i = \lambda \frac{\Delta\theta_i}{2\theta_B d_{hkl}^2} \tag{C.2}$$

$$\frac{s_i^2}{n_k^2} + \frac{1}{\xi_g^2 n_k^2} = \frac{1}{t^2} \tag{C.3}$$

Figure C.1 lists the parameters involved in our case for the pure nickel in a 200 keV TEM with a diffracting plane type (220). Finally, we assigned n_k=1 for the first fringe spacing $\Delta\theta_1$ and obtained the first set of values $\frac{s_1^2}{1}^2$ (see Figure C.2). By tracing the $\frac{s_i}{n_k}^2 = f(\frac{1}{n_k}^2)$, it can be found in Figure C.3 that the first set of values does not plot a straight line. We then alter the first integer to 2 and find the second set of values (see Figure C.2). This method should be applied alternatively until a straight line is plotted and stopped with the smallest integer, as shown by the third set of value in Figure C.2. Finally, the thickness t is given by the intercept. In this example, the thickness of selected zone is about 140 nm.

a (Ni)	λ (200 keV)	$d_{(2\text{-}20)}$	$2\theta_B$	i	$2\Delta\theta_i$	$\Delta\theta_i$	s_i
nm	nm	nm	1/nm		1/nm	1/nm	1/nm
0,352	0,00251	0,124	7,941	1	1,144	0,572	0,012
				2	2,166	1,083	0,022
				3	2,969	1,485	0,031
				4	3,772	1,886	0,039

FIGURE C.1 Parameters for thickness measurement by CBED.

	n_k	$1/(n_k)^2$	$(s_i/n_k)^2$	Intercept	Slope	thickness	Extinction distance
	/	/	1/nm^2	1/nm^2	1/nm^2	nm	nm
first set	1	1,000	1,39E-04	1,01E-04	4,04E-05	100	/
	2	0,250	1,24E-04				
	3	0,111	1,04E-04				
	4	0,063	9,43E-05				
second set	2	0,250	3,47E-05	6,66E-05	-1,24E-04	123	90
	3	0,111	5,53E-05				
	4	0,063	5,84E-05				
	5	0,040	6,04E-05				
third set	3	0,111	1,54E-05	5,05E-05	-3,15E-04	141	56
	4	0,063	3,11E-05				
	5	0,040	3,74E-05				
	6	0,028	4,19E-05				

FIGURE C.2 Alternative CBED data for thickness determination.

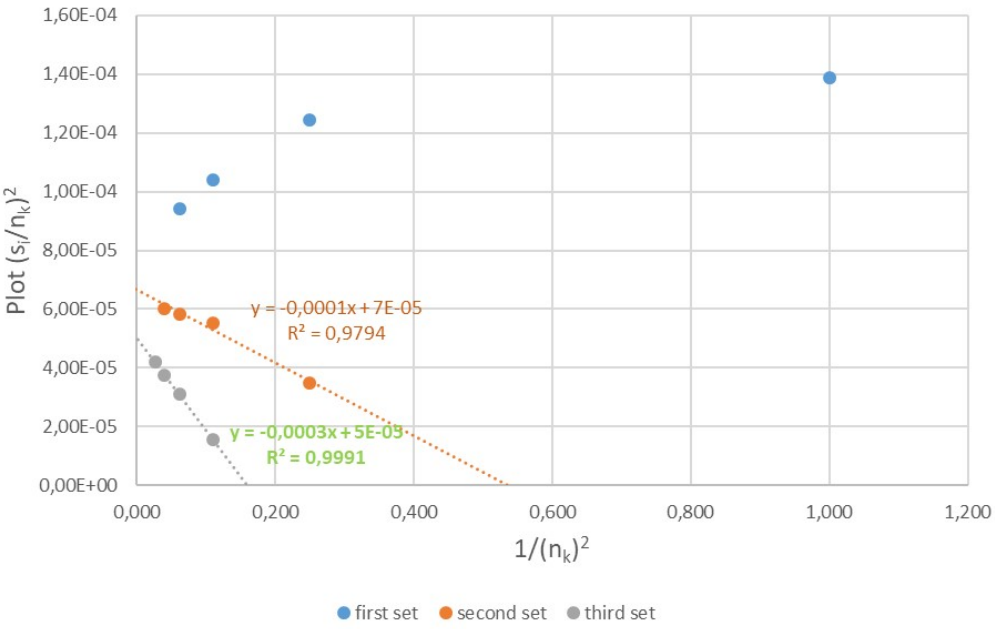

FIGURE C.3 Plot $\frac{s_i}{n_k}^2$ against $\frac{1}{n_k}^2$: if the plot is the straight line, extrapolate to the axes to find intercept.

RÉSUMÉ

Les aciers austénitiques sont prévus comme matériaux pour la gaine combustible dans les réacteurs de génération future. Le problème majeur des aciers est leur gonflement sous irradiation. La résistance au gonflement peut être améliorée en ajustant la tenue en solutés majeurs (Ni, Cr) et en alliant les solutés mineurs (Ti). L'objective de cette thèse est d'apporter une meilleure compréhension sur le comportement sous irradiation des aciers austénitiques. Nickel pur (Ni) et ses alliages (Ni-0.4Cr, Ni-0.4/0.8/1.2Ti et Ni-0.4Ti-0.1C, % en poids) sont utilisés comme matériaux modèle pour étudier les effets du Cr ou du Ti (seul ou avec carbone). Les irradiations aux ions du nickel sont effectuées aux différentes températures. L'évolution microstructural est étudiée pendant l'irradiation. Après l'irradiation, la nature des boucles de Frank, la microstructure irradiée (la densité et la taille moyenne) et l'évolution microstructural sont étudiées dans Ni en tant qu'un système de référence. Ensuite, les études comparatives sont faites dans les alliages. Les défauts sont caractérisés par Microscopie Electronique en Transmission (TEM). La ségrégation est analysée par le MET couplé à l'analyse dispersive en Energie des Rayons-X (TEM-EDS) et Sonde Atomique Tomographique (SAT).

Dans Ni, pour la première fois, les grandes boucles de Frank lacunaires sont trouvées avec une mécanisme d'éradication par les boucles de Frank interstitielles. De plus, un épaisseur critique pour la densité et la taille moyenne des boucles est identifié afin d'affranchir l'effet de surface. Dans les alliages, l'ajout du soluté change drastiquement la nature, la densité, la taille, la vitesse de montée et la mobilité des boucles de dislocation. La morphologie des boucles de Frank dépend drastiquement de leur nature. En terme de la ségrégation, une déplétion du Ti autour des boucles de dislocation dans Ni-0.4Ti irradié. Une formation des précipités TiC est identifié avec un ajout du C dans Ni-0.4Ti. Les discussions se focalisent sur les mécanismes de l'effet de surface, l'origine des boucles lacunaires et l'effet du soluté.

Nos observations des propriétés fondamentales des défauts induits par l'irradiation introduisent de nouvelles considérations dans les modélisations et contribuent à une meilleure compréhension des mécanismes fondamentales de l'endommagement d'irradiation et des effets des solutés dans la structure cubique face centré.

MOTS CLÉS

endommagement d'irradiation, alliage modèle du Ni, effet de soluté, nature de boucle de Frank, caractérisation du MET, ségrégation

ABSTRACT

Austenitic steels are foreseen as cladding materials in future reactors. The major issue of these materials is the void swelling under irradiation. Their swelling-resistance can be experimentally improved by adjusting major elements (Ni, Cr) and by alloying minor elements (Ti). This thesis aims to better understand the irradiation behavior of austenitic steels. Ultra-high purity Ni and micro-alloyed Ni (Ni-0.4Cr, Ni-0.4/0.8/1.2Ti and Ni-0.4Ti-0.1C, weight percent) are used as fcc model materials to study the influence of Cr and Ti (alone or with carbon). Self-ion irradiation experiments are performed at different temperatures. The Frank loop nature, irradiated microstructure (loop density and average size) and the real-time microstructural evolution (loop growth rate) are firstly studied in Ni as a reference system. Then, comparative studies are conducted in the alloys to reveal solute effects. The characterization is performed mainly by TEM. STEM-EDS and APT analysis are also conducted to study the segregation.

In Ni, for the first time, large stable intrinsic Frank loops are identified and an eradication mechanism of intrinsic Frank loops is clearly identified. A critical thickness is identified in function of temperature to avoid surface effects on loop density and size. In the alloys, micro-alloying of Cr and Ti (alone and with carbon) changes drastically the Frank loop nature and reduces loop mobility. The effects of Ti depend strongly on Ti concentration. Moreover the morphology of Frank loops is shown to be characteristic of their nature. The segregation is also studied in Ni-0.4Ti and Ni-Ti-C. A depletion of Ti on dislocation loops is detected in Ni-0.4Ti. Precipitation of TiC is identified in Ni-Ti-C. Discussions focus on the mechanisms of the surface effect, origin of vacancy loops and drastic effects of solute.

These observations of fundamental properties of radiation-induced defects in this thesis introduce new considerations in theoretical calculations, which will contribute significantly to a better understanding of the elementary mechanisms of radiation damage and solute effects in fcc structure.

KEYWORDS

radiation damage, Ni-based model alloys, solute effect, Frank loop nature, TEM characterization, segregation